Production and interaction of photons using atomic polaritons and Rydberg interactions

Erwan Bimbard

INSTITUT D'OPTIQUE GRADUATE SCHOOL

ÉCOLE DOCTORALE ONDES ET MATIERE

DISCIPLINE : PHYSIQUE

THÈSE

pour l'obtention du grade de Docteur en sciences
de l'Institut d'Optique Graduate School
préparée au Laboratoire Charles Fabry

soutenue le 01/12/2014

par

Erwan BIMBARD

Production and interaction of photons using atomic polaritons and Rydberg interactions

Composition du jury :

Président du Jury :	Pierre PILLET	–	Laboratoire Aimé Cotton, Orsay
Rapporteurs :	Charles S. ADAMS	–	Joint Quantum Center, University of Durham
	Jean-Michel RAIMOND	–	Laboratoire Kastler-Brossel, Paris
Examinateurs :	Pascale SENELLART	–	Laboratoire de Photonique et de Nanostructures, Marcoussis
	Matthias WEIDEMÜLLER	–	Physikalisches Institut, Universität Heidelberg
Membre invité :	Alexei OURJOUMTSEV	–	Laboratoire Charles Fabry, Palaiseau
Directeur de thèse :	Philippe GRANGIER	–	Laboratoire Charles Fabry, Palaiseau

Remerciements

Je voudrais remercier mon directeur de thèse Philippe Grangier, grâce à qui j'ai eu la chance de pouvoir travailler sur une expérience particulièrement riche, dans un contexte scientifique très motivant. Merci de m'avoir fait confiance : j'ai particulièrement apprécié de pouvoir explorer au gré de mes envies les différentes façons de progresser sur nos problématiques, expérimentales et théoriques, en pouvant toujours bénéficier en cas de souci d'un point de vue ayant bien plus de recul et d'expérience que le mien.

Je remercie aussi chaleureusement Alexei Ourjoumtsev : pour l'énergie et le temps que tu as investi dans tout le travail relié à cette thèse, en étant disponible pour répondre à toutes mes questions jusqu'au bout. Notre facilité à communiquer et à coopérer ont rendu le travail de tous les jours, au labo ou au bureau, extrêmement appréciable et enrichissant. J'ai appris une quantité de choses impressionante grâce à nos échanges, toujours en sachant que mon avis pouvait aussi être pris en compte et intégré à la réflexion. Enfin nos divers points communs comme le goût pour le voyage, l'escalade et d'autres sont autant de bonus qui se sont ajoutés au plaisir de travailler ensemble.

Je souhaite remercier Jean-Michel Raimond, Charles Adams, Pascale Senellart, Matthias Weidemüller et Pierre Pillet, pour avoir accepté de faire partie du jury qui a examiné cette thèse. J'ai été honoré qu'ils évaluent mon travail et les remercie de leurs commentaires.

Cette thèse est bien sûr le résultat d'un travail d'équipe, sans lequel rien n'aurait été possible. Je suis arrivé en 2011 dans une équipe expérimentale constituée d'Alexei et de Valentina Parigi, supportée par Florence Nogrette. Merci donc à Valentina qui a supervisé mes débuts au plus près. Le fait de pouvoir me reposer sur ton caractère calme et posé a sans aucun doute aidé à épargner ma santé mentale pendant mon début de thèse, et ta présence, dans un groupe qui a ensuite été principalement masculin, a été un plus indéniable pour l'ambiance générale ! Il en va de même pour Florence, même si tu n'es jamais partie très loin de notre labo. Grâce à toi je suis maintenant un peu moins ignorant en techniques de vide, et ton oeuvre sur le montage expérimental (en plus d'être très utile) nous aura donné l'impression de présenter une rockstar quand on présente la manip !

J'ai par la suite partagé un temps variable au labo avec plusieurs personnes, que je remercie toutes d'avoir su me supporter. J'ai eu beaucoup de plaisir à travailler avec Nicolas Vitrant : j'espère que tu en auras gardé un souvenir suffisamment bon pour continuer sur cette voie. Je remercie et je souhaite le meilleur à Rajiv Boddeda, qui a vaillament pris la suite sur notre expérience, sans jamais se décourager face aux challenges et à l'exigence toujours plus importants des manips. Thank you for always having been so kind and calm, and for your interest in understanding and discussing everything required to take control of the setup. Le montage expérimental est maintenant aux mains de Rajiv et d'Imam Usmani. Bonne chance pour la suite, et merci Imam pour ton style détendu qui m'a aidé à relacher un peu la pression sur la fin. Je remercie aussi Claude et Ti-Kai

qui ont, chacun à une extrémité de la durée de ma thèse, apporté leur pierre à l'édifice de notre expérience.

Nous avons aussi heureusement eu la chance de pouvoir compter sur des théoriciens de choc pendant toute ma thèse : Jovica Stanojevic, Andrey Grankin et Etienne Brion, avec qui discuter a toujours été très agréable et enrichissant. Merci pour votre travail et vos connaissances complémentaires aux notres qui m'ont beaucoup aidé à mieux cerner la physique de notre système.

J'ai beaucoup apprécié de participer à l'enseignement en TD et TP à l'Institut durant ma thèse. Je remercie Lionel Jacubowiez, Sébastien de Rossi et toute l'équipe des TPs, Thierry Avignon, Cédric Lejeune et Fabienne Bernard, avec qui ça a été un plaisir d'échanger, ainsi que les enseignants avec qui j'ai travaillé Gaëtan Messin, Jean-Michel Jonathan, Henri Benisty et Yvan Sortais. Enseigner m'a aussi permis de mieux connaitre des doctorants tous fort sympathiques : Samuel Lellouch, Alexandre Dobroc, Josselin Ruaudel, Quentin Bouton et Flavie Gillant (merci pour ta bonne humeur et ton optimisme à toute épreuve qui ont été un rayon de soleil dans les heures sombres de ma fin de thèse).

Je remercie également les nombreux membres des groupes voisins au LCF avec qui j'ai eu le plaisir de pouvoir interagir, et en particulier ceux du "groupe Optique Quantique étendu". Merci à Lucas Béguin pour les nombreuses discussions physiques (ou pas) et pour des délires divers et variés à base de South Park et autres ; à sa compère Aline Vernier pour des échanges toujours sympas sur la physique, la musique, les recettes de cuisine ou l'escalade ; à Ronan Bourgain pour des rencontres et des repas partagés dans des endroits relativement improbables, et pour l'enseignement en TP ; à Joseph Pellegrino pour toutes les discussions qu'on a pu avoir et pour le plaisir que j'ai eu à enseigner en TD avec toi ; à Henning Labuhn pour des découvertes musicales et des trajets en RER moins ennuyant ; aux permanents Antoine Browaeys, Yvan Sortais, Thierry Lahaye et Rosa Tualle-Brouri pour avoir toujours accueilli mes questions l'esprit ouvert ; à Guillaume Salomon et Raphaël Lopes que j'ai eu le plaisir d'apprendre à connaitre aux Houches pendant des randos/courses avec Lucas ; et dans le désordre j'ai aussi grandement apprécié le voisinage de Jean Etesse, Sylvain Ravets, Stephan Jennewein, Martin Bouillard, Mauro Persechino, Daniel Barredo, Rémi Blandino, Margaux Barbier, Mélissa Ziebell, Bashkar Kanseri, Andrew Hilliard et bien d'autres.

Je souhaite aussi adresser de vifs remerciements aux experts de l'Institut, grâce à qui nos manips sont idéalement équipées, André Guilbaud et Patrick Roth à la mécanique, Frédéric Moron et André Villing à l'électronique, Gilles Colas et Christian Beurthe en optique, ainsi qu'au personnel des services techniques Jean-Luc Cadoré, Jacky Robin, Fabrice Cartier et Nicolas Rodriguez. Merci également à toute l'administration de l'Institut, entre autres Nathalie Baudry, Aziz Aboulahyane et Jocelyne Armand, à l'administration côté école et études doctorales, ainsi qu'à Marie-Laure Edwards et Fatima Pereira à la médiathèque, qui assurent tous que l'on puisse travailler dans de bonnes conditions. Je voudrais remercier particulièrement Pierre Chavel ainsi que Eric Charron pour leur disponibilité et leur réactivité dans les procédures administratives liés à la thèse.

Enfin je veux remercier sincèrement tous les gens à l'extérieur du labo qui ont contribué à me faire garder la tête hors de la thèse régulièrement, ce qui m'a permis au final de rester sain d'esprit dans une certain mesure. Parmi eux certains ont traversé l'aventure de la thèse

en simultané de la mienne : merci à Kévin, mon presque-voisin pour toutes nos expériences filmiques, musicales, gustatives, pour l'escalade, pour ton soutien et ton aide dans toutes les situations ; merci à Guillaume, dont les multiples déménagements auront eu le mérite de me faire faire du sport, pour les soirées passées à refaire le monde en mangeant comme 4, et pour toutes les passions originales que tu auras pu me faire partager, du HTML aux RJPs et j'en passe. Merci aussi à la triplette David-Rémi-Vincent et à leurs conjoints respectifs, avec qui j'ai eu le grand plaisir de pouvoir garder contact au cours de ces années pour échanger nos expériences diverses. Merci à Aurélien, Arnaud, Jules, Maxime, Julie, Solène, Nitin, et tous les autres pour votre amitié qui ne s'essoufle pas.

Merci beaucoup aux membres de ma famille et belle-famille de m'avoir soutenu infailliblement pour aller au bout de ce que j'avais entrepris, en particulier à mes parents, à ma soeur et mon frêre (visiblement on doit avoir la thèse dans le sang, pour le meilleur et le pire !), pour tout ce que vous m'apportez.

Merci à Morgane pour toutes ces années, et pour m'avoir supporté jusqu'au bout, en me rappelant de multiples façons tout au long de ces 3 ans qu'il y avait aussi beaucoup d'autres choses, dont pas mal plus importantes qu'une thèse, qui se passaient dans le monde extérieur.

Contents

Introduction

The manipulation of isolated and controlled quantum systems has been one key effort in research over the last decades, assisted by very fast technological progress. Throughout this period, a number of elementary quantum objects have been prepared and studied in conditions close to "textbook situations". This has allowed for practical tests of the fundamental laws ruling their behaviour, which in turn deepened our understanding of these systems. It also permitted to build from bottom up structures of higher and higher degree of complexity, in which all parameters are very well controlled. These can then be used to study complex phenomena, such as magnetism in crystals [1] and other phase transitions, or more generally to design simulators to find the "answer" to a complex many-body quantum problem that cannot be solved otherwise [2, 3].

In addition, these advances in quantum systems manipulation have formed a solid basis for the development of quantum information processing, communication and computation [4]. These fields rely on the fact that one can choose, among the many microscopic systems whose behaviour is ruled by quantum mechanics, a particular elementary block in which two quantum states can be isolated and coherently manipulated, to serve as a quantum bit or *qubit*. Replacing a classical bit by a two-level quantum system opens new ways to encode, store and process information. The potential advantages can be fundamentally secure communications (quantum cryptography), as well as enhanced computation and simulation capabilities [4].

The constraints on what is expected from a "good" qubit are strict enough [5] that no general prevalence of a physical system over all others can be determined yet [4]. As a result, even two decades after the emergence of the field, many candidates are still being investigated as potential physical qubits.

Quantum information processing and communication with optical photons

When it comes to communicating quantum information over long distances and/or at high speed, optical photons constitute a plain choice of support. On top of their obvious advantages (low losses, propagation speed, simple fiber transmission ...), their relatively numerous degrees of freedom allow for various choices of encoding methods, each best adapted in different situations [6, 7]. Furthermore, a large number of simple operations can be realized very easily on photons with standard linear optics devices.

On the other hand, in order to use them as qubits, two main long-lasting hurdles must be taken. One is the deterministic on-demand generation of single-photon wavepackets in a controlled electromagnetic field mode. The second is that some sort of interaction or deterministic logical quantum operation on two photons is required in order to process the information carried around by quantum light [8]. This is for example necessary in quantum communications since for very long distances, photons are eventually submitted to losses, reducing the transmission rate and annihilating the "quantum security" of the

communications. The current widely acknowledged approach to solve this issue is to make use of quantum repeaters, which allow to propagate efficiently a quantum state over long distances using entanglement between distant photons [9, 10]. This scheme requires a logical operation between the target photon and the relay ones to transfer its information.

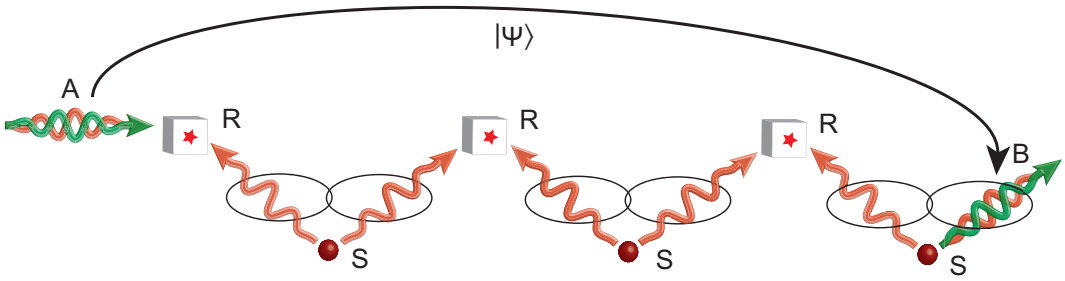

Figure 1: Principle of the quantum repeater scheme. The transmission channel is split into several smaller parts. In the middle of each portion is a source of entangled pairs of photons (S). Provided a logical operation can be realized between two photons within a given repeater node (R), and after application of entanglement purification protocols between neighbouring nodes, entanglement can be transferred efficiently to the two extreme nodes of the chain, so that finally a quantum state $|\psi\rangle$ arriving in A can be transmitted to point B with high fidelity even for large distances.

To address these practical concerns, photons in vacuum are clearly not sufficient: they are not naturally emitted in a suitable single-mode single photon state, and several photons together do not behave any differently than each of them individually. An intermediate material system is therefore necessary to enable the desired nonlinear evolutions.

More generally, the last decades of research in fields related to quantum information processing (QIP) have shown that if efficient quantum communication and computation can be achieved in a large-scale structure, it will involve a mixed architecture where different types of qubits are used for different tasks (transport, storage, processing ...), which must be able to connect to each other and exchange information in a coherent manner [11]. Photons must therefore be interfaced with matter in a way that allows for their efficient storage, processing and retrieval.

Few-photon level nonlinearities

Of very high impact for the previous matters (and many more) is the realization of optical nonlinearities active at the level of only a few photons. Standard nonlinear materials have an optical response (susceptibility, or complex refractive index) that changes under intense enough excitation, usually corresponding to large numbers of photons in the medium. Engineering systems in which the optical response is changed by only a single photon renders possible a large variety of applications, like deterministic generation of nonclassical light states, or photon-photon quantum gates, of major importance for photonic quantum information processing [12].

In the latter category, protocols are becoming experimentally realistic only recently, for a logical control-Z gate for example. Its principle is to induce a π phase shift on a photon pair's state conditioned on the fact that both are in state $|1\rangle$, in a way that preserves their overall coherence and mode properties. The physics of the process can be thought of as a very large dispersive nonlinearity. Among other things, the ability to realize such a gate is in principle a universal key to performing any quantum computation with photons [8].

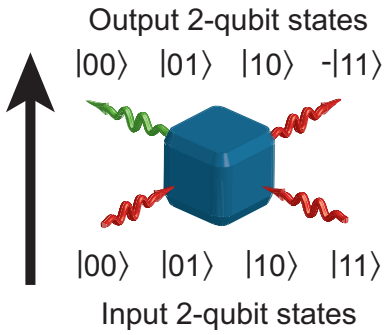

Figure 2: Principle of a control-Z gate. The two input photons, once an encoding is chosen, can be put in any superpositions of the input qubit states, and the gate should perform deterministically and coherently the described selective phase-shift of state $|11\rangle$.

The solutions imagined to reach this goal have evolved a lot in the last years, and developed in various directions in communities that use different material systems as bases for their purpose. Let us note at this general stage of the discussion that most often, in systems that are nonlinear for few photons, the full theoretical treatment of light propagation through the medium with effective photon-photon interactions is not yet available. Additionally, in some cases one can show that photons propagating together within a medium to dephase each other will exchange energy along the propagation, resulting in undesired effects on top of the nonlinearity, such as wavepackets/mode distortion [13–15]. As a result, most schemes considered as promising now try to decouple propagation and interactions, by sequentially storing the photons inside a medium, making them interact in a stationary way, and retrieving them.

The problematics of storage, generation, and interactions of photons therefore clearly overlap, and an interesting goal is to find a system that can combine efficiently solutions to all of them.

Existing solutions to generate, store and process photons

Single-photon sources

Single-photon production has been an active field for a quite long period now. Two types of avenues have mainly been explored: probabilistic heralded projection of entangled photon pairs' state, and controlled emission by a single quantum emitter.

In the first approach, atomic cascades were initially used to randomly generate correlated pairs of photons that can be separated in two modes [16]. Spontaneous parametric down-conversion in nonlinear crystals then became a widespread alternative to produce such photon pairs. Their entanglement allows one to project the state of one mode by measuring the presence of a photon in the second one, realizing an effective nonlinearity that has been used for many photonic quantum state engineering experiments [17, 18]. Protocols can be implemented in cold atomic clouds using the same principles, that will be discussed in details in this document [19–21]. The main issue with this kind of sources is their low success rate and intrinsically probabilistic behaviour.

The second approach relies on the fact that if one isolates a single two-level quantum

system, it can only emit a single photon after controlled excitation. A wide variety of emitters has been studied for this purpose, such as single atoms [22, 23], single molecules [24], Nitrogen-Vacancy centers in diamond [25, 26], or quantum dots in semiconductor structures [27]. Control over the system's properties is one of the main problems in these cases: stability of the atom-resonator coupling, or reproducibility of the quantum dots' properties due to the fabrication techniques, for example. Another recurrent issue is the collection efficiency of a photon into a usable mode once it has been emitted. However, in the field of semiconductor-based sources for example, extremely fast progress is being made toward high degree of tunability and efficiency thanks to an ever-improving fabrication technique and to the embedding of quantum dots in pillar microcavities [28].

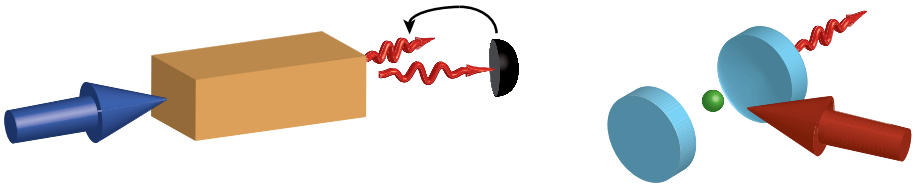

Figure 3: Two possible schemes for single-photon generation. In one case (left) a strong pump is sent into a nonlinear crystal and through frequency conversion generates pairs of correlated photons. When one of them is detected in one arm, it projects the second mode onto a single-photon state. In the second case (right) a single quantum emitter like a two-level atom is strongly coupled to the mode of an optical cavity which collects the only photon it can emit after excitation.

Quantum memories

In addition to generating photons, a versatile quantum light-matter interface must ideally also allow for their coherent storage [29, 30]. This, among other applications, would make the use of QIP schemes with limited success probabilities more realistic, as one could store the product of a certain operation step while waiting for the other steps to complete (for example in a quantum repeater). Quantum memories for light constitute alone a vast field of research, in which the decoherence of the excitations once they are stored is one of the crucial issues to be tackled. Several systems have proved interesting candidates for this task, ranging from optical cavities to hot or cold atomic vapors [31–34]. Techniques like photon echo have been developed that allow for long storage times in systems like doped crystals, through controlled rephasing of the many inhomogeneously dephased absorbers [35]. For classical light, memories with lifetimes up to a minute were demonstrated in similar systems with more sophisticated strategies [36].

Another challenge in this field is to deterministically and coherently convert an incoming few-photon quantum state into material excitations. This last point is experimentally hard to achieve for the same reasons as the reverse problem of efficient generation and collection of photons [37, 38]. The key requirement is to reach a very strong coupling between photons in a given field mode and the chosen material support, in order for them to exchange information in a coherent way.

Photon-photon interactions

Finally the last task is to realize few-photon nonlinearities and logical operations. A scheme was proposed by Knill, Laflamme and Milburn using only linear optics, but it is

probabilistic and relies on postselection of successful events, which are prohibitively rare as soon as a large number of operations is needed [39]. The principle of the CNOT gate they proposed, using projective measurements, was realized in 2003 [40].

In order to implement deterministic photon-photon interactions, the aforementioned strong coupling is required again. The principle is to let one photon couple to a system and modify its properties, so that the second one impinging on it experiences a different response. One of the photons not being strongly coupled with the system would result in the nonlinearity being either suppressed or probabilistic.

Using a single two-level system inside a high-finesse optical cavity has been known to enable very strong nonlinearities, and was proposed as a realistic basis for scalable photonic quantum computing [41]. In the strong-coupling regime, the eigenstates and energies of the total system are significantly rearranged by the coupling, leading to strong anharmonicity, and thus a completely different response for one or two excitations. The study of this regime, known as cavity Quantum Electrodynamics (QED), is motivated in the optical domain by the numerous demonstrations of quantum state manipulation achieved in microwave cavity QED [42, 43]. Implementations of this scheme with optical photons already lead to major results in the last decade, in very different physical systems. Using a "bulk" high-finesse cavity and "real" atoms, the large nonlinearity of this system's spectrum was investigated and exploited to observe photon-photon blockade [44] or binding [45], as well as very recently to deterministically entangle a photon with an atom or with another photon [46]. An analogous system can be realized in solid state structures with quantum dots as "artificial" atoms embedded in semiconductor microcavities. Very similar phenomena lead in these systems to observe large phase modulations by few-photon light pulses [47], generation of non-classical light [48] and all-optical switching of the system's behaviour by pulses at the single-photon level [49]. Finally, the requirement to achieve strong atom-light coupling while keeping the photons modes under control lead to an original approach using the mode confinement of an optical fiber, whose mode can be directly coupled to a microresonator. The latter plays the role of the enhancing cavity, in the evanescent field of which a single atom can be placed to generate strong effective photon-photon interactions. This resulted in the recent observation of single-photon switching [50] or large single-photon nonlinear phase-shifts [51].

Our roadmap

This thesis presents different experiments addressing more or less directly some of the points raised in the above discussion. They were realized using a cold (but thermal) trapped atomic cloud in a low-finesse optical cavity as a common experimental basis. This system was chosen for its versatility and assets as an interface and processing tool for photons: for both storage and generation of non-classical states of light, atomic ensembles are known to have high-level capabilities. In addition, the recent developments around Rydberg physics in many-atom clouds have made them a high-interest platform to study large optical nonlinearities, in systems that are relatively easy to prepare and manipulate, as will be discussed in this manuscript.

The experimental roadmap of our project is therefore based on the following elements:

• **Atoms and cavity:** Using cold atoms, one benefits from well established preparation techniques to generate a system that has stable, well defined and narrow optical transitions around the visible spectrum, with relatively slow and understood decoherence processes. This makes them a prime choice for interfacing with optical photons, as well as for being the source of large nonlinearities.

An optical cavity increases the effective atom-photon coupling by making them interact a large number of times, and defines discrete modes that can be used to keep a good control over the photons' shape in the process. However, if one wants to strongly couple light to a single atom in the cavity, it has to be done in very stringent conditions (small mode volume, high cavity finesse), which we want to avoid.

• **Polaritons and EIT:** The alternative way to strongly couple a cavity-mode photon to a cold atomic medium is to make use of collective interference effects that arise when many atomic dipoles are excited or radiate together. A photon is then coupled to collective excitations of the cloud, which are delocalized and can support a spatial phase pattern covering many wavelengths [37]. Then, when for example many atoms radiate collectively a single excitation, interferences between all the emitted fields can lead to an overall highly directional or phase-matched emission, in a situation where a single atom would have radiated isotropically [52]. A cloud of atoms can therefore be effectively coupled to a specific field mode more efficiently than a single one.

From a different viewpoint, a photon propagating in the cloud can be described as a delocalized collective pseudo-particle, usually called a polariton (or spin wave) [53]. This excitation inherits properties partially from light and from the atoms. If light only couples resonantly ground-state atoms to a short-lived excited state, the main effect will be that the excitation acquires a finite lifetime, and will be scattered and lost rapidly.

However, using a lambda three-level atomic scheme, where Electromagnetically Induced Transparency is enabled by a strong coupling beam to a third long-lived state, the situation is quite different [54]: the control beam transfers all excitation amplitudes directly to the second ground state, which means the excitation can now survive in the cloud for a long time in principle. The properties of the polaritons propagating through the medium can be set via the control beam, especially their effective propagation speed. Photons can then cross the atomic sample almost without losses, but at an extremely low speed [55], and can also be entirely converted into motionless atomic excitations [37].

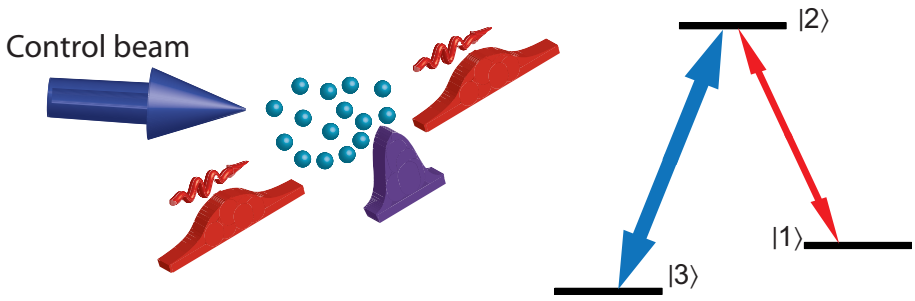

Figure 4: Picture of the propagation of a photon inside a medium as an EIT-polariton. A photon sent in the medium close to the $|1\rangle \rightarrow |2\rangle$ transition, in the presence of the control beam coupling toward the long-lived state $|3\rangle$, is mapped onto a slow and compressed excitation wave which propagates inside the medium partially carried by the atomic coherences, before exiting it as a photon again.

Due to these various properties, the use of collective excitations in cold atomic clouds, in schemes related to EIT, has been a very fruitful platform for studying light-matter quantum interfaces [30]. However, one must remember that at all times, for the excitation to behave as described, it must keep its collective phase coherence, which also makes it a relatively fragile object, especially versus temperature and atomic motion.

• **Atomic nonlinearities in photonic evolution:** The approach we (and others) chose to follow is therefore to use the cavity to efficiently map photons in and out of the cloud as atomic polaritons, and to take advantage of all the possibilities of cold atomic physics to make them effectively act on photons. In particular, atomic nonlinearities can in principle be mapped onto the state of light to realize photon-photon interactions.

One possibility is to use the intrinsic nonlinearity of the atomic response: the behaviour of few-level atoms under carefully designed excitation conditions can induce a very strong nonlinear optical response, which could be put to contribution in our system [56]. However it does not really make the most of this system as it uses only "single-atom" types of response, and after a considerable research effort in these directions the achievement of few-photon level nonlinearities has remained elusive so far (outside the cavity-QED regime).

• **Rydberg atoms:** An idea in constant expansion during these last years is to use directly the interactions between atoms to generate interactions between photons. Making neutral atoms interact can be done by temporarily exciting them from their ground state (where their interactions are negligible in our range of parameters) into a highly excited Rydberg state (with large principal number n). These atomic states can carry an extremely large dipole moment, and thus exhibit strong dipole-dipole interactions [57]. After the first direct observation of the effect of these interactions in thermal atoms [58] and in cold atomic clouds [59, 60], the number of potential applications of such strong controllable interactions has been quickly increasing. For short enough interatomic distances, the total blockade of double excitation possibility by the interactions in atom pairs was proposed [61] and later on demonstrated [62, 63] as a mean to realize a controlled two-qubit gate on two individual atoms. This Rydberg excitation blockade mechanism and its consequences have also been extensively studied in cold many-atoms systems: it has in particular the effect of limiting the number of excitations a finite cloud can accommodate [64–66]. This alone has strong consequences and allows in some regimes to use an entire cloud containing Rydberg excitations as a support for quantum information processing [67].

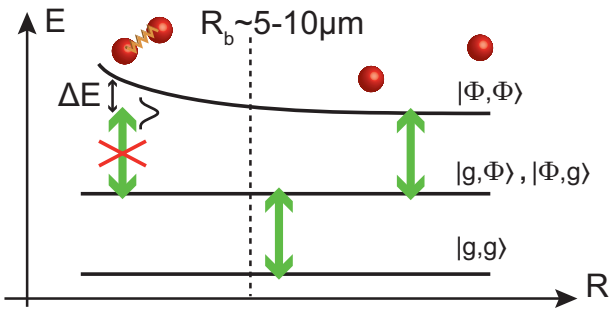

Figure 5: Rydberg blockade mechanism. In the two-atom basis, the system starts from its ground state $|g,g\rangle$, and due to a laser excitation with a finite linewidth (green arrows), each atom can be excited from $|g\rangle$ to a Rydberg state $|\Phi\rangle$. However, from the singly excited state, the interactions shift the doubly excited one $|\Phi,\Phi\rangle$ out of resonance for interatomic distances R below a certain blockade radius R_b.

A more detailed overview of the possibilities of Rydberg atoms in quantum information

is presented in this manuscript at the beginning of part V (or see [68]). Among the proposals of broadest interest based on these, let us quote the implementation of efficient deterministic quantum repeaters [69, 70], or the realization of a Rydberg-based quantum simulator [71].

Besides the purely QIP motivations, Rydberg atoms provide a interesting way to probe different aspects of many-body interacting systems, such as interaction-induced atomic motion [72], collective behaviours [73], emergence of strong spatial correlations [74], or sub-poissonian excitation statistics [75].

From a practical side, Rydberg states can be addressed using a two-photon coupling scheme very close to the EIT situation, in a ladder configuration [76]. As these states are also relatively long-lived, it is possible in this situation to map photons onto delocalized Rydberg polaritons in the atomic cloud, which behave in a strongly nonlinear way. Using such schemes and the peculiar properties of Rydberg polaritons, it was very recently demonstrated that one could experimentally realize effective optical nonlinearities so strong that they become efficient at the single-photon level [12, 77], as will be discussed in details in the main text.

• **Homodyne tomography:** When trying to realize a quantum gate on two photons for example, one should fully characterize their state to assess the quantum coherence of the process: from two arbitrary qubit states it should retrieve photons in the corresponding output entangled quantum state, and in subsequently usable optical modes [78]. Depending on the type of encoding, this full characterization may be difficult to implement in practice. Based on the past experience of the group and the different members of the team, our goal is to implement optical quantum state tomography as a characterization technique. This, as will be described in the main text, allows one to reconstruct completely the quantum state of light generated by a process, thereby giving access to all necessary information. Due to its principle, the ability to detect efficiently the output photons with this method also constitutes a direct proof of a very good control over their mode. In the past, it has been for example extensively applied to parametric down-conversion sources [17].

Thesis layout

This manuscript is organized in the following manner:

• In Part I, we set the general framework, and introduce the theoretical tools useful to describe our experiments. We discuss the effective susceptibility of the atoms in the cavity mode, that summarizes the interactions between classical light and atomic medium in the system. A particular interest is directed to reviewing the classical lowest-order nonlinearities that can be induced by few-level atomic clouds, and their relative strengths. In the low-light regime where we will be interested in describing the quantum state of light interacting with the system, we recall briefly the fundamentals of quantum state reconstruction by optical homodyne tomography.

• In Part II, we present the various parts of our experimental setup. The atom trap and the necessary setup to load it and characterize it, together with the optical cavity, constitute the physical basis of all our experiments. These elements are driven and characterized by the laser sources and the control/acquisition system.

• In Part III, an experiment in the "quantum light" regime is described, with no Rydberg interactions introduced in the system yet. We demonstrate how our setup can be used to store photons as collective atomic excitations, and retrieve them later on in a single free-propagating mode with high efficiency. The protocol used allows us to generate high-quality single photons, as is evidenced by the full quantum state reconstruction performed via homodyne detection.

• In Part IV, we turn to the investigation of the properties of a Rydberg cloud in the cavity. Realized in the classical regime, this experiment explores the dispersive nonlinear effects at very low intensities that are induced by the interactions between Rydberg atoms in the cloud. This allows to comment, in the dispersive regime, on a simple and practical description of Rydberg excitations in cold gases as generating "blockade spheres" inside which the medium's behaviour is changed. These spheres can have very large influence on the overall response, which leads to the exaggerated nonlinearity of these media.

• In Part V, we discuss the last and still ongoing project we undertook, to bring together the Rydberg interactions in cold atomic clouds and the capabilities of homodyne tomography. Achieving large few-photon nonlinear effects is now known to be achievable in Rydberg clouds, but requires to work in quite stringent experimental conditions. We describe how we modified our system in order to reach this quantum nonlinear regime. We also discuss some theoretical ideas to use Rydberg nonlinearities inside a cavity in order to design quantum state processing protocols, to be characterized by tomographic reconstruction.

Part I

Description of light, atoms and their couplings

Chapter 1

Matter-field coupling effects in a many atoms-cavity system

Contents

In this chapter we will set the general framework for the description of the coupling between the cavity mode photons and the atoms, through different levels of analysis, as summarized in table (1.1).

In a classical picture, the way to access the medium's optical susceptibility will be discussed. Throughout this work, its experimental characterization or theoretical evaluation will help us understand the medium's properties and how useful they can be in different regimes.

The full quantum treatment of the system will then be presented, via Bloch equations. In the case of a classical feeding, it will be related to the classical description, and the cooperativity C will be introduced to quantify the effective coupling of the atomic ensemble to the cavity mode [79].

Model	System considered as ...	Meaningful quantity
Fully classical	global homogeneous medium having an index effect on the classical field's propagation	Susceptibility
Fully quantum	N individual atoms with coherences coupled to the cavity field's quantum operator	Atomic coherences
Semi-classical	cavity field in a classical coherent state affected by the N atoms' coherences	Effective susceptibility

Table 1.1: Different descriptions of the {cavity+atoms} system.

The quantum description also allows for the definition of the effective atomic susceptibility, taking into account the spatial variations of the light modes and atomic density in the system. It will be particularly important when characterizing the effects of a nonlinear susceptibility, such as optical bistability [80, 81]. The aim is to propose a single uniform definition for quantities that will be used in the rest of this manuscript, in particular to quantify the strong dispersive nonlinearities we will be interested in.

Starting from the simplest example of two-level atoms in the cavity, the established framework will then be used to briefly describe the linear behaviour of the system, and the strength of the nonlinearity it can produce.

Finally, this work deals mostly with one specific atomic excitation scheme, with three-level atoms and strong couplings inducing phenomena like Electromagnetically Induced Transparency [54]. The description of its effects in our system –linear and nonlinear– is the last part of this chapter.

Table (1.2) summarizes the different schemes that will be discussed, with their characteristic linear features and mechanisms for dispersive nonlinearities.

Two-level atoms	
linear regime	dispersion and absorption, cooperativity
nonlinear regime	off-resonant saturation of the transition
Multilevel atoms	
linear regime	electromagnetically induced transparency
nonlinear regime	off-resonant saturation of the 2-photon transition resonant schemes in 4-level atoms

Table 1.2: Different cases of atoms-cavity coupling schemes with their linear characteristics and possibilities in terms of dispersive nonlinearities.

1.1 Classical description

We consider simply the linear optical cavity of length L containing an arbitrary atomic medium, driven by a classical light field at frequency ω, corresponding to a wave vector $k = \frac{\omega}{c}$. The cavity has an eigenmode with frequency ω_c close to resonance with the incident light field.

1.1.1 Classical matter-field interactions: susceptibility

The classical optical response of the medium is fully described by its complex susceptibility χ [82], which links the average dielectric polarization $\vec{P}$ to the driving field $\vec{E}$[1]: $\vec{P} = \epsilon_0 \chi \vec{E}$. The susceptibility in return describes the absorption and dephasing effects of the medium on the light, through its refractive index ($n^2 = 1 + \chi$). Experimentally, it can be accessed by measuring the transmission of a probe beam through the cavity.

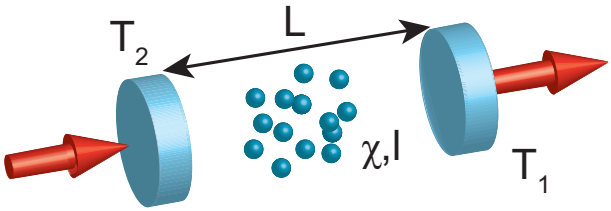

Figure 1.1: Configuration of the cavity and atomic medium..

The configuration we are interested in is an asymmetric cavity, with mirror transmissions T_1 (output mirror) and T_2 (injection mirror), as depicted in figure (1.1). The one-way propagation factor for light amplitude through the cavity is $e^{ik(L+(n-1)l)} \approx e^{ikL+ik\frac{\chi}{2}l}$, l being the effective length of the medium. The cavity transmission in intensity is, under the assumptions that $k|\chi|l, T_1, T_2 << 1$ and $T_2 << T_1$ [79]:

$$T_{cav} = \frac{T_1 T_2}{(\frac{T_1}{2} + kIm[\chi]l)^2 + 4\sin^2(kL + \frac{kRe[\chi]}{2}l)} \approx \frac{T_0}{(1 + \frac{2k}{T_1}Im[\chi]l)^2 + (\theta + \frac{2k}{T_1}Re[\chi]l)^2} \tag{1.1}$$

The second expression is obtained in the vicinity of a given resonance ($\omega \approx \omega_c = p\frac{\pi c}{L}$, p integer, and $|(\omega - \omega_c)\frac{L}{c} + \frac{kRe[\chi]}{2}l| << 1$). The cavity detuning $\theta = \frac{\omega - \omega_c}{\kappa}$ has been defined, and $\kappa = \frac{cT_1}{4L}$ is the cavity field damping rate.

With no atoms in the cavity ($\chi = 0$), one recognizes the approximate Lorentzian expression of a transmission line of the Fabry-Pérot cavity around resonance:

$$T_{cav}^{noatoms} = \frac{T_0}{1 + \theta^2} \tag{1.2}$$

Therefore, the general effect of an atomic susceptibility present in the cavity is to distort a resonance line, in terms of its position in the variable θ (line shifted from $\theta = 0$ because the medium changes the cavity's effective optical length) and in terms of its amplitude of transmission (the medium absorbs and scatters some light from the cavity mode). Each of these effects in turns give access to measurements of the real or imaginary parts of χ.

1.1.2 From classical to semi-classical: quantized atoms

If the medium is constituted of an atomic cloud of density μ, assuming homogeneous conditions where each of them carries the same individual dipole $\vec{d}$, the dielectric polarization is:

$$\vec{P} = \mu \vec{d} \tag{1.3}$$

1. In this section the general convention is that a complex quantity Q (like $\vec{P}$, $\vec{E}$ or $\vec{d}$) corresponds to a real measurable value written $Q_R = Q + Q^\dagger$.

This induced dipole could very well be considered as a completely classical one. Here, in a semi-classical point of view, the atomic states are considered as quantized, with a given optical transition $|1\rangle \rightarrow |2\rangle$ of frequency ω_a close to resonance with the driving field, responsible for the value of the susceptibility.

On this transition, the dipole operator is:

$$\hat{\vec{d}}_R = \hat{\vec{d}} + \hat{\vec{d}}^\dagger = d_0 \vec{u}(\hat{\sigma} + \hat{\sigma}^\dagger) \tag{1.4}$$

where $\hat{\sigma} = |1\rangle\langle 2|$. The equivalent of the classical complex dipole is $\vec{d} = d_0 \vec{u}\langle\hat{\sigma}\rangle$, where $\langle\hat{\sigma}\rangle$ is the average coherence between levels $|1\rangle$ and $|2\rangle$ created by the field, which must be calculated quantum-mechanically.

The classical field $\vec{E}_R = \vec{E} + \vec{E}^* = E_0\vec{u}(e^{i\omega t} + e^{-i\omega t})$ (with E_0 real) interacts with the quantized atoms via the following Hamiltonian, introducing the Rabi frequency Ω [2], and performing the rotating wave approximation [83]:

$$-\hat{\vec{d}}_R.\vec{E}_R = -d_0 E_0(e^{-i\omega t}\hat{\sigma}^\dagger + e^{i\omega t}\hat{\sigma}) = \frac{\hbar\gamma\Omega}{2}(e^{-i\omega t}\hat{\sigma}^\dagger + e^{i\omega t}\hat{\sigma}) \tag{1.5}$$

With these definitions, the susceptibility can be re-expressed as:

$$\chi = \frac{\vec{P}.\vec{u}}{\epsilon_0 \vec{E}.\vec{u}} = -\frac{\mu d_0^2}{\epsilon_0 \hbar}\frac{\langle\hat{\sigma}\rangle}{\gamma\Omega/2} = -\frac{\alpha_0}{k}\frac{\langle\hat{\sigma}\rangle}{\Omega/2} \tag{1.6}$$

where in the last step we used the expressions of the dipole damping rate $\gamma = \frac{d_0^2 k^3}{6\pi\epsilon_0\hbar}$, of the effective resonant atomic cross-section $\sigma_{eff} = \frac{3\lambda^2}{2\pi} = \frac{6\pi}{k^2}$, and $\alpha_0 = \mu\sigma_{eff}$.

The cavity transmission can therefore be put in the following form, to which we will come back later, where the relevant quantity $\frac{\langle\hat{\sigma}\rangle}{\Omega/2}$ was isolated, that will be called "reduced susceptibility":

$$T_{cav} = \frac{T_0}{\left(1 - \frac{2\alpha_0 l}{T_1} Im[\frac{\langle\hat{\sigma}\rangle}{\Omega/2}]\right)^2 + \left(\theta - \frac{2\alpha_0 l}{T_1} Re[\frac{\langle\hat{\sigma}\rangle}{\Omega/2}]\right)^2} \tag{1.7}$$

The exact expression of the reduced susceptibility then depends on the details of the excitation scheme, and can also depend on the light intensity itself. A more rigorous description of these aspects requires a complete quantum model for both the field and the atoms.

1.2 Quantum treatment of the many atoms-cavity system

Quantum-mechanically speaking, our system is made of a single quantized field mode in the cavity, behaving as a harmonic oscillator, coupled to an assembly of many atoms with several possible transitions and potentially complex dynamics, with various external feedings. Its quantum description will depend on the exact excitation scheme used, but relies on a basis model that will be expressed here in a stand-alone manner.

1.2.1 Notations and model for the quantum evolution of the system

Cavity mode

The quantum description will be restricted to photons sent to the cavity in its fundamental Gaussian $TEM00$ transverse mode [84], its axis being oriented along the z direction

2. Everywhere, for notation simplicity, the Rabi frequency is defined normalized by γ, the first excited state decay rate.

by definition. These photons excite close to resonance one specific high-order longitudinal cavity mode. For this mode, the Schrödinger picture operator for the field polarized along direction $\vec{u}$, with wave vector $k_c = \frac{\omega_c}{c}$, is defined as [85]:

$$\hat{\vec{E}}_R(\vec{r}) = \sqrt{\frac{\hbar\omega_c}{2\epsilon_0 V_g(z)}}\vec{u}\cos(k_c z)\mathrm{e}^{-\frac{x^2+y^2}{w(z)^2}}(\hat{a}^\dagger + \hat{a}) = \sqrt{\frac{\hbar\omega_c}{2\epsilon_0 V_g(0)}}\phi(\vec{r})\vec{u}(\hat{a}^\dagger + \hat{a}) \tag{1.8}$$

The $\hat{a}$ operator is the annihilation operator of a photon inside the cavity mode. The spatial mode function $\phi(\vec{r}) = \frac{w_0}{w(z)}\cos(k_c z)\mathrm{e}^{-\frac{x^2+y^2}{w^2}}$ describes a radial Gaussian profile with a z-dependent waist $w(z) = w_0\sqrt{1+\frac{z^2}{z_R^2}}$ where $z_R = \frac{\pi w_0^2}{\lambda}$ is the Rayleigh range, and a longitudinal standing wave pattern along the cavity axis. The normalization is given by the effective volume[3] $V_g(z) = \frac{\pi}{4}Lw(z)^2$. In all the following we will consider atoms localized within the Rayleigh range of the cavity mode, such that the field seen by the atoms will be taken with $w(z) \approx w(0)$.

Hamiltonian

In a general approach, the systems described are made of an ensemble of N atoms, indexed by k, with at least one interesting optical transition interacting with the only relevant cavity mode. These atoms can have other transitions excited in an arbitrary scheme by other beams, but the cavity mode interacts only with this isolated transition. The Hamiltonian of this system therefore reads in the electric dipole approximation [83]:

$$\hat{H} = \hbar\omega_c\hat{a}^\dagger\hat{a} + \sum_k \hbar\omega_a\hat{\sigma}_k^\dagger\hat{\sigma}_k - \sum_k \hat{\vec{d}}_{R,k}.\hat{\vec{E}}_R(\vec{r}_k) + \hat{H}_{sup} \tag{1.9}$$

where $\hat{H}_{sup}$ contains the additional excitation scheme's components, but in particular does not involve $\hat{a}$.

In the rotating wave approximation [83], this simplifies to:

$$\hat{H} = \hbar\omega_c\hat{a}^\dagger\hat{a} + \sum_k \hbar\omega_a\hat{\sigma}_k^\dagger\hat{\sigma}_k - \sum_k \hbar g_k(\hat{a}\hat{\sigma}_k^\dagger + \hat{a}^\dagger\hat{\sigma}_k) + \hat{H}_{sup} \tag{1.10}$$

where the coupling coefficient for each atom is $g_k = g_0\phi(\vec{r}_k)$ with $g_0 = d_0\sqrt{\frac{\omega_c}{2\epsilon_0\hbar V}}$. $V = V_g(0) = \frac{\pi}{4}Lw_0^2$ is the optimum effective mode volume.

Density matrix and master equation description

Due to the finite lifetime of the atomic excited state and to the cavity mirrors losses, the system is not fully hamiltonian and closed. Its quantum state must therefore be described by the density matrix $\hat{\rho}$, whose evolution follows the master equation $\dot{\hat{\rho}} = \mathcal{L}[\hat{\rho}]$. $\mathcal{L}$ is the

3. The normalization volume $V_g(z)$ is found by imposing the value of the energy flux through a plane at fixed z due to one of the propagating components of the field $\hat{\vec{E}}_+$. It must be given by the quantized energy in the mode and the time it takes one photon to achieve a full round trip in the cavity $\frac{c}{2L}$. That is to say with $\hat{\vec{E}}_+(\vec{r}) = \sqrt{\frac{\hbar\omega_c}{2\epsilon_0 V_g(z)}}\vec{u}\frac{e^{ikz}}{2}\mathrm{e}^{-\frac{x^2+y^2}{w(z)^2}}(\hat{a}^\dagger + \hat{a})$:

$$\Phi = \epsilon_0 c\int \mathrm{d}^2\vec{r}\left\langle\hat{\vec{E}}_+(\vec{r})^2\right\rangle = \hbar\omega_c(\langle\hat{a}^\dagger\hat{a}\rangle + \frac{1}{2})\frac{c}{2L}$$

Liouvillian operator of the evolution [86, 87], containing non-hamiltonian loss terms in addition to the hamiltonian component.

For the average value $\left\langle \hat{A} \right\rangle = Tr(\hat{A}\hat{\rho})$ of any operator $\hat{A}$, the master equation translates into:

$$\frac{\mathrm{d}}{\mathrm{d}t}\left\langle \hat{A} \right\rangle = Tr(\dot{\hat{\rho}}\hat{A}) = Tr(\hat{A}\mathcal{L}[\hat{\rho}]) \tag{1.11}$$

The hamiltonian part of the evolution is given by $\mathcal{L}_H[\hat{\rho}] = -\frac{i}{\hbar}[\hat{H}, \hat{\rho}]$ such that in the purely hamiltonian case the evolution of $\left\langle \hat{A} \right\rangle$ is given by $\frac{\mathrm{d}}{\mathrm{d}t}\left\langle \hat{A} \right\rangle = -\frac{i}{\hbar}\left\langle [\hat{A}, \hat{H}] \right\rangle$.

Cavity and atomic decay terms

The intracavity field's decay is described by the Liouvillian:

$$\mathcal{L}_c[\hat{\rho}] = \kappa(2\hat{a}\hat{\rho}\hat{a}^\dagger - \hat{a}^\dagger\hat{a}\hat{\rho} - \hat{\rho}\hat{a}^\dagger\hat{a}) \tag{1.12}$$

With this definition, κ describes the cavity field's amplitude damping rate.

Along the same line, spontaneous emission from excited atoms is described by a sum over all atoms of independent decay Liouvillians of the following form:

$$\mathcal{L}_a^k[\hat{\rho}] = \gamma(2\hat{\sigma}_k\hat{\rho}\hat{\sigma}_k^\dagger - \hat{\sigma}_k^\dagger\hat{\sigma}_k\hat{\rho} - \hat{\rho}\hat{\sigma}_k^\dagger\hat{\sigma}_k) \tag{1.13}$$

$$\tag{1.14}$$

With these conventions, γ is well defined as the dipole damping rate of an individual atom.

Complete Liouvillian of the system

Consider the evolution of the atoms coupled to the cavity mode, which is in turn fed externally by a classical field at frequency ω. The corresponding Liouvillian operator is:

$$\begin{aligned}\mathcal{L}[\hat{\rho}] \;=\; & -\frac{i}{\hbar}[\hbar\omega_c\hat{a}^\dagger\hat{a} + \sum_k \hbar\omega_a\hat{\sigma}_k^\dagger\hat{\sigma}_k - \sum_k \hbar g_k(\hat{a}\hat{\sigma}_k^\dagger + \hat{a}^\dagger\hat{\sigma}_k) + \hbar\lambda(\hat{a}\mathrm{e}^{i\omega t} + \hat{a}^\dagger\mathrm{e}^{-i\omega t}) + \hat{H}_{sup}, \hat{\rho}] \\ & +\kappa(2\hat{a}\hat{\rho}\hat{a}^\dagger - \hat{a}^\dagger\hat{a}\hat{\rho} - \hat{\rho}\hat{a}^\dagger\hat{a}) + \gamma\sum_k(2\hat{\sigma}_k\hat{\rho}\hat{\sigma}_k^\dagger - \hat{\sigma}_k^\dagger\hat{\sigma}_k\hat{\rho} - \hat{\rho}\hat{\sigma}_k^\dagger\hat{\sigma}_k)\end{aligned} \tag{1.15}$$

where λ is related to the feeding light field's amplitude.

After transforming the operators $\hat{a}$ and $\hat{\sigma}$ into the frame rotating at frequency ω, the Bloch equations resulting from this Liouvillian can be written as:

$$\begin{cases} \frac{\mathrm{d}}{\mathrm{d}t}\langle\hat{a}\rangle & = i\left(\kappa(\theta+i)\langle\hat{a}\rangle - \lambda + \sum_k g_k\langle\hat{\sigma}_k\rangle\right) \\ \frac{\mathrm{d}}{\mathrm{d}t}\langle\hat{\sigma}_k\rangle & = -\frac{i}{\hbar}\left\langle[\hat{\sigma}_k, \hat{H}_{sup}]\right\rangle + i\left(\gamma(\Delta+i)\langle\hat{\sigma}_k\rangle - g_k\langle\hat{a}\hat{\sigma}_{z,k}\rangle\right) \\ \frac{\mathrm{d}}{\mathrm{d}t}\langle\hat{\sigma}_{z,k}\rangle & = -\frac{i}{\hbar}\left\langle[\hat{\sigma}_{z,k}, \hat{H}_{sup}]\right\rangle - 2\gamma(1+\langle\hat{\sigma}_{z,k}\rangle) + 2ig_k\left(\left\langle\hat{a}\hat{\sigma}_k^\dagger\right\rangle - \left\langle\hat{a}^\dagger\hat{\sigma}_k\right\rangle\right) \end{cases} \tag{1.16}$$

where the normalized laser-atoms detuning $\Delta = \frac{\omega-\omega_a}{\gamma}$ has been defined. Here $\hat{\sigma}_{z,k} = |2\rangle_k\langle 2|_k - |1\rangle_k\langle 1|_k = 2\hat{\sigma}_k^\dagger\hat{\sigma}_k - 1$ is the population difference operator of atom k. Note that the first equation does not contain $\hat{H}_{sup}$ because by construction it does not involve $\hat{a}$ and thus commutes with it.

1.2.2 From quantum to semi-classical: coherent field

Cavity transmission from Bloch equations

Under the assumption that the fields in and out of the cavity are classical, one can set the cavity mode's field operator to a classical coherent state $\hat{a} \approx \alpha$. The first Bloch equation above in steady state gives:

$$\frac{\lambda}{\kappa} = (\theta + i)\alpha + \sum_k \frac{g_k}{\kappa} \langle \hat{\sigma}_k \rangle \tag{1.17}$$

As α is related to the intracavity field and λ to the incident one, an arbitrarily normalized cavity transmission would be $\left|\frac{\alpha}{\lambda/\kappa}\right|^2$. From the previous equation one gets:

$$\frac{\alpha}{\lambda/\kappa} = \frac{1}{\theta + i + \sum_k \frac{g_k}{\kappa} \frac{\langle \hat{\sigma}_k \rangle}{\alpha}} = \frac{1}{\theta + i + \sum_k \frac{g_k^2}{\kappa\gamma} \frac{\langle \hat{\sigma}_k \rangle}{g_k \alpha/\gamma}} \tag{1.18}$$

This can be put in parallel with equation (1.7), as it is equivalent to:

$$T_{cav} = \frac{T_0}{\left(1 + Im[\sum_k \frac{g_k^2}{\kappa\gamma} \frac{\langle \hat{\sigma}_k \rangle}{g_k \alpha/\gamma}]\right)^2 + \left(\theta + Re[\sum_k \frac{g_k^2}{\kappa\gamma} \frac{\langle \hat{\sigma}_k \rangle}{g_k \alpha/\gamma}]\right)^2} \tag{1.19}$$

To complete the comparison, let us note that for $\hat{a} \approx \alpha$, the atom-field coupling Hamiltonian considered here is $-\sum_k \hbar g_k \alpha(\hat{\sigma}^\dagger + \hat{\sigma})$. This is completely equivalent to the semi-classical description of section 1.1.2, defining an intracavity position-dependent Rabi frequency $\Omega(\vec{r}_k) = -2\alpha g_k/\gamma = \Omega_0 \phi(\vec{r}_k)$.

Homogeneous case: cooperativity

Inside the cavity, each atom's coherence $\langle \hat{\sigma}_k \rangle$ is driven locally by the Rabi frequency $\Omega(\vec{r}_k)$, and its steady state value is therefore function of $\Omega(\vec{r}_k)$, linear in the lowest order. Therefore in the case of a homogeneous system, but also in simple cases like the linear regime in some excitation schemes, the quantity $\frac{\langle \hat{\sigma}_k \rangle}{\Omega(\vec{r}_k)/2}$ is the same for all atoms.

In these cases, equation (1.19) is equivalent to:

$$T_{cav} = \frac{T_0}{\left(1 - (\sum_k \frac{g_k^2}{\kappa\gamma}) Im[\frac{\langle \hat{\sigma} \rangle}{\Omega/2}]\right)^2 + \left(\theta - (\sum_k \frac{g_k^2}{\kappa\gamma}) Re[\frac{\langle \hat{\sigma} \rangle}{\Omega/2}]\right)^2} \tag{1.20}$$

Thus, under the same assumptions (classical field and homogeneous system), equations (1.7) and (1.20) obtained from different approaches give the same result, up to a multiplying factor in the susceptibility. In the classical susceptibility description it is $\frac{2\alpha_0 l}{T_1}$, whereas in the full quantum calculation it is $\frac{\sum_k g_k^2}{\kappa\gamma}$. These two factors can be shown to be equal: first note that in the approximation of a continuous medium of density μ and length l, $\sum_k g_k^2 = g_0^2 \mu \frac{\pi}{4} l w^2$. From the expressions of g_0, κ, γ and σ_{eff}, one easily shows the following equality: $\frac{g_0^2}{\kappa\gamma} = \frac{8\sigma_{eff}}{\pi T_1 w^2}$, from which the identity of the two expressions follows.

The quantity $\frac{\alpha_0 l}{T_1} = \frac{\sum_k g_k^2}{2\kappa\gamma}$ is defined as the cooperativity parameter C of the atomic cloud in the cavity. It is a measurement of the collective coupling of the atoms to the cavity mode [79]. As is visible here, it can take different interpretations: classically it would be described as the ratio of the "coupling losses" (absorption of the cloud) to the pure exit losses (transmission through the lossy mirror) in a single pass through the cavity. Quantum-mechanically it shows as a ratio between the coupling coefficients of all the atoms to the mode and the two damping rates of the system (atoms and cavity).

General expression of the effective reduced susceptibility

In the general case, the cavity transmission can then be put in the form:

$$T_{cav} = \frac{T_0}{\left(1 - 2CIm[\left\langle \frac{\sigma}{\Omega/2} \right\rangle]\right)^2 + \left(\theta - 2CRe[\left\langle \frac{\sigma}{\Omega/2} \right\rangle]\right)^2} \tag{1.21}$$

In the classical approach, which implicitly assumes no spatial dependences of any quantity, $\left\langle \frac{\sigma}{\Omega/2} \right\rangle = \frac{\langle\hat{\sigma}\rangle}{\Omega/2}$ is a single well-defined value. The quantum approach which treats completely the possible variations of conditions from one atom to another, gives a general expression of the effective reduced susceptibility:

$$\left\langle \frac{\sigma}{\Omega/2} \right\rangle = \frac{\sum_k \frac{g_k^2}{\kappa\gamma} \frac{\langle\hat{\sigma}_k\rangle}{\Omega(\vec{r}_k)/2}}{\sum_k \frac{g_k^2}{\kappa\gamma}} = \sum_k \frac{\phi(\vec{r}_k)^2}{\sum_k \phi(\vec{r}_k)^2} \frac{\langle\hat{\sigma}_k\rangle}{\Omega(\vec{r}_k)/2} \tag{1.22}$$

For atoms interacting with a given cavity mode, the relevant quantity is therefore the projection of the susceptibility on this spatial mode ($\Omega \to \Omega(\vec{r}) = \Omega_0\phi(\vec{r})$). For a sufficiently large and dense ensemble of atoms, one can then make a continuous medium approximation with local density $\mu(\vec{r})$ and express the effective reduced susceptibility as [88, 89]:

$$\sum_k \frac{\phi(\vec{r}_k)^2}{\sum_k \phi(\vec{r}_k)^2} \frac{\langle\hat{\sigma}_k\rangle}{\Omega(\vec{r}_k)/2} = \int d^3\vec{r} \quad \mu(\vec{r}) \frac{\langle\hat{\sigma}(\vec{r})\rangle}{\Omega(\vec{r})/2} \phi_n(\vec{r})^2 \tag{1.23}$$

Where $\phi_n(\vec{r}) = \frac{\phi(\vec{r})}{\sqrt{\int d^3\vec{r}\mu(\vec{r})\phi(\vec{r})^2}}$ is the normalized cavity mode function.

For a given excitation scheme, calculating from single-atom Bloch equations with no cavity and a classical driving the value of $\frac{\langle\hat{\sigma}_k\rangle}{\Omega(\vec{r}_k)/2}$ for a given position is easier than taking the complete problem from start. With this, solving the full problem then only requires to perform the spatial integration written above.

1.2.3 Spatial inhomogeneities: case of nonlinear susceptibilities in cavity, bistability

It is worth noting that so far (except for introducing the cooperativity), no hypothesis was made on the driving conditions or the atomic excitation scheme. Equations (1.21), (1.22) and (1.23) are therefore completely general.

In the specific case of the linear regime, the atomic response $\left\langle \frac{\sigma}{\Omega/2} \right\rangle$ does not depend on Ω. In this situation, although the exact expression of the effective susceptibility might be complicated, the effect of the atoms always amounts to a shift and an attenuation of the Lorentzian cavity transmission resonance.

However, the goal is to make use of highly nonlinear phenomena where ideally the evolution of light should strongly depend on the number of photons it contains, down to a single one. It is therefore useful to understand, and we want to show here, how such strong nonlinearities appear on the transmission of the atoms-cavity system.

In the nonlinear regime, χ or $\left\langle \frac{\sigma}{\Omega/2} \right\rangle$ depend on $\left|\vec{E}\right|$ or $\frac{\Omega}{2}$. The medium can then be characterized in lowest order by its effective third-order nonlinear susceptibility $\chi^{(3)}$ (the second order one vanishes for an atomic gas):

$$\chi^{(3)} \propto \left(\frac{\chi(\Omega)-\chi(0)}{\Omega^2}\right)_{\Omega\to 0} \tag{1.24}$$

As by definition in this regime $\frac{\langle\hat{\sigma}\rangle}{\Omega/2}$ depends on space in the cavity mode, the complete quantum description developed above is necessary in order to characterize the effective $\chi^{(3)}$ for example.

In order to show more explicitly the effect of the nonlinearity on the cavity transmission, the following normalized variables will be used:

$$X = \frac{\Omega_0^2}{2} = \frac{|\alpha|^2}{\gamma^2/2g_0^2} \qquad Y = \frac{(\lambda/\kappa)^2}{\gamma^2/2g_0^2} \tag{1.25}$$

X is directly proportional to the intensity circulating inside the cavity ($X = \frac{I}{I_{sat}}$ for the maximum intracavity intensity), and Y is relative to the incident intensity. The previous expressions of T_{cav} translate into:

$$X = \frac{Y}{\left(1-2CIm[\left\langle\frac{\sigma}{\Omega/2}\right\rangle]\right)^2 + \left(\theta-2CRe[\left\langle\frac{\sigma}{\Omega/2}\right\rangle]\right)^2} \tag{1.26}$$

Y is thus normalized to be the maximal value X can take, for a cavity on resonance with no atoms inside.

The nonlinearity translates in the fact that $\left\langle\frac{\sigma}{\Omega/2}\right\rangle$ is a function of the intracavity intensity X that will be noted:

$$\left\langle\frac{\sigma}{\Omega/2}\right\rangle = f(X) \tag{1.27}$$

Equation (1.26), determining X for a given value of the input power Y, therefore becomes self-consistent: to enter the cavity, the probe light must be resonant with the cavity mode's effective frequency. This frequency is shifted by the presence of the atoms, by an amount that depends on the probe power. The consequence is a distortion of the cavity transmission lines.

For large enough atomic nonlinearity, the cavity-atoms system can reach a bistable state [80, 81]. In general, this can happen in two different ways: either the dispersive nonlinearity ($Re[f(X)]$) makes the transmission as a function of θ multivalued, or the absorptive nonlinearity ($Im[f(X)]$) makes the possibilities for X as a function of Y become multiple. In both cases, the system acquires a memory, in the sense that its state at a given time depends on its past history. It can then in principle be used as an optically manipulated memory.

From this point on, we will always focus on dispersive bistability or nonlinearity, because the light's phase is affected by its intensity, while losses can be kept low. The qualitative picture of the emergence of bistability in this kind of system is sketched on figure (1.2).

One of the main goals of our research is therefore to find conditions in which the medium's real part of susceptibility is highly nonlinear while the imaginary one stays small. Depending on the excitation scheme used to couple light to the atoms, different types of nonlinearities can be achieved. What will be of primary interest in the following is the knowledge of the power necessary, for a given type of nonlinearity, to reach a situation approaching bistability (see section 1.3.3).

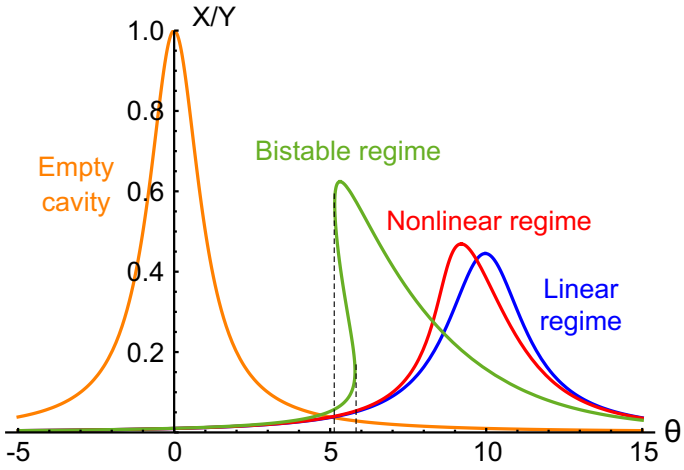

Figure 1.2: Normalized ratio X/Y for a nonlinear susceptibility, for values of Y in different regimes. For high enough Y, ranges of θ where the transmission is multivalued can exist (between the two dashed lines).

1.3 Two-level atoms

1.3.1 Linear regime

Let us first consider the simple case of two-level atoms coupled to the cavity. The schematic of the system considered is shown on figure (1.3).

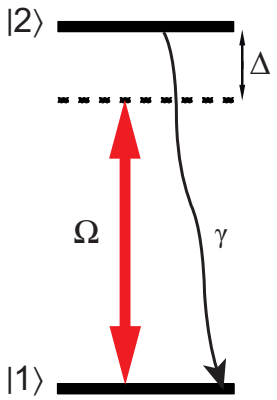

Figure 1.3: Two-level system.

The steady-state value of the atomic coherence for one two-level atom driven with a Rabi frequency Ω is [90]:

$$\langle\hat{\sigma}\rangle = \frac{\Omega}{2}\frac{\Delta - i}{1 + \Delta^2 + \frac{\Omega^2}{2}} \tag{1.28}$$

When considered in the low-intensity range ($\frac{\Omega^2}{2} << 1 + \Delta^2$), this is simply $\frac{\langle\hat{\sigma}\rangle}{\Omega/2} = \frac{\Delta - i}{1+\Delta^2}$ and describes the usual behaviour of dispersion and absorption around an atomic resonance, shown in figure (1.4).

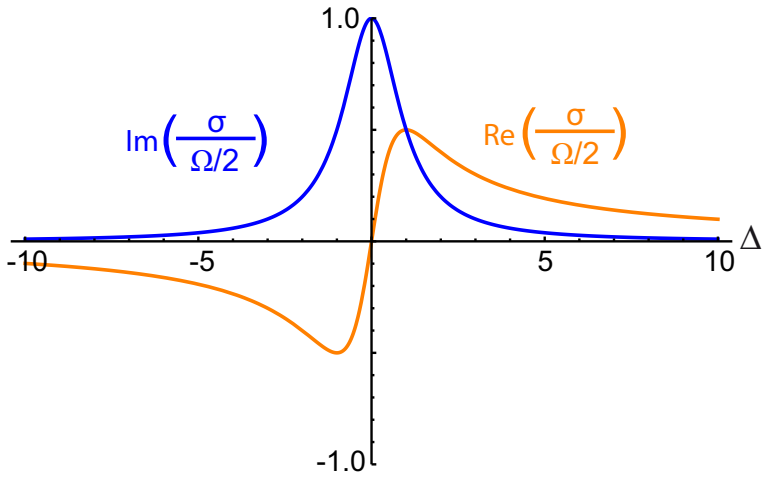

Figure 1.4: Real and imaginary parts of the reduced susceptibility $\frac{\langle\hat{\sigma}\rangle}{\Omega/2}$ for two-level atoms in the linear regime.

This quantity only depends on atomic constants, so that $f(X \to 0) = \frac{\langle\hat{\sigma}\rangle}{\Omega/2}$ for any atom, and the linear cavity transmission is:

$$T_{cav} = \frac{T_0}{(1 + 2C\frac{1}{1+\Delta^2})^2 + (\theta - 2C\frac{\Delta}{1+\Delta^2})^2} \tag{1.29}$$

The effect of the atoms and their cooperativity on the cavity transmission line is illustrated in figure (1.5).

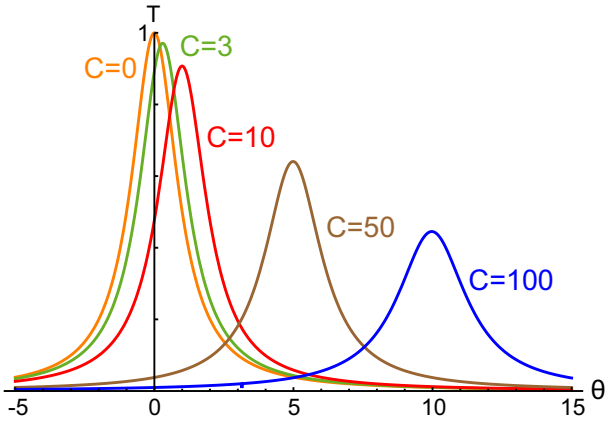

Figure 1.5: Cavity transmission line as observed when scanning its length, for two-level atoms with different values of the cooperativity and an atomic detuning fixed at $\Delta = -20$.

1.3.2 Two-level nonlinearities

One way to obtain optical bistability in our system is to make use of the natural nonlinearity of the two-level susceptibility. The nonlinearity here originates in the fact that a two-level atom is intrinsically limited in the amount of light it can interact with,

and when it spends half of its time in the excited level it no longer sees the incident light and its response saturates. This is of course the first scheme in which all kinds of bistability were studied experimentally with cold atoms [91–93].

Starting again from equations (1.23) and (1.28), one can show that the effective reduced susceptibility $f(X)$ is, in the case of a uniform density:

$$f(X) = \frac{4(\Delta - i)}{X} ln\left(\frac{1 + \sqrt{1 + \frac{X}{1+\Delta^2}}}{2}\right) \tag{1.30}$$

In order to quantify the strength of this nonlinearity, one can estimate the intensity X_{max} necessary to produce a nonlinear resonance shift $2C\,|Re[f(X_{max}) - f(0)]|$ on the order of the atom-broadened resonance linewidth $1 + \frac{2C}{1+\Delta^2}$. For two-level atoms, the critical value of $\tilde{X} = \frac{X_{max}}{1+\Delta^2}$ satisfies:

$$1 + \frac{2C}{1+\Delta^2} = \frac{2C\,|\Delta|}{1+\Delta^2}\left[1 - \frac{4}{\tilde{X}} ln\left(\frac{1+\sqrt{1+\tilde{X}}}{2}\right)\right] \tag{1.31}$$

$$\approx \frac{2C\,|\Delta|}{1+\Delta^2}\left|0.33\tilde{X} - 0.09\tilde{X}^2 + 0.01\tilde{X}^3\right| \tag{1.32}$$

where the last expression is an approximate description of the previous function, correct for $\tilde{X} < 4$.

In order to see dispersive nonlinearities without too much absorption with two-level atoms, one must get reasonably far from resonance, where the atoms initially shift the line position by $2CRe[f(0)] \approx \frac{2C}{\Delta}$. The effect of the nonlinearity is to bring the line position back to $\theta = 0$ with increasing power ($f(X >> 1) \to 0$). As a result, in order for a nonlinear shift of the line by its width to make sense, one must look at regimes where at least $\frac{2C}{\Delta} > 1$. Together with the approximate condition of small absorption $\frac{2C}{\Delta^2} < 1$, the overall range of parameters for dispersive nonlinearities can be summarized in: $\Delta^2 > 2C > \Delta > 1$. Physically this regime exists because dispersion decreases slower than absorption when moving away from the resonance.

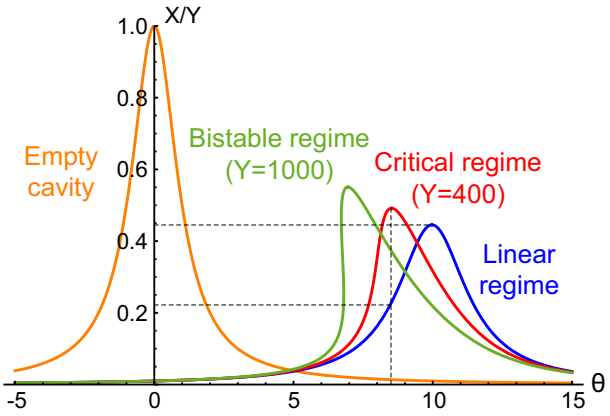

Figure 1.6: Critical regime for bistability with two-level nonlinearity. With $C = 100$ and $\Delta = -20$, the critical level for X is around 200, which is reached on resonance when $Y = 400$. One sees on the curves that this indeed corresponds to a transmission peak having shifted by half the width of the linear regime peak. Real bistability appears slightly above this level.

Under these conditions, the "close-to-bistability" situation is reached when:

$$\left|0.33\tilde{X} - 0.09\tilde{X}^2 + 0.01\tilde{X}^3\right| = \frac{1+2C+\Delta^2}{2C\,|\Delta|} = \beta \tag{1.33}$$

An approximate solution to this equation, as long as $\beta < 0.5$, is $\tilde{X} \approx 3\beta + 16\beta^3$. On all the interesting range this solution is such that $\tilde{X} < 4$. From this simple result one can easily estimate, for given parameters $\{\Delta,C\}$, the intensity required to reach a large dispersive nonlinearity. This is demonstrated on an example in figure (1.6).

Some additional physical meaning can be attached to this result by re-expressing $\tilde{X}$ as $\frac{n_{ph}}{n_{sat}(\Delta)}$, where n_{ph} is the steady-state number of photons inside the cavity. The immediate expression of $n_{sat}(\Delta)$ from the definition of X is $n_{sat}(\Delta) = \frac{\gamma^2(1+\Delta^2)}{2g_0^2}$. After some manipulations, this can be written:

$$n_{sat}(\Delta) = \gamma\frac{L}{c}\frac{\pi w^2/4}{3\lambda^2/(2\pi(1+\Delta^2))} = \gamma t_{cav}\frac{S_{mode}}{\sigma_{eff}(\Delta)} \tag{1.34}$$

Where t_{cav} is the one-way travel time of light inside the cavity, S_{mode} is the effective transverse area of the cavity mode, and $\sigma_{eff}(\Delta)$ is the absorption cross section for an atom interacting with light at a detuning Δ.

Conclusion on the two-level atoms nonlinearity's efficiency

The conclusion is that, in order to reach interesting dispersive nonlinear regimes, the typical number of photons in the cavity is around $n_{sat}(\Delta) = \gamma t_{cav}\frac{S_{mode}}{\sigma_{eff}(\Delta)}$ (as $\tilde{X}$ is of order 1). This is equivalent to saying that, with or without cavity, the nonlinearity shows up when the two-level atomic system gets saturated, *i.e.* when each individual atom sees photons coming at a rate larger than γ. To achieve this in free space means having $s = \frac{I/I_{sat}}{1+I/I_{sat}+\Delta^2} \to 1$. In the cavity the steady-state photon flux is set by the mode geometry, and to saturate an atom with few photons one needs to focus the mode down to very small S_{mode}, and short t_{cav}.

In the range of parameters where our experiment is carried out, we consider a cavity mode waist of a few tens of microns, a light-atoms detuning of at least ten linewidths, and the surface ratio in n_{sat} is of the order of $10^5 - 10^6$. With a cavity of few centimeters length and a typical atomic linewidth of a few megahertz, the total comes to n_{sat} of a few thousands of photons.

In order to improve this, one would need to use much smaller cavities with large single atom-field coupling, which is more challenging to realize and manipulate. It corresponds to the cavity-QED regime, which is not the parameter range in which the present work is carried out.

1.3.3 Note on the intensity criterion for the nonlinearity

Going to stronger types of nonlinearities seems to mean decreasing the steady-state number of intracavity photons required to reach the bistability threshold. However this criterion can be deceiving in practice when using more complicated schemes.

In practice we look for a system with a large enough nonlinearity that, while two photons are inside it (and only them), their quantum state gets significantly affected. However while inside the system they can exist as photons, or as atomic excitations, which do not have the same lifetime. Therefore, if the total lifetime of the excitations in the system is

τ_{tot}, we must look for a situation where the nonlinearity is large for a quantity $\Phi_c\tau_{tot}$ approaching one, where Φ_c is the external photon flux feeding the system's excitations. Let us picture the system as a box, containing excitations, in any possible form: their number n_{exc} would obey dynamics of the form $\frac{dn_{exc}}{dt} = -\frac{n_{exc}}{\tau_{tot}} + \Phi_c$. Characterizing the quantity $\Phi_c\tau_{tot}$ is then exactly the same as counting the total number of excitations, photonic or atomic, present in the system in steady state $n_{exc} = n_{ph} + n_{at}$.

For two-level atoms, this does not make a large difference as most of the excitations in the cavity are anyway photons. In fact, the bistability threshold is reached when each atom's optical transition is saturated by light, so that the excited state population is of order $\frac{1}{2}$ (calculating the population of this state for the maximal Rabi frequency Ω_0 gives exactly $p_2 = \frac{1}{2}\frac{\tilde{X}}{1+\tilde{X}}$, and the threshold is for $\tilde{X}$ of order 1). Therefore the total number of atomic excitations in the system, if the total number of atoms is $N = \frac{2C\kappa\gamma}{g_0^2}$, is of order $p_2 N \approx \frac{N}{2} = \frac{C\kappa\gamma}{g_0^2} = \frac{\kappa}{\gamma}\frac{2C}{1+\Delta^2}n_{sat}$. In the dispersive regime $\Delta^2 > 2C$, so this number is at worst of the same order of magnitude as n_{sat}.

Another way to put it is that at the threshold:

$$n_{exc} = n_{at} + n_{ph} \approx \frac{N}{2} + n_{sat} = \frac{N}{2}(1 + \frac{(1+\Delta^2)\gamma}{2C\kappa}) \tag{1.35}$$

Among all excitations present in the system in steady state, a large part of them are therefore photons in the usual parameter range. However this may not always be the case when long-lived atomic excitations can exist, as will be shown next in three-level systems for example. Atomic excitations must then be taken into account to compare the strength of the nonlinearity in different systems.

1.4 Multilevel atoms

Different ways of enhancing the atomic nonlinearities can be envisioned. In multilevel systems, schemes where Electromagnetically Induced Transparency cancels the medium's absorption in a narrow frequency window make it possible to work closer to resonance, and thus largely enhance the atomic dispersion. Optical bistability in three- and four-level system was also largely studied both theoretically and experimentally [94, 95].

The importance of three-level atomic excitation schemes and EIT in this work being quite large, we want here to introduce some of their general characteristics.

1.4.1 Electromagnetically induced transparency

To improve on the two-level system results, we first consider atoms where a set of three levels in a Λ scheme has been isolated, two long-lived and an excited one (see figure (1.7)) [4]. Target photons are sent on the probe transition (with a detuning Δ and Rabi frequency Ω), while on the other transition a continuous classical "control" beam is used, with a detuning Δ' and Rabi frequency Ω_b.

4. The model system chosen can seem not very realistic from the spontaneous decays point of view. However it leads to simple expressions on which we can illustrate easily our point here, and is equivalent, once unfolded to a ladder configuration, to the two-photon Rydberg state excitation that will be used later when neglecting the decay of the Rydberg state.

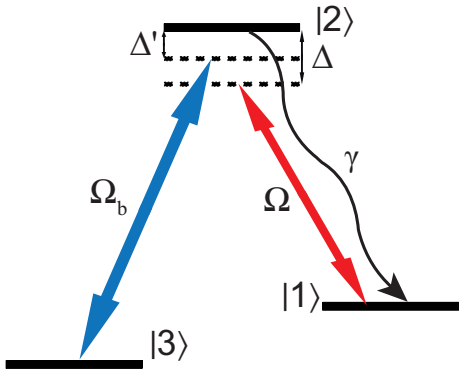

Figure 1.7: Three-level system.

Close to two-photon resonance ($\Delta = \Delta'$), interferences between different excitation paths lead to a cancellation of the probability to excite the decaying state. More precisely, the system acquires a dark eigenstate in which the short-lived state $|2\rangle$ is not populated at all, expressed in the resonant case as: $|\Psi_d\rangle \propto \Omega_b |1\rangle + \Omega |3\rangle$. This results, for $\Delta = \Delta' = 0$, in a spectral window where the medium becomes transparent, precisely at the maximum of the two-level absorption line. The properties of the medium are therefore greatly affected by the presence of this additional coupling beam [54].

This phenomenon opens possibilities for excitation schemes with enhanced nonlinearity and low absorption, which are of course very interesting for large loss-free nonlinearities in a QIP context.

1.4.2 Linear regime susceptibility

Solving the single-atom Bloch equations in steady state for the system of figure (1.7) with classical beams leads to the following expression of the reduced susceptibility on the probe transition ($\delta = \Delta - \Delta'$ is the two-photon detuning):

$$\frac{\langle\hat{\sigma}\rangle}{\Omega/2} = \frac{\tilde{\Delta} - i}{1 + \tilde{\Delta}^2 + \frac{\Omega^2}{2}(1 + \frac{X_b}{2\delta^2}) + \frac{\Omega^4}{16\delta^2}} \tag{1.36}$$

Where $X_b = \frac{\Omega_b^2}{2}$, and $\tilde{\Delta} = \Delta - \frac{X_b}{2\delta}$ is the effective detuning to resonance in the three-level system including the effect of the control beam. In the linear regime, the susceptibility is only:

$$\frac{\langle\hat{\sigma}\rangle}{\Omega/2} = \frac{\tilde{\Delta} - i}{1 + \tilde{\Delta}^2} \tag{1.37}$$

This is exactly the same as for the two-level system, with an effective detuning $\tilde{\Delta}$.

Resonant case

If the control beam is exactly on resonance ($\Delta' = 0$), the effective detuning is $\tilde{\Delta} = \Delta - \frac{X_b}{2\Delta}$. It is approximately Δ sufficiently far from the probe resonance, but at $\Delta = 0$ it diverges and the system reacts as if light was not interacting with the atoms at all. The absorption of the medium is zero exactly on the resonance, corresponding to EIT.

The absorption and dispersion curves as a function of Δ in this case are shown on figure (1.8).

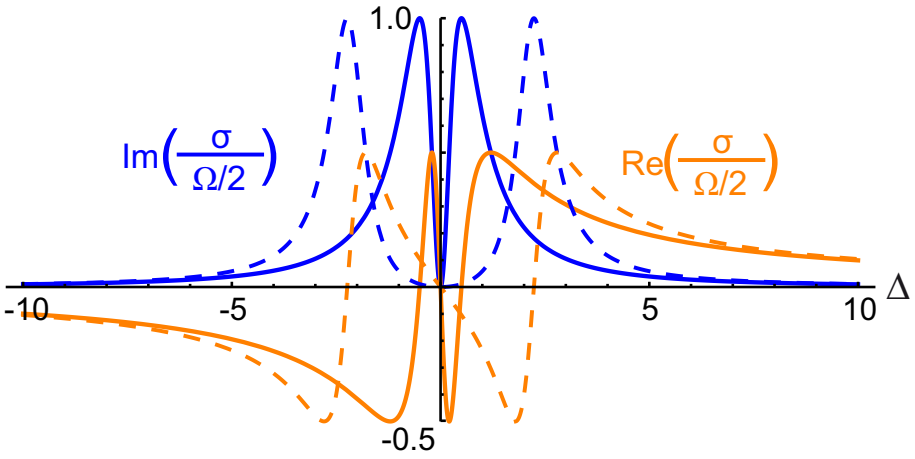

Figure 1.8: Real and imaginary parts of the reduced susceptibility $\frac{\langle\hat{\sigma}\rangle}{\Omega/2}$ for three-level atoms in the linear regime. Case of a resonant coupling beam ($\Delta' = 0$), with $X_b = 0.5$ (full lines) and $X_b = 10$ (dashed lines).

On resonance the dispersion is modified by a sharp feature, making the slope of the refraction index very large. This is the origin of very interesting and investigated effects like slow light [55]. The EIT window's width is controlled by the control beam power X_b.

Detuned case

For a far-detuned control beam, around resonance where $\tilde{\Delta} \approx \Delta$ the absorption line from the two-level atom survives almost unaffected. When $\Delta \approx \Delta'$, the effective detuning diverges and a secondary absorption line is crossed, which corresponds to the coherent two-photon transition from one ground state directly to the other.

The susceptibility therefore exhibits two independent lines, the second one (the two-photon resonance) being intrinsically very narrow in frequency and power-broadened by the control beam for large X_b, as shown in figures (1.9) and (1.10).

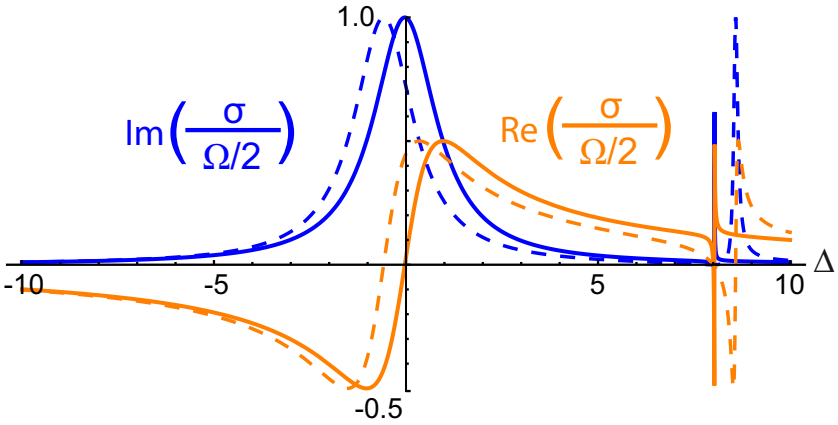

Figure 1.9: Real and imaginary parts of the reduced susceptibility $\frac{\langle\hat{\sigma}\rangle}{\Omega/2}$ for three-level atoms in the linear regime. Case of a non resonant coupling beam ($\Delta' = 8$), with $X_b = 0.5$ (full lines) and $X_b = 10$ (dashed lines).

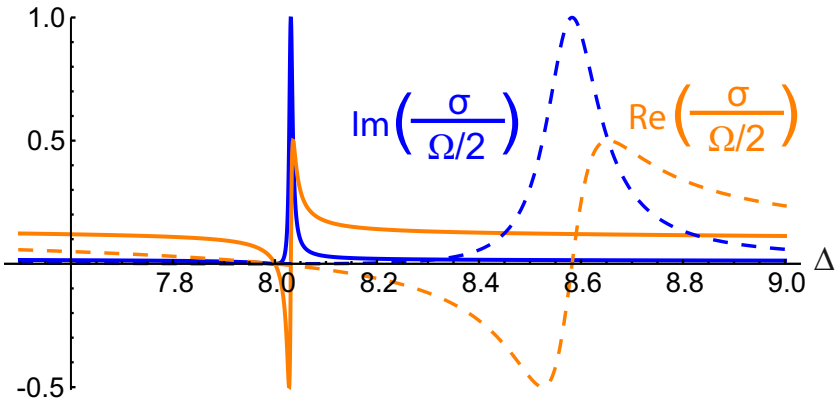

Figure 1.10: Zoom of figure (1.9) around the region of the two-photon resonance.

The exact positions of the two resonances are given by the solutions of $\tilde{\Delta} = 0$, $\Delta = -\frac{X_b}{2\Delta'}$ and $\Delta = \Delta' + \frac{X_b}{2\Delta'}$. These are the one- and two-photon resonances, shifted by the control beam-induced light shifts.

1.4.3 Three- and four-level nonlinearities using EIT

The influence of a third atomic level makes the system's response more complex and opens several possibilities to produce large dispersive non-linearities.

Saturation of the two-photon resonance

The detuned two-photon line is an effective resonance of the system which can be much narrower than the plain two-level transition, and can be saturated faster. Based on this, large nonlinearities were investigated in these systems, by characterizing directly the nonlinear index of the medium [96] or more indirect effects related to the nonlinearity, such as the possibility of observing quadrature squeezing on the light field [97–100].

If the parameters are adjusted in such a way that $\frac{\Omega^2/2}{4\delta^2+2X_b} << 1$, the fourth order term in the space-dependent susceptibility in equation (1.36) can be neglected. Its expression is then just the same as for the two-level system with rescaled parameters depending on the control field intensity. As a result, the integration to obtain the effective reduced susceptibility is the same and the result is, with $\tilde{X} = \frac{\Omega^2(1+X_b/2\delta^2)}{2(1+\tilde{\Delta}^2)}$:

$$f(X) = \frac{\tilde{\Delta} - i}{1+\tilde{\Delta}^2}\frac{4}{\tilde{X}} ln(\frac{1+\sqrt{1+\tilde{X}}}{2}) \tag{1.38}$$

The conclusions from the two-level system also directly apply to this case. Therefore, bistability can be observed for $\tilde{\Delta}$ on the order of ten and $\tilde{X}$ of a few units. One distinctive feature of this scheme is that the necessary value for X in the two-level case has been rescaled by $1 + \frac{X_b}{2\delta^2}$ in the definition of $\tilde{X}$, so that one needs fewer intracavity photons to get the same nonlinearity.

However, the system can also contain atomic excitations in both states $|2\rangle$ and $|3\rangle$, so that one should really look at the total number of excitations as pointed out in section 1.3.3. Calculating the steady state populations corresponding to the maximum Rabi frequency Ω_0, the result is, under the same approximations as before:

$$p_2 = \frac{1}{2}\frac{\tilde{X}}{(1+\tilde{X})(1+\frac{X_b}{2\delta^2})} \qquad p_3 = \frac{1}{2}\frac{\tilde{X}}{1+\tilde{X}}\frac{\frac{X_b}{2\delta^2}}{1+\frac{X_b}{2\delta^2}} \tag{1.39}$$

Going from two to three levels can therefore reduce a lot the population of state $|2\rangle$ if $\frac{X_b}{2\delta^2} >> 1$, but it is actually just transferred to state $|3\rangle$ where the population is again on the order of $\frac{1}{2}$. As a result, by the same reasoning, one finds that the total number of excitations in the system at the threshold is of order:

$$n_{exc} \approx n_{at,|3\rangle} + n_{ph} \approx \frac{N}{2}(1 + \frac{(1+\tilde{\Delta}^2)\gamma}{2C\kappa(1+\frac{X_b}{2\delta^2})}) \tag{1.40}$$

Compared to the two-level case, the photonic contribution has indeed been suppressed by a factor $1+\frac{X_b}{2\delta^2}$, but the atomic contribution is still of the order of the number of atoms participating. For practical considerations (to get $C >> 1$ with a low finesse cavity) this will always be much larger than one. Even though improving the nonlinearity's efficiency may be possible using this scheme, it is not enough unless one goes to a completely different regime, working with a single atom strongly coupled to the cavity.

The existence of long-lived excitations in the system translates in the fact that the high-nonlinearity regimes are also the ones where the bandwidth of the interesting effect becomes very small, which has been a recurrent problem in these systems.

Resonant EIT-induced nonlinearities in a four-level system

As the resonant EIT susceptibility profile has a very sharp dispersion feature around resonance, it has been thought that it could generate very strong dispersive nonlinearities. However, exactly on resonance, the transparency is good, but the dispersion is always exactly zero whatever the probe power.

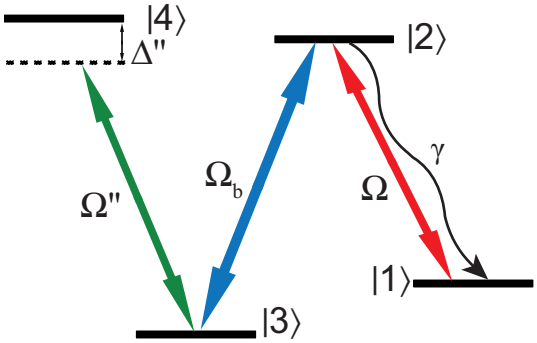

Figure 1.11: Four-level system for resonant crossed nonlinearities using EIT and light shifts.

Schemes were then designed using an off-resonant coupling to an additional atomic level in order to induce an intensity-dependent shift of the susceptibility profile, and thus a large change in the dispersion seen by the resonant probe (see figure (1.11)) [56, 101].

Starting from a doubly resonant situation in the three-level system, a third beam is applied with normalized intensity X'' on an additional transition with detuning Δ'', resulting in an effective detuning for the coupling beam's transition $\Delta' = \frac{X''}{2\Delta''}$. The susceptibility seen by the probe is then given by the linear one with $\tilde{\Delta} = \frac{X_b}{2\Delta'} = \frac{X_b\Delta''}{X''}$:

$$f(X'') = \frac{\frac{X_b\Delta''}{X''} - i}{1 + (\frac{X_b\Delta''}{X''})^2} \tag{1.41}$$

This, in lowest order in X'', is simply $f(X'') = \frac{X''}{X_b\Delta''}$, which clearly shows that absorption remains low even in the presence of the nonlinearity. From this very simple model it seems like, using very small coupling beam power and detuning on the shifting transition, arbitrarily large nonlinearities can be achieved.

This was used in several configurations to induce cross phase modulation between two beams with very low power [55, 102], or to study self-induced nonlinearities (when the dephasing beam and the probe are actually the same). Here also, although it was possible to demonstrate extremely large nonlinear effects, the fast reduction of the bandwidth accompanying the increase of nonlinearity made it impossible to reach the single-photon regime in practice.

Another way of understanding this effect is that the photons interact for a long time in the medium as they propagate very slowly, due to EIT [55]. However it is also the source of problems, because the nonlinear propagation in the medium induces distortion of the light's wavepacket, or mismatch of propagation speed of the various beams. To overcome these issues, more carefully designed free space schemes were proposed where one could engineer the propagation speeds of all beams, which start to be quite involved experimentally [103]. Different four-level schemes with resonant couplings were also studied, but lead to the same kind of conclusions [104, 105].

Later on, theoretical investigations demonstrated using restricted hypotheses that whatever scheme would be used, large nonlinear phase shifts at the single-photon level with local Kerr nonlinearities are fundamentally unusable as such [13, 14, 106]. The general reason is again that such nonlinearities have quite localized efficiency ranges both spatially and spectrally, which leads to unavoidable distortion of the involved photons, rendered unusable afterward.

1.4.4 EIT with interacting atoms – Qualitative picture

As we saw, EIT schemes can be used to produce large nonlinearities in a many atoms-cavity setup, but the intrinsic properties of the atomic medium lead to practical limitations that can hardly be avoided. It seems that a new external element is required to put the system into a regime where the nonlinearities are really large even for few photons.

One can re-use the idea of a three-level system in EIT-like conditions, where the nonlinearity comes from the intensity dependent shift of one level. The change will be in the mechanism producing this shift, that should be much more efficient than light shifts.

Atoms excited to state $|3\rangle$ could exhibit strong long-range interactions: the population in state $|3\rangle$, fixed by the probe intensity, would then effectively detune the control beam for other atoms by shifting level $|3\rangle$, hence the nonlinearity. As we will see in more details later, this kind of scheme can be implemented in a ladder (instead of Λ) configuration with excitations to Rydberg states.

The phenomenon can also be interpreted as a temporary mapping of photons onto atomic excitations that can efficiently interact with each other through dipole-dipole coupling, thereby mediating strong photon-photon interactions. As one excitation influences many atoms, the effect of a single photon sent in the medium is significantly enhanced. One can get to a fully quantum regime where a few excitations in the system already make it highly nonlinear, in which case the theoretical framework has to be re-thought to deal with light in non-classical states.

Chapter 2

Photonic quantum state characterization

Contents

The susceptibility provides information about the action of a medium on a classical field, and consequently about the physical processes at work inside it. However, when the medium interacts with only a few photons, the classical field approximation fails and the susceptibility does not really contain the interesting information anymore.

To set up the proper picture for some of the experiments presented here, one has to reconsider the regime of description for the light field's degrees of freedom. What is of interest then is the modification of the light's quantum state induced by the interaction with the atoms.

As a result, we will discuss in this chapter the useful tools to characterize the quantum state of a given "packet" of light, which could have been in contact with a nonlinear medium.

2.1 Wigner function of a field mode's quantum state

As introduced earlier, the quantum state of the light leaving the cavity is, in general, described by a density matrix. This density matrix can be conveniently written in the discrete Fock basis for example, in terms of number of photons [82, 85, 107].

On the other hand, light can also be considered as a wave. Its quantum state can therefore be described in phase space using an amplitude and a phase instead of a number of photons, or any other pair of conjugated continuous variables like the Cartesian quadratures $\hat{x}$ and $\hat{p}$. In this vision, the most useful tool to describe a quantum state is the Wigner function W, which can be univoquely related to the density matrix [82, 85, 107]. It is explicitly defined by the following expression:

$$W(x,p) = \frac{1}{2\pi\hbar} \int \left\langle x - \frac{q}{2} \middle| \hat{\rho} \middle| x + \frac{q}{2} \right\rangle e^{ipq/\hbar} dq \tag{2.1}$$

The field quadratures $\hat{x}$ and $\hat{p}$ are defined from the annihilation operator of the mode by: $\hat{x} = \sqrt{\frac{\hbar}{2\omega}}(\hat{a} + \hat{a}^\dagger)$ and $\hat{p} = i\sqrt{\frac{\hbar\omega}{2}}(\hat{a} - \hat{a}^\dagger)$. They are analogous to the position and momentum of the quantum oscillator.

	discrete variables	continuous variables
Variables	photon number	quadratures
Operators	$\hat{a}$, $\hat{a}^\dagger$	$\hat{x}$, $\hat{p}$
State description	$\langle n\vert\,\hat{\rho}\,\vert m\rangle$	$W(x,p)$
Coherent state	poissonian distribution	Gaussian with variance 1/2
Particular case	diagonal density matrix	phase-invariant Wigner function

Table 2.1: Two complementary descriptions of light's quantum states.

The Wigner function, for a given quantum state, can be viewed as a pseudo-probability distribution in phase space of the complex electric field (pseudo because, as $\hat{x}$ and $\hat{p}$ do not commute, a real joint probability to get precise values x and p cannot be defined). The main property of this function is that projecting it along a certain direction in phase space, one obtains the probability distribution of the quadrature along the orthogonal axis, for example:

$$\int W(x,p)dp = Pr(x) \tag{2.2}$$

The vacuum state $|0\rangle$ contains a field of zero average amplitude, but exhibits intrinsic fluctuations, that are characterized by a Gaussian Wigner function. Other states, mostly the ones that are closest to the classical fields (coherent states), have Gaussian Wigner functions positive on the whole phase space, as displayed in figure (2.1).

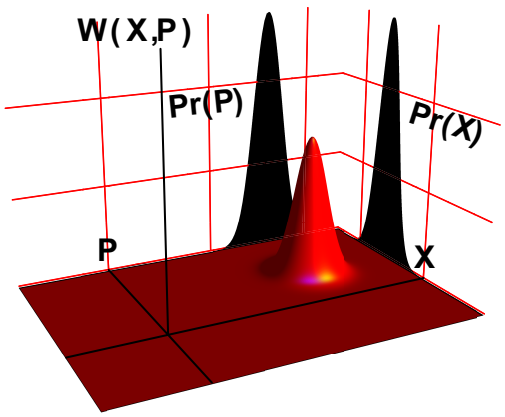

Figure 2.1: Wigner function and projections for a quasi-classical (coherent) state. The Wigner function is in this case a Gaussian of fixed size, off-centered on what would be the classical complex field's amplitude. The probability distributions for the in-phase and out-of-phase quadratures of the field are obtained by projecting the Wigner function on a given plane, as shown by the two Gaussian shadows here.

However, it is not the case of more "typically quantum" states, like the single photon Fock state $|1\rangle$ (see figure(2.2)). Its Wigner function is negative around the center of phase

space, direct manifestation of its non-classical properties.

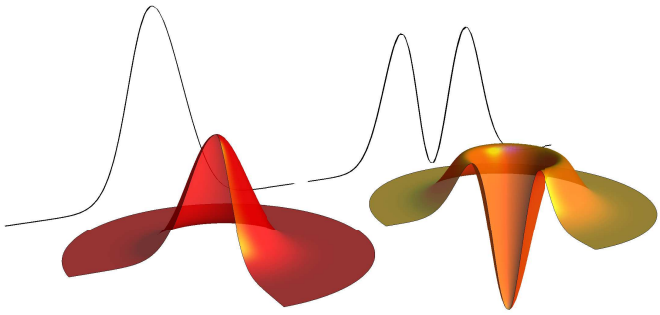

Figure 2.2: Wigner functions and quadrature distributions of the vacuum $|0\rangle$ and single-photon $|1\rangle$ states.

Note that the Wigner function of the vacuum and single-photon states are phase-invariant, *i.e.* rotational symmetric around the origin. This is true for all Fock states, and therefore also for any statistical mixture of those.

There is a one-to-one relationship between density matrices and Wigner functions, so that characterizing one or the other to study a quantum state is strictly equivalent in theory.

2.2 Homodyne tomography – Principles

Reconstructing the Wigner function of a light mode requires to measure the quantum statistics of the electric field, which can be done using optical homodyne tomography. Just like medical 3D imaging reconstructs from several 2D images of a medium its full spatial structure, the idea here is to use the quadrature probability distributions (projections of the Wigner function on several different planes) to infer the most likely Wigner function that can be at their origin [17, 107].

Performing quadrature measurements can be done using a homodyne detection setup as depicted in figure (2.3).

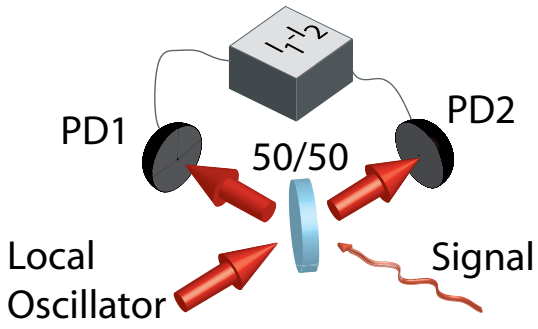

Figure 2.3: Principle scheme for homodyne detection of the field quadratures of a signal state. PD1 and PD2 are two identical high quantum efficiency photodiodes.

In this scheme, the state to be characterized is brought to interfere with a strong classical coherent field called Local Oscillator (LO). On the difference of the two photocurrents

$I_1 - I_2$, the average amplitude of the LO cancels out, to leave only noise which is sensitive to the quantum fluctuations of the two quantum states interfering.

Based on the simple assumption that the LO's amplitude fluctuations are negligible compared to its average α_{LO}, one can show that the difference photocurrent operator is proportional to a quadrature operator of the signal field, magnified by the large LO amplitude. This can be the quadrature $\hat{q}_\theta$ along an axis rotated by any arbitrary angle θ in phase space ($\hat{q}_{\theta=0} = \hat{x}$, $\hat{q}_{\theta=\pi/2} = \hat{p}$) [17, 107]:

$$\hat{I}_1 - \hat{I}_2 \propto |\alpha_{LO}|\, \hat{q}_\theta \tag{2.3}$$

The phase at which the quadratures are sampled in the complex plane in practice is directly given by the optical phase difference θ between the local oscillator and the signal beam, which can in principle be freely adjusted.

Theoretically, the way to measure a quantum state is then straightforward: sampling the homodyne detector's output current, one measures histograms of the quadratures of the signal field. This can be done repeatedly for many different angles in phase space by adjusting the LO phase, until the number of projections of the Wigner function obtained is enough to infer it completely with a good degree of precision.

In practice, for technical reasons, the inversion from the quadrature distributions to the Wigner function is not so straightforward [17]. The most direct possibility is to exploit the linearity of the projection relation (2.2) to mathematically invert it. This method, involving inverse Radon transforms or other similar integral inversions, in theory allows to get directly from the measured quadratures the Wigner function, from which the density matrix can be obtained if necessary. However it has the disadvantage of being very sensitive to measurement noise, and can easily lead to seemingly unphysical features in the final reconstructed state. An explanation of this problem is that one tries to directly constrain from a finite number of noisy projection samples a full 2D function, which contains an infinite number of degrees of freedom.

What is commonly done is rather to use reasonable experimental constraints in order to limit the dimension of the research parameter space. This is particularly efficient if one looks directly for the state's density matrix in a restricted Fock basis: then the parameters to be found are only discrete coefficients, and if one physically sets an upper limit to the number of photons in the expected state, there can be only a few complex values to extract. The search for the density matrix elements can be done using specific optimization algorithms that iteratively look for the best match, among all possible physical density matrices, given the sets of experimentally measured quadratures [17]. A nice feature of these "Maximum Likelihood" algorithms is that one can, from the start, restrict the research space to density matrices that are physically well behaved (trace of 1, hermitian), which makes the number of parameters to determine even smaller, and overall makes these algorithms relatively easy to implement, efficient and fast, as will be shown in more details in the experiment description. When the density matrix has been estimated, obtaining the Wigner function is immediate from its definition (2.1).

2.3 Practical measurement of transient modes' states

One must take care that the simple reasoning underlying the result above is intrinsically single mode. This means, in real experiments, that a homodyne detector is only sensitive to the signal field in the mode of the local oscillator. The projection onto the spatiotemporal mode of the LO takes place because the measurement relies on interferences between the two beams.

If the spatiotemporal shapes of the modes excited by the signal light to be characterized and the LO are respectively described in the transverse plane of the detectors by $u_s(x, y, t)$ and $u_{LO}(x, y, t)$, then their overlap is given by (phase conventions are taken such that it is real):

$$\xi = \int u_s^*(x, y, t).u_{LO}(x, y, t)\ dx\ dy\ dt \tag{2.4}$$

It is possible to show that for non-optimal mode-matching $\xi < 1$, the mode whose quadratures are actually measured by the homodyne setup is a combination of the signal one and vacuum modes [107]. This can be written as:

$$\hat{a} = \xi\ \hat{a}_s + \sqrt{1 - \xi^2}\ \hat{a}_0 \tag{2.5}$$

where $\hat{a}$, $\hat{a}_s$ and $\hat{a}_0$ are annihilation operators corresponding to the measured mode, the signal mode, and a vacuum mode respectively. This is exactly equivalent to losses being induced on the signal detected, corresponding to an intensity transmission of ξ^2 (the detector only sees the fraction of the signal that interferes with the LO, the rest is lost). Overall, all losses experienced by the signal before being detected can be described through a formulation like equation (2.5), by mixing the initial signal mode with vacuum [107]. As we will see in more details later, this leads to very fast degrading of the non-classical states one can reconstruct via this technique, so that all types of losses must be minimized by all means.

As a result, a large part of the difficulty in implementing homodyne tomography in practice is that one must a priori know in advance the full spatiotemporal mode of the signal to be characterized, and match the LO to the exact same mode. Getting sufficient control and information about the transverse spatial mode and central frequency of a signal is usually relatively easy (if the system was at least partially optimized for this purpose). However when one wants to characterize a quantum state that is temporally localized within an unknown pulse shape, as will be the case in our experiments, it can be difficult to know exactly this shape or how to match the LO to it.

The immediate approach would require a LO physically shaped to match the signal's temporal envelope, and synchronized with it. This is doable only if one has good reasons to expect the signal pulse to be fixed by some external reference shape which can also be used for the LO, such as in parametric down-conversion schemes driven by short identical laser pulses.

If the signal envelope is mostly set by intrinsic dynamics of an independent system, like a cloud of atoms, there is a priori no easy way to give directly the right shape to the LO, even though numerical simulations can help predicting the expected time behaviour of the output field and try to adapt to it.

The solution can thus be to play with this mode-matching condition on the temporal envelope: as such it appears because, to access a quadrature measurement inside a mode, one must integrate in time over its duration, and if the signal and detection modes are not well adapted this integration does not extract correctly the desired information. Then, instead of trying to have this timeshape-matched integration done directly during the measurement, one can on the contrary record time-resolved data affecting them as little as possible, to realize the time integration afterward numerically. This can be done with a continuous LO, on the condition that the time resolution of the acquisition is much shorter than the typical timescale describing the signal pulse shape. It is then perfectly equivalent, to obtain a signal quadrature sample from a given pulse, to integrate the signal obtained with a temporally matched LO with field envelope $f(t)$ over the pulse, or to acquire data

with a constant LO field and afterward weigh numerically the signal with function $f(t)$ and integrate it.

This method has very nice advantages from the point of view of the experimental implementation, such as the possibility to acquire homodyne data once only, on which all possible virtual shapes of LO pulse can be tested in post-processing, but it also has drawbacks, as will be discussed in details in the description of the experiments. In order to find the right weighing function to apply to the raw data if the temporal mode is totally unknown, efficient methods relying on the analysis of the signal's autocorrelation function have been proposed [108]. Another possibility is to first get partial information about the mode using a different, less sensitive detection technique, and optimize the effective mode used for homodyne detection around this rough guess. Note that in any case the spatial mode-matching of the signal and LO beams is still absolutely crucial if one wants to measure anything at all.

Let us emphasize here that this issue of quality and control of the mode in which quantum states are produced is of prime importance if one wants to use them for further QIP schemes, in particular for interfacing them with other material systems, or making two of them interfere, which is a condition for several schemes [78]. The proper characterization of a quantum state with homodyne detection guarantees, among other things, that the optical field within the pulse oscillates with a clean single frequency and does not present problematic nonlinear phase drifts, which would ruin the overlap and the detection efficiency.

Part II

Experimental tools

Chapter 3

Lasers

Contents

In our experiments, lasers are necessary for trapping, cooling, optically pumping, probing the atoms – which can be performed on many different atomic transitions – as well as for quantum state analysis or cavity locking. As a result, the complete laser system is constituted of six different laser sources. Since all of them have to be stable with respect to some atomic resonance frequency, they are all stabilized on a common reference or "transfer cavity". The laser wavelengths are adapted to the use of rubidium 87 atoms, as explained in chapter 5.

3.1 Master laser

The main reference in the laser assembly is a TA Pro system from Toptica working at 780 nm to address the D2 transition of ^{87}Rb.

At the output of the tapered amplifier, approximately 1 W of light is split in different arms to be used in the two atomic traps (main and source ones, see chapter 5), as well as in various probe beams.

This laser is frequency-stabilized via saturated absorption on an atomic vapor cell heated to $\approx$ 40 °C, to compensate for very slow frequency drifts by acting on a piezo element inside the laser cavity.

For high frequency noise cancellation, the reference is given by the transfer cavity.

3.2 Transfer cavity

Most of the lasers are frequency-stabilized using the reflection of a sample beam onto this common optical cavity. This ensures a good relative frequency stability.

In practice we use a Z-shaped linear optical cavity with four mirrors mounted on Invar steel mounts linked by three ULE glass rods making the cavity insensitive to temperature variations, shown in figure (3.1). One of the Invar mounts provides the X and Y adjustments required to align the cavity. One of the mirrors rests on a low-voltage piezo stack used for low-frequency length stabilization.

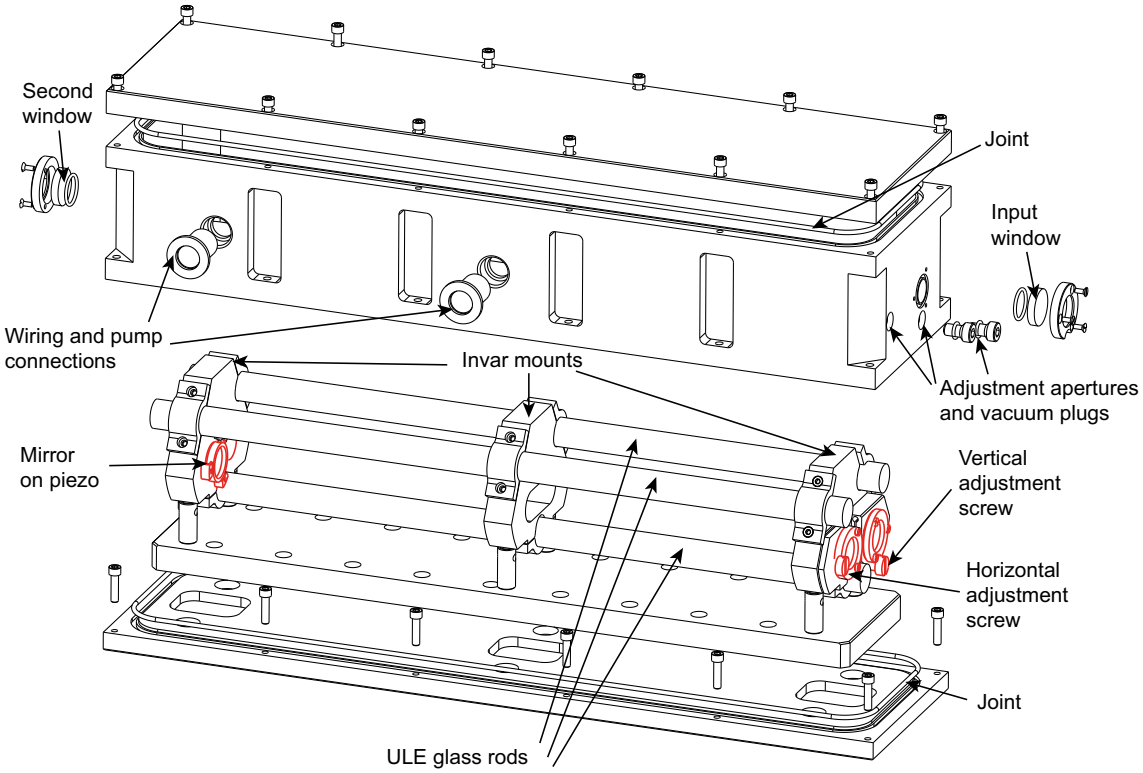

Figure 3.1: Transfer cavity (full assembly). Expanded schematic of the full cavity assembly and vacuum chamber. The whole Dural framing box can be hermetically sealed. Mechanically isolated from it by joints in the baseplate, the cavity structure is made of four mirrors mounted on Invar mounts hold together by ULE glass rods. On the right end, each mirror has one-axis adjustment possibility to align the cavity via screws that are accessible from outside through small apertures. On the left end the final mirror of the cavity is mounted on a low-voltage piezo. Original image by André Guilbaud.

Humidity and temperature effects are minimized by placing the cavity inside a dedicated sealed chamber, pumped under primary vacuum. The total expanded length of the cavity is around 1.5 m, corresponding to a free spectral range of 110 MHz. The finesse, wavelength-dependent, is approximately 10^3 at 780 nm. Once pumped under primary vacuum, all the lasers can be locked on the exact same transfer cavity line every day for over a year without having to readjust anything about it. The cavity linewidth itself was measured to ≈ 150 kHz, and the laser linewidth when locked on it is < 50 kHz.

This reference resonator's length is very stable with respect to high frequency noise, but its offset has to be stabilized on an absolute reference. This is done using a two-ways lock between the master laser at 780 nm and the transfer cavity. For high frequency stabilization, the laser is locked on the cavity through retroaction on the diode's current, while at low frequencies it is the cavity length which is stabilized actively to follow the laser frequency, which is fixed with respect to atomic transitions. All laser frequencies are

then stabilized with respect to the atomic resonances.

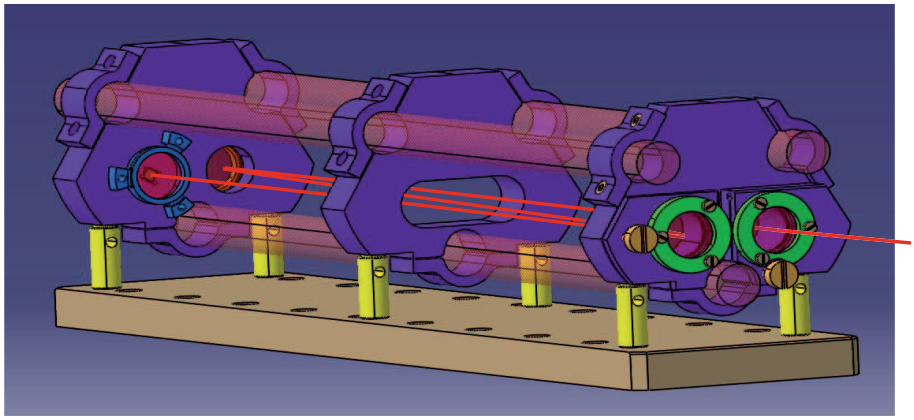

Figure 3.2: Transfer cavity (cavity structure alone). The beampath is represented by the red solid line. Original image by André Guilbaud.

The schematic of the locking system for the full laser system is summarized on figure (3.3). See also figure (4.1).

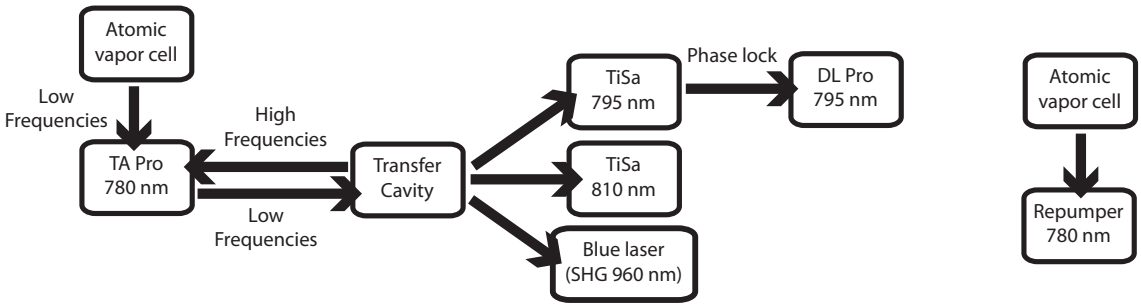

Figure 3.3: Schematic of the "influence" of one device on the others in the locking chain of the complete laser system.

3.3 Titanium-Sapphire lasers

We use two Coherent MBR-110 Titanium-Sapphire lasers, one at 795 nm to address the D1 transition of ^{87}Rb, and the second at 810 nm in order to be far away from all atomic transitions and interact weakly with the atoms. Both are pumped by Verdi lasers producing around 9 W of pump power, to produce in total an approximate 2 W of infrared power.

The locking scheme for these two lasers is identical. The TiSa frequencies are stabilized on an error signal coming from a built-in internal reference cavity. This cavity's length is adjusted to match the common atomic standard by following the error signal from a locking beam on the transfer cavity. By choosing the transfer cavity resonance line and adjusting the frequency of the Acousto-Optic Modulator (AOM) generating the locking beam, the laser's frequency can be locked to any interesting value, and have it stable compared to atomic references.

The interest of these two lasers is to deliver an important intensity at a very adjustable wavelength, convenient to strongly excite one of the atomic transitions (for the 795 nm TiSa) , or to realize a conservative optical dipole trap (for the 810 nm one).

3.4 Repumper, DL 795, blue laser

Three additional lasers are used in different ways in our various experiments.

Due to the multilevel structure of atoms, a repumper is necessary to avoid losing them in dark states when exciting them on an open transition with the trap light. It is a DL Pro laser from Toptica, giving an output power of approximately 30 mW, of which only a few are generally used. As its frequency stability is not crucial, it is locked separately from the others, with a plain saturated absorption signal from a dedicated hot vapor cell.

A similar laser, working at 795 nm, is used to interact with yet another atomic transition on which only little power is necessary. For reasons that will be explained later, it has to be extremely stable with respect to the 795 nm TiSa, so that it is frequency stabilized with respect to it by a phase locking loop.

Finally, in the experiments where atoms are excited to Rydberg levels, a specific laser is required. It is a Toptica system where a 960 nm initial laser beam is frequency doubled in a Second Harmonic Generation cavity to produce a beam around 480 nm, the so-called blue laser. The laser itself is frequency-stabilized by sending a small part of the 960 nm beam to the transfer cavity, through an AOM. This allows us to make use of approximately 400 mW of light at an arbitrarily chosen frequency around 480 nm.

Master laser	1.2 W at 780 nm
TiSa 1	2 W at 795 nm
TiSa 2	2W at 810 nm
DL795	30mW at 795 nm
Repumper	30mW at 780 nm
Blue laser	400mW at 480 nm
Transfer cavity FSR	110 MHz
Transfer cavity finesse (780 nm)	10^3

Table 3.1: Lasers and transfer cavity: summary.

Chapter 4

Control and acquisition setup

Contents

Cold atoms bring intrinsic timescale constraints to experiments. Loading the trap from zero can take several seconds, while some of the pulses used to drive the atoms have to be of duration close to the natural lifetime of some excited state, which can be of a few tens of nanoseconds.

Therefore, for atom preparation or measurements, a complex sequence has to be finely controlled over a large range of timescales. Data acquisition/processing also has to be interfaced in the sequence in a fast and efficient way. In addition to this, the control/acquisition system has to be completely reconfigurable when going from one experiment to another.

Our computer-based input-output system is designed and optimized for the kind of experiment described in this manuscript, and the point of this chapter is to give an idea of its constituents and how it works.

4.1 Hardware

A large part of the necessary sequencing is controlling the frequencies and powers of several laser beams. For that, each beampath is typically designed to pass twice through a dedicated AOM (MT-80 or MT-110 from AA Opto-Electronic), before being injected in a fiber to be transferred from the laser bench to the atomic setup, as shown in figure (4.1). As a result, a set of RF signals sent to many different AOMs must be controlled in frequency, analog power setting, and fast digital 0/1 operation.

For stability, repeatability and relative phase control, we use digital RF synthesizers of two different kinds as sources, directly controlled by a dedicated computer. Two static Novatech modules 409B, with 4 channels each, produce RF signals that do not require fast active control. The dynamical ones are produced by four Acquitek Synth300 cards (1 master and 3 slaves), each having two Direct Digital Synthesizer outputs (100 kHz-300 MHz, 0.233 Hz increments). Each of these DDSs can be programmed to memorize four different generation profiles (values of frequency and phase), and switch upon external

trigger from one to another, or to start and stop frequency ramps with predefined slopes. This behaviour is controlled with two TTL inputs, corresponding to two logical control bits, for each card. In order to control the RF power sent to the AOMs, each of the Synth300 outputs is passing through a variable RF attenuator with a digital switch, before supplying an AOM (see figure (4.1)).

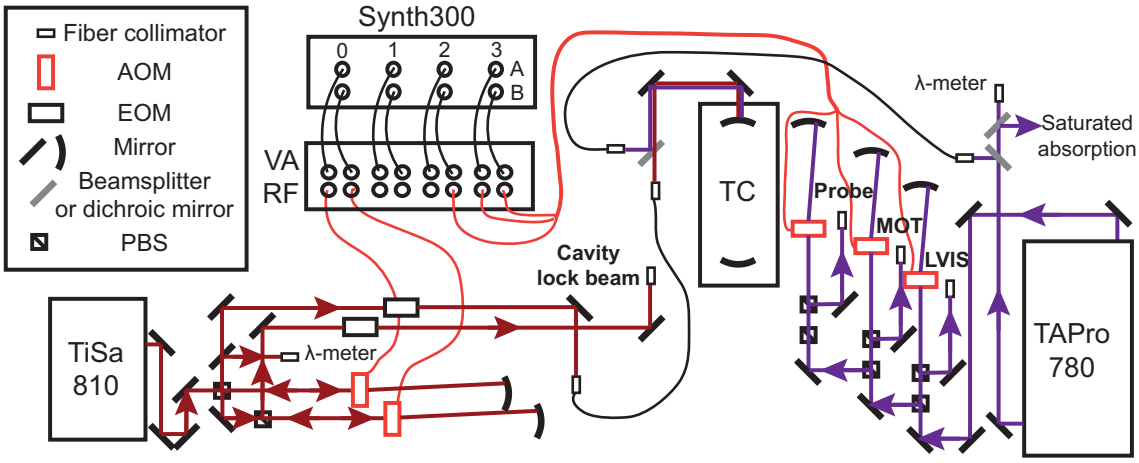

Figure 4.1: Typical setup of beam preparation and control on the laser bench. A typical example is given, restricted to the master laser (TAPro 780) and the 810 nm TiSa, of the way the various beams are prepared, and the use made of RF synthesizers to control AOMs. A locking beam from the 780 laser is used for saturated absorption and locking on the transfer cavity (TC). Various beams (MOT, LVIS, Probe – see next chapter for details) are prepared from the main laser beam, each going through a dedicated AOM. From the 810 TiSa a beam is prepared, shifted by an AOM and modulated by an Electro-Optic Modulator (EOM), then sent to the transfer cavity to lock the laser at an adjustable frequency. The locking beam for the main science cavity (see chapter 6) is produced from this laser, controlled by yet another dedicated AOM. All the AOMs are supplied by digital RF synthesizers (only the Synth300 are shown for the example), which allows us if needed to react dynamically on their frequency and efficiency (analog or digital control, using the variable attenuators VA RF). PBS: Polarizing BeamSplitter.

All in all, most of the needs for the experimental control can be summarized in a large number of analog and digital input and output channels, programmable in a sequence to be perfectly synchronized. That is enabled by a custom made National Instruments PXI controller, with a selection of input/output cards. Three analog output cards are used to produce all the analog signals, for the active power control of some optical beams for example (DAQ: 2x PXI-6713, 8x1MHz channels, 1x PXI-6722, 8x180kHz channels). Slow analog signals, mostly for monitoring purposes, are acquired by a simple analog input card (DAQ: PXI-6143, 8x250kHz analog inputs). Fast input/output operations are handled by two modules working on FlexRIO FPGA PXIe-7962R bases. One fast digital input/output module provides the numerous TTL controls (DIO NI 6581, 54x100MHz input/output channels). Fast digital data (like the very short TTL pulses coming from single photon counters) are also registered by this module. And finally a fast analog 4-channels input module is absolutely crucial to record the kind of analog signals a fast homodyne detector produces for example, on the timescale of a photon's wavepacket (AI NI 5761, 4x250MHz analog inputs, 14bits).

A summary of the overall structure of our hardware control/acquisition setup is shown

in figure (4.2).

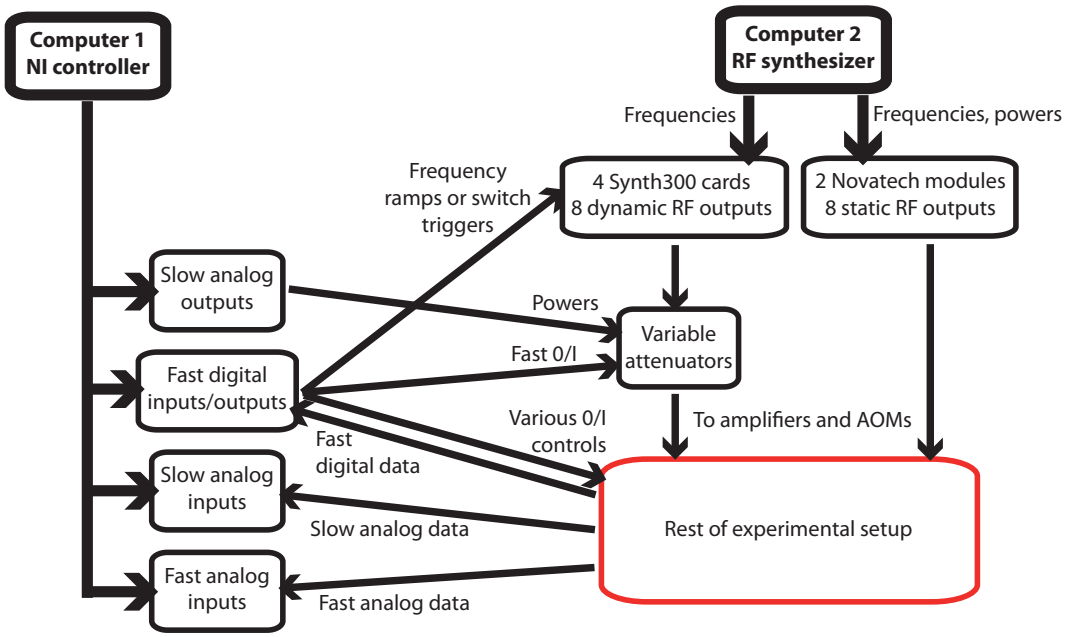

Figure 4.2: Schematic of the structure of our complete control and acquisition system.

4.2 Software

What is expected from the software handling all these inputs and outputs is rather demanding. It has to be able to generate loops and subloops of different experimental steps, some of them containing very fast instructions ($\approx$ 10 ns), while continuously streaming some fast data acquisition, and adjust in real time (still on the timescale of few tens of nanoseconds) parts of the sequence depending on the measurements results, all of this while being completely reconfigurable between one experiment and the following one.

A complete Labview software was developed specifically for these purposes, in an "event-based" type of programming [1], thanks to the expertise of M.-H. Pottier from Arcale. The FPGA basis for the fast input/output was chosen to enable the fast logic and data processing. The fast channels' instructions and the sequence's conditional logic are hard-coded on the FPGA before running any experimental sequence, so that during the actual execution all of it runs "on its own", independent from all possible software-induced delays etc ...

The reconfigurable part of the sequences is defined through the Graphic User Interface, where three main levels of configuration are accessible:

1. The software is split in a few sub-modules, each handling one layer of the tasks to be dealt with (graphic interface, channels behaviour encoding and execution, data processing ...). Each of these modules has several profiles defined, corresponding to the kind of tasks it should be executing in given conditions (for example streaming data, or reading a certain number of points and saving them into a dedicated memory). The communication between modules and switching from one profile to another is done as follows: each module registers to some particular channels of events, and can react to what happens on these channels. On the other hand, each of them is also able to "publish" events on a channel upon particular conditions (a button is pressed, or a task is finished), that can be detected by other modules.

1. Selection of the digital/analog input/output channels involved in the sequence (see figure (4.5)). The necessary channels are selected from all physically available I/O ports of the different cards. They are identified by a name, which is linked to their physical address in a ".ini" file, loaded at the opening of the software, that can be modified by hand. When the sequence is loaded, only the useful physical addresses are identified, activated and initialized.

2. Definition of the experimental sequence in terms of global steps of various durations (see figure(4.6)). A typical sequence always contains steps of the form: trap loading – cooling (optical molasses, see next chapter) – atom cloud preparation (optical pumping, ...) – measurements. The totality of the sequence is repeated over relatively long timescales, with possible shorter loops and subloops inside the main sequence for time optimization, as shown in figure (4.3).

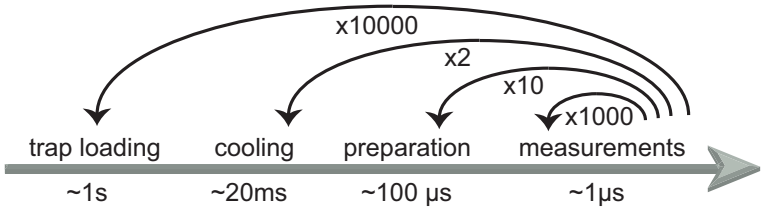

Figure 4.3: Typical sequence behaviour. The measurements themselves are made of short periods ($\sim 1\mu$s) repeated a large number of times (~ 1000) which have to be alternated with preparation steps regularly, and maybe integrated into some larger loop of re-cooling the atoms, before having to reload the trap. The generation and data acquisition inside a measurement step must be resolved on ~ 10 ns timescale.

   The total number of independent steps is thus specified at this stage, as well as their individual durations, and the loops structures. These parameters are passed on to the module handling the actual execution, in order to control the synchronized switching of all channels from one step to the next.

3. Definition of the detailed behaviour of each useful output channel, for each step of the sequence. For a digital output, the behaviour inside each step is a series of pulses, defined by three values (time low-time high-time low) and a number of iterations (see figure (4.7)). For analog channels, the behaviour in a step is split in a variable number of simple instructions with their durations: constant output value, ramp from one value to another, or generation of a series of values defined in an external file to create arbitrary waveforms (see figure (4.8)). The subdivision of a step can be different from one channel to another.

All values defining the sequence steps and the channels' behaviours are transmitted to the FPGA code which can then execute, handling in parallel all channels with a 100 MHz update rate. The FPGA allows us to implement fast conditional logic among the channels: one specific detection channel (typically an SPCM's firing events) can be used as a trigger to activate or deactivate other parts of the sequence in the subsequent steps. This way, when for example a repeated low-probability excitation process has succeeded, it can be suppressed in the following cycles, and a probing laser pulse can be sent instead. Data saving can also be selectively activated during the probing, and at the same time the trigger events can be ignored to avoid background re-triggering during measurements.

Software gates can also be defined, that behave as virtual digital channels ("GateTrig" and "GateAcq"), to perform logical gating of the acquired signals and determine when they should be taken into account. This allows for an efficient noise reduction on the trigger for example, by opening a gate only in the "region" where the excitation is realized and "true" triggers are expected (see figure (4.4)).

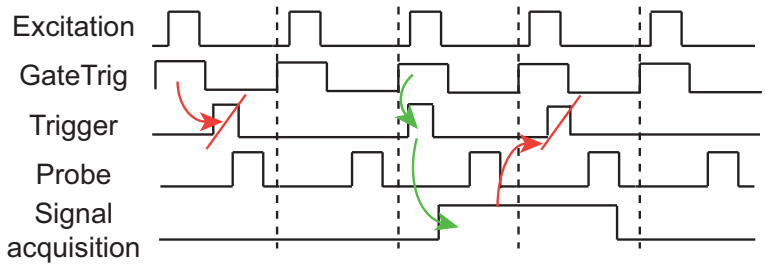

Figure 4.4: Example of conditional behaviour. The events on the trigger channel are taken into account only if the GateTrig is high. When this happens, it enables the acquisition of the interesting signal during the following probing, which in turns deactivates the possible re-triggering for the duration of the acquisition.

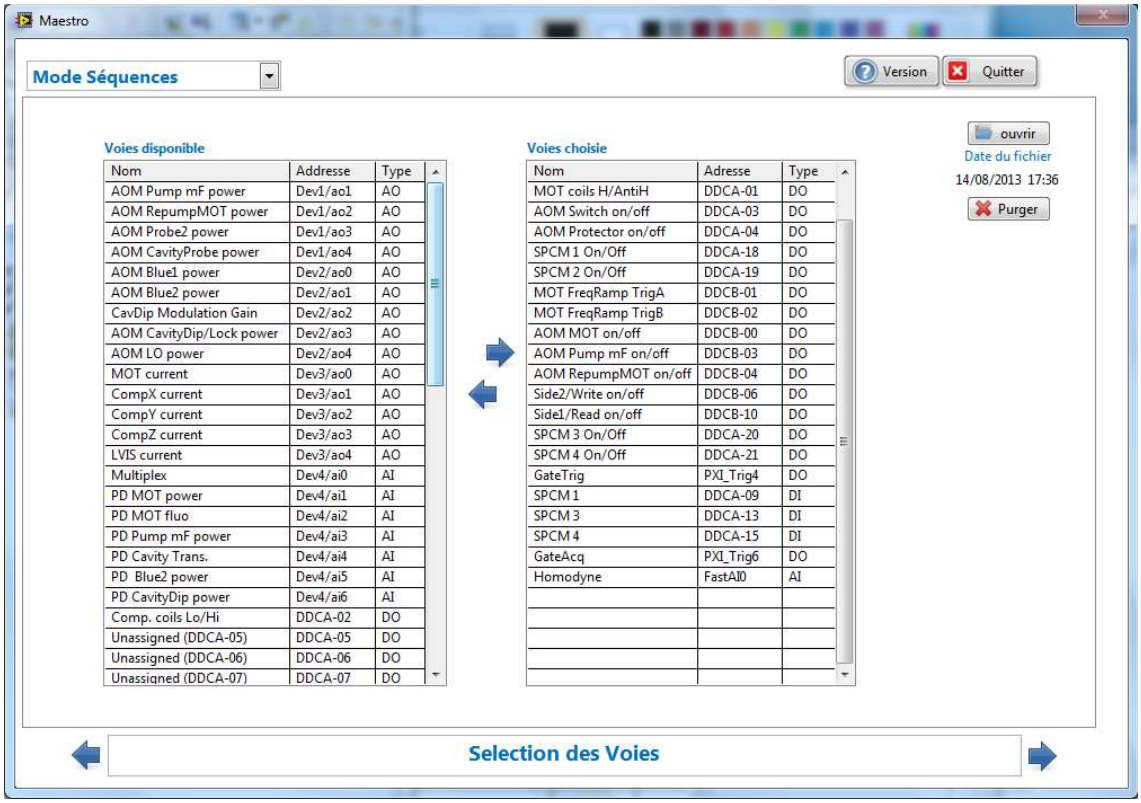

Nom	Addresse	Type
AOM Pump mF power	Dev1/ao1	AO
AOM RepumpMOT power	Dev1/ao2	AO
AOM Probe2 power	Dev1/ao3	AO
AOM CavityProbe power	Dev1/ao4	AO
AOM Blue1 power	Dev2/ao0	AO
AOM Blue2 power	Dev2/ao1	AO
CavDip Modulation Gain	Dev2/ao2	AO
AOM CavityDip/Lock power	Dev2/ao3	AO
AOM LO power	Dev2/ao4	AO
MOT current	Dev3/ao0	AO
CompX current	Dev3/ao1	AO
CompY current	Dev3/ao2	AO
CompZ current	Dev3/ao3	AO
LVIS current	Dev3/ao4	AO
Multiplex	Dev4/ai0	AI
PD MOT power	Dev4/ai1	AI
PD MOT fluo	Dev4/ai2	AI
PD Pump mF power	Dev4/ai3	AI
PD Cavity Trans.	Dev4/ai4	AI
PD Blue2 power	Dev4/ai5	AI
PD CavityDip power	Dev4/ai6	AI
Comp. coils Lo/Hi	DDCA-02	DO
Unassigned (DDCA-05)	DDCA-05	DO
Unassigned (DDCA-06)	DDCA-06	DO
Unassigned (DDCA-07)	DDCA-07	DO

Nom	Adresse	Type
MOT coils H/AntiH	DDCA-01	DO
AOM Switch on/off	DDCA-03	DO
AOM Protector on/off	DDCA-04	DO
SPCM 1 On/Off	DDCA-18	DO
SPCM 2 On/Off	DDCA-19	DO
MOT FreqRamp TrigA	DDCB-01	DO
MOT FreqRamp TrigB	DDCB-02	DO
AOM MOT on/off	DDCB-00	DO
AOM Pump mF on/off	DDCB-03	DO
AOM RepumpMOT on/off	DDCB-04	DO
Side2/Write on/off	DDCB-06	DO
Side1/Read on/off	DDCB-10	DO
SPCM 3 On/Off	DDCA-20	DO
SPCM 4 On/Off	DDCA-21	DO
GateTrig	PXI_Trig4	DO
SPCM 1	DDCA-09	DI
SPCM 3	DDCA-13	DI
SPCM 4	DDCA-15	DI
GateAcq	PXI_Trig6	DO
Homodyne	FastAI0	AI

Figure 4.5: Channel selection. Channels are selected by name, associated with a physical address on one of the cards and a channel type (AI/AO/DI/DO), and sent from the list of available channels (left) into the list of chosen channels (right).

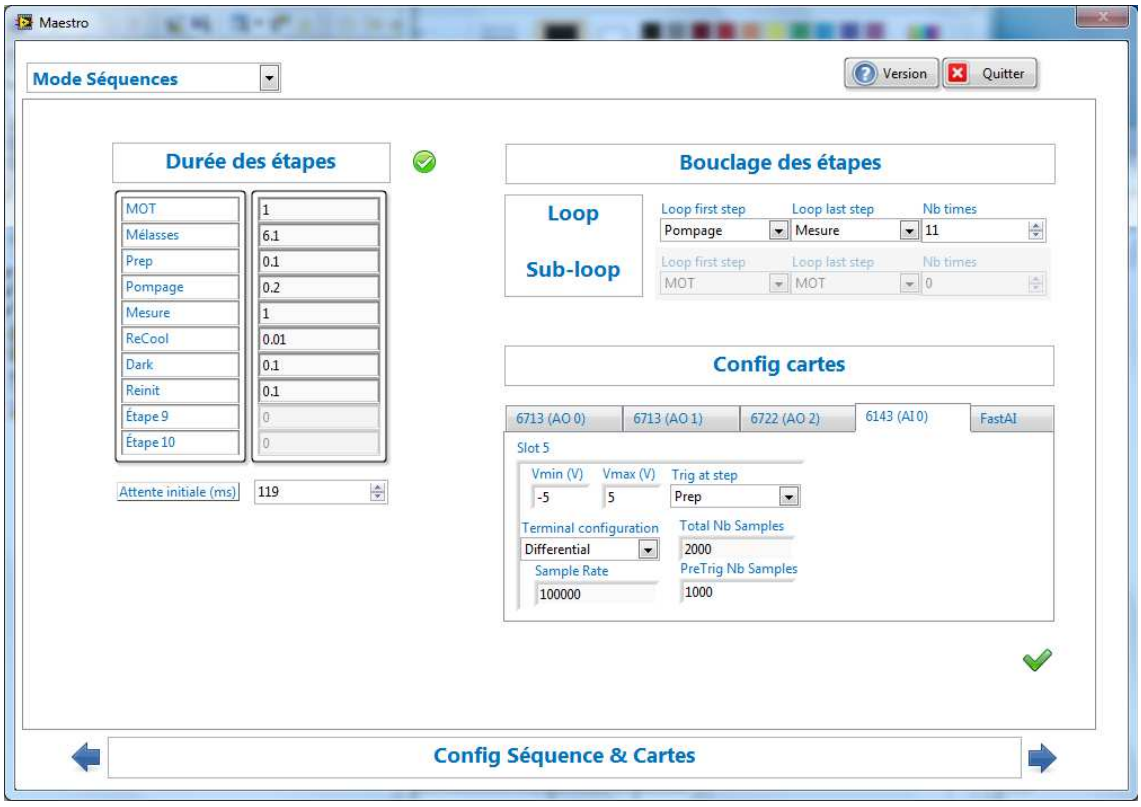

Figure 4.6: Overall sequence configuration. On the left, the independent steps of the sequence are defined by a name, an order, and a duration. An initial waiting time at the beginning of each sequence can be defined. On the top right, one indicates if loops should be performed, defined by their starting step, final step, and the number of times the steps in between should be repeated. Subloops can also be performed inside each loop. Here are also configured the general settings of the cards, like their total generation/acquisition range and sampling rate.

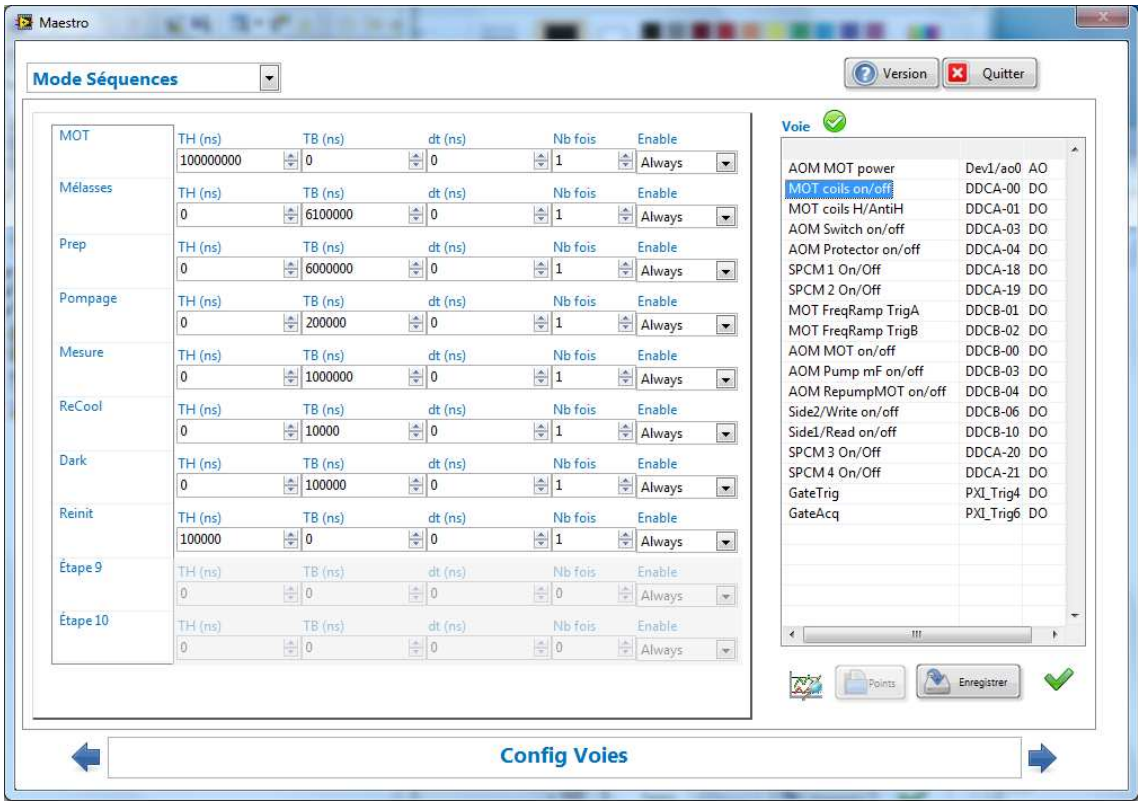

Figure 4.7: Digital channel configuration. For one channel selected in the list on the right, the behaviour for a given step is displayed in a line on the left. It is made of a repetition of time low ("dt", third column), time high ("TH", first column), time low ("TB", second column), a given number of times ("Nb fois", fourth column). The channels can be selectively enabled in different steps based on different criteria (see main text).

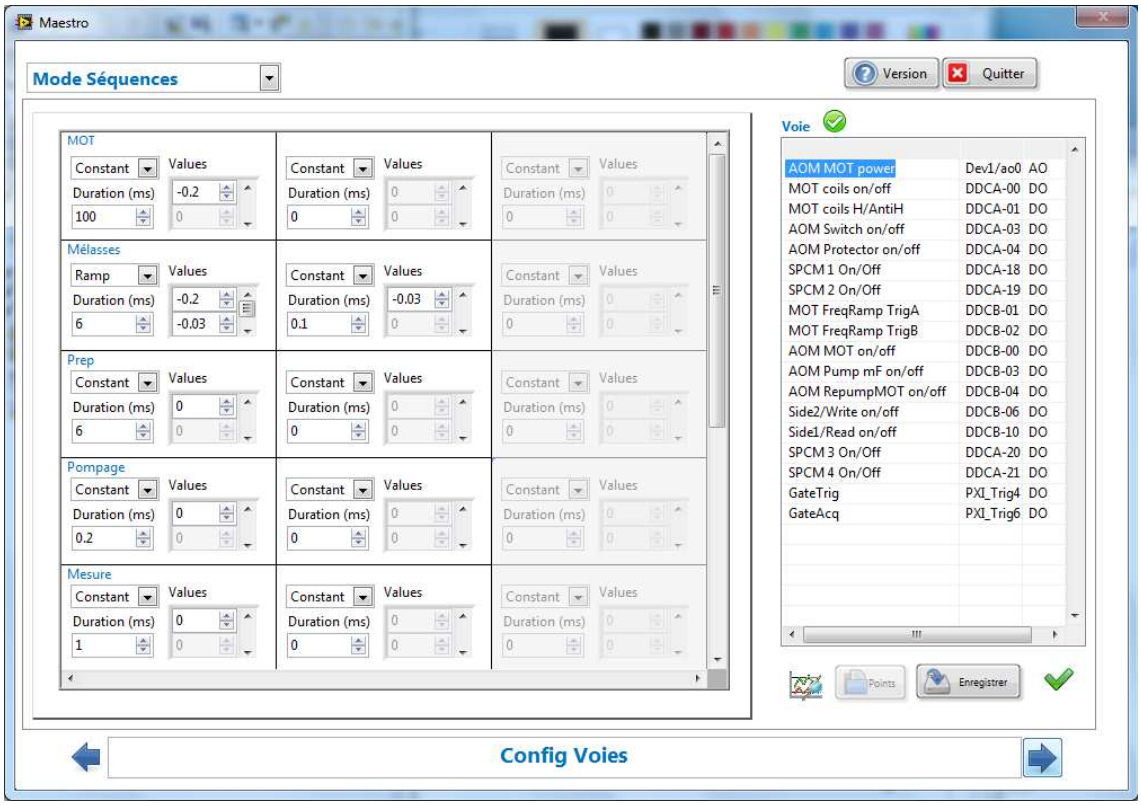

Figure 4.8: Analog channel configuration. For one channel selected in the list on the right, the behaviour for a given step is displayed in a line on the left. A variable number of boxes in a line can be activated, each one containing one of the possible instructions (constant, ramp, or waveform) and a total duration. The total of the durations of all boxes on one line is normally equal to the duration of the corresponding step.

Chapter 5

Atomic system

Contents

Here we will describe the main elements of the experimental setup – the vacuum chamber and the atom trap setup – and the typical properties of the clouds that can be trapped.

Most of the important information about the atoms-cavity-vacuum chamber system is summarized at the end of section 5.4 in figure (5.4).

5.1 Rubidium 87 structure

We work with one of the common isotopes of rubidium, ^{87}Rb. Its atomic structure is well known (see figure (5.2)), and its spectrum exhibits fundamental lines in the visible spectrum, with a rich fine, hyperfine and Zeeman substructure that can be used to implement efficient trapping, cooling, and many different excitation schemes.

The fine fundamental doublet is made of the D1 and D2 lines, whose main properties are summarized below.

All the level structure –and more– for rubidium is very well summarized in the document by Daniel Adam Steck [109]. The structure of the D1 and D2 lines is also shown on figure (5.2).

D1 line	795 nm
D1 hyperfine components	$F = 1, 2 \rightarrow F' = 1, 2$
D2 line	780 nm
D2 hyperfine components	$F = 1, 2 \rightarrow F' = 0, 1, 2, 3$
Excited state decay time	27 ns
Population decay rate $\Gamma = 2\gamma$	$2\pi.6$ MHz

Table 5.1: ^{87}Rb D1 and D2 lines: summary.

5.2 Experimental setup – Vacuum chamber

For a trapped cloud of cold atoms, ambient pressure means losses due to collisions [110]. Our vacuum chamber, described in [111], is a cylinder with a 25cm radius and a 25cm height made of non-magnetic 316L stainless steel. The global volume of the chamber (≈ 0.05 m^3) is maintained at a pressure around $1 - 5.10^{-10}$ mBar in running conditions by a large capacity ion pump (Varian VacIon Plus 300, model 919-2641, 240 L/s pumping speed, with controller Dual 929-7004, occasionally helped by a Titanium Sublimation Pump of the 916-0050 series).

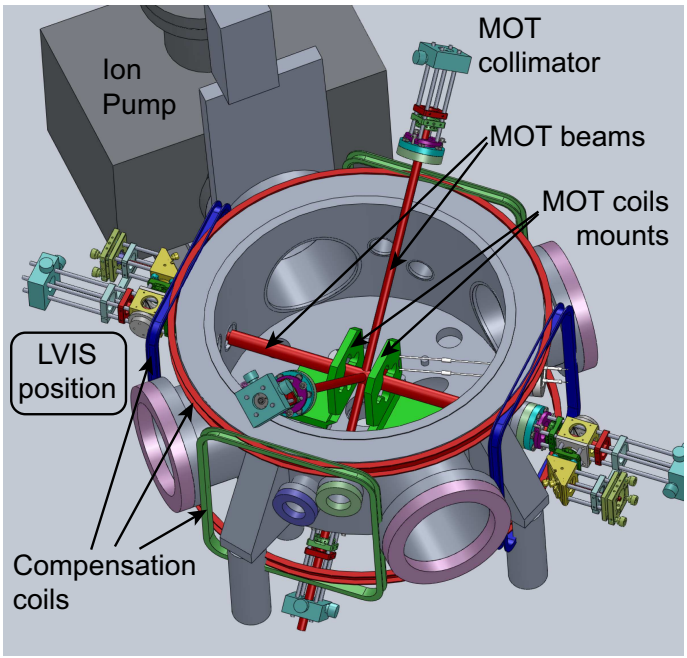

Figure 5.1: Practical configuration of the vacuum chamber and some of the elements related to it. Original image by Florence Nogrette.

The coils that produce the magnetic field necessary for the atomic trap are inside the chamber. The two coils are spiral shaped, flat, facing each other at a distance of 5 cm. They are made of hollow-core copper wires connected through vacuum-compatible ceramic connectors to the outside, cooled down by an air flow circulating inside them. The wire of each coil is doing only 8 full revolutions around the center in order to keep the inductance to a minimum and allow for a fast switching of the magnetic field at a sub-ms scale ($\sim$ 300 μs), using a custom-made current switch. The geometrical configuration used leads,

in anti-Helmholtz configuration, to a gradient on axis at the center of approximately 0.5 G/cm per 1 A current.

Another crucial part of the setup being inside the vacuum is the optical cavity itself. More details about it are given in the next chapter.

Connected to the main vacuum chamber is also a secondary one in which the atomic source is setup. More details about that will be given in section 5.4.

5.3 Magneto-optical trap

The main trap in which the atom cloud is formed is made of a standard Magneto-Optical Trap (MOT) [112, 113].

The six large independent trapping beams ($\sim$ 1 cm diameter) are produced through a Schäfter-Kirchhoff variable fibered splitter with two inputs and six outputs. One main beam from the TA Pro laser and a second, weaker one, from the repumper diode are mixed together and split equally between all six output fibers, mounted on collimators fixed directly on the vacuum chamber. The MOT is therefore realized on the $D2$ line at 780 nm: the main trap light is at an adjustable frequency close to the $5S_{1/2}, F = 2 \rightarrow 5P_{3/2}, F = 3$ transition, while the repumping light is set on resonance with the $5S_{1/2}, F = 1 \rightarrow 5P_{3/2}, F = 2$ to avoid losses of atoms to the $5S_{1/2}, F = 1$ state (see figure (5.2)). This is achieved, in the case of the trap light, by locking the main 780 laser on the crossover between the transitions from $5S_{1/2}, F = 2$ to $5P_{3/2}, F = 1$ and $5P_{3/2}, F = 3$, and adjusting the frequency of the AOM controlling the beampath for the trapping light.

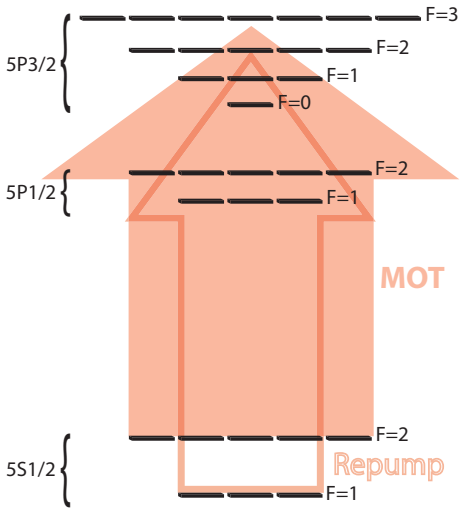

Figure 5.2: Level scheme of the magneto optical trap showing the level structure on the D1 and D2 lines of rubidium 87 and the levels coupled by the MOT and repumping beams.

Compensation of constant stray magnetic field at the trap position is realized with three orthogonal pairs of coils outside the chamber. Each pair is supplied by a bipolar current source from High Finesse (BCS 2/25). After magnetic field compensation, the two trap coils (inside the vacuum), in anti-Helmholtz configuration, produce the necessary field gradient in all directions for the trap.

After experimental optimization of the number of atoms and their temperature, the

configuration used is the following: the MOT beams are detuned by 18 MHz to the red of the transition (-3Γ), each trapping beam has an intensity at its center of around 5 mW.cm^{-2}, and the on-axis magnetic field gradient is usually between 5 and 10 G/cm (corresponding to a current in the coils of 10 to 20 A). In this situation the number of atoms loaded in steady state in the trap depends a lot on the regime of use of the atom source (see following section), reaching at most the order of magnitude of 10^9 atoms, for a cloud size varying from few hundreds of microns to almost a millimeter of radius. We could verify the limitation of the temperature by Doppler processes in the MOT, by measuring around 150 μK which corresponds to the rubidium Doppler temperature ($T_D = \frac{\hbar\gamma}{k_B} = 146\mu\text{K}$).

In order to get past the Doppler limit, the configuration is switched from full MOT to optical molasses, by switching off the magnetic field gradient. In optical molasses, the equilibrium temperature is proportional to the cooling light's intensity and inversely proportional to the detuning to the transition [114, 115]. Therefore once the magnetic field is switched off, the optimal molasses step includes a progressive decrease of both the trap beam intensity and of its frequency. In order not to lose too many atoms in the process, the whole sequence was once again optimized. Lasting in total 6 ms, our standard molasses phase contains during the first 3 ms a ramp of the detuning from -18 to -48 MHz, which is then maintained until the end, while the intensity of the beams is divided by a factor close to 10 linearly from the beginning to the end of these 6 ms. This molasses phase leads to a decrease of the temperature of the atomic cloud to between 30 and 50 μK depending on the exact conditions.

In all these processes the repumper power is usually much above saturation level and could be decreased by a factor 10 without seeing any effect on the loading.

5.4 Atom source LVIS

Loading of a magneto-optical trap can be realized in many different ways. Many experiments make use of an oven where hot rubidium gas is prepared and then decelerated in a Zeeman slower [116]. This is a bit space-consuming, and the slowing beam that has to be sent precisely on axis with the MOT position itself can sometimes be a problem.

We use another type of rubidium source, called LVIS for Low Velocity Intense Source [117, 118]. It works like a full MOT being made in a secondary chamber, with its own setup of anti-Helmholtz coils and trapping beams (see figure (5.3)). This chamber is linked to the main one by a small tube ($\sim$ 2 mm diameter) through which differential pumping can be established, maintaining the secondary chamber at a pressure $\sim$ 100 times higher than the main one. On the axis of this differential tube, oriented toward the center of the main chamber, one trapping beam is sent and reflected on itself by a mirror with a hole in the middle coinciding with the entrance of the tube. As a result, everywhere in this secondary chamber the atoms are trapped and cooled like in a full MOT configuration, except on the tube's axis where the total force exerted on them by the beams is unbalanced and pushes them through the differential pumping link toward the main MOT's trapping region. Figure (5.3) shows an overall schematic of the configuration used in the LVIS. The trap in the LVIS is operated in parameter ranges very similar to the ones of the main MOT.

The interest of this configuration is that due to the differential pumping, the ambient pressure in the LVIS chamber can be much higher than in the main one ($\sim 5.10^{-8}$ mBar) without increasing too much the loss rate of the main MOT. On the other hand inside the LVIS itself the trapping lifetime is less important because the atoms trapped are very

quickly pushed out of the chamber through the tube. The trap in the LVIS is then filled efficiently from the ambient rubidium vapor at relatively high pressure, produced by a reserve of solid rubidium contained in a small cell. The cell is heated around 37°C to establish a certain equilibrium between solid and vapor that fills the LVIS chamber.

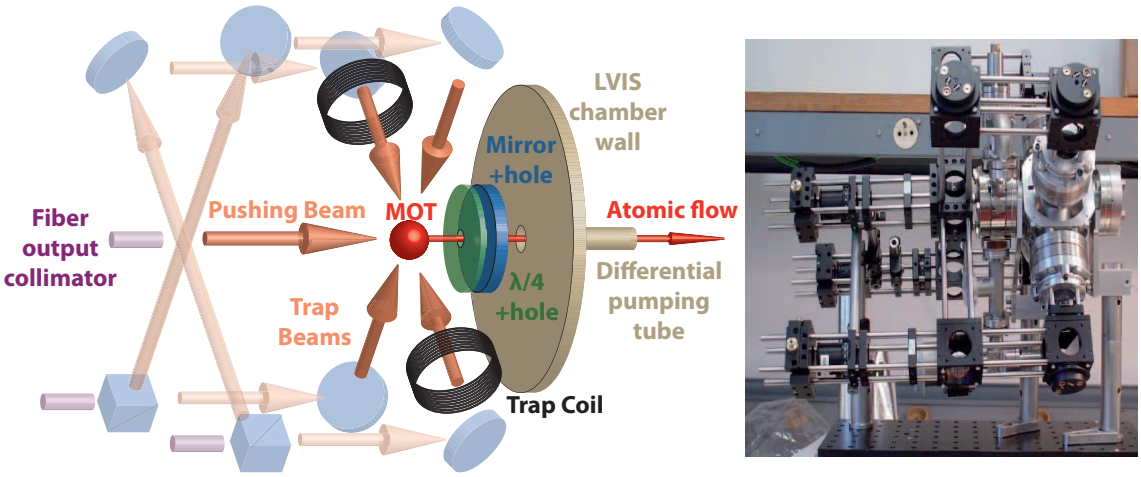

Figure 5.3: Schematic structure of the LVIS (left) and picture of it before being mounted on the main chamber (right). The beam setup counts three laser inputs, among which two are split on cubes to realize the transverse pairs of trapping beams, and one is the pushing beam. All the optics are held in a metallic cage structure fixed around the LVIS vacuum chamber. The pierced mirror and quarter-wave plate necessary to close the trapping scheme around the hole are inside the vacuum chamber, but the trap coils are outside, wrapped around two of the viewports of the chamber. They were not set up yet when the picture was taken.

Using the LVIS, the atomic flow sent toward the main MOT is dense, collimated, cold and slow. The distance between the LVIS chamber and the center of the main one ($\sim$ 30 cm) is enough for the atoms to fall out of the pushing beam during their flight (the pushing beam does not contain any repumping light, so that atoms exiting the LVIS are immediately pumped into a dark state and fly in free fall afterward). As a result, the pushing beam passes $\sim$ 1 cm above the main trap region and does not disturb it in any way. Moving the whole LVIS chamber's assembly, mounted on the main vacuum chamber through a flexible bellow, one can optimize the aiming of the flow of atoms into the trapping region of the main MOT.

The loading capacity of this source is controlled quite intuitively by the density of atoms in front of the connecting tube. If the LVIS cloud forms not exactly on axis with the tube, the transfer efficiency is very low. It is therefore important to have the necessary degrees of freedom to adjust the cloud's position. In our case it can be done by changing the power balance of two transverse counterpropagating trapping beams, as they are produced by splitting a single beam on a cube depending on its polarization. At the same time, changing the loading of the main trap without affecting its own parameters is made quite easy by changing the field gradient in the LVIS, and thus the source's efficiency.

Depending on the parameters of the LVIS and the main trap, the LVIS flux is able to load it at a rate of $\sim 0 - 3.10^8$ atoms per seconds, allowing us to reach a steady state number of atoms in the MOT up to $\sim 10^9$ with a characteristic time of $\sim$ 4 seconds. The average speed of atoms flying from the LVIS to the MOT was measured to 9 m.s^{-1}.

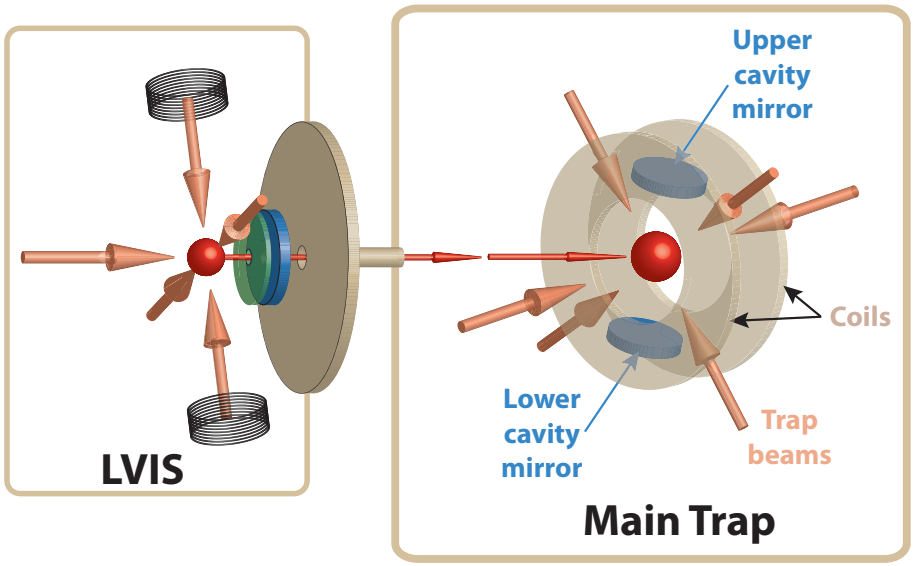

Figure 5.4: Overview of the atomic setup.

Main chamber pressure	1-5.10^{-10}mBar
Magnetic field gradient on axis	5-10 G/cm
Trapping beam intensity	$\sim$ 5 mW.cm^{-2}
Trapping light detuning	-18 MHz
LVIS chamber pressure	5.10^{-8}mBar
LVIS trap to main trap distance	30 cm
atoms propagation speed from LVIS to main trap	9 m.s^{-1}
Characteristic trap loading time	$\sim$ 4s
Steady state loading	0-10^9 atoms
Cloud size R_c	0.1-1 mm
Temperature (after molasses)	30-50 μK

Table 5.2: Typical operating parameters of the atomic system: summary.

5.5 Atom cloud diagnostics

Getting precise *in situ* information about the atomic cloud, like its size and density, can be crucial, especially when studying effects due to interactions between atoms. We mostly use direct fluorescence imaging as a diagnostic tool, but absorption measurements are also possible.

5.5.1 Fluorescence imaging

The fluorescence from the atoms can be collected when they are illuminated with the MOT beams, with a geometrical collection efficiency $\eta_{coll} \approx 0.1\%$ (limited by the size of the collection lense and the viewport through which we image, 30 cm away from the MOT). We use a Princeton Instruments CCD camera PIXIS 400BR connected to a computer, to which it sends images on external trigger. It works ideally when cooled down to -70°C, with a very high sensitivity and low noise (dark current $<$ 0.1 electron/pixel/second at

-70°C). The array is 400*1340 pixels of 20 μm size. The quantum efficiency at 780 nm is $\eta_{CCD} = 94\%$. Because we initially had no mechanical shutter, and in order to make the image acquisition cleaner, the camera is used in a specific mode (Kinetics) where on trigger it realizes two exposure periods, separated by a fast shifting of the CCD array by half its size (without readout, taking 640 μs). This was meant to provide within a quick response time a fresh CCD array that was not spoilt by stray light collected before the intended exposure (the total readout time of the camera's array is 274 ms which is much too long for taking pictures at atomic timescales). Hence the aspect of a typical MOT image captured by the camera in figure (5.5).

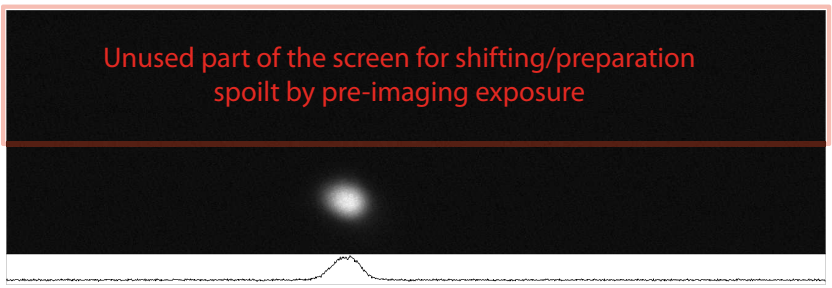

Figure 5.5: Typical MOT image taken by the camera.

From an image taken on the camera, the size of the cloud can be estimated by taking into account the magnifying ratio of the imaging system (depending on the version of the imaging setup, it was between 0.5 and 2). The scattering rate of one atom illuminated by a total intensity I with a detuning Δ (normalized by γ) is given by $\frac{I/I_{sat}}{1+\Delta^2+I/I_{sat}}\gamma$. The total number of atoms in the cloud N_{at} is thus estimated from the total number of "digital units" detected by the camera N_{det} by using the following relation:

$$N_{at} = \frac{1}{\eta_{coll}} \frac{g}{\eta_{CCD}} \frac{1}{T} \frac{1+\Delta^2+I/I_{sat}}{\gamma(I/I_{sat})} \frac{1}{t_{exp}} N_{det} \tag{5.1}$$

where g is a variable gain that the camera itself applies when counting its "digital units", and T is the optical transmission of the imaging path.

Collection efficiency η_{coll}	$\sim 10^{-3}$
Quantum efficiency η_{CCD} (780 nm)	0.94
Dark current at -70°C	<0.1e$^-$/pix/s
Array size	400x1340 pixels
Pixel size	20x20 μm
Magnifying ratio	0.5-2

Table 5.3: Imaging system's technical properties: summary.

When not limited by diffraction and aberrations in the imaging system, the determination of the number of atoms and effective size of the cloud is quite straightforward. In order to infer from that the atomic density in the cloud, a model for the 3D density distribution is necessary. It is usually close to Gaussian for low loadings, but for high number of atoms multiple scattering of photons in the cloud limits the density, which becomes uniform in most of the cloud [119]. This has to be taken into account when analyzing

carefully the images, which are projections along one direction of these density distributions. Experimentally, the transition between Gaussian profiles for low MOT loading to quadratic ones (resulting from the integration of a sphere of constant density along two dimensions) when the density saturates is visible, as shown in figure (5.6).

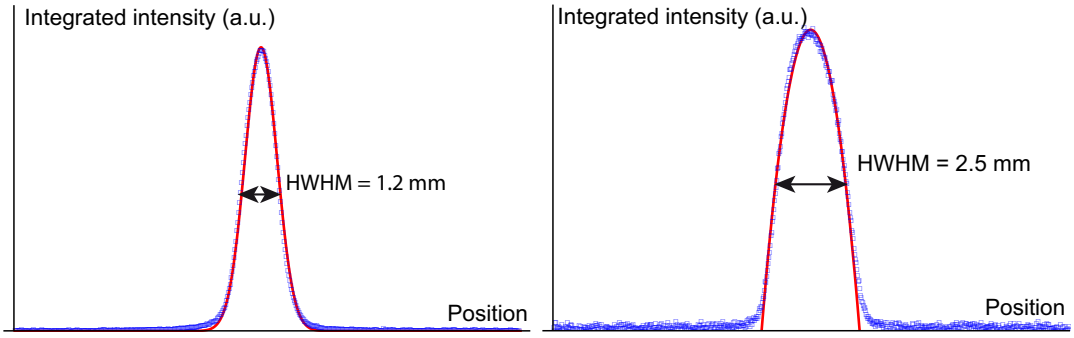

Figure 5.6: Integrated density profiles of a MOT in different regimes. Low loading and approximately Gaussian shape (left), and high loading and inverted parabola shape (right).

Temperature measurements can be carried out by time of flight methods, measuring the free expansion of the cloud due to its equilibrium velocity spread [120]. When released in free fall, after a time t the one-dimensional rms size R_c of the atomic density distribution (corresponding to $\mu(\vec{r}) \propto e^{-\vec{r}^2/2R_c^2}$ for Gaussian profiles) grows according to the following expression, where Δp_0^2 is the initial one-dimensional variance of the momentum distribution and m the atomic mass:

$$R_c(t) = \sqrt{R_c(t=0)^2 + \frac{\Delta p_0^2}{m^2} t^2} \tag{5.2}$$

Since for a cloud initially in thermal equilibrium $\frac{\Delta p_0^2}{m} = k_B T$, one can extract the temperature from the variation of its measured size with time (example on figure (5.7)).

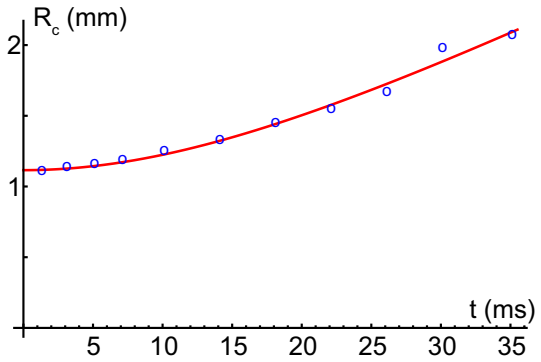

Figure 5.7: Time of flight measurement. Radius of the cloud as a function of the time of free evolution, fitted by $R_c(t) = \sqrt{R_c(t=0)^2 + \frac{k_B T}{m} t^2}$ with $T \approx 30 \mu K$.

5.5.2 Absorption

A complementary approach to measuring the density and size of the cloud is to probe its optical density, by sending a probe focused through its center and looking at the transmission as a function of the probe frequency when scanning through a resonance. The result in this case depends on the product of density and effective size. The expected variation of transmission with detuning is $\propto e^{-\alpha_0 l/(1+\Delta^2)}$, where $\alpha_0 l$ is the optical density on resonance, which can be extracted from the fit of the full variations of the transmission with Δ, as in figure (5.8).

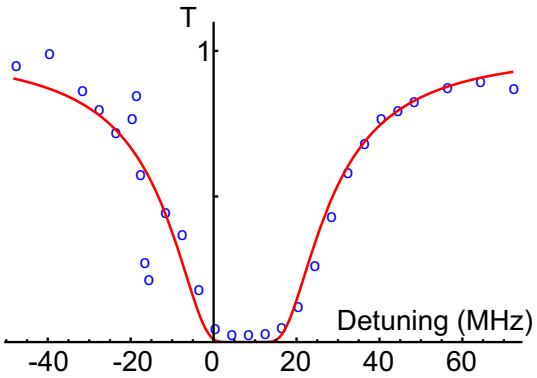

Figure 5.8: Absorption of a weak probe through the MOT in continuous regime, as a function of the detuning to atomic resonance. The sharp feature on the left of the resonance as well as the shift toward the blue of the line are due to the presence of the MOT beams interacting with the cloud at the same time (detuned by around -18 MHz) [121]. In this particular case the measurement yields $\alpha_0 l = 35$ for $l \approx 3$ mm, measured on the MOT transition.

All in all, the estimated value of the density at saturation in our MOT is of ~ 0.05 atoms/μm^3.

5.5.3 Cooperativity measurement

An additional useful way of characterizing the cloud is its cooperativity in the cavity mode, most directly related to the expected performances of the system when studying "single-atom" effects (without interactions). It depends on the transition on which it is measured, and ideally to make sense it should be characterized in a closed two-level system. For this reason, when it must be measured directly, the stretched transition of the $D2$ line at 780 nm is used, which is closed in the dipole approximation: $5S_{1/2}, F = 2, m_F = +2 \rightarrow 5P_{3/2}, F = 3, m_F = +3$. This is possible only when the cloud to be characterized has been optically pumped to the extreme Zeeman sublevel first.

In practice, the measurement can be realized by sending a weak off-resonant probe (in the linear regime) on the stretched transition, and looking at its transmission through the cavity as its length is scanned. In order to reach the linear regime and still get measurable transmission, we were lead to do the probing with injection through the upper, high-reflectivity mirror, and look at the outcoming light through the output coupling mirror. From equation (1.29), one sees that the atoms shift the transmission line's position by $\sim \frac{2C}{\Delta}$ (in units of κ), and attenuate it by a factor $1 + \frac{2C}{\Delta^2}$. This therefore allows very conveniently to estimate the cooperativity.

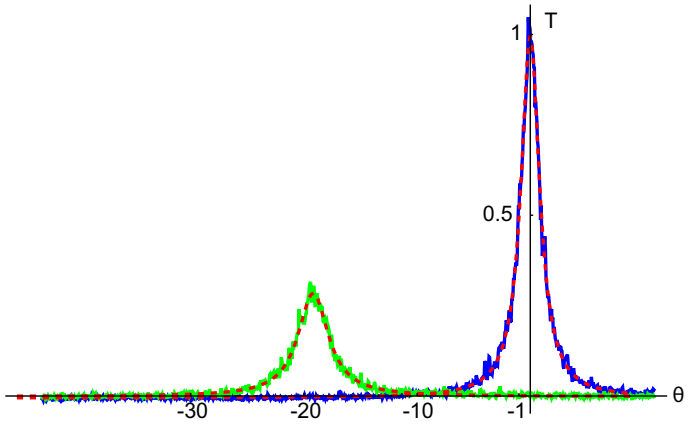

Figure 5.9: Example of transmission curves for cooperativity measurements. Cavity transmission versus θ, with (green) and without (blue) atoms, and Lorentzian fits (dashed red). Knowing the detuning $\Delta = -25$, the only fit parameter is the cooperativity, whose value here is $C = 239$.

The cooperativity is usually adjusted according to the needs by keeping all parameters of the main MOT constant, and changing only the current sent in the LVIS trapping coils. When loading more and more atoms in the trap, as the cooperativity scales like the optical depth, it first increases by a joint density-size effect, and then continues increasing when the MOT density saturates by a pure size effect. In standard conditions, the obtainable range is between 0 and ~ 1000 for the cooperativity on this stretched transition (limited by the current the LVIS coils can support, up to $\sim 6-7$ A). Its value on other transitions can then be deduced from the theoretical ratio of coupling coefficients.

Property	Low-loading regime	High-loading regime
Number of atoms	$\sim 5.10^7$	$\sim 10^9$
Effective radius R_c	~ 0.5 mm	≈ 1.1 mm
Density	~ 0.03 atoms/μm^3	≈ 0.05 atoms/μm^3
Cooperativity (stretched transition)	~ 100	~ 1000
Optical density (stretched transition)	~ 5	~ 50

Table 5.4: Typical atom clouds characteristics: summary.

Chapter 6

Optical cavity

Contents

The optical cavity in which the MOT is formed plays a key role in defining a proper spatial mode to the photons interacting with the cloud. Its characteristics also completely define their interaction strength, both by the volume of its mode and by its finesse. Simultaneously, some of its properties can be very constrained, for example by resonance conditions with some of the light beams whose frequencies are set by the atomic lines. Additionally, requirements like the centering of the MOT on the cavity mode put strong geometrical constraints on the system. Here we will describe how the actual design of the cavity gave us some possibilities to address these concerns.

6.1 Physical properties

The optical cavity is made of two 15mm-diameter mirrors held in a metallic structure hanging vertically from the top lid of the vacuum chamber between the two MOT coils (see figure (5.4)). The two mirrors have 780 nm coatings, high reflectivity for the top one ($R > 99.9\%$, $T \sim 0.5 - 1\ .10^{-5}$), 5% transmitting for the lower one. Photons inside the cavity mode therefore leave through the lower mirror with probability $> 98\%$, to later on exit the chamber through a viewport at its bottom. The resulting cavity finesse is ≈ 120, and the cavity resonances' Half Width at Half Maximum (HWHM) is $\kappa \approx 2\pi.10$ MHz.

The mirrors have a 60 mm curvature radius, and the fundamental transverse mode of the cavity has a waist at the center of 86 μm at 780 nm. The free spectral range is ≈ 2.3 GHz, and as it is not confocal the transverse modes are split by ≈ 110 MHz $\gg \kappa$ [84]. This conveniently allows to optimize the mode-matching of beams to the fundamental transverse mode in practice, and ensures the coupling to other modes can then be neglected.

The cavity was designed to be fully adjustable from outside even in vacuum, and initially setup to a length of ≈ 6.6 cm. Three long screws allow for movement of one part of the metallic structure with respect to the other, which moves the upper mirror only and enables a coarse tuning of the cavity length and alignment. The whole upper mirror

assembly is also resting on three piezos, that are used to realize the fine adjustments of the cavity length (see figure (6.1)).

Length	~6.6 cm
Finesse (IR)	120
FSR	2.3 GHz
HWHM (IR)	10 MHz
Mode waist (780 nm)	86 μm
Lower mirror output probability	> 98 %
Transverse mode splitting	~110 MHz

Table 6.1: Cavity's physical properties: summary.

The entire cavity structure is connected to the vacuum chamber by a flexible metal bellow, and rests on the top lid supported by three thick adjustable screws. These settings allow to move the cavity in its entirety, in order to center its mode on the precise spot where the atom cloud is formed. The reason for the cavity length to be ≈ 6.6 cm is to have two resonant frequencies separated by the ground state hyperfine splitting of rubidium ($\approx$ 6.8 GHz), which is crucial for some of our experiments. Simultaneously, as these two frequencies resonate in the cavity with different standing wave patterns, the atomic cloud must be placed at a given position (1/3 of the cavity length) along the cavity axis so that it couples efficiently to both (both modes are in phase at this position).

The structure of the cavity assembly is sketched on figure (6.1).

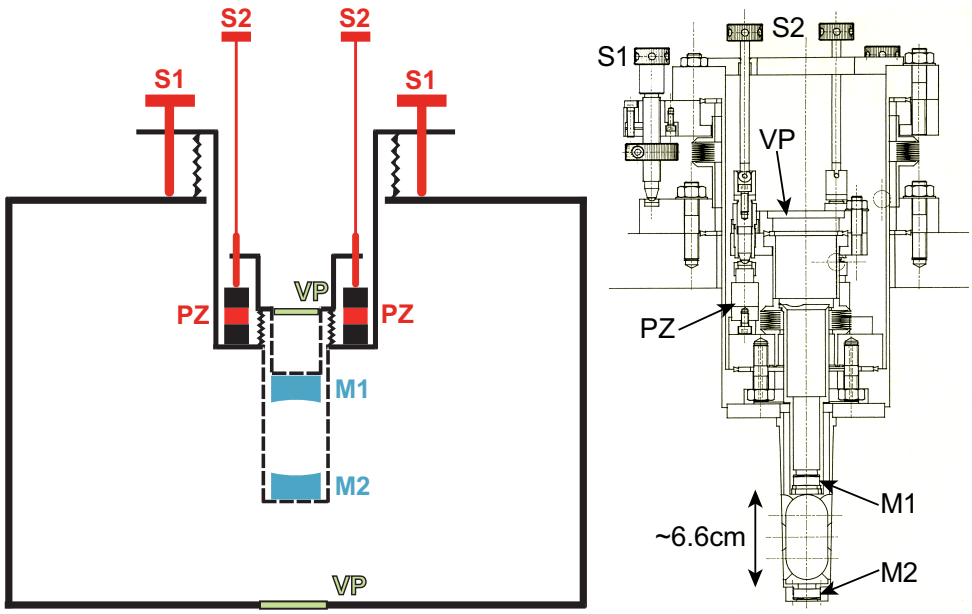

Figure 6.1: Left: Simplified structure of the cavity in the chamber and various degrees of freedom. Solid lines are vacuum-proof surfaces, dashed lines are metal structures with apertures or not hermetic. **Right: Technical drawing of the cavity structure.** S1 are the screws setting the global position of the entire cavity. S2 are cavity length tuning screws. PZ are the piezos (in air) moving the upper mirror. VP are viewports for light input/output. M1 and M2 are the two cavity mirrors.

6.2 Length locking

Due to the sensitivity of the cavity's architecture to acoustic noise, as well as thermal effects, its length spontaneously experiences particularly large vibrations and long-term drifts. In order to lock the cavity length during any experiment, a dedicated light beam is continuously sent to the cavity and its reflection on it is monitored. To be of very little influence on the atoms, around 100 μW of light from the 810 nm TiSa laser are used. The cavity is locked on a resonance with this beam using the Pound-Drever-Hall method [122]: the beam is phase-modulated at 100 MHz in an Electro-Optic Modulator before being sent to the cavity, so that its spectrum contains two sidebands in addition to the carrier frequency. When the carrier resonates inside the cavity, the sidebands do not, and their relative phases get shifted, which is the basic mechanism at the origin of the error signal that can be obtained when demodulating the signal obtained from the reflection of that beam on the cavity with a local reference at 100 MHz.

When the cavity must be locked on resonance with a particular beam, the frequency of the 810 nm beam is adjusted (its precise frequency does not matter for the atoms) so as to get a coinciding cavity resonance of the two. The 810 locking beam's frequency can be adjusted by setting the frequency of its dedicated AOM, or by changing the locking point of the laser. The difference of spacing between two cavity resonances in length for the 810 beam and for the 780 light for example is large enough that by tuning the cavity length in a reasonable range it is always possible to find a joint resonance.

Despite the time and efforts spent on trying to optimize the quality of the cavity length stabilization, the structure's various very sharp mechanical resonances made it quite difficult to have a really useful backaction above 50 Hz frequency. The cavity length is therefore set on average to a desired value, but randomly moving around it within a typical frequency range of ± 2 MHz.

Lock beam wavelength	810 nm
Lock beam power	~ 100 μW
PDH modulation frequency	100 MHz
Cavity frequency stability	$\pm$ 2 MHz

Table 6.2: Cavity length locking: summary.

As will be described in more details later, for some experiments (and for cooperativity measurements for example), the locking stability issue was circumvented by doing the measurements while the cavity length was scanned, and keeping track in the meantime of the 810 nm error signal to serve as a reference scale.

Part III

Single-mode source of single photons based on a cavity-enhanced cold atom quantum memory

Introduction

In this part, we describe the characterization of photons emitted from the cold atomic cloud in the low-finesse cavity. The experiment is based on a now well-known and already thoroughly studied protocol, that was part of a series of innovative proposals for building optical quantum communication systems with atomic ensembles and linear optics by Duan, Lukin, Cirac and Zoller in 2001 [123].

On one hand the protocol, consisting in the sequential storage and readout of an excitation in the cloud, is known to be usable for coherent storage of excitations [31, 32] and high-quality single-photon production [19–21, 124, 125]. This experiment can therefore be considered as related to the photonic QIP problematics of controlled production and storage of single qubits. This kind of sources were previously mostly characterized by photon-counting techniques, giving access to purely intensity-dependent measurements and global characteristics of the photon-number distribution, like the $g^{(2)}$ or other correlation functions. With homodyne tomography, a deeper and complementary characterization of this source can be given, confirming that it can produce photons with high probability, good indistinguishability, very low level of parasitic multi-excitation components, and that the mechanisms limiting the storage time and production efficiency are understood and controlled.

On the other hand, in the framework of this thesis, the implementation of this protocol is also a test bench for dealing with a slightly different problematic. Finding configurations in which photon-photon interactions are observed was already an outstanding challenge until recently. In atomic systems, one can now use properties like the Rydberg-Rydberg interactions to mediate nonlinear photonic state evolutions. It is then also important, in order to prove their practical interest and applicability, to answer the following general question: assuming one manages to store and process the quantum state of some excitations in an atomic cloud somehow, is it possible to then re-extract them with high efficiency in the form of photons that have well enough controlled properties to be reusable in a subsequent complex QIP process ? In this respect, photon-counting tools gave some partial answers, but in a way that is rather restricted to the particular DLCZ protocol [20, 124, 126]. As is shown in the Results section of this part, homodyne tomography allows us to probe directly the right properties (quantum state, spatio-temporal mode, collection efficiency) to answer this question in general and to show, temporarily putting aside the Rydberg component of the system, that our setup in principle has suitable coherent excitation conversion abilities.

In comparable systems, homodyne tomography was applied to the generated photons in the group of A. Lvovsky in Calgary [127], where the authors were using hot vapor in free space and a different excitation scheme, as will be discussed (continuous excitation with no Zeeman pumping). A similar scheme was also investigated in the group of J. Laurat in Paris. Their results also confirm the interest and validity of ours.

A short version of the description of this experiment is available in the publication [128]. It is also directly related to the previous theoretical publication [129].

Chapter 7

Presentation of the DLCZ protocol

Contents

As previously suggested, a multilevel atomic cloud offers very rich possibilities of interaction processes with light. In Λ three-level atoms, even without any control beam, the probe light can randomly eject atoms from the two probe-coupled levels into the third one, creating an isolated long-lived excitation.

We will describe here the basic aspects of the so-called DLCZ protocol, that makes use of these processes not only to store the quantum state of light in cold atoms as polaritons and retrieve it, but also to effectively process it so as to build a semi-deterministic [1] single-photon source [123].

7.1 Principle and properties of the scheme

7.1.1 Two-step protocol and measurement-induced nonlinearities

The protocol, sketched on figure (7.1), generates photons in a manner close to the heralded parametric down-conversion sources [130], with a controllable delay between the heralding and the signal photon emission.

It consists, in an optically pumped medium, of a first (Write) step of very weak off-resonant driving that can lead to a Raman transition of an atom from one ground state $|g\rangle$ to the other $|f\rangle$. The detection of the Raman-scattered photon (Write photon) heralds the creation of an atomic excitation, which happens with intentionally low probability, in order to avoid multiple excitation processes. A strong Read field can afterward be applied

1. Here semi means non-deterministic loading but fully deterministic readout.

on the reverse transition to re-transfer the unique atomic excitation, therefore emitting on-demand a second single Raman photon (Read photon).

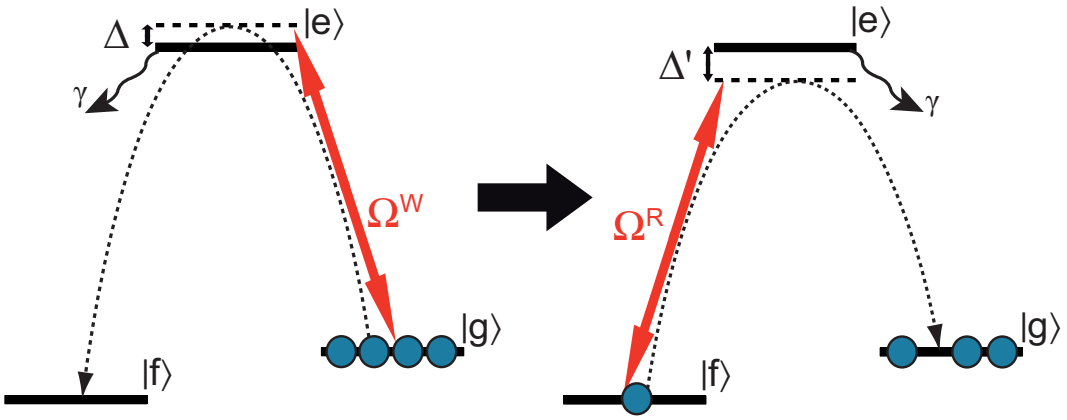

Figure 7.1: Schematic of the DLCZ protocol. Left: Write step. **Right:** Read step.

An interesting feature of this process is the effective nonlinearity induced by the measurement of the first Raman photon, which projects the atomic state on the excited subspace. This system therefore acts as a highly nonlinear material at the few-photons level, only with a probabilistic action: a successful Write step simultaneously processes and stores the quantum state [18, 39, 123]. Note that this step of the protocol could in principle be made deterministic using the Rydberg blockade mechanism (see for example [131]). On another line of ideas, if the storage time in this system can be of the same order as the typical time between two heralding events, the generation of a single photon is then close to deterministic.

The main challenge to be addressed here however is more the high-efficiency readout of the stored excitation back into a usable propagating photon, with well controlled characteristics. This can be realized under carefully controlled conditions as we will show.

7.1.2 How to achieve efficient and controlled readout of a stored excitation

In principle the protocol can be realized in a number of configurations: with any number of atoms, in free space [125], in an optical lattice [32] or in a cavity [21], with any temporal shape of the driving fields, even continuous [127]. Our system's features aim at optimizing its implementation in the cavity, using well-defined time-separated pulses of the Write and Read fields.

The high-efficiency conversion of an atomic excitation into a photon in a fixed mode requires strong coupling between the atoms and the field in this specific mode. Although a cavity helps in this sense, using a too high-finesse or too confined one together with very few atoms (down to a single one) makes it very difficult in practice to control well enough all the properties of the system to achieve large extraction and collection efficiency out of the cavity [132].

Using a low-finesse, relatively large cavity, the small single atom-cavity field coupling can be compensated for by using many atoms participating collectively in the process [123, 133]. As the detection of a Write photon in the cavity mode does not allow to distinguish which atom it was emitted from, the excitation created is a so-called ground-state polariton involving all atoms [53]. As will be discussed in details later, this delocalized

excitation has a phase coherence over the whole cloud that leads to an increased effective coupling to the cavity field during readout. The conversion into a cavity mode photon can then still be efficient, and the extraction out of the cavity is still easy thanks to the relatively large mirror transmission.

As will be extensively discussed thereafter, the interesting and distinctive properties of the Write and Read steps can be summarized and compared as in table (7.1).

	Write	Read
Type of process	Single-atom process	Collective process
Driving	Weak	Strong
Cavity mode emission	Very low probability	High probability
Initial atomic state	All in ground state	Delocalized excitation
Final atomic state	Projection on delocalized excitations	All in ground state

Table 7.1: Comparison of the characteristics of the two steps of the protocol.

Besides retrieval and collection efficiency matters, our implementation features advantages in the control of the emitted photon's mode in particular. The cavity provides the definition of the spatial shape and frequency of its eigenmodes (which have to be resonant with the Raman photons of course). Additionally, as the photon is emitted in response to the coherent driving of the atomic excitation by the Read field, its temporal shape can be partially controlled by shaping the Read pulse.

7.2 Excitation conversion efficiency with a single atom

We first consider the case of a single atom in the cavity submitted to the protocol, to point out the important quantities at stake and the general behaviour of the system.

7.2.1 Competition between two processes

For a single three-level atom in the cavity excited by a Raman field, the Write and Read steps are equivalent. The problem of the extraction efficiency in the cavity is then a matter of competition between processes with scales given by three quantities: the atom-cavity coupling g, the atomic decay rate γ and the cavity decay rate κ.

If the coupling to the cavity mode is not extremely high, the excited atom will still see a continuum of other field modes in which it can incoherently decay at a rate γ, corresponding to a loss of the excitation. For too large γ the photon will therefore leave the system in a random mode before being able to "feel" the coupling to the cavity. On the other hand, if κ is too large, the cavity does not really play the role of selecting a preferential mode in which excitations can be coherently exchanged back and forth with the atom. The coherent buildup of the cavity field extracting energy from the atom will be spoilt by its too fast leakage toward the outside.

Therefore we expect that the behaviour of the system should be ruled by the previously defined cooperativity C (which is for a single atom $g^2/2\kappa\gamma$).

7.2.2 Lowest-order emission rates and efficiency

To estimate the probability that a scattered photon would be inside the cavity mode, the system that must be described is made of the atom and the cavity field, resonant on

the Raman transition (see figure (7.2)). It has three interesting quantum states and two different possible decay processes: starting from $|g,0\rangle$, it reaches after excitation of the atom $|e,0\rangle$, and can be coupled via excitation transfer with the cavity mode to $|f,1\rangle$, with coupling strength g. State $|e,0\rangle$ decays at rate γ, while $|f,1\rangle$ is subject to cavity losses at rate κ.

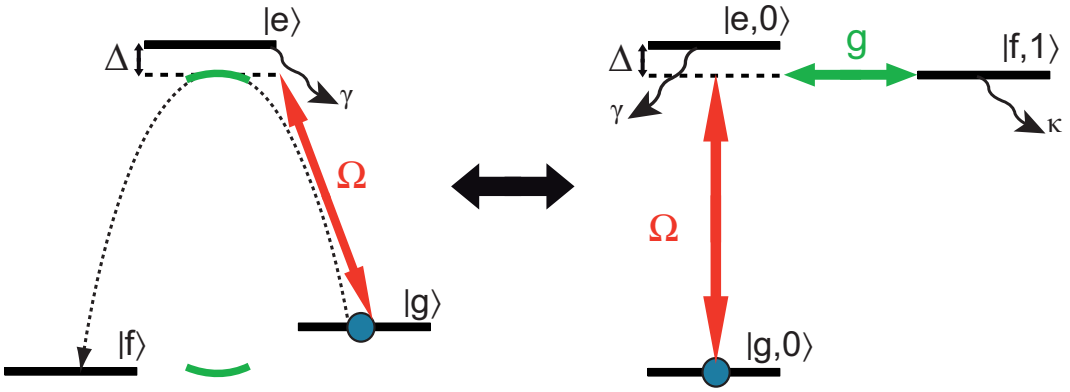

Figure 7.2: {Atom+cavity field} states considered in the treatment of the single three-level atom case. On the left picture, the cavity mode frequency is figured in green, resonant with the Raman photon.

In presence of a driving field with Rabi frequency Ω and detuning Δ on the $|g\rangle \rightarrow |e\rangle$ transition, one can calculate the steady-state populations of states $|e,0\rangle$ and $|f,1\rangle$, considering that after a decay process the system gets reinitialized to its original state (decays γ and κ bring it back to $|g,0\rangle$). In the lowest order in excitation power Ω^2, they are:

$$P_{e0} \approx \frac{\gamma^2\Omega^2\kappa^2/4}{(g^2+\kappa\gamma)^2+(\kappa\gamma)^2\Delta^2} = \frac{\Omega^2}{4}\frac{1}{(1+\frac{g^2}{\kappa\gamma})^2+\Delta^2} \tag{7.1}$$

$$P_{f1} \approx \frac{\gamma^2\Omega^2 g^2/4}{(g^2+\kappa\gamma)^2+(\kappa\gamma)^2\Delta^2} = \frac{\gamma\Omega^2}{4\kappa}\frac{\frac{g^2}{\kappa\gamma}}{(1+\frac{g^2}{\kappa\gamma})^2+\Delta^2} \tag{7.2}$$

This treatment gives the rates at which the first excitation coming out of this system is emitted from the "useful" state $|f,1\rangle$ or as pure losses from $|e,0\rangle$:

$$P_{e0}\ 2\gamma \approx \frac{\Omega^2}{2}\frac{1}{(1+\frac{g^2}{\kappa\gamma})^2+\Delta^2}\gamma \tag{7.3}$$

$$P_{f1}\ 2\kappa \approx \frac{\Omega^2}{2}\frac{\frac{g^2}{\kappa\gamma}}{(1+\frac{g^2}{\kappa\gamma})^2+\Delta^2}\gamma \tag{7.4}$$

One therefore has: $P_{f1}\ 2\kappa = \frac{g^2}{\kappa\gamma}\ P_{e0}\ 2\gamma$. The probability that the first scattered photon is in the cavity mode is purely governed by the cooperativity, and in particular is independent of the excitation detuning:

$$\frac{P_{f1}\ 2\kappa}{P_{e0}\ 2\gamma + P_{f1}\ 2\kappa} \approx \frac{\frac{g^2}{\kappa\gamma}}{1+\frac{g^2}{\kappa\gamma}} \tag{7.5}$$

It is important to note that for the experiments presented here, as the single-atom coupling coefficient g is small compared to κ or γ ($g/2\pi \sim 0.2$ MHz on the stretched 780 nm transition, while $\gamma/2\pi = 3$ MHz and $\kappa/2\pi = 10$ MHz), this is always very small, so that when exciting one atom in our cavity, the collection of a photon in the mode is very unlikely. Before this happens, many other photons will first have been scattered in free space. In particular, we are not at all in the "Purcell" regime where the cavity has the effect of forcing spontaneous emission to happen faster than the natural rate and only through the cavity mode [134].

In other words, the presence of the cavity does enhance the emission probability of one single atom in its mode as compared to if it was not here, but it is still much smaller than the total emission in all other modes.

The single-atom picture is already very instructive because, as will be discussed thereafter, the N-atom Write and Read steps can in some cases be modeled as in an equivalent single-atom scheme, with scaled coupling parameters that depend on the number of atoms. This last point is what makes all the richness of this system.

Chapter 8

Cooperative effects and expected readout efficiency

Contents

It is observed that in an atomic cloud, although during the Write step all atoms act independently and the cavity emission probability simply scales with their total number N, the readout can give rise to coherent enhancement, with very large cavity retrieval probabilities achievable (N^2-scaling phase-matched behaviour). The physical reason for the difference between the two steps will be discussed here.

This chapter will also detail how cooperative effects, taking place during a delocalized excitation's readout, can be theoretically taken into account in a realistic imperfect system. The first step is to find the most practical formulation of the origin of these effects, to be able to manipulate a model where they play a role. After using it to express the achievable retrieval efficiency in the "perfect system" case, the effect of the main practical defects on the efficiency will be estimated.

As the conditional probability of retrieving a photon in the cavity mode during a Read step is a crucial figure of merit for this source, this physical understanding of its cooperative enhancement and of the various limiting processes is very important.

Some of the description detailed here was initially inspired by the ideas presented in J. Simon's PhD thesis [135].

8.1 Write step (in the uniform-coupling case)

The single-atom case is an interesting starting point because the Write step of the DLCZ protocol can be described as a "single-atom process", were all atoms act independently.

To show this more explicitly, let us consider for simplicity N atoms equally coupled both to the Write field with Rabi frequency Ω^W and to the cavity mode with coupling g^W, corresponding to the following coupling Hamiltonian ($\hat{a}^\dagger_W$ is the Write cavity mode creation operator):

$$\hat{H}_W = \sum_{k=1}^{N} \frac{\hbar\gamma\Omega^W}{2} |e\rangle_k \langle g|_k + \sum_{k=1}^{N} \hbar g^W |f\rangle_k \langle e|_k \ \hat{a}^\dagger_W + h.c. \tag{8.1}$$

Starting from state $|G\rangle = \left[\bigotimes_{k=1}^{N} |g\rangle_k\right] |0\rangle = |\Psi_0\rangle |0\rangle$, and restricting the evolution subspace to a single atomic excitation, the states reached by the system are found by applying $\hat{H}_W$ to $|G\rangle$:

$$|E\rangle = \left[\frac{1}{\sqrt{N}} \sum_{k=1}^{N} \left(\bigotimes_{j\neq k} |g\rangle_j\right) |e_k\rangle\right] |0\rangle = |\Psi_{exc}\rangle |0\rangle \tag{8.2}$$

$$|F\rangle = \left[\frac{1}{\sqrt{N}} \sum_{k=1}^{N} \left(\bigotimes_{j\neq k} |g\rangle_j\right) |f_k\rangle\right] |1\rangle = |\Psi_{int}\rangle |1\rangle \tag{8.3}$$

These states are the simplest examples of perfectly symmetric delocalized atomic excitations, involving coherent superpositions of all possible states where one atom among all has left its initial state.

One can show easily that $\langle F| \hat{H}_W |E\rangle = g^W$. In this sense the cavity photon emission in this system will be the same as for each individual atom, and there is no collective effect that would particularly favour the emission in the cavity mode.

The only influence of N here is in the fact that, to keep the maximum number of excitations in the cloud around 1, it is $\sqrt{N}\hbar\gamma\Omega^W = 2 \langle E| \hat{H}_W |G\rangle$ that should remain small enough [1] instead of just $\hbar\gamma\Omega^W$, which is also obvious from the consideration of N independent atoms independently driven by Ω^W.

The full system during the Write step can therefore be treated, within these approximations, in the same way as the single-atom case with the excitation structure shown in figure (8.1).

However at the end of a successful Write step, the detection of the Write photon leaves the atomic system into the following intermediate collective state (polariton), that will lead to coherent enhancement of the efficiency during the readout:

1. From equation (7.3), this collective Rabi frequency must remain small as compared to $\hbar\gamma\sqrt{1+\Delta^2}$.

$$|\Psi_{int}\rangle = \frac{1}{\sqrt{N}} \sum_{k=1}^{N} \left(\bigotimes_{j \neq k} |g\rangle_j \right) |f_k\rangle \tag{8.4}$$

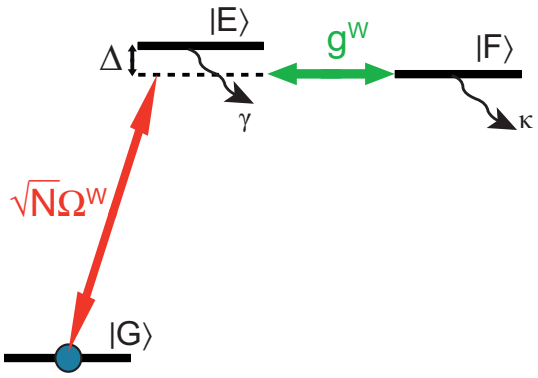

Figure 8.1: {N atoms+cavity field} states considered in the treatment of the Write step.

8.2 Description of cooperative effects during the Read step

As was just shown, the Write step is simply the juxtaposition of many single-atom processes independent from each other, leading to incoherent summation of the emission probabilities of all N atoms. However, because of the nature of this preliminary preparation of the system and heralded projective measurement, the Read step has a qualitatively different behaviour. We present thereafter different ways of understanding the fact that the conditional excitation readout can be of very high retrieval efficiency in the cavity mode. For reference, characteristics of these different viewpoints are summarized in table (8.1).

Viewpoint	Steps considered	Mechanism
Atom-by-atom	Write+Read	Interferences between N possible paths where one atom is excited and brought back to its ground state
N-atom states	Read only	Excitation by the Read beam of a precise phased-matched N-atom state that has a collectively enhanced coupling to the cavity field

Table 8.1: Different interpretations of the cooperative readout.

8.2.1 Coherent 4-photon closed loop processes

One possible interpretation is in terms of possible excitation paths of each atom in the sample, as proposed for example in [136] (in the free-space case).

Considered in its entirety, the DLCZ protocol involves 4-photons processes: Write excitation - emission of Write photon - Read excitation - emission of Read photon. Among all processes that can take place in these four steps, there are “loops” where only one given

atom among all goes through a closed path to come back to its original state. All these loops (for all possible choices of the excited atom) start and end in exactly the same quantum state for the whole system (see figure (8.2)).

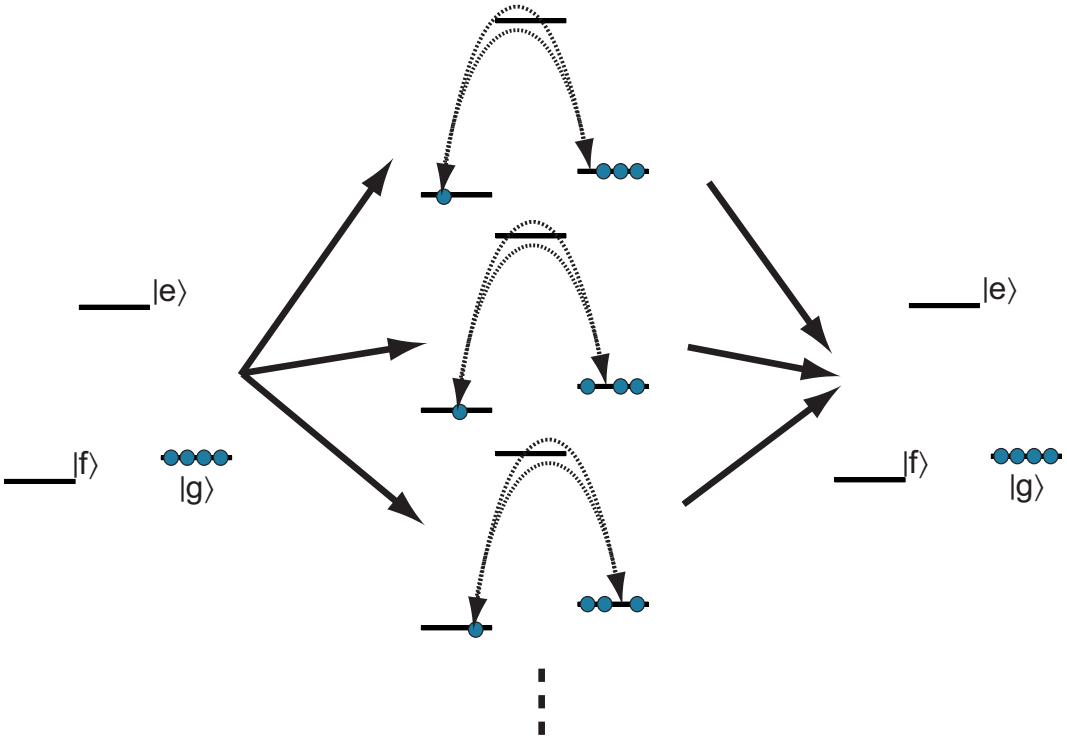

Figure 8.2: Indistinguishable 4-photons loops interfering during the complete protocol.

When calculating the probability of observing a given pair of Raman-scattered photons during the protocol, the contributions of these processes are therefore summed in amplitude. If they all interfere in phase, the result can be greatly enhanced and dominate over all other processes. As will be discussed in more details later, this is precisely what happens when phase-matching conditions are fulfilled (the combination of all optical excitations phases is the same for all atoms). Put another way, it means that after having observed a Write photon in a given mode (cavity one for example), the Read photon's emission will be preferentially oriented by these "loops" processes into the mode that respects the phase-matching conditions (which is also the cavity one in this case).

Unfortunately, thinking in terms of 4-photons loops for individual atoms leads to a quite heavy ab initio theoretical treatment of the problem which is not very straightforwardly adapted to our specific case. Thus, in order to model the system in realistic conditions, a different point of view is adopted.

8.2.2 N-atom states description

For simplicity, considering separately the Write and Read steps in the theoretical treatment of the protocol would be preferable. This may seem incompatible with the previous description of the Read cooperative effects as due to those 4-photons loops. Fortunately, this preponderance of certain transitions that are part of indistinguishable closed loops can take a different form if one considers the N-atom states of the system.

After detection of the Write photon, the atomic cloud is projected onto a given intermediate state ($|\Psi_{int}\rangle$ in the uniform-coupling case). During the Read step, the Hamiltonian is in the general case (with possible non-uniform couplings, and Read cavity mode creation operator $\hat{a}_R^\dagger$):

$$\hat{H}_R = \sum_{k=1}^{N} \frac{\hbar\gamma\Omega_k^R}{2} |e\rangle_k \langle f|_k + \sum_{k=1}^{N} \hbar g_k^R |g\rangle_k \langle e|_k \ \hat{a}_R^\dagger + h.c. \tag{8.5}$$

The Read pulse coupling Hamiltonian (first part of $\hat{H}_R$) is first applied to the intermediate state. Taking into account the couplings' optical phase variations only for now, the resulting atomic state is of the form: $\frac{1}{\sqrt{N}} \sum_{k=1}^{N} e^{i\phi_k} \left(\bigotimes_{j\neq k} |g\rangle_j\right) |e_k\rangle$.

Each of the components of this state is individually coupled by the Read photon emission Hamiltonian (second part of $\hat{H}_R$) to the initial atomic state $|\Psi_0\rangle$ (same for all components): $\langle 1| \langle \Psi_0| \hat{H}_R \left(\bigotimes_{j\neq k} |g\rangle_j\right) |e_k\rangle |0\rangle = \hbar g_k^R$. Now the indistinguishability comes into play because the coupling of the total coherent superposition state to $|\Psi_0\rangle$ is:

$$\langle 1| \langle \Psi_0| \hat{H}_R \frac{1}{\sqrt{N}} \sum_{k=1}^{N} e^{i\phi_k} \left(\bigotimes_{j\neq k} |g\rangle_j\right) |e_k\rangle |0\rangle = \frac{1}{\sqrt{N}} \sum_{k=1}^{N} e^{i\phi_k} \hbar g_k^R \tag{8.6}$$

If the g_k^R's are such that $arg(g_k^R) = -\phi_k$ (phase-matching condition), this is of order $\sqrt{N}$ larger than a typical single-atom coupling. Thus in this description the readout is dominated by one specific very large coupling to the initial state of the system, which is similar to the previous observation about single-atom loops.

8.2.3 Maximally coupled state and condition for collective enhancement of the efficiency

This formulation of the cooperative coupling's origin allows us to take it into account in a quite general and efficient form, even in the presence of imperfections in the system and the process.

Looking back on the previous considerations, the conclusion, independent from the presence of imperfections, is that high efficiency during readout can be achieved only when making use of the very large Read photon coupling associated with a system coming back to its initial N-atom state. Considering the last step of the readout backwards, there is only one well-defined N-atom quantum state containing one excitation that can be coupled at all to the initial state $|\Psi_0\rangle$. This optimal atomic state is obtained by acting on $|\Psi_0\rangle$ with the Read photon emission Hamiltonian:

$$|\Psi_{exc,opt}\rangle = \left[\sqrt{\sum_{k=1}^{N} |g_k^R|^2}\right]^{-1} \sum_{k=1}^{N} (g_k^R)^* \left(\bigotimes_{j\neq k} |g\rangle_j\right) |e_k\rangle \tag{8.7}$$

Note that it of course satisfies perfectly the previous condition for phase-matching ($arg(g_k^R) = -\phi_k$). The fact that this is the only state coupled to $|\Psi_0\rangle$ means that in order to efficiently readout the excitation in the cavity mode, it must be prepared and maintained in a state of precise phase and amplitude coherence over all atoms. This state's structure can easily be spoilt by many practical imperfections as we will see.

If the system ends up somehow in a state orthogonal to $|\Psi_{exc,opt}\rangle$ it can be considered as lost in terms of Read retrieval efficiency. On the other hand, if because of some defects

$|\Psi_{exc,opt}\rangle$ is also coupled to some other state than $|\Psi_0\rangle$, it will necessarily be with a non-cooperative coupling. Thus, for large N, we can neglect in the lowest order all other couplings.

Taking this reasoning one step further, the only part of the state created after the Write step that has any chance to participate in the retrieval efficiency is the one that, once excited by the Read classical field, falls exactly onto $|\Psi_{exc,opt}\rangle$. This state can be written, in lowest-order approximation, as:

$$|\Psi_{int,opt}\rangle = \left[\sqrt{\sum_{k=1}^{N}\left|\frac{g_k^R}{\Omega_k^R}\right|^2}\right]^{-1} \sum_{k=1}^{N}\frac{(g_k^R)^*}{\Omega_k^R}\left(\bigotimes_{j\neq k}|g\rangle_j\right)|f_k\rangle \tag{8.8}$$

The readout process starting from state $|\Psi_{int,opt}\rangle$ can be considered in the subspace of the {atoms + Read photon field} system spanned by $\{|\Psi_{int,opt}\rangle|0\rangle = |F_{opt}\rangle, |\Psi_{exc,opt}\rangle|0\rangle = |E_{opt}\rangle, |\Psi_0\rangle|1\rangle = |G'\rangle\}$. They are coupled to each other by $\hat{H}_R$ with coupling strengths:

$$\langle E_{opt}|\hat{H}_R|F_{opt}\rangle = \frac{\hbar\gamma}{2}\sqrt{\frac{\sum_{k=1}^{N}|g_k^R|^2}{\sum_{k=1}^{N}|g_k^R/\Omega_k^R|^2}} = \frac{\hbar\gamma\Omega_{eff}^R}{2} \tag{8.9}$$

$$\langle G'|\hat{H}_R|E_{opt}\rangle = \hbar\sqrt{\sum_{k=1}^{N}|g_k^R|^2} = \hbar\sqrt{N}g_{eff}^R \tag{8.10}$$

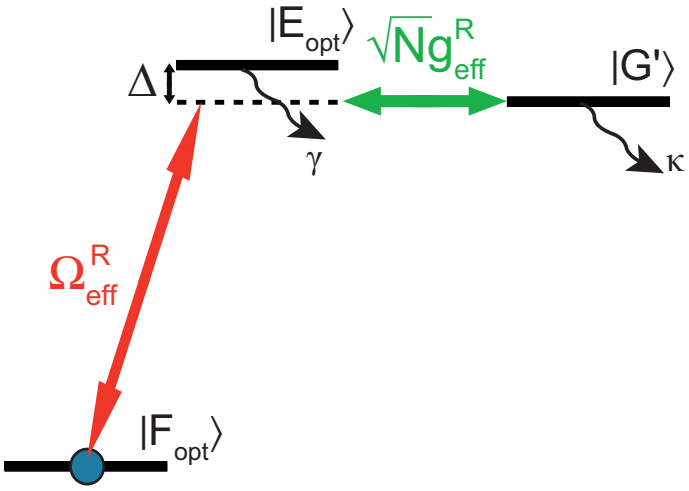

Figure 8.3: {N atoms+cavity field} states considered in the treatment of the Read step from the optimally coupled state.

Therefore, singling out these precise states and restricting the description to their subspace, the Read can also be described as in the single-atom case, except that the coupling of the cavity emission process can be very large due to the cooperative enhancement, as shown in figure (8.3). The quantity ruling the retrieval efficiency here will then be the equivalent of $\frac{g^2}{\kappa\gamma}$ in the single-atom case: $\frac{(\sqrt{N}g_{eff}^R)^2}{\kappa\gamma} = \frac{\sum_{k=1}^{N}|g_k^R|^2}{\kappa\gamma} = 2C$ where C is precisely the cooperativity defined earlier in a different context when looking at susceptibilities.

8.3 Efficiency limits without defects

Similarly to what was done before in the single-atom case, let us define rates at which a system in state $|F_{opt}\rangle$ emits through the cavity mode Γ_{cav} or in free space Γ_{fs}. These rates depend on $\Omega^R_{eff}(t)^2$ during the readout, linearly in the lowest order.

The total cavity retrieval efficiency for a system in state $|\Psi(t)\rangle$ will thus be written as:

$$P = \int |\langle \Psi(t)|F_{opt}\rangle|^2 \, \Gamma_{cav}(t)dt \tag{8.11}$$

The meaning of this expression is that between times t and t+dt, the probability for emitting a photon in the cavity is the probability for the system to be in state $|F_{opt}\rangle$ times the probability that this state emits in the cavity $\Gamma_{cav}(t)dt$.

Now $|\langle \Psi(t)|F_{opt}\rangle|^2$ can be split in two contributions: P^0_{opt}, the probability to occupy state $|F_{opt}\rangle$ at the end of the Write step, before the Read has begun; and $P_{opt}(t)$, the probability for the system to still be in $|F_{opt}\rangle$ at time t knowing that it was at time 0 (before the Read starts). Hence:

$$P = P^0_{opt} \int_{pulse} P_{opt}(t)\Gamma_{cav}(t)dt \tag{8.12}$$

$P_{opt}(t)$ itself will necessarily decrease with time as the excitation is extracted from the atoms. It can be decomposed into the probability for the excitation to have stayed into the cloud until time t, and the probability that the atomic state is still $|F_{opt}\rangle$ knowing that the excitation stayed in the cloud, $P^{nojump}_{opt}(t)$.

$$P = P^0_{opt} \int_{pulse} P^{nojump}_{opt}(t) e^{-\int^t (\Gamma_{cav}(t')+\Gamma_{fs}(t'))dt'} \Gamma_{cav}(t)dt \tag{8.13}$$

In the case of a perfectly prepared system that does not suffer from any deformations during readout, one would have $P^0_{opt} = P^{nojump}_{opt}(t) = 1$. Any defect in the preparation or loss of coherence of the collective excitation during the process will have the effect of decreasing one of these two values.

8.3.1 First approach of efficiency limits

To first consider the simplest case, let us take $P^0_{opt} = P^{nojump}_{opt}(t) = 1$ and assume $\Omega^R_{eff}(t)$ constant, so that $\Gamma_{cav}(t)$ and $\Gamma_{fs}(t)$ are also constant:

$$P = \int \Gamma_{cav} e^{-(\Gamma_{cav}+\Gamma_{fs})t} dt = \frac{\Gamma_{cav}}{\Gamma_{cav}+\Gamma_{fs}} \tag{8.14}$$

From the parallel with the single-atom result established above, we get:

$$\Gamma_{cav} = \frac{(\Omega^R_{eff})^2}{2} \frac{2C}{(1+2C)^2+\Delta^2}\gamma \tag{8.15}$$

$$\Gamma_{fs} = \frac{(\Omega^R_{eff})^2}{2} \frac{1}{(1+2C)^2+\Delta^2}\gamma = \frac{\Gamma_{cav}}{2C} \tag{8.16}$$

And the efficiency is:

$$P = \frac{2C}{1+2C} \tag{8.17}$$

which is exactly symmetric to the single-atom case but can be made much closer to 1 by having many atoms. This, as will be discussed, is the upper efficiency bound for the retrieval, as also shown in [129, 137].

8.3.2 Time-dependent photon extraction stimulated by the Read pulse

The extraction efficiency directly depends on the Read power sent on the atoms to convert the excitation, which is not visible in the previous simple result. Taking into account the time-dependence of $\Omega^R_{eff}(t)$, and keeping relation $\Gamma_{fs}(t) = \Gamma_{cav}(t)/2C$ at all times we can write:

$$P = \int \Gamma_{cav}(t) e^{-\int^t (\Gamma_{cav}(t') + \Gamma_{fs}(t'))dt'} dt = \int \Gamma_{cav}(t) e^{-\xi \int^t \Gamma_{cav}(t')dt'} dt \tag{8.18}$$

where $\xi = \frac{1+2C}{2C}$. This integrates to:

$$P = \frac{2C}{1+2C}\left(1 - e^{-\xi \int^\infty \Gamma_{cav}(t')dt'}\right) \tag{8.19}$$

This expression, with equation (8.15), gives the explicit dependence of the efficiency for a "perfect" system, in the lowest-order approximation in Ω^2 for Γ_{cav} and for long pulses (quasi-steady state). It depends only on C, Δ and Ω^R_{eff}, and tends to the upper limit $\frac{2C}{1+2C}$ for large enough integrated Read power.

We showed in [129] that using a different approach, writing Langevin equations for the different excitation operators in the system, the same conclusions are reached (both the Rabi frequency and the cooperativity definitions differ by a factor 2 in this article compared to the present document). Using the same kind of approximations (long pulses, large collective coupling), an approximate expression for the intracavity field amplitude $\mathcal{E}(t)$ is also found in this article (equation 30).

The expression of the extraction efficiency obtained from $2\kappa \int |\mathcal{E}(t)|^2 \, dt$ can then be compared to the present result. Using equation 30 of [129] and re-expressing parameters in terms of the ones used here, this is:

$$P = \frac{2\kappa N g^{R2}}{\gamma^2 |w|} \int \frac{(\Omega^R(t)/2)^2}{|w + (\Omega^R(t)/2)^2|} \exp\left[-\int^t Re\left(\frac{2\kappa(\Omega^R(t')/2)^2}{w + (\Omega^R(t')/2)^2}\right) dt'\right] dt \tag{8.20}$$

$$w = (N g^{R2} + \kappa\gamma(1 + i\Delta))/\gamma^2 \tag{8.21}$$

Taking the low Read power expansion corresponding to $(\gamma\Omega^R/2)^2 << N g^{R2} + \kappa\gamma)$, this gives:

$$P = \int \frac{\Omega^R(t)^2\gamma}{2} \frac{2C}{(1+2C)^2 + \Delta^2} \exp\left[-\int^t \frac{\Omega^R(t')^2\gamma}{2} \frac{1+2C}{(1+2C)^2+\Delta^2} dt'\right] dt \tag{8.22}$$

This corresponds exactly to the combination of equations (8.18) and (8.15), found with the "emission rates" approach. It therefore validates this approach, and gives an estimate of the range of validity of the lowest-order expansion in $\Omega^R_{eff}(t)^2$ performed here. In practice, we should therefore check that $(\gamma\Omega^R_{eff}/2)^2 < N g^{R2}_{eff} + \kappa\gamma = \kappa\gamma(1+2C)$, which is made easier by the fact that $C >> 1$.

8.4 Analytical expressions of the inefficiencies due to defects

The goal here is to use the previous description and progressively include in it the main defects of the experimental system in order to estimate the realistic Read photon retrieval efficiency, while keeping the form of the result to a manageable level of complexity.

8.4.1 Inhomogeneous Read beam light shifts

During the Read pulse, the large single-atom Rabi frequency induces non negligible light shifts on the atomic coherence's evolution frequency. Due to the inhomogeneity of the Read power in a realistic beam, this leads to differential dephasing of the atoms that distorts the collective excitation away from the perfectly phase-matched state, eventually causing a decrease of $P_{opt}^{nojump}(t)$.

The evolution frequency of the $g-f$ coherence of an atom exposed to Rabi frequency Ω^R is shifted by the amount $\frac{(\Omega^R)^2\gamma}{4\Delta}$. Even in a perfect situation with initial state $|\Psi_{int,opt}\rangle$ (equation (8.8)), the state will then dynamically evolve during the Read pulse into $|\Psi(t)\rangle$, where each component with atom k excited has acquired a phase $\int^t \frac{(\Omega_k^R(t'))^2\gamma}{4\Delta}dt'$. The overlap of this time-evolved state with $|\Psi_{int,opt}\rangle$ is:

$$\langle\Psi_{int,opt}|\Psi(t)\rangle = \frac{\sum_{k=1}^N \left|g_k^R/\Omega_k^R\right|^2 \exp\left[i\int^t \frac{(\Omega_k^R(t'))^2\gamma}{4\Delta}dt'\right]}{\sum_{k=1}^N \left|g_k^R/\Omega_k^R\right|^2} \tag{8.23}$$

For simplicity, we drop the amplitude variations to focus on the phase for now, consider the atomic cloud as a continuous medium of Gaussian density profile, and make the reasonable approximation that the Read field is uniform along its propagation direction (x) and Gaussian in the transverse plane (y,z), of waist w_b. As a good efficiency requires a Read beam much larger than the atomic distribution (almost homogeneous), the intensity's spatial variations can be developed in lowest order to get:

$$\begin{aligned}\langle\Psi_{int,opt}|\Psi(t)\rangle &\approx \frac{1}{2\pi R_c^2}\int \exp\left[-\frac{y^2+z^2}{2R_c^2} + i\int^t \frac{(\Omega^R(0,t'))^2\gamma}{4\Delta}\left(1-\frac{2(y^2+z^2)}{w_b^2}\right)dt'\right]dydz \\ &= \left[1+i\frac{4R_c^2}{w_b^2}\int^t \frac{(\Omega^R(0,t'))^2\gamma}{4\Delta}dt'\right]^{-1}\exp\left[i\int^t \frac{(\Omega^R(0,t'))^2\gamma}{4\Delta}dt'\right]\end{aligned} \tag{8.24}$$

As $P_{opt}^{nojump}(t) = |\langle\Psi_{int,opt}|\Psi(t)\rangle|^2$ and since under the approximations made so far $\Gamma_{cav} \propto (\Omega^R)^2$, the total efficiency coming back to equation (8.13) can be written as:

$$P = \frac{2C}{1+2C}\int\left[1+(\frac{\beta}{\xi})^2(\int^t \xi\Gamma_{cav}(t')dt')^2\right]^{-1}\xi\Gamma_{cav}(t)e^{-\int^t \xi\Gamma_{cav}(t')dt'}dt \tag{8.25}$$

where $\beta = \frac{(R_c/w_b)^2(\Omega^R)^2\gamma/\Delta}{\Gamma_{cav}}$ is a constant measuring the importance of the inhomogeneity.

For small inhomogeneity, the denominator in the integral should be close to 1, so that the first order correction comes from its lowest-order expansion in β. The result exactly integrates to:

$$P \approx \frac{2C}{1+2C}\left(1-e^{-h}-(\frac{\beta}{\xi})^2\left[2-(h^2+2h+2)e^{-h}\right]\right) \tag{8.26}$$

where $h = \int^\infty \xi\Gamma_{cav}(t)dt \propto \int(\Omega^R(t))^2dt$ is a normalized integrated weight of the Read pulse's power.

This general form includes all the dynamical effects caused by the Read pulse itself, showing in particular the already discussed two first terms, that are maximized for maximum h. The light shifts term of course disappears for a uniform Read beam ($w_b/R_c \to \infty, \beta \to 0$). Otherwise, it depends directly on h as shown in figure (8.4), in a way that makes the inhomogeneity effect worse for larger integrated power.

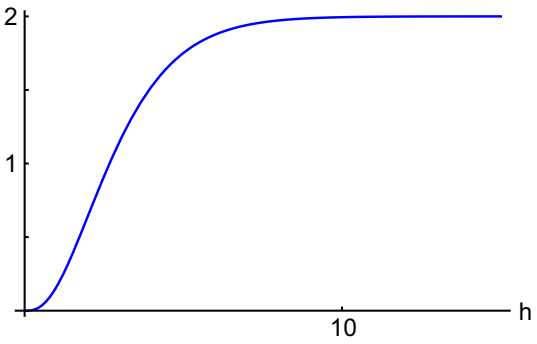

Figure 8.4: Weight of the light shifts term in the efficiency $(2-(h^2+2h+2)e^{-h})$ **as a function of** h**.**

This therefore leads in practice to an optimum to be found as one does not always win by increasing the Read power or the cooperativity. For realistic experimental parameters, the total efficiency given by equation (8.26) is plotted on figure (8.5) as a function of the cooperativity for different effective Read pulse power.

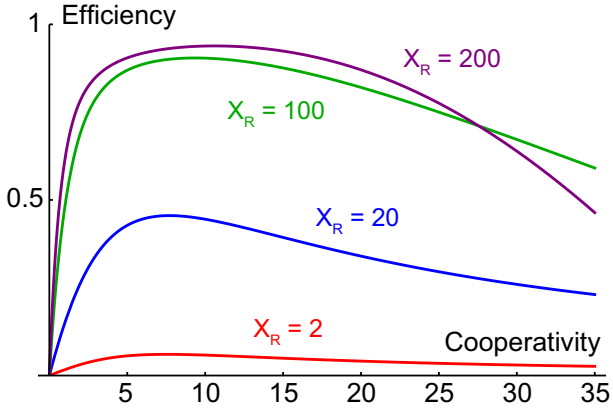

Figure 8.5: Efficiency given by equation (8.26) for realistic parameters. Assuming $\Delta = 15$, taking $R_c/w_b = 1/8$ for $C = 8$ and assuming $(R_c/w_b)^2 \propto C$ (see section 9.2.3 for justification), the efficiency is plotted as a function of C for different values of $X_R = \int (\Omega^R_{eff})^2 \gamma / 2dt$. This shows that one does not always win by increasing the Read power or the cooperativity.

The reason of this behaviour is qualitatively the following: when increasing the cooperativity, the size of the cloud increases, and a larger Rabi frequency is also required to efficiently extract the excitation (Γ_{cav} decreases with C when it is large enough). Both make the inhomogeneous light shift effect worse and decrease the efficiency.

8.4.2 Initial state and optimally coupled intermediate state for non-ideal optical pumping

One of the important experimental defects is the imperfect optical pumping of the atoms. Instead of being confined properly in a three-level system, they start the protocol in a mixed state between at least two ground states $|g_1\rangle$ and $|g_2\rangle$, described by the following initial density matrix for atom k:

$$\hat{\rho}_k^0 = p\,|g_1\rangle_k\,\langle g_1|_k + (1-p)\,|g_2\rangle_k\,\langle g_2|_k \tag{8.27}$$

The situation for the Write step from a single-atom point of view would therefore be described as in figure (8.6) (couplings are also indexed by 1 or 2 as the Clebsch-Gordan coefficients will differ on the different transitions).

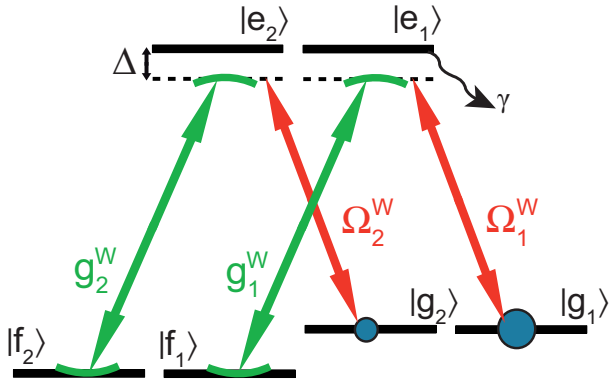

Figure 8.6: Simplified atomic level scheme in the Write step for an imperfect optical pumping into state $|g_1\rangle$.

The initial N-atom density matrix would therefore be:

$$\begin{aligned}\hat{\rho}^0 &= \bigotimes_{k=1}^{N} \hat{\rho}_k^0 \\ &= \hat{\rho}_{1:N,2:0} + \hat{\rho}_{1:N-1,2:1} + \ldots + \hat{\rho}_{1:0,2:N}\end{aligned} \tag{8.28}$$

where $\hat{\rho}_{1:n,2:N-n}$ is a (not normalized) N-atom density matrix with n atoms in the $|g_1\rangle$ state, the rest being in $|g_2\rangle$. When developing the first line of the previous equation, each $\hat{\rho}_{1:n,2:N-n}$ is a sum of $\binom{N}{n}$ terms, with an overall weight $p^n(1-p)^{N-n}$. For large N, the expression of $\hat{\rho}^0$ is therefore dominated by one specific configuration where $n = Np$ with small relative fluctuations:

$$\hat{\rho}^0 \approx \hat{\rho}_{1:Np,2:N(1-p)} \tag{8.29}$$

The density matrix $\hat{\rho}_{1:Np,2:N(1-p)}$ itself is a statistical mixture of all possible quantum states where among the N atoms, Np are in the $|g_1\rangle$ state. When calculating the result of a physical measurement based on $\hat{\rho}_{1:Np,2:N(1-p)}$, all of these quantum states may behave differently depending on how the Np atoms in $|g_1\rangle$ and the $N(1-p)$ atoms in $|g_2\rangle$ are spatially distributed, what couplings they see and so on. However once again one can argue that statistically the result will be largely dominated by the contribution of "typical" states. These states are the ones where both the Np atoms and the other $N(1-p)$ form ensembles randomly distributed over the whole sample, sampling on average always the same ensemble of values of couplings.

As a conclusion, we will consider the initial pure atomic quantum state:

$$|\Psi_0\rangle = \bigotimes_{k=1}^{Np} |g_1\rangle_k \bigotimes_{k=Np+1}^{N} |g_2\rangle_k \tag{8.30}$$

Under the condition that the two sub-ensembles of atoms have spatial distributions covering similarly the entire cloud, calculating the result of a physical process based on

this quantum state will give a good approximation of the result starting from $\hat{\rho}^0$, for large enough N.

If the couplings on the Read photon transition are respectively g_1^R and g_2^R for atoms of type 1 and 2, the excited state optimally coupled to $|\Psi_0\rangle$ is:

$$|\Psi_{exc,opt}\rangle \propto \sum_{k=1}^{Np} (g_{1k}^R)^* \bigotimes_{i\neq k=1}^{Np} |g_1\rangle_i \bigotimes_{j=Np}^{N} |g_2\rangle_j \ |e_1\rangle_k + \sum_{k=Np}^{N} (g_{2k}^R)^* \bigotimes_{i=1}^{Np} |g_1\rangle_i \bigotimes_{j\neq k=Np}^{N} |g_2\rangle_j \ |e_2\rangle_k \tag{8.31}$$

This state is reached by the Read field classical coupling (Ω^R indexed by 1 or 2 may depend on the atom type again) if we start the readout from state:

$$|\Psi_{int,opt}\rangle = \tag{8.32}$$
$$\left[\sum_{k=1}^{Np} \frac{(g_{1k}^R)^*}{\Omega_{1k}^R} \bigotimes_{i\neq k=1}^{Np} |g_1\rangle_i \bigotimes_{j=Np}^{N} |g_2\rangle_j \ |f_1\rangle_k + \sum_{k=Np}^{N} \frac{(g_{2k}^R)^*}{\Omega_{2k}^R} \bigotimes_{i=1}^{Np} |g_1\rangle_i \bigotimes_{j\neq k=Np}^{N} |g_2\rangle_j \ |f_2\rangle_k\right] /$$
$$\sqrt{\sum_{k=1}^{Np} \frac{|g_{1k}^R|^2}{|\Omega_{1k}^R|^2} + \sum_{k=Np}^{N} \frac{|g_{2k}^R|^2}{|\Omega_{2k}^R|^2}}$$

8.4.3 Optical pumping defects

The inefficiency due to optical pumping corresponds to a $P_{opt}^0 \neq 1$ in equation (8.13), as the state after the Write process will differ from $|\Psi_{int,opt}\rangle$. To quantify it, the actual state prepared after detection of a Write photon must be expressed. It is in a good approximation (as the Write is a very weakly-driven, linear process):

$$|\Psi_{int}\rangle = \tag{8.33}$$
$$\left[\sum_{k=1}^{Np} g_{1k}^W \Omega_{1k}^W \bigotimes_{i\neq k=1}^{Np} |g_1\rangle_i \bigotimes_{j=Np}^{N} |g_2\rangle_j \ |f_1\rangle_k + \sum_{k=Np}^{N} g_{2k}^W \Omega_{2k}^W \bigotimes_{i=1}^{Np} |g_1\rangle_i \bigotimes_{j\neq k=Np}^{N} |g_2\rangle_j \ |f_2\rangle_k\right] /$$
$$\sqrt{\sum_{k=1}^{Np} |g_{1k}^W|^2 |\Omega_{1k}^W|^2 + \sum_{k=Np}^{N} |g_{2k}^W|^2 |\Omega_{2k}^W|^2}$$

To write the overlap of these two states, let us use the hypothesis that the two types of atoms 1 and 2 have similar, large and dense distributions in space to write for example: $\sum_{k=1}^{Np} \left|g_{1k}^W\right|^2 \left|\Omega_{1k}^W\right|^2 = Np \ \overline{|g_1^W|^2 |\Omega_1^W|^2}$ and similarly for all other sums, where quantities like $\overline{|g_1^W|^2 |\Omega_1^W|^2}$ will be appropriately weighted spatial averages of the mode functions defining the various couplings. Then the overlap $\langle\Psi_{int,opt}|\Psi_{int}\rangle$ is:

$$\frac{Np \ \overline{g_1^W \Omega_1^W g_1^R/\Omega_1^{R*}} + N(1-p) \ \overline{g_2^W \Omega_2^W g_2^R/\Omega_2^{R*}}}{\sqrt{\left(Np\overline{(\frac{|g_1^R|^2}{|\Omega_1^R|^2})} + N(1-p)\overline{(\frac{|g_2^R|^2}{|\Omega_2^R|^2})}\right)\left(Np\overline{(|g_1^W|^2 |\Omega_1^W|^2)} + N(1-p)\overline{(|g_2^W|^2 |\Omega_2^W|^2)}\right)}} \tag{8.34}$$

Now the difference between couplings for atoms of type 1 or 2 may come from different Clebsch-Gordan coefficient, but their spatial dependences will be exactly the same, so

that they can be written $g_2^R/\Omega_2^R(\vec{r}) = \epsilon_1\ g_1^R/\Omega_1^R(\vec{r})$ and $g_2^W\Omega_2^W(\vec{r}) = \epsilon_2\ g_1^W\Omega_1^W(\vec{r})$, and the result splits into:

$$\begin{aligned}\langle\Psi_{int,opt}|\Psi_{int}\rangle &= \frac{\overline{g_1^W\Omega_1^W g_1^R/\Omega_1^{R*}}}{\sqrt{\left(\overline{|g_1^R|^2/|\Omega_1^R|^2}\right)\left(\overline{|g_1^W|^2|\Omega_1^W|^2}\right)}}\frac{p+(1-p)\epsilon_1\epsilon_2}{\sqrt{(p+(1-p)\epsilon_1^2)\,(p+(1-p)\epsilon_2^2)}} \\ &= C(g_1^W\Omega_1^W, \frac{g_1^{R*}}{\Omega_1^R})\frac{p+(1-p)\epsilon_1\epsilon_2}{\sqrt{(p+(1-p)\epsilon_1^2)\,(p+(1-p)\epsilon_2^2)}} \qquad (8.35)\end{aligned}$$

The first part of the result measures the correlations of the Write and Read coupling functions in space, and it is therefore exactly what describes all the phase and amplitude matching issues in the retrieval, and will be discussed in more details after this section.

The second term is, properly speaking, what describes the negative effect of an imperfect optical pumping. It shows once again that what really matters is whether the different atoms are distinguishable from one another when they undergo the full Write-Read process: if $p \neq 1$ and $\epsilon_1 \neq \epsilon_2$, then the two populations of atoms existing in the cloud can be distinguished by their couplings to the fields, so that the efficiency drops. In the opposite case ($p = 1$, or $\epsilon_1 = \epsilon_2$), the optical pumping term is 1, because all atoms are again indistinguishable from the point of view of the protocol.

To give an example we take the experimental values of $\epsilon_1 = \frac{3}{2\sqrt{2}}$ and $\epsilon_2 = \frac{1}{2\sqrt{2}}$ (see section 9.1.1) and plot the square of the pumping term in the overlap in figure (8.7).

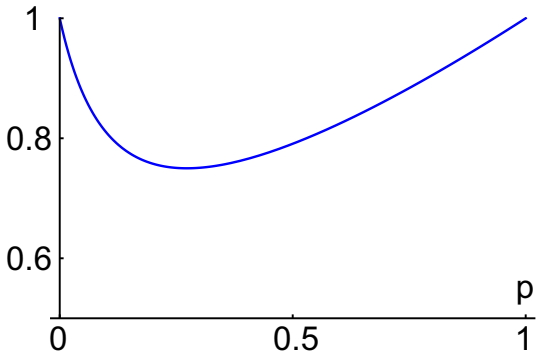

Figure 8.7: Optical pumping efficiency term $\frac{(p+(1-p)\epsilon_1\epsilon_2)^2}{(p+(1-p)\epsilon_1^2)(p+(1-p)\epsilon_2^2)}$ as a function of p ($\epsilon_1 = \frac{3}{2\sqrt{2}}$ and $\epsilon_2 = \frac{1}{2\sqrt{2}}$).

In real multilevel atoms, this whole model only makes sense for an optical pumping efficiency p not too far from 1 (otherwise even more states would be populated). With the numbers given above, the efficiency would for example drop to 0.95 for $p = 0.9$, only due to this optical pumping term.

8.4.4 Mode overlap efficiency

The remaining factor in the efficiency, $C(g_1^W\Omega_1^W, \frac{g_1^{R*}}{\Omega_1^R})$ depends on the geometry of the modes of the Write and Read beams, and of the two Raman photons. These have to combine together nicely both in phase and amplitude for the retrieval process to be efficient. The mode overlap part of the efficiency is expressed in the continuous approximation as:

$$P_{mode} = \left| C(g_1^W \Omega_1^W, \frac{g_1^{R*}}{\Omega_1^R}) \right|^2 \tag{8.36}$$

$$= \frac{\left| \int \mu(\vec{r}) g_1^W(\vec{r}) \Omega_1^W(\vec{r}) g_1^R(\vec{r}) / \Omega_1^{R*}(\vec{r}) d^3\vec{r} \right|^2}{\left(\int \mu(\vec{r}) \left| g_1^R(\vec{r}) \right|^2 / \left| \Omega_1^R(\vec{r}) \right|^2 d^3\vec{r} \right) \left(\int \mu(\vec{r}) \left| g_1^W(\vec{r}) \right|^2 \left| \Omega_1^W(\vec{r}) \right|^2 d^3\vec{r} \right)} \tag{8.37}$$

Now some information about the experimental geometry must be specified (see figure (8.8)). To be consistent with the actual experimental setup we will take the following definitions:

$$g_1^R(\vec{r}) = g_{10}^R \, cos(k_p^R(z - z_0)) \, e^{-\frac{x^2+y^2}{w^2}} \tag{8.38}$$

$$g_1^W(\vec{r}) = g_{10}^W \, cos(k_p^W(z - z_0)) \, e^{-\frac{x^2+y^2}{w^2}} \tag{8.39}$$

$$\Omega_1^W(\vec{r}) = \Omega_{10}^W \, e^{ik_f^W x} \, e^{-\frac{y^2}{w_{Wy}^2} - \frac{z^2}{w_{Wz}^2}} \tag{8.40}$$

$$\Omega_1^R(\vec{r}) = \Omega_{10}^R \, e^{ik_f^R x} \, e^{-\frac{y^2}{w_{Ry}^2} - \frac{z^2}{w_{Rz}^2}} \tag{8.41}$$

$$\mu(\vec{r}) = \mu_0 \, e^{-\frac{\vec{r}^2}{2R_c^2}} \tag{8.42}$$

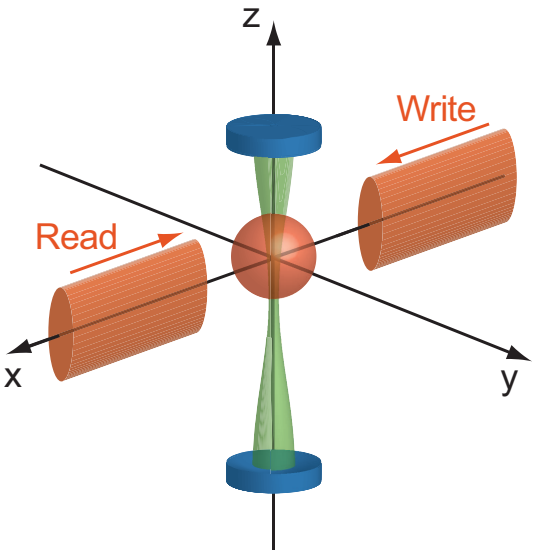

Figure 8.8: Sketch of the geometry for our DLCZ experimental setup.

The cavity axis is still z. The two Raman photons are emitted into the fundamental transverse mode of the cavity, but with two different frequencies, both resonant on one longitudinal mode, so they have different wave vectors k_p^R and k_p^W. As a result their two standing waves are not everywhere in phase, and the position z_0 of the cloud relative to the point where they are in phase is important. The Write and Read beams are counter-propagating along the x axis with different wave vectors k_f^R and k_f^W, and an adjustable and different aspect ratio in the (y, z) plane. Indeed, in this geometry the atomic sample

participating in the process has a size defined by R_c along z, but by w the cavity mode waist in x and y dimensions. It can therefore be very asymmetric.

Then the mode overlap can be calculated and gives:

$$\begin{aligned} P_{mode} &\approx \left(1-2(a_{Rz}^2+a_{Wz}^2)^2\right)\left(1-\frac{(a_{Ry}^2+a_{Wy}^2)^2}{8}\right) \\ &\quad * \exp\left[-\frac{\Delta k^2}{2}\left(\frac{w^2}{2}+\frac{2R_c^2}{1+2(a_{Wz}^2-a_{Rz}^2)}\right)\right] cos^2(\Delta k z_0) \end{aligned} \tag{8.43}$$

In the first two terms, a lowest-order expansion has been performed in $a_{W/Rz}=\frac{R_c}{w_{W/Rz}}$ and $a_{W/Ry}=\frac{w}{w_{W/Ry}}$, quantifying the homogeneity of the beams on the useful section of the cloud. $\Delta k = \left|k_p^R\right| - \left|k_p^W\right| \approx \left|k_f^R\right| - \left|k_f^W\right|$ is the wave vector mismatch. It is responsible for an exponential term measuring how much the phases of the Write and Read can differ over the size of the useful sample, thus really an unavoidable phase-matching term. It also comes into play if the cloud is not centered where the two cavity modes are in phase $z_0 = 0$ (last term), so that this will be an important criterion for setting up the experiment.

8.4.5 Atomic motion

The last important effect that will be considered here is related to the "memory" aspect of the protocol: the previous considerations give the memory's retrieval efficiency, when nothing spontaneously degrades the overlap with the perfectly matched collective state during storage. In practice, due to the atoms' finite temperature, they randomly move and carry their coherence's phase with them in space. After some time, the phase pattern defining the proper collective excitation mode will thus be washed out.

To account for this, each atom is considered to move for a time t with its velocity $\vec{v}_k$ between the Write and Read steps. Motion during the Read itself is neglected, so that this effect behaves as an "initial preparation defect" (described by a P_{opt}^0) and not a dynamic one. Now the atomic intermediate state is still described by equation (8.33), but after each atom has moved from $\vec{r}_k$ to $\vec{r}_k + \vec{v}_k t$, the optimal state for readout is given by a modified version of equation (8.32), with the Read field coupling applied at these new positions. Therefore when calculating the overlap, the result still splits just like in equation (8.35), but the pure mode-matching term is now:

$$\frac{\sum_k \exp\left[i\vec{k}_f^R.\vec{v}_k t\right]\ g_{1k}^W \Omega_{1k}^W g_{1k}^R/\Omega_{1k}^{R*}}{\sqrt{\left(\sum_k \left|g_{1k}^W\Omega_{1k}^W\right|^2\right)\left(\sum_k \left|g_{1k}^R/\Omega_{1k}^{R*}\right|^2\right)}} \tag{8.44}$$

In the continuous approximation for the atomic distributions, this involves two independent averages, one on the position distribution of the atoms with weight $\mu(\vec{r})$, and one on the velocity distribution in order to process the phase term. As the two distributions are independent in a thermal cloud, the two terms split to give back exactly the mode overlap P_{mode}, multiplied by the average of the phase term $e^{i\vec{k}_f^R.\vec{v}_k t}$ over the atomic velocity distribution. Under the hypothesis that this distribution is a Maxwell-Boltzmann one, characterized by a temperature T, this velocity average is calculated to give:

$$P_{Doppler}(t) = e^{-t^2/2\tau_D^2} \tag{8.45}$$

where $\tau_D = \frac{1}{2k_f^R}\sqrt{\frac{m}{k_B T}}$ is the Doppler-limited decoherence time of the collective excitation, for atoms of mass m (specific to our geometry). The result of the random thermal motion

of the atoms is therefore a progressive loss of phase-matching while the excitation stays in the cloud, and thus a limitation on the storage time, described by a Gaussian decay as one waits before retrieving the excitation. For rubidium 87 at 50 μK, this time is 900 ns.

8.4.6 Summary and expression of the retrieval efficiency

To summarize, under the approximations made here, for an excitation that has been stored for a time t in a cloud of cooperativity C optically pumped with efficiency p, readout with a Read pulse whose parameters are summarized in h, the total retrieval efficiency can be written as:

$$P = P_{Doppler}(t)\ P_C\ P_{Read}(h)\ P_{pump}(p)\ P_{mode} \tag{8.46}$$

Where:

$$\begin{aligned}
&P_{Doppler}(t) = e^{-t^2/2\tau_D^2}\\
&P_C = \frac{2C}{1+2C}\\
&P_{Read}(h) = \left(1 - e^{-h} - (\frac{\beta}{\xi})^2(2-(h^2+2h+2)e^{-h})\right)\\
&P_{pump}(p) = \frac{(p+(1-p)\epsilon_1\epsilon_2)^2}{(p+(1-p)\epsilon_1^2)\ (p+(1-p)\epsilon_2^2)}\\
&P_{mode} = \left(1-2(a_{Rz}^2+a_{Wz}^2)^2\right)\left(1-\frac{(a_{Ry}^2+a_{Wy}^2)^2}{8}\right)e^{-\frac{\Delta k^2}{2}(\frac{w^2}{2}+\frac{2R_c^2}{1+2(a_{Wz}^2-a_{Rz}^2)})}cos^2(\Delta k z_0)
\end{aligned} \tag{8.47}$$

The numerical values achieved for these different terms in our actual experimental configuration will be discussed in details in section 9.5.1. Their dependence on the relevant parameters is illustrated in figures (8.4), (8.5) and (8.7).

Chapter 9

Experiment

Contents

This chapter will describe how the DLCZ protocol was implemented in practice, and the way the parameter range was chosen and optimized for optimal retrieval efficiency. The results of two types of measurements on the retrieved light will be presented, pure intensity and correlation ($g^{(2)}$) analysis as a first step, and homodyne tomography as a more precise and complete characterization of all its degrees of freedom.

9.1 Experimental setup

9.1.1 General properties of the photon source's constituents

The protocol as such is so versatile that it can theoretically be adapted in many different geometries, on any kind of transitions, for example using only the hyperfine structure of the rubidium level scheme in the absence of magnetic field, with no differentiation of the Zeeman sublevels [127]. In our case, the optical accesses on the vacuum chamber forced the Write and Read beams to be sent orthogonally to the cavity axis, which in turns puts some constraints on the exact level scheme to be used in the Write and Read transitions.

Excitation scheme and optical pumping

We chose to work on Zeeman-selective transitions with Zeeman optical pumping. The final excitation scheme implemented, sketched on figure (9.1), uses the $D1$ line at 795 nm as support. The atoms are initially optically pumped in the extreme Zeeman sublevel $\left|5S_{1/2}, F = 2, m_F = +2\right\rangle$ by a dedicated σ^+-polarized beam matched to the fundamental transverse mode of the cavity, which defines the quantization axis. The Zeeman pumping is realized on the $5S_{1/2}, F = 2 \rightarrow 5P_{1/2}, F = 2$ transition in the presence of the MOT hyperfine repumper.

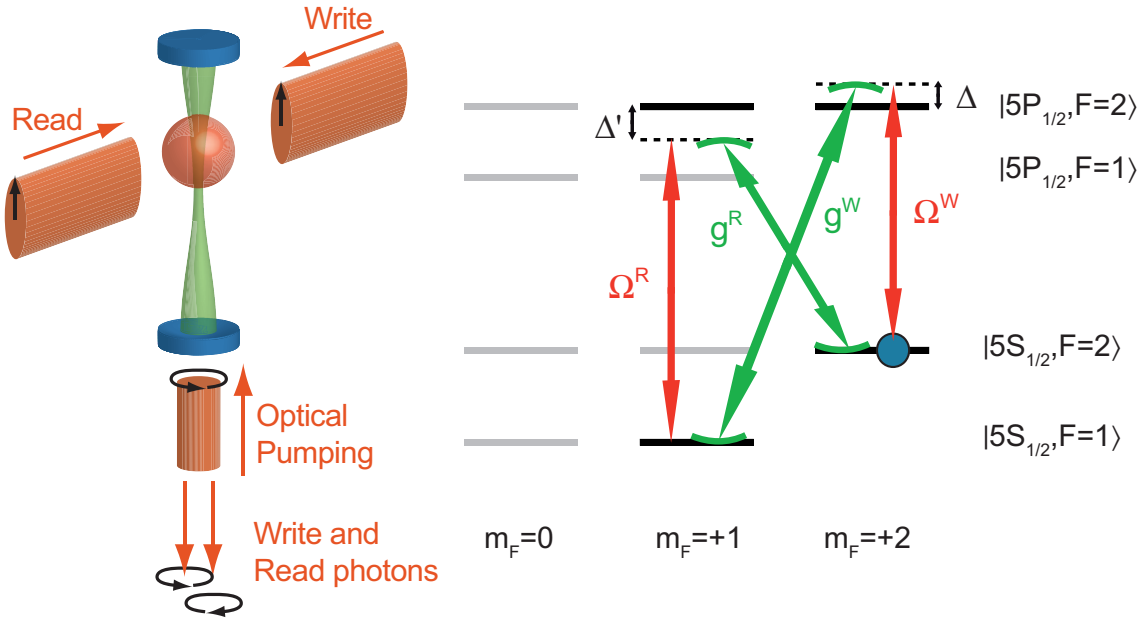

Figure 9.1: Sketch of the basic properties of our practical implementation of the DLCZ scheme.

Write and Read beams

The Write and Read excitation fields are both π-polarized: this is easy to achieve as they propagate orthogonally to the quantization axis, makes the Write photon's polarization uniquely determined, and allows the two Raman photons to get emitted along the cavity axis with opposite circular polarizations, which makes them easier to separate than only by their frequency (see figure (9.1)). For that we use a different state as relay for

the Write and Read transitions, which does not change anything to the physics of the protocol.

As can be seen from figure (9.1), the Write and Read beams must be separated in frequency by the ∼6.8 GHz hyperfine splitting of the fundamental state, and their frequency stability is crucial for the phase-matching efficiency of the readout. The 795 TiSa is used to produce the high-power Read beam, and the 795 diode which is phase-locked on it to produce the Write. An external oscillator (Rohde & Schwarz SMB100A + SMB-B112L 100kHZ to 12.75GHz generator, frequency precision better than 10^{-6}) gives the reference on which the beatnote signal between the two lasers is locked, using an mFALC110 module from Toptica (Mixing Fast Analog Linewidth Control) with electronic bandwidth 100 MHz.

The Write and Read beams are asymmetrically shaped using cylindrical lenses to match the elongated shape of the "useful" part of the cloud. They are designed symmetric to each other, with waists at the level of the atomic cloud $w_y \approx 325\mu$m and $w_z \approx 3100\mu$m and aligned by checking that the Write beam is coupled into the Read fiber, in order to start from the best phase-matching condition possible.

The power used in these two beams was subject first to an estimation using numerical simulations, then to experimental optimization to study the effect on the efficiency, as will be explained in section 9.2.2. The optimal values depend in particular on the cooperativity of the cloud.

Atomic cloud and cooperativity range

As will be explained in details in section 9.2, the choice of the cooperativity is of great importance for the protocol, and it is interdependent of many other parameters. The experimental optimization of the source's efficiency lead to a regime where it is typically 7-8 on the Read photon transition. This situation is the default reference in which all the numbers are given hereafter, unless stated explicitly otherwise.

Because of the Clebsch-Gordan coefficients ratio, the cooperativity on the Read transition is 6 times smaller than what would be measured on the reference closed transition at 780 nm. Such cooperativity is reached rather easily (see section 5.5.3), for a cloud with a typical effective number of coupled atoms of 5 - 7 $.10^4$, and a size of $R_c \sim 350\mu$m.

9.1.2 Optical and technical layout

Most of the important technical data concerning the photons' detection setup (Write and Read), and the setup of other beams coupled to the cavity, are given thereafter in relation with figure (9.2).

The Write and Read photons are separated at the output of the cavity on a polarizing beamsplitter, after passing through a quarter-wave plate, defining two optical arms (Trigger and Detection). The question of losses in the different arms will be discussed in details as part of each section concerning photon counting and homodyne detection.

Optical pumping path and lock beam

Because it is matched to the cavity mode, close in frequency to the Read photon, and due to its polarization, the optical pumping beam must be sent to the cavity from the Detection arm itself. In order to minimize the losses introduced on this arm by doing this, we use an AOM (called Switch AOM) to switch sequentially between a configuration (On) where optical pumping is sent through order 1 diffraction to the cavity, and another (Off)

where the Read photon goes through from the cavity to the detection setup. To avoid cutting the beam with the AOM's aperture, the mode of the Detection path is focused to a waist of 350 μm in the AOM.

The locking beam also has to be sent to the cavity mode. Being at 810 nm, it is reflected towards the cavity on tilted a Semrock LL01-808 filter (IF1), transmitting 795 nm light up to 97-98 %, without measurable distortion of the mode.

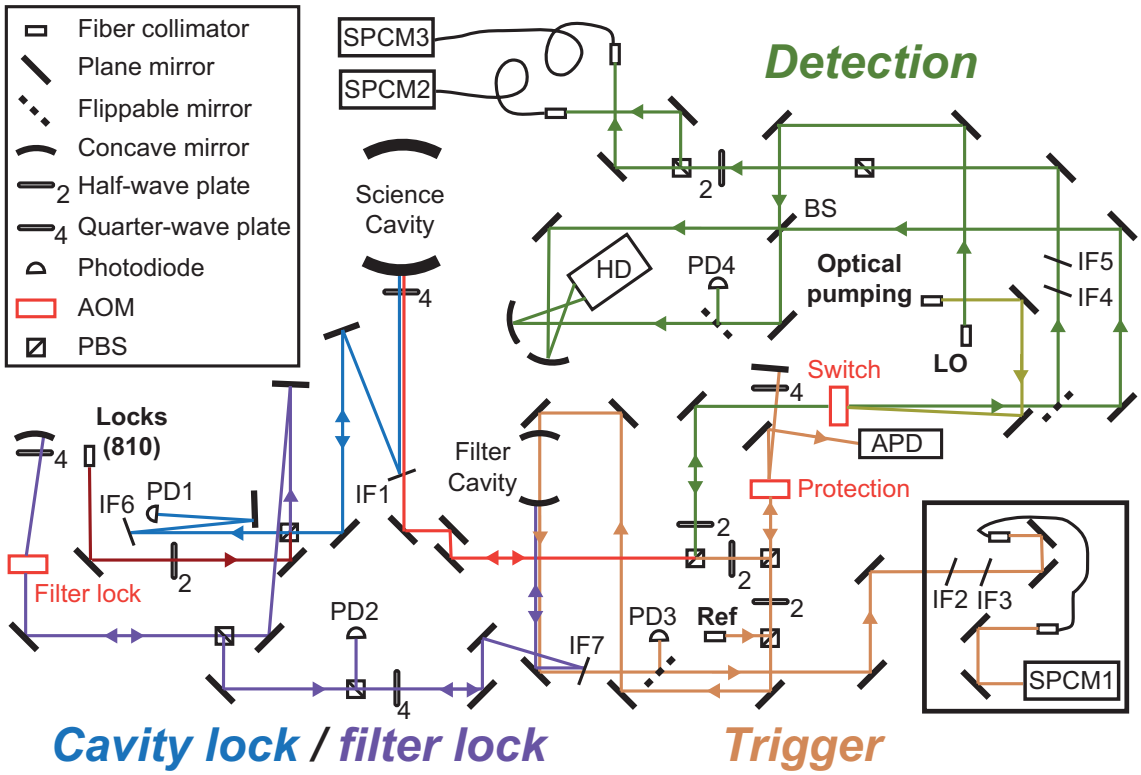

Figure 9.2: Optical layout at the input/output of the cavity. BS is a 50:50 beamsplitter. IF are interference filters whose use is detailed in the text. Among the detectors: HD is the Homodyne Detector, PD1 is used to get the locking signal of the science cavity, PD2 has a similar use but for the lock of the filter cavity, PD3 is used during alignments to match the Write path into the filter cavity, PD4 is used when optimizing the mode-matching between the Read photon's mode and the LO, the Avalanche PhotoDiode APD is used to monitor low-power classical light transmitted through the cavity from top, in particular to lock the intensity of the transmitted alignment beam that can be used to mode-match the LO.

Trigger path, single-photon counters and filtering

The Write photon in principle only needs to be sent to a detector to herald the success of the Write step. This heralding is done by a Single Photon Counting Module (SPCM1) from Perkin-Elmer SPCM-AQRH-15, that generates a 20 ns long TTL pulse for each photon detected. It has a specified intrinsic dark count rate of 50 Hz, a quantum efficiency around 800 nm estimated to 65 %, a dead time after detection of $\sim$ 30 ns and a maximum usable incident photon rate of 30 MHz (but above 5 MHz the detected countrate starts being quite nonlinear with the incident photon rate).

Compared to this, the setup contains several beams of intensity above the μW level (1 μW corresponding to a 4.10^6 MHz photon countrate) matched on purpose to the exact same mode as the Write photon. As a result, a progressively strengthened filtering is applied to the Trigger arm, to protect the counter and avoid too large background countrate during the detection of the Write photons (signal corresponding to a typical rate of $\sim$ 1 kHz). The protection from stray light and continuous sources of light in the mode (like the locking beam) is ensured by a black box built around the counter and two tilted interference filters IF2 and 3 (LL01-808) piled up in the path (each one with transmission $< 10^{-5}$ at 810 or 780 nm). The Zeeman optical pumping light, though sent in a separate time-window from the measurements, is entirely reflected from the cavity on the counter and can generate long-lived charges that disturb the readout. A double-pass order 1 AOM (called Protection AOM) is switched off outside measurement periods to temporally protect SPCM1 (the fraction of optical leaking when Off is $< 10^{-8}$). Finally, when using the homodyne detection's local oscillator (several mW of power) together with the counter, the strong back-reflections of the LO on the detector disturb the functioning of the Trigger SPCM, and lead to the implementation of spatial filtering with a 2 m long single-mode fiber, as well as spectral filtering with a custom Fabry-Pérot cavity (that must be locked to transmit the Write photons and reflect LO light typically 6.8 GHz away). This will be described in more details in the homodyne detection section.

The SPCMs' TTL-drivable gate input are also used to switch off the high voltage generating the single-photon avalanches outside measurement steps, to increase the counters' safety with respect to high-power beams.

Detection path

The setup contains two complete detection apparatus, and the possibility to reversibly switch from one to the other. A flippable mirror in the Detection path directs light towards the photon-counting setup when it is in, or to the homodyne detection setup when it is out.

Intensity correlation measurements are realized with two SPCMs (SPCM2 and SPCM3), that are the fibered-input version of SPCM1 (model SPCM-AQRH-15-FC). As this part of the setup is never used together with the homodyne detection LO, and the optical pumping light is by construction not directed towards it, the necessary filtering for these SPCMs is restricted to two interference filters IF4 and 5 (LL01-808). Light coming from the cavity is shaped to fiber-compatible mode with two lenses, and split in two halves injected in the two SPCMs' single-mode fibers by an adjustable PBS-halfwaveplate-PBS setup.

For homodyne detection, the signal light is mixed with a mode-matched LO beam on the 50:50 beamsplitter from Layertec (part number 110895 – its angle with respect to the beams, as well as the incident polarization, have to be adjusted to make it precisely 50:50). The plate itself is wedged (angle of 30 arcmin) to minimize backreflections in the same mode. The two arms of the mixed homodyne beam are then focused with concave mirrors (radius of curvature 20 cm) onto the photodiodes of the homodyne detector. The detector we use is a customized version of HCA-S model from Femto with S3883 photodiodes(1.5 mm active diameter, quantum efficiency 91%). It has a specified intrinsic bandwidth of 100 MHz, and electronic noise described in figure (9.12) corresponding in practice to a noise standard deviation of $\approx$ 7 mV.

Reference beam

A reference beam(Ref), for alignment purposes, can be sent backwards from the Trigger arm, and can propagate after reflection on the cavity towards any arm of the setup by changing the angles of waveplates. This "reference" channel can be fed by light corresponding to either of the Write or Read frequencies.

It is used, once mode-matched to the cavity, to align all the mode-sensitive parts of the setup on a common reference, supposed to simulate the Raman photons' mode: the filtering Fabry-Pérot cavity and the single-mode fiber in the Trigger arm, the SPCMs' fiber inputs in the photon-counting part of the Detection arm, and the alignment of the LO on the signal for the homodyne detection. It also gives the frequency reference on which is set the lock position of the main cavity as well as the filter one, so that they respectively satisfy the right resonance conditions (see section 9.2.1) or transmit efficiently the Write photons.

Although this alignment method is practical and simple to implement, it has the disadvantage that a mismatch between this reference beam and the Raman photons' mode reflects on all the alignment. Therefore a second technique is used to generate a beam in the cavity's fundamental transverse mode, mostly for the critical LO-signal mode-matching, by making the locked cavity itself act as a mode-filter on a resonant beam sent from the top. The technical details will be given in the homodyne detection section.

9.1.3 Experimental sequence

After the initial trapping and cooling stages (already described in section 5.3), the atoms are optically pumped before measurements can start. The optical pumping's lifetime was found of the order of 1 ms. The way this was estimated is presented in figure (9.3).

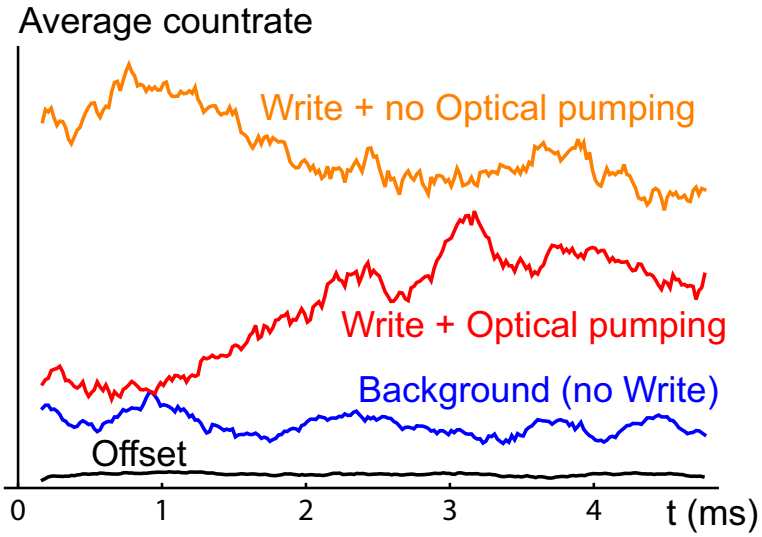

Figure 9.3: Zeeman pumping quality lifetime measurement. The average countrate on one of the Detection counters is measured (counting σ^- photons, as opposed to the Trigger counter). When the atoms are not correctly pumped (some are in state $F = 2, m_F \neq +2$), some σ^- photons can be emitted when Write pulses are sent to the cloud. For ideal optical pumping, no σ^- photons should be emitted in response to Write pulses, as on the red curve during the first ~ 1 ms, before the counts rise again with time.

This observation determines the time structure of the typical experimental sequences, summarized in figure (9.4).

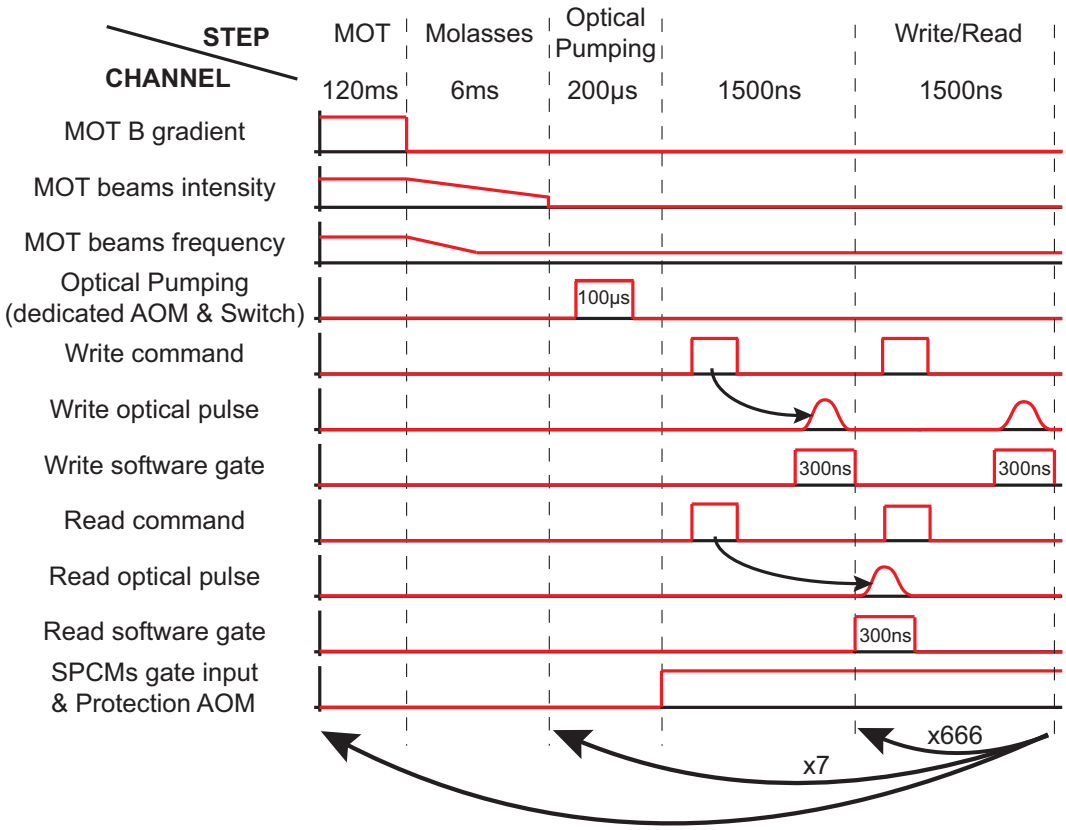

Figure 9.4: Experimental sequence. The temporal proportions of the different steps are not at scale. During the measurements, series of 666 Write-Read cycles are generated, forming "useful" windows of 1 ms length. The first 1500 ns cycle is shown separately because it is singular due to the production delays of the optical pulses (it does not contain any Read pulse). These measurement windows are alternated with optical pumping pulses until the cooperativity is too low and the full cycle restarts.

The measurement step is split into windows of 1 ms separated by 200 μs interruptions during which a 100 μs optical pumping pulse is sent to the cavity (its power is adjusted as described in section 9.2.2). During each of these 1 ms measurement windows, alternate pulses of Write and Read beams are repeatedly sent to the atoms. Because of incompressible delays between the command and the actual pulse generation, the total repetition period of this Write-Read cycle is 1500 ns, which defines the shortest elementary step in the software conditional logic (see next paragraph). One measurement window therefore contains 666 trials of the protocol. The pulses' shapes are designed by sending one single arch of a sine function at 2.5 MHz to the analog RF power control of the AOMs sending the Write and Read beams to the experiment. The sine arches are produced by two externally triggered function generators (TTI TG4001), and transformed by the AOM's nonlinear response into an output optical pulse that is approximately Gaussian with $1/e$ half width ≈ 80 ns, as can be seen on figure (9.5). Due to different electronic and acoustic delays in the two channels, when the trigger is sent to both simultaneously the optical pulses come out in the configuration of figure (9.5) where the Read happens just after the Write.

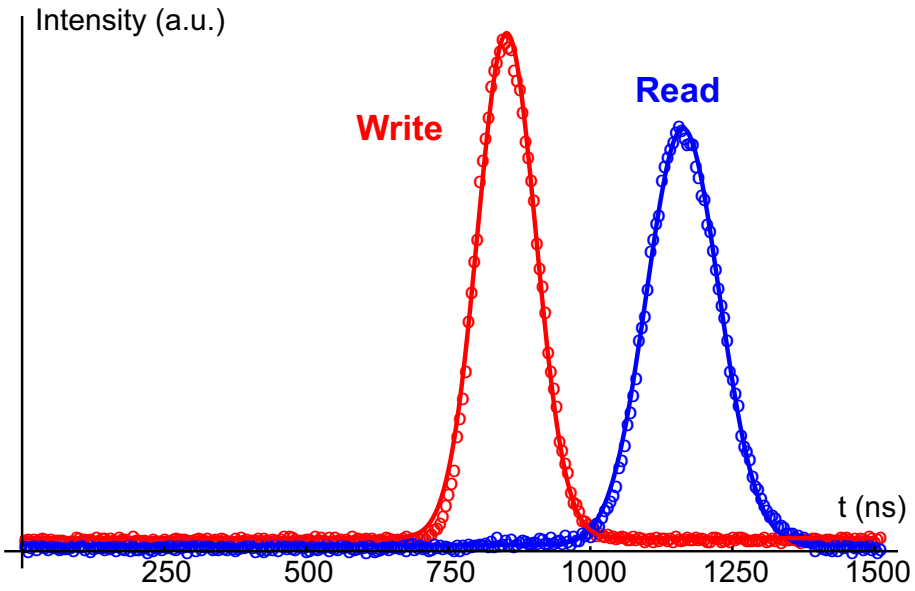

Figure 9.5: Measured intensity profiles of the Write (red) and Read (blue) driving pulses (open circles), and Gaussian fits (solid lines). The trigger is sent at time $t = 0$ for both channels. The fitted $1/e$ half-width is 72 ns for the Write and 90 ns for the Read. The settings of the Write and Read pulses were not yet optimized at the time these data were acquired.

After $\sim$ 7 repetitions of this pumping-measurement, the cloud's expansion starts to make the cooperativity decrease too much, and a complete cycle starts again by loading atoms. In the overall regime of these sequences, to optimize the duty cycle of the measurements, the MOT is never fully loaded, but is in a quasi-steady state alternately being partially loaded by the trapping step (120 ms) and partially emptied during the rest of the sequence cycle ($\sim$ 15 ms).

Software gating and conditional behaviour

In order to optimize the selectivity of the photons detection, software gating is applied to the counters detections: once the time slot in which the Write photons arrive on the Trigger SPCM is located, a 300 ns range is defined around it where the impacts detected are taken into account, otherwise they are discarded. The same can be done on the Detection counters when using them. This allows to minimize the false detection events due to background counts or remaining detection of Write photons on the Detection counters for example.

By placing in time the Write and Read photons one on each side of the limit between two software-defined 1500 ns Write-Read cycles (as in figure (9.4)), we can also do conditional adjustments of the software behaviour: the reading of the Detection setup is taken into account only during Read pulses preceded by a successful Write trial. This can save a large amount of disk space when saving analog homodyne detection data, and it also allows for monitoring in real time of quantities like the conditional retrieval efficiency.

9.2 Finding the optimum parameter range

9.2.1 Cavity resonance conditions

For the protocol to be efficient, the cavity must be resonant for both the Write and Read photons. For given Write and Read frequencies, there is only one reachable cavity length that can satisfy the double resonance condition: the two photons being separated by roughly 6.8 GHz, the wavelength of the beatnote between the two is ∼4.4 cm, so that when the cavity (with length ∼6.6 cm) is properly adjusted they can only resonate in modes that are 3 free spectral ranges (FSR) apart. The optimal position for the MOT is thus at 1/3 of the cavity length, as the two standing waves are in phase at this position.

Large-scale tuning of the cavity length using the external screws being unpractical, it is done once and for all based on rough estimates and sets the value of the FSR to ∼ 2300 MHz (the length can still be finely tuned in a range of ∼10 λ's afterward with the piezos). The Write photon must have a frequency corresponding to one of the cavity modes ν_0. On the Read transition, when the photon is emitted, the cloud contributes with its cooperativity to the effective cavity resonance frequency, that has to match the photon's one. The Read photon's frequency must therefore match $\nu_0 - 3FSR + \frac{2C}{\Delta'}\kappa$. Consequently, taking into account the bare 6.835 GHz hyperfine splitting, the Read beam detuning must satisfy a precise relation, that we experimentally checked to be: $\gamma(\Delta - \Delta') = 64\text{MHz} - \frac{2C}{\Delta'}\kappa$.

The cavity length, the Write and Read frequencies, and the cooperativity therefore have to be chosen consistently. Once this is done there is no degree of freedom left to adjust for example the resonance of the optical pumping beam in the cavity. To be efficient it should be close to atomic resonance, which means $\Delta'\gamma - \frac{2C}{\Delta'}\kappa$ away from the cavity resonance. An experimental compromise must therefore be found, as discussed in the next section.

9.2.2 Detunings and powers

In the theoretical protocol, very few constraints are put on the detunings and only slightly more on the powers of the Write or Read beams. The optimum settings depend on the cooperativity in particular. The parameters to be used were initially estimated using simulations and assuming a cooperativity of 50, but the subsequent experimental optimization lead to the readjustment of many parameters (see section 9.2.3).

Write parameters

First, a combination of Write power and detuning was determined, based on the following considerations: knowing the repetition rate of the Write pulses in a measurement window (one every 1500 ns), the Write photon detection rate on the Trigger SPCM must be much higher than the background countrate, which fixes a minimum reasonable probability of producing a Write photon per pulse. The aim was fixed at having on average around one Write photon detected per millisecond window of Write trials (corresponding to an effective average countrate around the kHz level). This low probability of trigger per pulse (∼ 1/666) ensures automatically that multiple excitations contributing to degradation of the single photon produced are very unlikely.

At the same time, one should avoid depumping too much the cloud with the failed Write trials, so that the number of atoms having scattered photons in free space during a full 1 ms window should remain small compared to the total number of atoms in the cavity mode. Numerical simulations were carried out, using the previously established models for

the Write step and an approximate Write temporal envelope, to look for a regime where these two criteria are satisfied.

Finally the settings used are a Write detuning Δ of 28 MHz, and a peak single-atom Rabi frequency of order $\gamma\Omega^W/2\pi \approx 260$ kHz at the optimum.

Read parameters

To determine the appropriate settings of the Read pulses, the result of simulations in presence of defects was also taken into account, in particular polarization misalignment of the Write and Read beams. This defect was not described here in the theoretical model because it is not estimated as one of the main sources of inefficiencies in our case, but it has the specific effect of degrading the efficiency when one goes close to resonance with the Read beam, so this should be avoided.

On the other hand, as described in the section 9.2.1, for a given cooperativity the Read frequency is fixed by the cavity resonance frequency and the Write detuning. In practice it means that when changing the cooperativity to optimize the efficiency, the Read frequency must be readjusted accordingly, while making sure not to go too close to resonance.

In optimum conditions, the detuning Δ' is of -45 MHz, which works with a cooperativity $C \approx 7.5$, and the peak Read Rabi frequency is $\gamma\Omega^R/2\pi \approx 34$ MHz.

Optical pumping parameters

The optical pumping is kept close to atomic resonance (7 MHz red-detuned), which makes it around 30 MHz $\approx 3\kappa$ detuned from the closest cavity resonance. Its power has to be adjusted to compensate for this, and is experimentally optimized to 3 μW. It was tested by measurements similar to what is explained in figure (9.3), as well as by measuring the cooperativity of the optically pumped cloud with two probes of opposite circular polarization, and maximizing the ratio of C seen by σ^+ light to C seen by σ^-. The optical pumping efficiency estimated from this is ~ 92 %.

9.2.3 Practical parameter range optimization

Without a complete model of the various dependences of the retrieval efficiency, it is tempting to go to relatively high cooperativity ($C \sim 50$) to maximize it. However for higher cooperativities, the cloud size grows and one also needs a higher Read power for efficient extraction, so that the Read inhomogeneous light shifts spoil the efficiency (this is a balance between the two efficiency terms P_C and P_{Read} of equation (8.46)). Taking into account the experimental parameters of the Read beam (size, detuning, power), one can plot the expected efficiency dependence on the cooperativity, to find that it has an optimal plateau around 10, as shown in figure (9.6).

Iteratively optimizing the retrieval efficiency therefore lead us to decrease the cooperativity to reach an optimum around 7-8, while each time having to readjust the Read frequency to match the cavity resonance condition on the Read transition. At each iteration the Read power was progressively increased until reaching the plateau of efficiency. The experimental efficiency variations with the Read power are presented in details in section 9.5.3.

The cavity was also translated along its axis, to optimize the MOT position with respect to the point of phase synchronization of the Write and Read photons' modes are. Finally, as it seemed that in the best configuration the inhomogeneity of the Read beam was still one of the limiting factors, its size was increased to improve the efficiency.

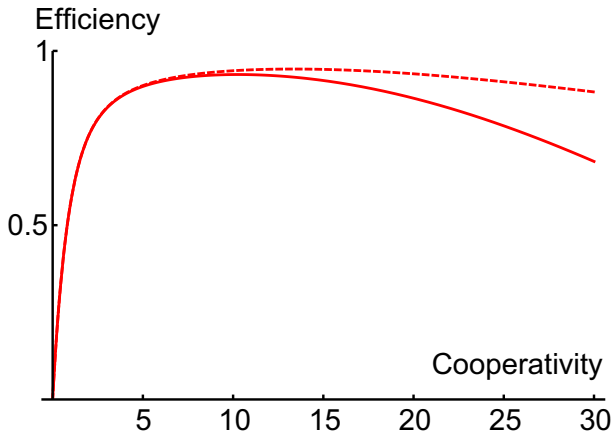

Figure 9.6: Cooperativity dependence of the efficiency. Terms $P_C * P_{Read}$ of section 8.4.6 using the experimental parameters (with an effective homogeneity ratio at $C = 8$ of $R_c/w_b = 1/8$ in both directions) and taking into account the first-order variation of the cloud size with the cooperativity (this in practice only affects the homogeneity along the cavity axis z, so we take an approximate scaling $(R_c/w_b)^2 \propto C$). Dashed line: efficiency for the same parameters but perfectly homogeneous Read beam. For too large difference between the two the estimation of the inhomogeneity effect is anyway not valid anymore, but the qualitative effect of optimum is visible.

The overall relevant parameters of the experiment used in standard configuration are summarized in table (9.1).

Optical pumping power and detuning	3 μW at -7 MHz
Optical pumping pulse shape	Square pulse of 100 μs
Write Rabi frequency and detuning	260 kHz at +28 MHz
Write pulse shape	Gaussian of 1/e half width 80 ns
Write beam waists	325 μm x 3.1 mm
Read Rabi frequency and detuning	34 MHz at -45 MHz
Read pulse shape	Gaussian of 1/e half width 80 ns
Read beam waists	325 μm x 3.1 mm, then x2
Write-Read peak to peak pulse delay	250 ns
Number of Write-Read trials in 1 ms	666
Write success in 1 ms	≈ 1
Cooperativity	7-8

Table 9.1: Summary of the parameters in the default optimized configuration.

9.3 Photon-counting and correlation measurements

Light extracted from the atoms during the Read pulse is first sent to the SPCM-based part of the detection setup for pure photon-counting characterization. The experiment is exactly similar to what was done in [21] (apart from the incidence angles of the Write and Read beams), and its principle is summarized in a schematic way in figure (9.7).

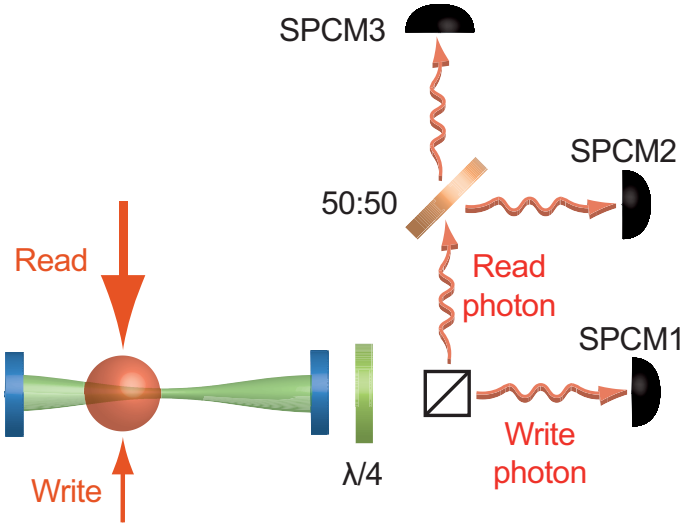

Figure 9.7: Simplified scheme of the experiment in the photon-counting regime.

9.3.1 Experiment and retrieval efficiency

Using the conditional software gates on the Trigger and Detection counters, only the useful data (located in the selected 300 ns window, and heralded by a Write success) are saved, in the form of timestamps at which a pulse produced by each counter is detected, with a resolution of 10 ns.

In this functioning mode, the conditional retrieval efficiency is measured directly by the ratio of the total number of clicks of the Detection SPCMs $n_{2\cup3} = n_2 + n_3$ to the number of clicks of the Trigger counter n_1 (assuming we never produce more than one photon at once). This quantity can easily be calculated in real time on a reasonable number of running samples and is displayed by the software while the experimental sequence is running, which allows for on-the-run optimization of some parameters (powers and orientations of the Write and Read beams, cavity length).

The low transmission of the trigger path, estimated to ≈ 27 % is not so much of a problem as long as it does not bring the number of successful events detected down to the background noise level of the counter: it mostly reduces the rate at which the state is prepared and at which we can accumulate data to characterize it. However the total losses in the Detection path (including SPCM efficiency) are of course directly reflected on the measured conditional efficiency. The typical working regime corresponds to the following numbers: during one full experimental cycle (7*666 Write trials), the number of triggers detected without Write beam is around 0.1-0.2, while the Write pulses produce a total of $\sim$ 7-8 Write photons detected, and $\sim$ 2 photons in total are detected in the conditioned gated windows of the Detection counters, corresponding to a raw retrieval efficiency of $\approx 30\%$.

Taking into account the total detection probability of a photon in the Detection arm once it has left the cavity of $37.5 \pm 2\%$ (optical transmission from cavity to counters 72%, coupling into the SPCMs' fibers 80% and detection efficiency of 65%), we measure light extraction efficiency from the cavity up to $79 \pm 3\%$.

In order to reach such high efficiency at the optimum, the data are sorted out: the first 10 s of acquisition on each run are not considered because the MOT takes time to settle to

its quasi-steady state loading, and we systematically discard data acquired during the first 1ms measurement window of each cycle as these were consistently giving lower efficiency, whatever the settings (this is attributed to charges accumulating on the Trigger SPCM during the preparation steps that are readout the first time the counter is switched on and leads to increased uncorrelated Write clicks).

The background countrate of the Trigger SPCM leads to a certain amount of false triggers, decreasing the conditional efficiency. This correction is of the order of 2% and is impossible to isolate from the functioning of the photon source itself for further applications, so we do not correct for it. Background on the Detection counters is negligible once we take into account only the heralded and gated clicks.

9.3.2 Histogram reconstruction

As the Write and Read pulses are temporally wider than the 10ns resolution of the photon-counting setup, this system can be used to get information on the modes of the Raman photons: plotting histograms of the arrival times inside a 1500 ns Write-Read cycle, one obtains a direct picture of the temporal intensity profile of the photon's wavepacket.

The results, superimposed with the temporal shapes of the Write and Read pulses themselves, are shown in figure (9.8).

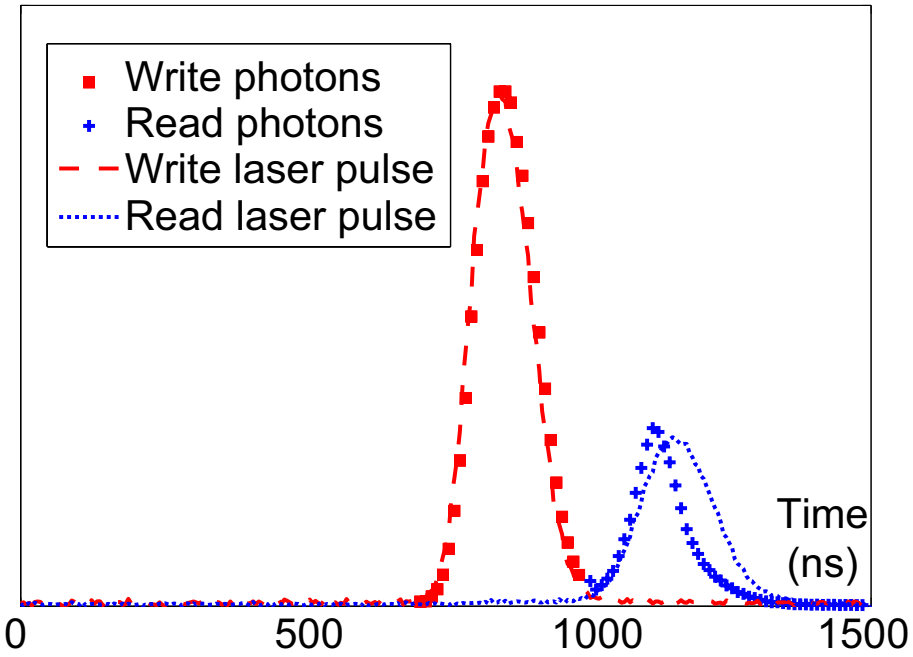

Figure 9.8: Histograms of arrival times for the Write and Read photons, superimposed with the Write and Read pulse profiles.

The consistency of this measurement can clearly be seen on the Write pulse/Write photon couple: the two profiles are identical within experimental precision, which is what is expected for a very weakly driven process like the Write one (the excitation probability is proportional to the driving intensity in the lowest order).

On the Read profile, it is interestingly not the case anymore. Being a high-efficiency process, this is expected, and was also predicted in [129]. Note that the linearity of the emission rates (equations (8.15) and (8.16)) with the Read power does not imply the

linearity of the excitation retrieval probability, because the system's behaviour is given by equations like (8.18). The shape of the Read photon's intensity profile can be qualitatively explained from this simple form, as shown by the comparison in figure (9.9).

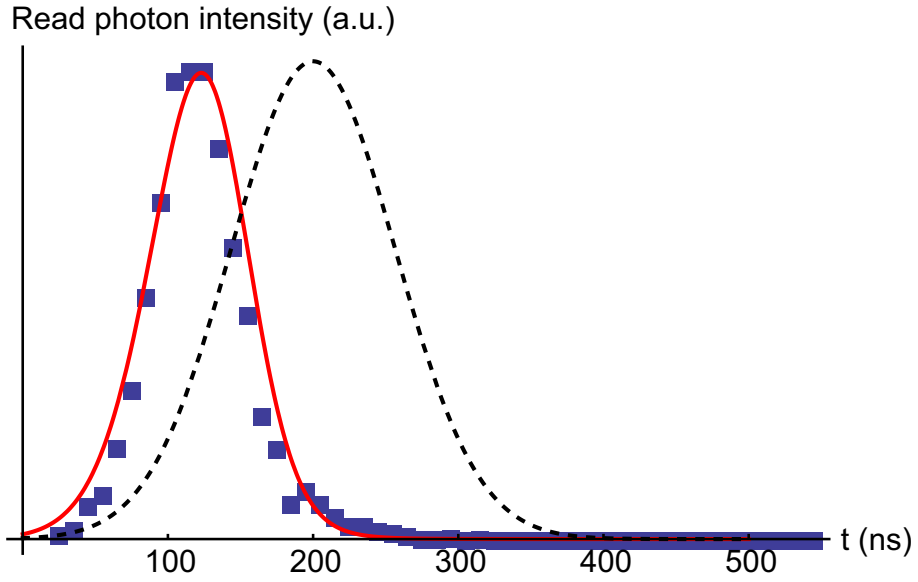

Figure 9.9: Histogram of arrival times of the Read photons (blue squares), superimposed with the form $\Gamma_{cav}(t)e^{-\int^t \xi\Gamma_{cav}(t')dt'}$ for approximate experimental parameters (solid red) and corresponding Read pulse profile (dashed black).

In optimized conditions, the Read photons histogram is approximately Gaussian-shaped with a $1/e$ half width of 40 ns.

9.3.3 Autocorrelation/antibunching measurement

In order to probe the single-photon nature of the light pulses emitted by the cloud during the Read process with the counters, intensity correlations measurements are then performed.

The $g^{(2)}$ function of the pulse's quantum state is a simple indicator of the nature of its photon number distribution, revealing interesting effects like photon bunching ($g^{(2)} > 1$) or antibunching ($g^{(2)} < 1$), and taking the distinctive value of 1 for classical light. It also has the interesting property that it is theoretically insensitive to linear losses introduced on the quantum state in the Detection arm.

In general the $g^{(2)}$ of the emitted quantum state would be measured by the quantity $\frac{\langle \hat{N}_2 \hat{N}_3 \rangle}{\langle \hat{N}_2 \rangle \langle \hat{N}_3 \rangle}$, where the $\hat{N}_i$ are the photon-number operators in the modes before counters 2 and 3, whose measured value can be larger than 1. To measure the $g^{(2)}$ the detectors should therefore be able to evaluate these operators, but in reality the SPCMs can only distinguish between "zero" and "one or more" photons. The double SPCM setup would thus be measuring the $g^{(2)}$ only in the limit case of large detection losses where there are never two or more photons hitting the same counter simultaneously, so that the SPCMs tend to behave as number-resolving detectors [138].

For not too low detection efficiency, as is the experimental case, what is measured is the normalized double click probability $\frac{p(2\cap 3|1)}{p(2|1)p(3|1)}$, by counting among the n_1 Write-heralded

cycles the number of clicks on each counter n_2 and n_3, the number of events where both fire in the same pulse $n_{2\cap3}$, and calculating $\frac{n_{2\cap3}n_1}{n_2n_3}$. This quantity is different from the $g^{(2)}$ but has similar properties (it goes to 0 for a single photon, and to 1 for uncorrelated light).

To be able to compare the pair probability inside one single heralded pulse to the expected decorrelation of photons in separated pulses, a circular permutation of the timestamps of counter 3 with respect to counter 2 is performed to measure the equivalent of a "non-zero time" $g^{(2)}$. The argument of the correlation function however here is not really a time but rather a number of successful Write events, as explained in more details in figure (9.10).

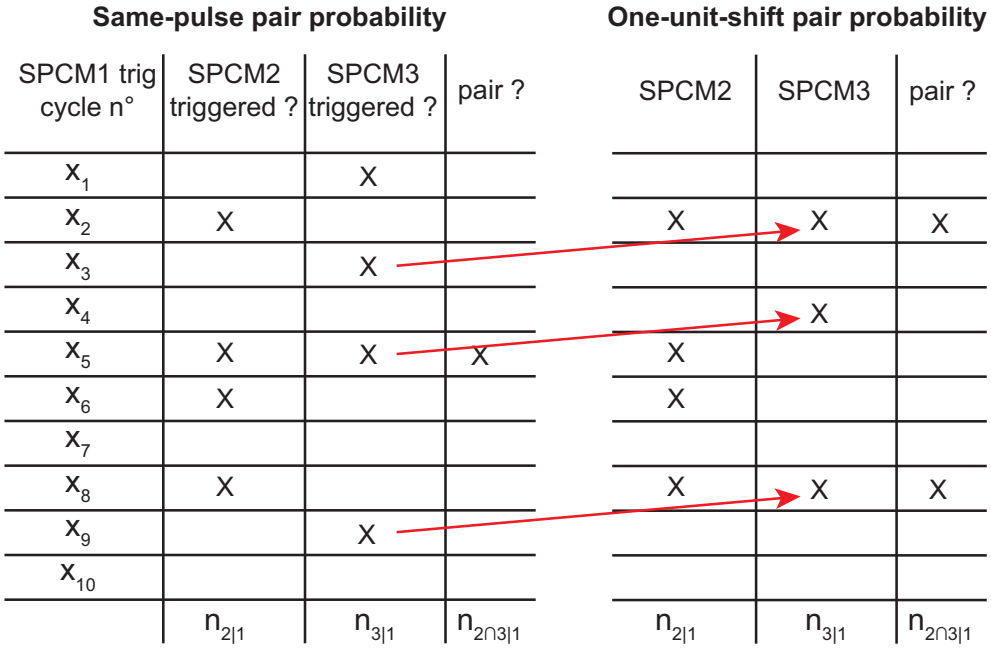

Figure 9.10: Definition of the normalized pair probability for events in arbitrary pulses. The $\{x_i\}$ are the randomly distributed indices of the Write-Read cycles in which a Write photon was detected. By shifting the list of 3-1 coincidence markers with respect to the 2-1 coincidences, we look for correlations between SPCMs 2 and 3 in completely distinct pulses.

The results for the normalized pair detection probability, calculated from an ensemble of ≈ 30000 Write trigger events, shown in figure (9.11), show clearly that it is very close to zero (0.04 ± 0.01) when counting photons within a single pulse. This therefore proves that what is detected when the Write and Read are successful is far below the classical pair-to-single proportion of photons. The characterized quantity also goes to 1 as expected for uncorrelated events. The remaining 0.04 measured in a single pulse can be explained by the small but non-negligible two-photon component remaining in the state, plus small contributions from technical noise leading to uncorrelated clicks, and low statistics in the counting of these rare coincidences.

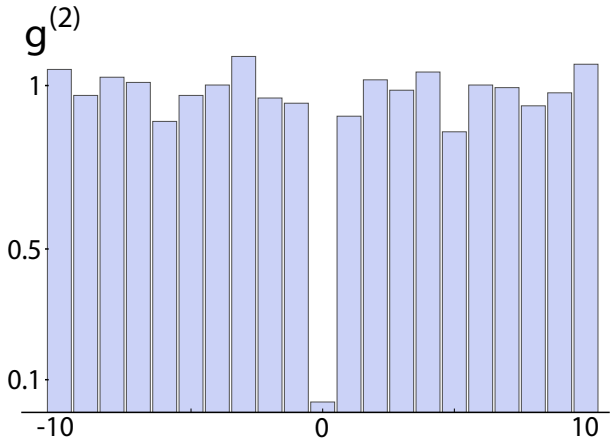

Figure 9.11: Normalized pair detection probability as a function of the pulses separation, in number of successful Write step.

9.4 Homodyne detection of the quantum state retrieved from the ensemble

From photon-counting measurements, one can get an idea of the Read photon's temporal mode but only in intensity, so that it is insensitive to the field's possible phase drifts within the pulse. Simultaneously, the $g^{(2)}$ gives information about one global characteristic of the photon number distribution, but it does not depend on the amount of losses between the cavity and the detectors. We will show here how homodyne detection gives access to the exact spatio-temporal mode and full quantum state of the light emitted, direct probe of how useful it could be for realistic QIP.

	Photon counting	Homodyne detection
Efficiency estimation	ratio of counts	single photon component
Temporal mode	intensity envelope	full temporal mode
Frequency/phase sensitivity	none	total
Spatial mode sensitivity	partial (fiber)	total
Info about quantum state	photon distribution $g^{(2)}$	full density matrix
Detection efficiency sensitivity	partial (none on $g^{(2)}$)	direct effect

Table 9.2: Compared characteristics (type of information and sensitivities) of homodyne detection versus correlation measurements with photon counters.

9.4.1 Homodyne detection in practice

For practical homodyne detection implementation, the Local Oscillator's intensity must be large enough (at least around 5 mW in our case) for the signal's quadrature noise amplified by the LO field to be much larger than the detector's purely electronic noise (typically 20 dB above). The use of this bright beam (compared to single photons) that must be finely controlled (in frequency, mode, dynamic power balance ...) gives rise to a number of experimental challenges. The solutions used in the present experiment are summarized here.

The two halves of the LO beam are sent on the detector's photodiodes by concave mirrors, at an angle with the surfaces ($\sim 30°$) to limit back reflections. The polarization-dependent transmission of the glass windows before the photodiodes ($\sim 2\%$ total modulation amplitude) allows for fine balancing to 0 of the detector's DC level (with a half-wave plate placed in one of the arms). In order to properly measure the signal's quadratures, the detector's spectral response must be balanced over the whole useful frequency range (100 MHz here). The photodiodes are placed away from the beamwaists (of typical size 50μm) to be reasonably well covered by the beams. As different spot sizes on the two photodiodes lead to asymmetric dynamical response, the precise position of the detector is then adjusted while looking at the spectrum to minimize parasitic high frequency components. In our case, a small amplitude modulation of the LO by its dedicated AOM leads to a peak at the AOM's frequency when the dynamical balance is off. See figure (9.12) for the noise spectrum of the detector.

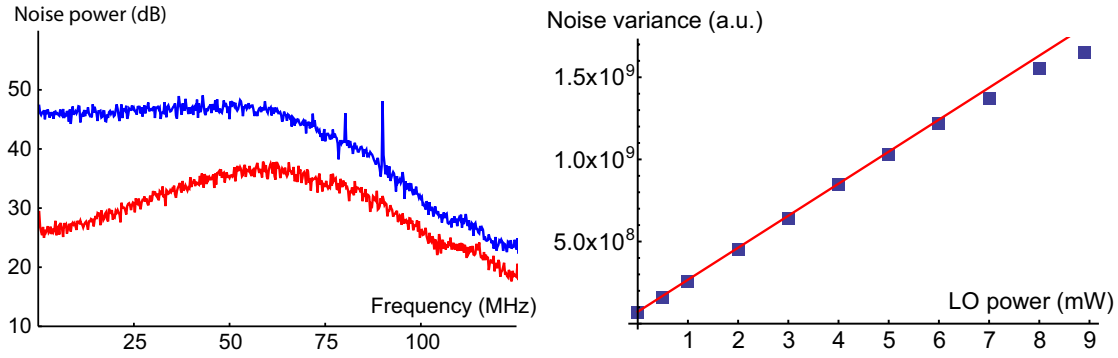

Figure 9.12: Left: noise spectrum of the homodyne detector's signal without LO (red) and with 7 mW of LO (blue) in a balanced configuration. Right: integrated noise (0 to 80 MHz) as a function of the LO power. In normal regime the noise variance is proportional to the LO power, as shown by the fit. For 7 mW, the integrated vacuum noise created by the LO is ~ 15 dB above the electronic noise.

Filtering of LO light in the Trigger path

For reasons explained in the next section, this experiment uses a continuous LO to record data. However, during periods where the Trigger counter is working, even a microwatt of LO initially produces enough backreflections on the optics and the detector to cover completely the signal at the level of SPCM1. The filtering of these LO photons unavoidably leads to losses, which implies it should be implemented on the Trigger path rather than on the Detection one (losses wash out very quickly the state's nonclassical features reconstructed from homodyne detection and should be minimized).

We tried several solutions to get around this problem, among which:

- The simplest solution was to use a Faraday isolator to block the LO light backpropagating, but it had to be set up in the Detection arm and introduced losses on the signal.
- Different trials amounting to spatially filtering the photons reaching SPCM1 (like setting up the single-mode fiber before it) did not solve the problem. The parasitic photons seen by SPCM1 are scattered by the detector's surfaces exactly in the right spatial mode.

– Switching Off the LO when it is not useful in the sequence, the dynamical response of the detector during the switch-on leads to an offset transient on the signal, so this method was abandoned.
– Spectral filtering is also a possibility. However the Write photons are separated from the LO ones only by the $\sim$ 6.8 GHz of the fundamental hyperfine splitting. Selective absorption by a vapor cell of hot Rb atoms optically pumped into $5S_{1/2}, F = 2$ could in principle be a solution [139, 140]. The quality of those we could test at that time did not allow us to reach good enough filtering.

Finally, a simple custom Fabry-Pérot cavity was designed, as sketched on figure (9.13): it is made of two HR mirrors (R$\sim$99.9 %) mounted in a Thorlabs 1" tube, separated by a steel spacer and a rubber joint on which one mirror is pressed by a tubular piezo element. The spacers give the cavity a length $\approx$ 1.1 cm, so that its free spectral range is approximately 2*6.8 GHz . Its linewidth (FWHM) is 6.8 MHz, allowing for optimum selectivity among the Write (transmission 76 %) and LO ($\sim 10^{-4}$) photons. It is locked using an auxiliary 810 nm beam, on resonance with the Write photons.

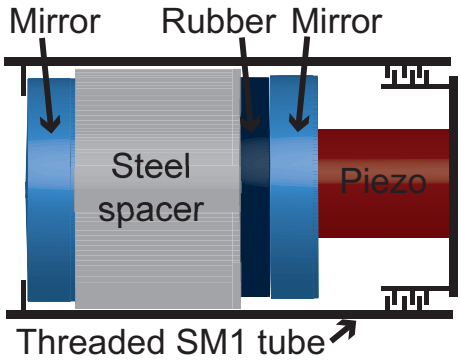

Figure 9.13: Schematic of the filter cavity. Elements shown are the two mirrors, the hollow steel spacer (1 cm thick), the circular rubber joint ($\approx$ 1 mm thick) and the hollow tubular piezo. The totality is held together in an SM1 tube from Thorlabs with a tightenable end on a threading to adjust the length.

LO-signal mode matching

Once the presence of the LO in the system is no longer a problem in itself, it remains to be matched to the signal mode as precisely as possible. As the measurement involves interferences with the LO field, the squared LO-signal overlap enters directly into the detection efficiency, as if it were pure losses (see section 2.3) [17].

In practice the LO is mode-matched on an alignment beam by adjusting mirrors and beam-shaping lenses while maximizing the contrast of their interferences, observed on a photodiode (PD4 on figure (9.2)). The alignment beam can be the "Reference" one but, being reflected on the science cavity, it is not necessarily exactly in its fundamental transverse mode. We therefore use an auxiliary beam sent from the top of the cavity, matched to the mode. The cavity is temporarily locked on its main transmission line, and acts then as a mode filter leaving only the resonant mode component at the output. Due to cavity lock noise, in order to get stable interferences of this transmitted beam with the LO, we also have to actively stabilize its intensity, by monitoring a fraction of it with the APD (see figure (9.2)).

The frequency stability of the LO with respect to the Read photon is ensured by the phase-lock between the two 795 nm lasers. The last important part of mode-matching between signal and LO is the temporal envelope, which is handled in a particular way described thereafter.

9.4.2 Data acquisition and processing system with a continuous local oscillator

In running conditions, we typically use 7 mW of continuous Local Oscillator. The data produced by the detector (analog voltage, with a time resolution of 4 ns) are continuously streamed by the fast AI card during an experiment. Only in the case of a trigger from SPCM1, an adjustable batch of datapoints (550 points, 2.2 μs long in practice), with a controllable amount of pre-trigger points, is saved to be processed later on.

The advantage of this CW LO configuration, discussed in section 2.3, is that it spares the necessity to physically shape the LO to the same temporal envelope as the signal one. The data obtained with a continuous LO are instead processed with an adjustable numerical weighting function $f(t)$ (see figure(9.14)). From each data batch with voltage $db_j(t)$, a sample of signal quadrature is calculated as $x_j = \int db_j(t) f(t) dt$. This is strictly equivalent to having done the measurement with a LO whose field varies as $f(t)$, up to a normalization.

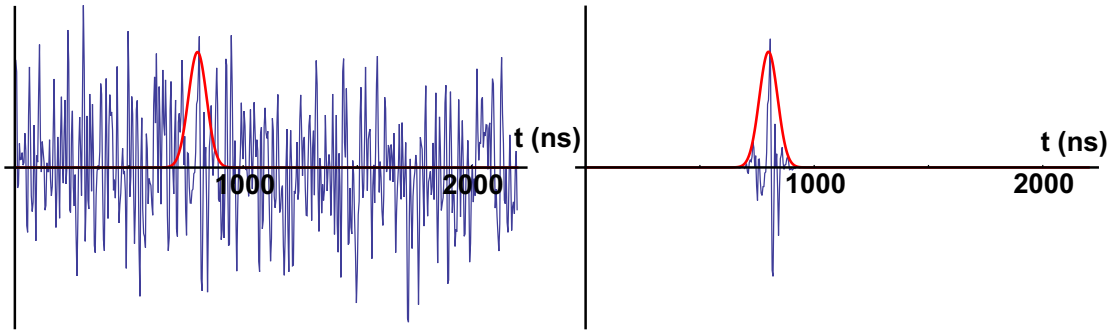

Figure 9.14: Example of homodyne signal for one 2.2 μs batch of data. A Gaussian envelope is applied to the raw signal (left) and the resulting weighted signal (right) will be integrated to give one quadrature sample.

The photon-counting experiment showed Read photon histograms that were roughly Gaussian with a $1/e$ half width of 40 ns. A Gaussian with width $\sqrt{2} * 40$ ns (for the field's width instead of the intensity) is therefore taken as an initial guess for $f(t)$, and positioned at the estimated place of the Read photon. The quantum state in this arbitrary field mode can then be reconstructed using the method described thereafter, and the position and width of the Gaussian envelope are adjusted to find the optimum of the reconstructed single-photon component (see the illustration of this in figure (9.15)).

Upon each trigger, much more data are saved than actually useful to see the Read photon. With an envelope function voluntarily shifted far away from the Read photon's position, the quadrature extraction procedure can thus be applied to all samples, characterizing a quasi-orthogonal field mode which is in principle in the vacuum state. From each acquisition, the same number of vacuum quadratures and signal ones is therefore obtained, in the same conditions. The vacuum quadrature histogram (which is Gaussian,

as shown on figure (9.16)) is then used to calculate the right normalization for all the quadratures (the vacuum variance is theoretically $\frac{1}{2}$ by definition).

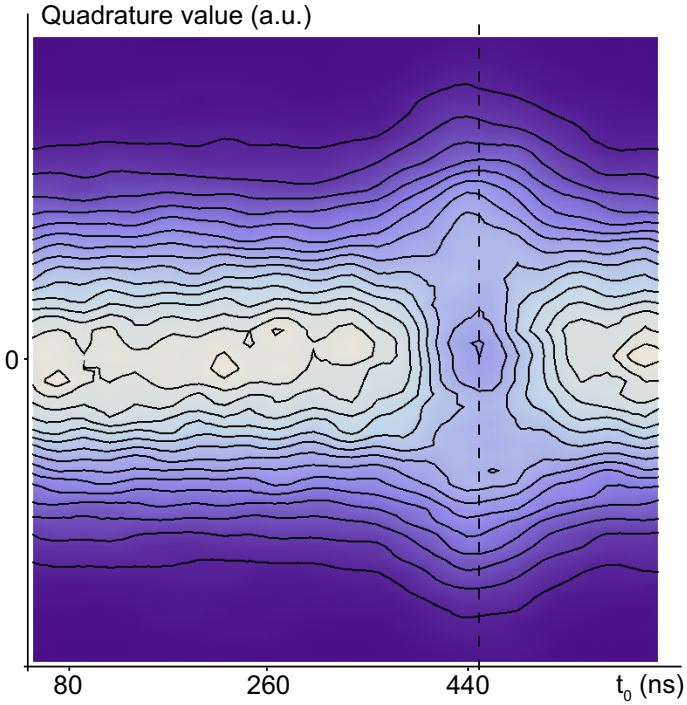

Figure 9.15: Visualization of the modification of the quadrature statistics with the time position in the acquisition. A Gaussian envelope of width $\approx \sqrt{2} * 40$ ns is applied to the datasets, centered on a variable time t_0, to extract quadratures in a mode with a variable time delay. The density of quadrature values is represented by the color scale. The dashed line represents the "right" position of the envelope: a cut of the density profile along this line would give a histogram like the second one in figure (9.16), with a dip at the center and a wider distribution. A cut along a line far away from this one would give a Gaussian vacuum histogram like the first one in figure (9.16).

With an approximate idea of the mode $f(t)$ and of the normalization, one can easily implement on-the-run calculation of the signal quadratures variance for example, on 1000 running samples, to be displayed while the sequence is running. It is easy to show that for the kind of state we expect to produce (inefficient single photon) $p\,|1\rangle\langle 1| + (1-p)\,|0\rangle\langle 0|$, the variance is $\frac{1}{2} + p$ [17], so that maximizing its value is a good first-order guide to realize real-time optimization of parameters such as the LO frequency. This is true only once a reasonable parameter range is reached at least (no multiple excitations in particular).

9.4.3 Density matrix and Wigner function reconstruction

In order to reconstruct an arbitrary state, one theoretically needs to sample its quadrature histograms for several known values of the relative signal-LO phase. Here, a single photon is expected to be produced, or a statistical mixture of Fock states (produced by incoherent loss of the photon due to optics' transmission, or by occasional multiple excitations). These have phase-insensitive Wigner functions, or equivalently diagonal density matrices in Fock space. The important assumption is thus made from the start that the state to reconstruct is diagonal or phase-invariant. This makes the reconstruction proce-

dure faster and easier, and allows us experimentally not to control at all the relative optical phase, which is simply left to fluctuate freely (its fluctuations are mechanical/thermal ones, much slower than the duration of our photon pulse).

From the measurements, after having done the same selection as in the photon-counting experiment (dropping the first 10s of a run, and the first 1ms of each cycle), one single quadrature histogram is therefore obtained for the signal, and one for the vacuum. Once correctly normalized, an example of results is shown in figure (9.16).

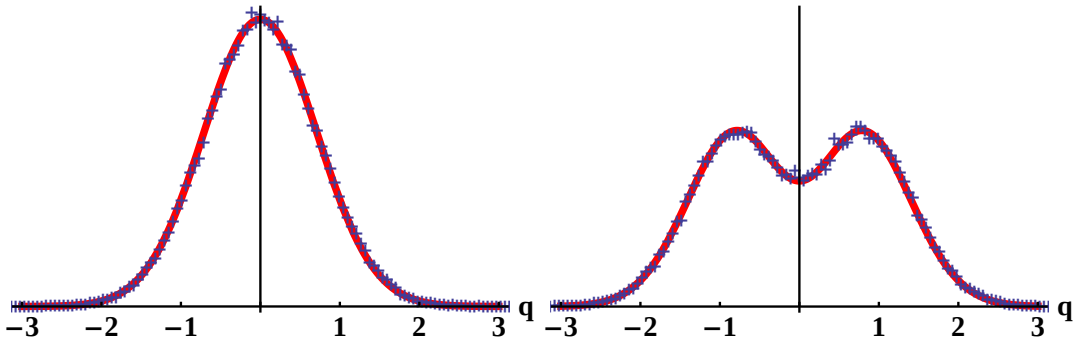

Figure 9.16: Quadrature histograms of the vacuum state and of our signal state. The histogram is fitted by a Gaussian for the vacuum, and by the combination of Hermite-Gauss functions corresponding to state $p\,|1\rangle\langle 1| + (1-p)\,|0\rangle\langle 0|$ for the signal.

From the signal histogram, a Maximum Likelihood algorithm iteratively converges to the density matrix in truncated Fock basis that is the most likely to be at the origin of the observed quadratures [17]. With the phase-invariance assumption, it takes a relatively simple form. The state at step i is described by its diagonal elements $\rho_n^{(i)} = \langle n|\,\hat{\rho}^{(i)}\,|n\rangle$. Starting from any initial diagonal density matrix, these elements are given by the following iterative formula, depending on the value of the measured quadratures $\{q_k\}$:

$$\rho_n^{(i)} = \frac{1}{N_q}\rho_n^{(i-1)} \sum_k \frac{|\langle q_k|n\rangle|^2}{\sum_m |\langle q_k|m\rangle|^2\, \rho_m^{(i-1)}} \tag{9.1}$$

where N_q is the total number of quadratures measured, and $\langle q_k|n\rangle$ is the wave function of Fock state $|n\rangle$ at the point of the measured q_k.

This procedure offers the possibility to correct the state for detection losses [17]. For that, one simply uses as a basis for the iteration decomposition the states $|n\rangle$ processed through a loss channel with transmission t: in the algorithm, $\langle q_k|n\rangle \to \langle q_k|\Psi_n\rangle = \sum_m \binom{n}{m} t^m (1-t)^{n-m}\,\langle q_k|n\rangle$. This allows for correction of the transmission losses between the cavity and the detector (82 ± 1 %), the mode-matching efficiency ($(96.5 \pm 1\ \%)^2$), and the efficiency of the photodiodes (91 %). One can also, as described in [141], correct for the $\approx 1\%$ contribution of the electronic noise in the measured quadrature histograms.

The algorithm converges on what can be considered as the best estimate for the diagonal elements of the state's density matrix, when it comes out of the cavity. As will be shown in the following section, the reconstructed state is with very good approximation composed of only zero-photon and one-photon components.

In this context, due to the state reconstruction method and hypotheses used, when a state $\approx p\,|1\rangle\langle 1| + (1-p)\,|0\rangle\langle 0|$ is reconstructed, it could in reality be, in the worst case, a coherent $\sqrt{p}\,|1\rangle + \sqrt{1-p}\,|0\rangle$ as the phase-randomization of the state does not change the

populations. This phase-invariance hypothesis could thus only lead to underestimate the state's purity. However there is no physical reason to expect that the process could be producing such fixed-phase coherent superposition state.

9.4.4 Results

Under optimal conditions, with the settings described in table (9.1), the quantum state of the Read photon is reconstructed using a total of $\approx 10^5$ quadrature samples. The optimal Gaussian temporal mode $f(t)$ has a width ≈ 55 ns $\approx \sqrt{2}.40$ ns, in agreement with what had been estimated from the photon-counting measurements.

Depending on the exact parameters used for the reconstruction (position selected for the "vacuum" envelope, size of the truncated Fock basis etc), the state always contains a negligible amount of components for $n > 2$ photons ($< 10^{-6}$), and a variable amount of 2-photon component, always below 1% even after correction for losses.

Using uncorrected data, the one-photon component of the reconstructed density matrix is 55 ± 2 %. After correction for all losses, it reaches 80 ± 2 %. The associated Wigner functions are represented on figure (9.17).

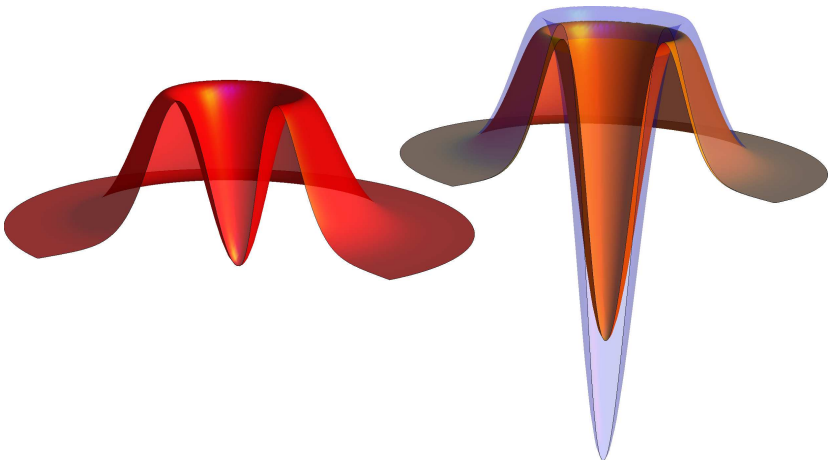

Figure 9.17: Wigner functions of the reconstructed state. Raw state without corrections in red (left), state after correction for inefficiencies in orange (right), and for comparison pure single photon in transparent blue.

Even before correcting for losses, the state exhibits a clearly negative Wigner function, proof of its non-classicality. This observation is made possible by the minimization of losses in the detection path. As this feature, measured by homodyne detection, is very sensitive to all inefficiencies, its direct observation is a clear indication of the efficiency and potential use of this state in realistic QIP.

The efficiency observed after correction for detection losses is in very good agreement with the one estimated from the counting measurements. This indicates both the consistency of the two measurements, and the fact that all photons "seen" by the counters are also characterized by homodyne detection. This observation means that the full mode of the produced photons is clean enough to be completely captured by our simple LO mode (single frequency, Gaussian envelope, simple transverse mode).

As the Write and Read pulses are unavoidably time separated by an average amount ($\approx$ 250 ns) not negligible compared to the Doppler decoherence time (= 900 ns), the efficiency can also be improved by post-selecting only the events where the Write photon

arrived in the second part of the Write pulse, thus decreasing the effective Write-Read delay. This usually gives an improvement of the order of 1 %, though it is also dividing by ~ 2 the number of quadratures and decreasing the precision.

Finally, to decrease the negative effect of the Read inhomogeneity, a x2 telescope lens configuration is added on the beam. The power in the beam must be increased accordingly, and this leads to maximum efficiencies of 82 ± 2 %. The corresponding density matrices are shown in figure (9.18).

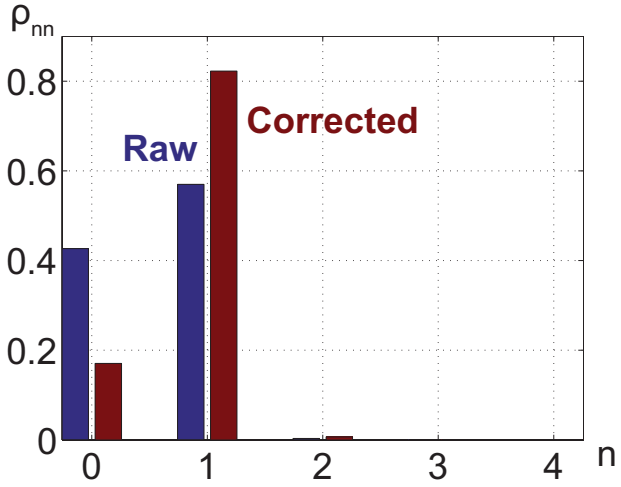

Figure 9.18: Reconstructed density matrix in the best configuration achieved. Raw state in blue with $\rho_{11} \approx 57\%$, and corrected state with $\rho_{11} \approx 82\%$.

9.5 Efficiency dependences

9.5.1 Maximum observed efficiency and interpretation

Altogether, we observed efficiencies of retrieval of the Read photon at the cavity output up to 80 ± 2 % (in standard configuration, before doubling the Read size). This value can be explained by taking into account the various terms of section 8.4.6 with the values of the experimental parameters.

Even with the Write and Read pulses as close as possible to each other, the best achievable is to have a ≈ 250 ns delay between their two maxima. With this as the average delay during which the excitation can decohere, $P_{Doppler} \approx 0.96$. For the estimated values of all other parameters, the other contributions are $P_C \approx 0.94$, $P_{Read} \approx 0.98$, $P_{pump} \approx 0.96$ (with $\epsilon_1 = \frac{3}{2\sqrt{2}}$, $\epsilon_2 = \frac{1}{\sqrt{2}}$ and $p = 0.92$). For $R_c = 350\mu$m and the beam sizes given previously, estimating that we can not be more precise when setting the MOT at the position where the two photons' modes are in phase ($z_0 = 0$) than 0.5 mm, the mode overlap is $P_{mode} \approx 0.99$.

The total comes to 0.84. The maximum achieved efficiency is therefore well understood, and if additional small effects are taken into account, like the cavity jittering around the Read photon resonance, which decreases further by 1 or 2 % the average efficiency, the combination of all these small inefficiencies can definitely explain what is observed.

In order to show better where the experimental parameters are located with respect

to the maximum efficiency along different directions in parameter space, the theoretical expressions of various pieces of the efficiency are plotted around the experimental range in figure (9.19).

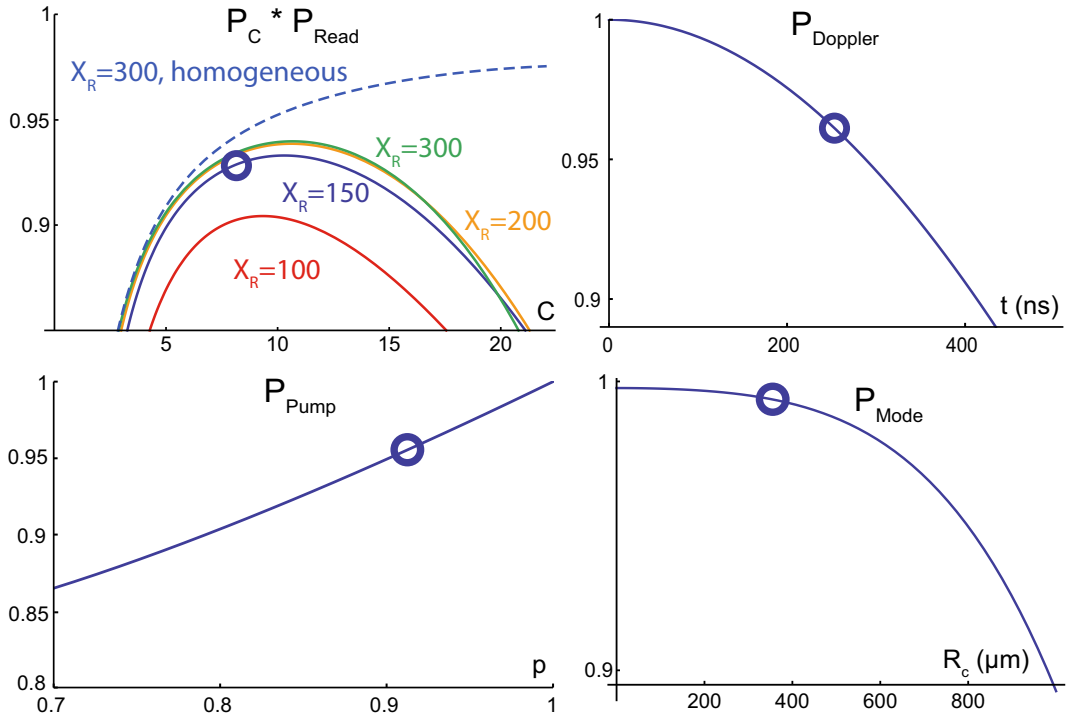

Figure 9.19: Estimated efficiency dependences around the working conditions. Upper left: term containing the effect of the cooperativity, the Read power and inhomogeneity. The different solid cures are plotted in similar conditions as before, for different integrated Read powers X_R around the experimental one ($X_R \approx 150$), and the totally homogeneous case for high Read power is given for reference (dashed line). **Upper right:** Doppler term as a function of the Write-Read delay (the experimental value between the maxima of the pulses is 250 ns). **Lower left:** optical pumping efficiency with $\epsilon_1 = \frac{3}{2\sqrt{2}}$, $\epsilon_2 = \frac{1}{\sqrt{2}}$. **Lower right:** mode amplitude and phase matching term, assuming $a_{Wy} = a_{Ry} \approx 0.25$, $a_{Wz} = a_{Rz} = R_c/(3.1\text{ mm})$ and neglecting $w^2/2$ before $2R_c^2$ in the interesting region, plotted as a function of R_c for $z_0 = 0$. All notations are defined in section 8.4.6. On all graphs the circle indicates the approximate parameters of the experiment.

The conclusion is that the total efficiency is limited by a collection of several relatively small effects. Among them the most meaningful are the cooperativity/Read parameters issue, the optical pumping efficiency and the Doppler decoherence. The last two could theoretically be made arbitrarily close to 1, but this is hard to achieve experimentally, as it requires improving on an already relatively good pumping efficiency, or using pulses closer to each other to limit decoherence. In the present case, when moved closer the two pulses would start overlapping which would lead to technical issues. Making them much shorter could on the other hand lead to distortions in the phase profile of the retrieved pulse as predicted by the theory. Another possibility would be to increase the coherence time by using colder atoms (but the gain would be marginal unless the temperature is decreased a lot), or a completely different cavity and excitation geometry to get closer to the Doppler-free case (our experimental configuration, with the Write and Read at 90°

from the cavity is actually the worst in that respect). As for the first term, one sees that by adjusting only slightly the parameters around our experimental configuration (Read power and size, cooperativity), we could probably win 1-2 %. Theoretically, making the Read beam really much more homogeneous and readjusting the Read power and cooperativity, one could in principle go from $P_C * P_{Read} \approx 0.92 - 0.93$ to ≈ 1, but this would require very large laser powers in the Read beam and large cooperativities.

9.5.2 Doppler decoherence

The stored excitation's lifetime can then easily be investigated: on figure (9.20), the single-photon component reconstructed via homodyne tomography is plotted versus the time delay between the maxima of the Write and Read pulses. The efficiency is clearly following the $e^{-t^2/2\tau_D^2}$ expected, with $\tau_D \approx 900$ ns, corresponding to the Doppler time for rubidium at 50 μK.

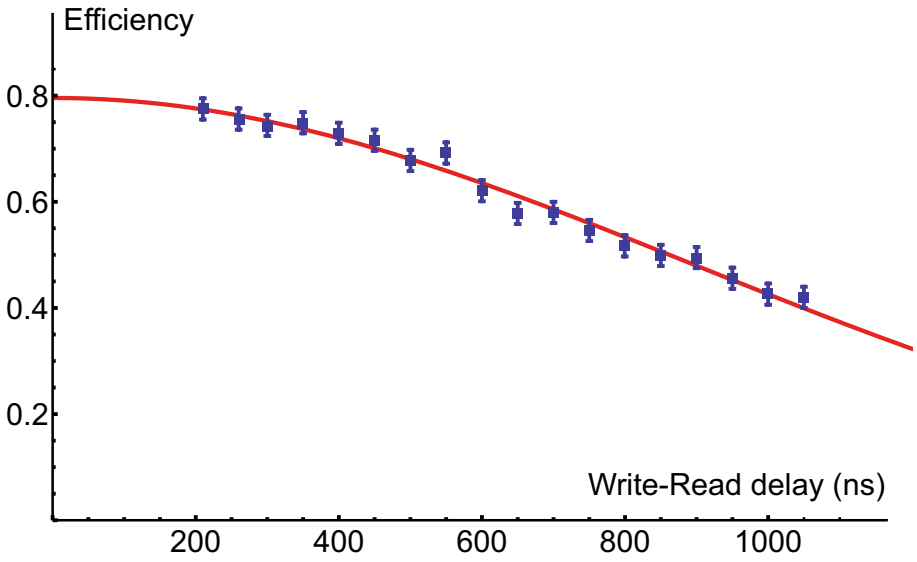

Figure 9.20: Delay dependence of the retrieval efficiency, showing the expected Gaussian Doppler decay.

9.5.3 Other dependences

Systematic studies of the efficiency variations with the cooperativity or the Read beam's size for example were not carried out, but the few discrete experimental observations are in qualitative agreement with the previous models of the efficiency limits. The relative flatness of the efficiency with cooperativity, optimum around 10, and the decrease observed for higher values of C, are consistent with the effect of Read inhomogeneities. The ≈ 2 % improvement obtained by multiplying by 2 the Read size and increasing the Read power is also well reproduced by the model.

Around the optimum parameter settings, the variations of the efficiency with the Read power are presented on figure (9.21), together with the prediction of the model given the experimental parameters. The agreement is good, indicating again that the mechanisms behind these results are understood.

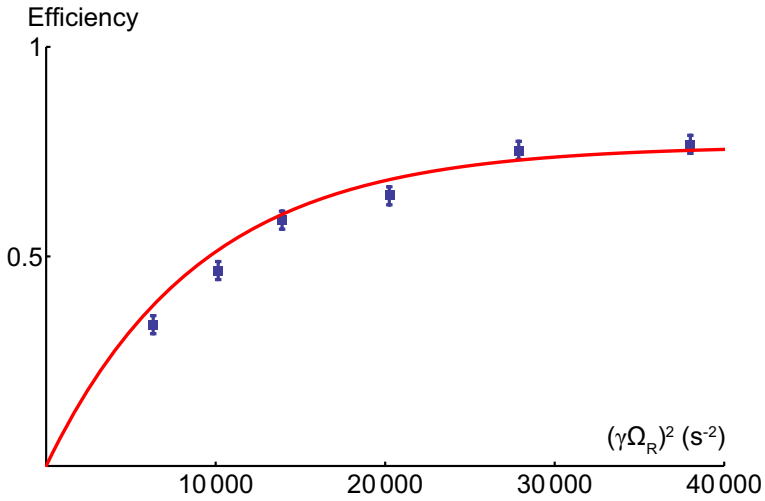

Figure 9.21: Read power dependence of the retrieval efficiency, superimposed with the result of the complete model using experimental parameters.

Finally, the experiments were intentionally carried out in a regime of low probability for multiple excitations, but by increasing the Write power several excitations can be stored in the cloud. This is characterized by the normalized double-click probability: when the usual value of the Write power is multiplied by 5, and again by 3, the number of Write photons detected approximately follows these factors, and the coincidence probability in the correlation measurement increases, indicating that more excitations are created in the cloud with each Write pulse.

Write power	Coincidence probability
x1	0.04
x5	0.2
x15	0.75

Table 9.3: Evolution of the pair detection probability with excitation power.

These results can be compared to the value of the normalized coincidence probability as calculated from the density matrix reconstructed via homodyne measurements in the same conditions, showing qualitative agreement. However, the reconstruction of this quantity from the density matrix requires a very good precision on the small 2-photon component in the reconstructed state, which is achievable only with very large amounts of data. Also, as the detection efficiency is not so small, the value of this quantity in our setup still depends on the exact losses, which are different in the SPCMs path or the Homodyne detector path.

Conclusion

These experimental results show that collective phase-matched excitations stored in an atomic cloud can, in the right conditions, be extracted as photons both with high efficiency and good control on their degrees of freedom. The fact that the retrieved photons interfere efficiently with the effective Local Oscillator which has a single Gaussian spatial mode, a coherent Gaussian temporal envelope (longer than cavity or atomic decay timescales), and purely linear phase variations with time, makes them very likely to be readily usable for any further processing or coupling to another system.

As compared to the closest comparable experimental results in [127], the present practical implementation of the protocol benefits from different features: using pulsed rather than continuous excitation allows us to separate clearly the Write and Read photon and gain some control over the retrieved temporal mode. The delay dependence of the efficiency (or storage time of the memory) can also be measured. The Zeeman-pumped scheme allows for a better control of the detunings and coupling coefficients, as well as easier separation of the Write and Read photons by their polarization. In terms of pure performances, this experiment demonstrates higher uncorrected single-photon production efficiency, as well as better single-photon quality ($g^{(2)}$), although this goes with a lower production rate. In [21], on a very similar setup, an excitation conversion efficiency of 0.84 was reported, but only after correcting for the probability that a photon in the cavity exits it through the expected port (0.175), which decreases by as much the "useful efficiency". Here, similar single-photon production efficiency is obtained without having to correct for the probability of extraction of the photon from the cavity. It therefore really corresponds to the probability of getting a photon that is readily usable in practice.

On the other hand, this experiment also demonstrates the general applicability of homodyne detection to the light states coming out of the cavity. Looking for nonlinear modifications of the quantum state of a few photons in this system, homodyne tomography should in particular allow us to reconstruct any coherent combination of Fock states that could be produced, not only single photons (on the condition that the LO-signal phase should be locked for arbitrary state reconstruction).

Part IV

Dispersive nonlinearities induced by interacting Rydberg atoms in the classical regime

Introduction

Three years ago, efficient and deterministic nonlinear effects acting at the level of a single photon had never been observed in the optical regime. The search for strong optical nonlinearities had led several research groups to investigate schemes where the target photons are coupled into an atomic cloud under EIT conditions for example (see Part I). In order to further enhance the strength of the nonlinearity, a proposed idea was to map the photons onto atomic polaritons involving highly excited Rydberg states, that exhibit dipole-dipole interactions. In particular a very interesting series of experiments was carried out during the years 2008-2011 in the group of Charles Adams in Durham, where the classical resonant susceptibility of a Rydberg-EIT medium was probed. The transparency window was modified depending on the probe intensity, corresponding to unprecedented absorptive optical nonlinearities at such a low level of intensity [142].

In this context, our group had the goal to study dispersive nonlinear effects where the photons are not lost after interaction, but which are weaker and thus harder to characterize. The presence of an optical cavity has the advantage of multiplying the effect of a small phase-shift on a light beam, and of transforming it into intensity variations on the transmitted light. However at that time, the setup did not contain yet a homodyne tomography apparatus or the full multichannel control system. Therefore, before turning to quantum state analysis on few photons coupled to the Rydberg-EIT medium, we set out with a simpler setup for an introductory step to the behaviour of this system: to characterize the classical susceptibility of the medium in a dispersive regime, at very low light level.

As it turned out, the observations did not exactly match our expectations at the beginning, but we surely learnt a lot about what can (and can not) be done in this system. This proved very valuable when trying to combine the properties of this setup with more complex and precise excitation schemes and measurements.

The results are described in the experimental publication [143], followed by a theoretical analysis in [144].

Chapter 10

Three-level atoms with Rydberg states

Contents

In this chapter we will give a general overview of "prerequisites" and context elements, that form the required basis to investigate the intracavity atomic cloud's behaviour in the presence of Rydberg excitations. Their strong mutual interactions and the qualitative expected effect in EIT conditions will be discussed.

10.1 Interactions between Rydberg atoms, blockade

10.1.1 Simplified description of the Rydberg-Rydberg interactions and blockade mechanism

As described in appendix A, the important properties of Rydberg atoms can be deduced from a hydrogenoid model with an effective principal quantum number n^*. Of particular interest here is the Rydberg wavefunctions' typical radius, scaling as $(n^*)^2$, that explains the extremely large dipole moments available from these states ($n^* >> 1$), and thereby the strong interactions they can experience.

In the relevant range of interatomic distances for the present experiments, the main contribution to the interaction between atoms A and B at a distance R is described using the dipole-dipole coupling hamiltonian (see appendix A):

$$\hat{H}_{dd} = \frac{1}{4\pi\epsilon_0} \frac{\hat{\vec{d}}_A.\hat{\vec{d}}_B - 3(\hat{\vec{d}}_A.\vec{u})(\hat{\vec{d}}_B.\vec{u})}{R^3} \tag{10.1}$$

where $\vec{u}$ is a unit vector pointing from A towards B (see figure (10.1)).

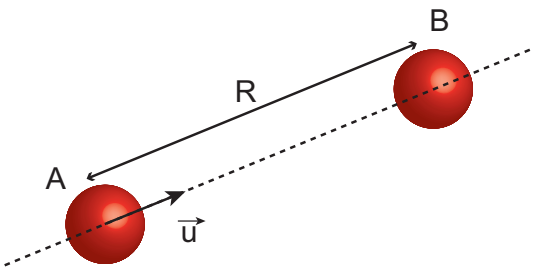

Figure 10.1: Configuration of two Rydberg atoms interacting with each other.

The resulting lowest-order energy shift ΔE of a given two-atom state $|\Phi\rangle \otimes |\Phi\rangle$ is obtained, in the absence of quasi-Förster resonances [1], by applying second-order perturbation theory to $\hat{H}_{dd}$:

$$\Delta E = \sum_{|\Phi'\rangle,|\Phi''\rangle} \frac{\left|\langle\Phi'| \otimes \langle\Phi''| \hat{H}_{dd} |\Phi\rangle \otimes |\Phi\rangle\right|^2}{(2E_\Phi - E_{\Phi'} - E_{\Phi''})} \tag{10.2}$$

where the sum runs over all possible combinations of states as shown in figure (10.2) (it is simplified in practice as the few levels with large dipole coupling to $|\Phi\rangle$ and small energy defects $2E_\Phi - E_{\Phi'} - E_{\Phi''}$ contribute for most of the shift) [145]. See appendix A for more details.

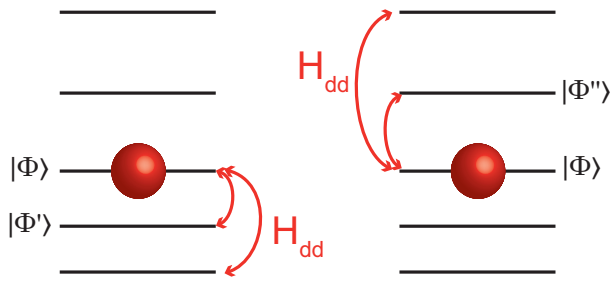

Figure 10.2: Principle of the couplings involved in the second-order van der Waals energy shift.

Once the sum over the relevant two-atom states has been calculated, the total interaction energy between the two atoms in state $|\Phi\rangle$ would then described by a single term, proportional to squared matrix elements of $\hat{H}_{dd}$, usually written as $\Delta E \propto -\frac{C_6}{R^6}$, characteristic of the van der Waals interaction.

The precise form of the interaction was recently measured in a very direct way using two single atoms trapped at a controlled distance from each other [146]. It leads to the now well-known Rydberg excitation blockade: when two atoms are close enough to each other, the doubly excited Rydberg state can be pushed by the interactions out of the frequency-resolved laser-driven excitation resonance, so that one atom prevents the second one from

1. These happen if for a given two-atom state $|\Phi\rangle \otimes |\Phi\rangle$, the atomic structure is such that another particular combination of states $|\Phi'\rangle \otimes |\Phi''\rangle$ is almost resonant in energy with $|\Phi\rangle \otimes |\Phi\rangle$.

getting excited (see figure (10.3)). Due to the long range and strength of the van der Waals interactions, this can happen up to distances conveniently accessible experimentally ($\sim$ 10 μm), creating a remarkably large influence sphere called blockade sphere around an excited atom.

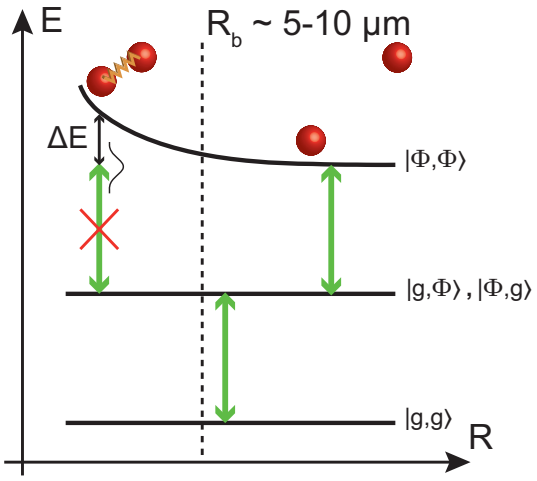

Figure 10.3: Rydberg blockade mechanism. In the two-atom basis, the system starts from its ground state $|g,g\rangle$, and due to a laser excitation with a finite linewidth (green arrows), each atom can be excited from $|g\rangle$ to a Rydberg state $|\Phi\rangle$. However, from the singly excited state, when one tries to reach the doubly excited one $|\Phi,\Phi\rangle$, the interactions shift it out of resonance for interatomic distances R below a certain blockade radius R_b.

First hints of this mechanism were observed in atomic gases at the end of the 1990s (see for example [59]). It was then demonstrated experimentally between two single atoms in 2009 [147, 148], and was already at that time proposed theoretically as a basis for a wide variety of quantum information protocols, in particular making use of it in cold atomic ensembles [52, 67, 68, 149]. For a more complete overview of the use of Rydberg interactions and blockade in quantum information, see section 13.1. This combination of possibilities lead many groups to study systems of cold atomic clouds with Rydberg excitations, including ours in which we started by considering the response of such a complex system to a classical off-resonant excitation.

10.1.2 Practical case – angular dependence, degeneracy and effective potential

In practical configurations, complications arise due to the anisotropy of the interactions: $\hat{H}_{dd}$ in general involves dependences on the angle between the quantization axis and the interatomic axis θ. A direct experimental measurement of this anisotropy on two isolated atoms is reported in [150]. In a cloud of cold atoms, all possible values of θ can be realized simultaneously.

Jointly, the problem arises that the Rydberg states in rubidium, described in the fine structure basis (n,l,j,m_j) [2], are all degenerate at least twice in m_j. This simple fact makes the treatment of second order perturbations in equation (10.2) wrong as such:

2. Hyperfine coupling can be neglected to a good approximation for high enough Rydberg states.

the different $\left|m_j; m'_j\right\rangle$ states of a given two-atom level $|n, l, j; n, l, j\rangle$ are mixed by the action to second order of the dipole interaction, and degenerate perturbations theory is required for a proper description. One should then proceed by looking for the $(2j+1)^2$ eigenstates and eigenvalues of the interaction matrix in this subspace, each of them defining a proper interaction potential with its associated strength. The eigenstates, combinations of $\left|m_j, m'_j\right\rangle$'s for a given j, have expressions that depend on θ [151–153].

As a result, apart from S states ($l = 0$) that have isotropic wavefunctions and for which the overall interaction potential is roughly isotropic [152, 153], in the general case the angular dependence of the interactions is complex, so that it should be treated with care.

In the experiments, the excitation scheme will address states $\left|nD_{5/2}, m_j = +5/2\right\rangle$, as defined in the fixed frame of the lasers and cavity setup (for practical reasons, that will be discussed later). For a given pair of atoms, this state will almost never correspond to an $m_j = +5/2$ with respect to the random interatomic axis, and neither to any of the eigenstates of the interaction at this given angle. To understand the experiments, it is therefore necessary that an averaging is carried out over all values of θ, and over the different eigen molecular potentials onto which the chosen state can be projected, with weights depending on θ. What quantity exactly must be averaged depends on the purpose, as will be discussed in more details later.

The experiment will look at global properties of the cloud like its susceptibility, in a regime where we voluntarily avoid getting close to resonance with any two-atom state. In that case, it is safe to consider that this averaging procedure will provide us in the end with an effective C_6^{eff} coefficient, and that the results can be interpreted as if all interactions were given only by $-\frac{C_6^{eff}}{R^6}$ [144].

10.2 EIT on a Rydberg level – Qualitative classical aspects

The long lifetime of Rydberg states allows EIT to be achieved in a ladder scheme, like ($5S \rightarrow 5P \rightarrow$ Rydberg state) in rubidium as shown in figure (10.4), as well as it can be in a standard Λ scheme [154, 155], and to look for a nonlinear response of the atoms to the probe light in this configuration.

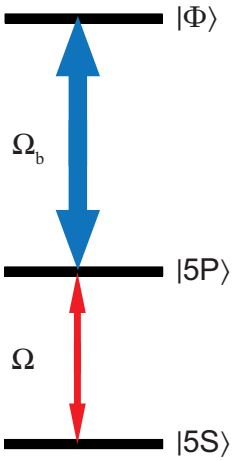

Figure 10.4: EIT in rubidium in a ladder scheme with Rydberg states.

This means that the complete picture of a transparency window in the susceptibility, in which photons are converted into mixed light-atoms excitations that propagate through the medium at reduced speed and with low losses can be reused directly in this context. The Rydberg excitations created by this two-photon scheme will however interact with each other, which comes as an additional modification to this usual EIT picture.

10.2.1 Qualitative expectations for the cloud's behaviour in Rydberg EIT conditions

The properties of the medium under EIT conditions are due to the coherent driving of the system into a long-lived dark state, which is only possible under very controlled conditions. In particular, both transparency in the resonant regime and coherent two-photon transitions in the detuned one can only be achieved under the right two-photon resonance condition. From the two-atom Rydberg blockade picture, it is clear that, in an atomic cloud, Rydberg interactions mean that the excited population created by a photon entering the cloud will significantly affect the EIT resonance condition for the atoms nearby. In the resonant regime for example, this perturbation of the EIT resonance will lead to a loss of the transparency, and more generally to a change in the susceptibility [155]. As will be shown in details, relatively simple models based on blockade mechanisms permit a good understanding of the overall behaviour of the cloud's susceptibility.

The interesting mechanism here is that the Rydberg population modifying the medium's optical response is itself created by light propagating in the cloud, so that this corresponds to a nonlinear susceptibility in the classical regime. This nonlinearity can be particularly strong because a single excited atom can modify the behaviour of many others around in the cloud, thereby amplifying the sensitivity of the medium to light.

From the point of view of the atoms, light coupled into the cloud should in principle be considered as exciting delocalized superposition states of all atoms. Distinctive features of this delocalized nature of the excitations have already been studied in similar systems [156]. This may seem hardly compatible with a pure atom-atom blockade sphere picture to interpret the effect of interactions, which is easier to visualize for localized Rydberg atoms. However, due to interactions themselves, multiple excitations sent into a cloud will spontaneously dephase each other and tend to localize at least partially, on a timescale that can be quite short compared to the Rydberg lifetime [157–159]. Therefore, when doing experiments like the one presented here, in the classical regime for the driving light and working on timescales much longer than the dephasing time, the picture of individual localized Rydberg excitations can be relevant.

10.2.2 Resonant Rydberg EIT

Using resonant EIT schemes in a cold atomic cloud, the clear signature of Rydberg interactions was first observed in 2008 in Charles Adams' group [155]. As the full system consists of N three-level atoms with long-range interactions and is analytically impossible to describe in the general case, the first experiments were interpreted on the basis of phenomenological models [155]. In the few following years, more precise measurements of absorption spectra exhibiting strong nonlinear response on resonance were realized for repulsive or attractive interactions [142, 160]. A full theoretical interpretation could be proposed only in the regime of low enough density, via ab initio resolution of the Hamiltonian for the typical number of atoms in the Rydberg influence sphere (≈ 3). The interpretation in terms of an effective susceptibility for the cloud modified by the

interactions came shortly afterward with the lowest-order calculation of the Rydberg $\chi^{(3)}$ nonlinearity on resonance [161].

In these experiments, the observation of a transparency window around resonance filled up by absorption growing very quickly as one increases the probe power, without line broadening, clearly indicated the interest and strength of the nonlinearity reachable in Rydberg EIT systems. With systems working in not yet optimized conditions, third-order nonlinearities were measured or predicted in the classical probe regime that were much larger than what had been achieved before in similar conditions [160, 161].

This resonant case leads in the quantum regime to what one could see as a photon blockade effect: taking the effect to the few-photon level, it was demonstrated recently [3] in different systems that the transmission of a particular photon through the cloud can be controlled by the presence of a second one [131, 162–165]. It was also shown theoretically that this effect of two photons not being able to propagate too close to each other could lead to the spontaneous appearance of spatial ordering – crystallization – of photons in a beam propagating in this medium [161].

10.2.3 Going to the dispersive regime

The goal of achieving coherent unitary gates between photons lead us to look for regimes where the interactions between Rydberg polaritons could lead to lossless phase-shifts rather than transmission modulations. Based on the blockade interpretation, it seems natural that Rydberg interactions in the cloud should lead to a nonlinear dispersion as well as the observed absorption. It is then "only" a matter of finding the right parameter range to observe it.

Despite the usual efficiency loss when moving off resonances to limit the absorption, one can look for a nonlinear modification of the wings of the two-photon line in this detuned case. The difficulty then is that, in the classical regime, measuring small phase-shifts on small amounts of light can be more challenging than measuring absorption. In this sense putting the medium in an interferometer like the cavity that multiplies the effect and translates phase-shifts into transmitted intensity variations proves very helpful.

3. After the experiment presented in this part was carried out.

Chapter 11

Theoretical ideas on the Rydberg susceptibility

Contents

Here we will discuss useful and efficient ways to theoretically characterize the dispersive Rydberg susceptibility, based either on Bloch equations or on a phenomenological "universal scaling" model. In practice, the behaviour of the system was significantly influenced by technical aspects like dynamics or spatial inhomogeneities, that will be discussed in the next chapter.

11.1 $\chi^{(3)}$ expansion

11.1.1 Complexity of the general problem

For simplicity, let us consider first the general situation of N 3-level atoms excited in free space with homogeneous probe and coupling Rabi frequencies Ω and Ω_b as represented in figure (11.1), corresponding to the following Hamiltonian (in the rotating wave approximation and interaction picture):

$$\hat{H}_0 = \sum_{k=1}^{N} -\hbar\gamma\Delta\hat{\sigma}_{22}^k - \hbar\gamma\delta\hat{\sigma}_{33}^k + \frac{\hbar\gamma\Omega}{2}(\hat{\sigma}_{12}^k + \hat{\sigma}_{21}^k) + \frac{\hbar\gamma\Omega_b}{2}(\hat{\sigma}_{23}^k + \hat{\sigma}_{32}^k) \tag{11.1}$$

where $\hat{\sigma}_{ij}^k = |i\rangle_k \langle j|_k$ and, for consistency with Part I, we will note $\hat{\sigma}_k = \hat{\sigma}_{12}^k$.

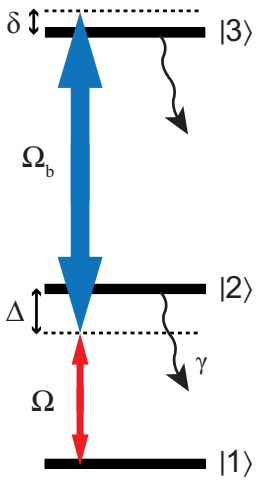

Figure 11.1: 3-level scheme considered for each single atom to write the evolution equations. In practice state $|1\rangle$ will be one of the $5S1/2$ states of rubidium, state $|2\rangle$ will belong to the $5P3/2$ manifold, and $|3\rangle$ is the Rydberg level we aim for, which will be of the form $nD5/2$ with variable n.

The Rydberg-Rydberg interactions are described by the additional Hamiltonian:

$$\hat{H}_{int} = \sum_{k=1}^{N} \sum_{l=1}^{k-1} \hbar\gamma C_{kl} \hat{\sigma}_{33}^{k} \hat{\sigma}_{33}^{l} \tag{11.2}$$

where $\hbar\gamma C_{kl}$ is the interaction energy of atoms k and l when both are in Rydberg state (the van der Waals interaction will correspond to $\gamma C_{kl} = -\frac{C_6}{|\vec{r}_k - \vec{r}_l|^6}$).

With the complete Hamiltonian $\hat{H} = \hat{H}_0 + \hat{H}_{int}$, a selection of the evolution equations for operators $\hat{\sigma}_{ij}$ is:

$$\begin{cases} \frac{\mathrm{d}}{\mathrm{d}t}\hat{\sigma}_k &= i\gamma \left((\Delta + i)\hat{\sigma}_k + \frac{\Omega}{2}(\hat{\sigma}_{22}^k - \hat{\sigma}_{11}^k) - \frac{\Omega_b}{2}\hat{\sigma}_{13}^k \right) + \hat{F}_{12}^k \\ \frac{\mathrm{d}}{\mathrm{d}t}\hat{\sigma}_{13}^k &= i\gamma \left((\delta + i\gamma_{13})\hat{\sigma}_{13}^k + \frac{\Omega}{2}\hat{\sigma}_{23}^k - \frac{\Omega_b}{2}\hat{\sigma}_k - \sum_{l\neq k} C_{kl}\hat{\sigma}_{13}^k\hat{\sigma}_{33}^l \right) + \hat{F}_{13}^k \\ \frac{\mathrm{d}}{\mathrm{d}t}\hat{\sigma}_{23}^k &= i\gamma \left(((\delta - \Delta) + i\gamma_{23})\hat{\sigma}_{23}^k + \frac{\Omega}{2}\hat{\sigma}_{13}^k + \frac{\Omega_b}{2}(\hat{\sigma}_{33}^k - \hat{\sigma}_{22}^k) - \sum_{l\neq k} C_{kl}\hat{\sigma}_{23}^k\hat{\sigma}_{33}^l \right) + \hat{F}_{23}^k \end{cases} \tag{11.3}$$

where the $\hat{F}_{ij}$'s are Langevin forces for each of the coherences, and γ_{13} and γ_{23} are decay rates of the corresponding coherences (normalized by γ). As several processes can lead to fast dephasing of the Rydberg coherence, these two rates are considered different from (and a priori larger than) γ_{33}, where $2\gamma_{33}$ is the Rydberg population decay rate. The purely radiative population lifetimes of Rydberg states are typically of several tens of microseconds, corresponding to γ_{33} of a few kHz [68].

Calculating the steady state susceptibility $\frac{\langle\hat{\sigma}\rangle}{\Omega/2}$, the interaction terms make it depend on 2-body correlators of the form $\left\langle \hat{\sigma}_{ij}^k \hat{\sigma}_{33}^l \right\rangle$. The evolution equations for these two-operator averages will depend on 3-body correlations and so on. This infinite hierarchy of correlation functions due to interactions must be truncated somehow in order to extract a closed form of the susceptibility.

One way around this problem consists, in the low probe power regime, in expanding all quantities in powers of $\frac{\Omega}{2}$. As higher-order correlators will also correspond to higher degrees in probe intensity, solving these equations for each degree allows to separate independent equation systems. This exactly corresponds to looking for an expansion of the

susceptibility in terms, in lowest order, of a linear one and a $\chi^{(3)}$ [144]. Keeping only order 1 in Ω first, the previous equations of course show that the interactions do not change anything, and the obtained linear susceptibility is exactly the one from equation (1.37).

11.1.2 Rydberg $\chi^{(3)}$ susceptibility

In the lowest order, interactions therefore come into play in the form of a $\chi^{(3)}$. In the interesting regime where the interaction-induced nonlinearity appears for very low light level, this $\chi^{(3)}$ will give information about this nonlinearity's characteristics and scaling laws. Note that in the lowest-order dependence on Ω^2 in the equations, even in the absence of interactions, there is a natural $\chi^{(3)}$ term induced by saturation behaviour. In the general case, the third-order susceptibility can then be written: $\chi = \chi^{(1)} + \chi^{(3)}_{nat}\Omega^2 + \chi^{(3)}_{int}\Omega^2$. In practice, we want only to characterize $\chi^{(3)}_{int}$, and ideally to work in a regime where it is much larger than $\chi^{(3)}_{nat}$, so that the latter could be neglected.

Removing index k for a homogeneous sample, and replacing $\langle\hat{\sigma}\rangle$ by σ, the equations obtained for the operator averages in steady state are:

$$\begin{cases} (\Delta + i)\sigma + \frac{\Omega}{2}(\sigma_{22} - \sigma_{11}) - \frac{\Omega_b}{2}\sigma_{13} & = 0 \\ (\delta + i\gamma_{13})\sigma_{13} + \frac{\Omega}{2}\sigma_{23} - \frac{\Omega_b}{2}\sigma - \sum_l C_{kl}\left\langle\hat{\sigma}_{13}\hat{\sigma}^l_{33}\right\rangle & = 0 \\ ((\delta - \Delta) + i\gamma_{23})\sigma_{23} + \frac{\Omega}{2}\sigma_{13} + \frac{\Omega_b}{2}(\sigma_{33} - \sigma_{22}) - \sum_l C_{kl}\left\langle\hat{\sigma}_{23}\hat{\sigma}^l_{33}\right\rangle & = 0 \end{cases} \tag{11.4}$$

Let us then make two approximations: from the third equation, σ_{23} is known to be at least of order 2 in Ω, and could be neglected in the evolution of σ_{13} (second equation). Simultaneously, if the population remains mostly in the ground state, the lowest-order approximation gives $\sigma_{22} - \sigma_{11} \approx -1$ in the first equation. These two approximations are exactly equivalent to neglecting the "natural" nonlinearity of the system to focus on the interaction-induced one at the $\chi^{(3)}$ order. The two terms neglected would indeed precisely be at the origin of the $\chi^{(3)}_{nat}$.

At this order of approximation the first two equations are:

$$\begin{cases} (\Delta + i)\sigma - \frac{\Omega}{2} - \frac{\Omega_b}{2}\sigma_{13} & = 0 \\ (\delta + i\gamma_{13})\sigma_{13} - \frac{\Omega_b}{2}\sigma - \sum_l C_{kl}\left\langle\hat{\sigma}_{13}\hat{\sigma}^l_{33}\right\rangle & = 0 \end{cases} \tag{11.5}$$

Leaving the interaction term as it is for now, the following form for the reduced susceptibility can be "artificially" extracted from the above equations:

$$\frac{\sigma}{\Omega/2} = \left[\Delta + i - \frac{(\Omega_b/2)^2}{\delta + i\gamma_{13} - \sum_l C_{kl}\frac{\left\langle\hat{\sigma}_{13}\hat{\sigma}^l_{33}\right\rangle}{\sigma_{13}}}\right]^{-1} \tag{11.6}$$

Without interactions ($C_{kl} = 0$) and neglecting γ_{13}, this is exactly the linear three-level susceptibility of equation (1.37). Forgetting about correlations, the interaction term would be proportional to σ_{33}, and is therefore expected to be at least of order 2 in Ω. In order to keep a consistent $\chi^{(3)}$ approach, this susceptibility must be expanded to get the lowest-order in the interaction term.

The term that must be calculated and contains the physics of the interactions here is the correlation function $\left\langle\hat{\sigma}_{13}\hat{\sigma}^l_{33}\right\rangle$. Within the approximations made here, its expression to third order in Ω is required. One possibility is to use the approximate expression found by

J. Stanojevic in [144], which is rather an ansatz based on numerical simulations, checked in the detuned regime $1+\Delta^2 >> \Omega_b^2/4$:

$$\left\langle \hat{\sigma}_{13}\hat{\sigma}_{33}^{l}\right\rangle^{(3)} \approx \sigma_{13}^{(1)}\sigma_{33}^{(2)}\frac{T}{T-C_{kl}} \tag{11.7}$$

where $\sigma_{13}^{(1)}$ and $\sigma_{33}^{(2)}$ are taken at their lowest-order dependence on Ω, and T is defined as:

$$T = \delta + i\gamma_{13} - \frac{(\Omega_b/2)^2}{\Delta+i} \tag{11.8}$$

A more general expression can be derived by taking the full Bloch equations for products of two operators and keeping only the terms of relevant order in the expansion in Ω. When no additional dephasing of the Rydberg coherence is considered, *i.e.* $\gamma_{13}=\gamma_{33}$, the expression can be put in the relatively simple form:

$$\left\langle \hat{\sigma}_{13}\hat{\sigma}_{33}^{l}\right\rangle^{(3)} \approx \sigma_{13}^{(1)}\sigma_{33}^{(2)}\frac{T}{T-C_{kl}\left[1-\frac{\Omega_b^2/4}{(\Delta+i)(\Delta+i+\delta+i\gamma_{13})}\right]} \tag{11.9}$$

This corresponds to the ansatz of equation (11.7) in the detuned regime.

For simplicity, in the following the first simplest form for the correlator will be used. This leads to the following expression of the third-order probe transition's coherence:

$$\frac{\sigma}{\Omega/2} \approx \frac{1}{\Delta+i-\frac{(\Omega_b/2)^2}{\delta+i\gamma_{13}}}\left(1-\frac{(\Omega_b/2)^2}{(\Delta+i)(\delta+i\gamma_{13})}\sum_l \frac{C_{kl}}{C_{kl}-T}\sigma_{33}^{(2)}\right) \tag{11.10}$$

Making explicitly the approximation of homogeneous and continuous medium, with atomic density μ, the interaction sum can be replaced by:

$$\sum_l \frac{C_{kl}}{C_{kl}-T} \approx \mu\int \frac{4\pi R^2 dR}{1+\gamma T R^6/C_6} = \mu\frac{2\pi^2}{3}\sqrt{\frac{C_6}{\gamma T}} \equiv n_b \tag{11.11}$$

which defines the complex dimensionless constant n_b (independent of probe power), that will be interpreted in more details later. As expected, the reduced susceptibility is therefore split into a linear part and a $\chi^{(3)}$ part due only to interaction terms: $\frac{\sigma}{\Omega/2} \approx \left(\frac{\sigma}{\Omega/2}\right)^{(1)} + \left(\frac{\sigma}{\Omega/2}\right)^{(3)}$ where:

$$\left(\frac{\sigma}{\Omega/2}\right)^{(1)} = \frac{1}{\Delta+i-\frac{(\Omega_b/2)^2}{\delta+i\gamma_{13}}} \tag{11.12}$$

$$\left(\frac{\sigma}{\Omega/2}\right)^{(3)} = -\frac{1}{\Delta+i}\frac{(\Omega_b/2)^2}{(\Delta+i)(\delta+i\gamma_{13})-(\Omega_b/2)^2}n_b\sigma_{33}^{(2)} \tag{11.13}$$

In the lowest order in Ω, the Rydberg population σ_{33} will not be modified by the interactions: as it is already at least $\propto\Omega^2$ naturally, the expression for $\sigma_{33}^{(2)}$ can be taken from the no-interaction case to calculate the $\chi^{(3)}$.

To give a complete example in a particular situation, under the assumptions that $\delta=0$ and $\Delta >> 1 >> \gamma_{13},\gamma_{33}$, an effective two-level model gives the following form:

$$\sigma_{33}^{(2)} \approx \frac{\Omega^2\Omega_b^2}{16\Delta^2}\frac{1}{(\gamma_{13}+\frac{\Omega_b^2}{4\Delta^2})^2+(\frac{\Omega_b^2}{4\Delta})^2}\frac{\gamma_{13}+\frac{\Omega_b^2}{4\Delta^2}}{\gamma_{33}+\frac{\Omega_b^2}{4\Delta^2}} \tag{11.14}$$

The obtained form of the $\chi^{(3)}$ (combination of equations (11.13) and (11.14)) is consistent with what was derived and used in various regimes in [143, 144, 161, 166–168].

11.2 "Universal scaling" model

To give further physical interpretation of the result, starting back from equation (11.10), the reduced susceptibility can be put in the following form:

$$\frac{\sigma}{\Omega/2} = (1 - n_b\sigma_{33}^{(2)}) \left(\frac{\sigma}{\Omega/2}\right)_{3lev} + n_b\sigma_{33}^{(2)} \left(\frac{\sigma}{\Omega/2}\right)_{2lev} \tag{11.15}$$

where $\left(\frac{\sigma}{\Omega/2}\right)_{3lev}$ and $\left(\frac{\sigma}{\Omega/2}\right)_{2lev}$ are the linear susceptibilities for a three-level atom without interactions, or for a pure two-level one, given by:

$$\left(\frac{\sigma}{\Omega/2}\right)_{3lev} = \frac{1}{\Delta + i - \frac{(\Omega_b/2)^2}{\delta + i\gamma_{13}}} \tag{11.16}$$

$$\left(\frac{\sigma}{\Omega/2}\right)_{2lev} = \frac{1}{\Delta + i} \tag{11.17}$$

Under the approximations made so far, atoms without interactions would behave linearly with respect to Ω, with a susceptibility given by $\left(\frac{\sigma}{\Omega/2}\right)_{3lev}$. The result above tells us that the effect of interactions is to mix the three-level susceptibility with some component of two-level one, with a weight given by $n_b\sigma_{33}^{(2)}$. This last term summarizes the effect of the interactions, and the nonlinearity comes entirely through the first-order dependence of $\sigma_{33}^{(2)}$ on the probe intensity.

Though so far n_b can be complex and was just introduced for convenience, the general form of the result can also be obtained from a phenomenological model of the effect of interactions, that will be called "universal scaling" model. Based on Rydberg blockade effects, it interprets n_b as a number of atoms in a blockade sphere. This alternative model will be discussed thereafter.

11.2.1 Physical reasoning in the dispersive case

To formulate a simple model that effectively takes into account the effect of interactions in a large sample, a convenient way is to follow the suggestion of [169]. Under the approximation that simultaneous multiple excitations of several atoms from ground to Rydberg states can be neglected with respect to lower-order processes, the effect of Rydberg interactions on the dynamics of one specific atom k can be summarized as a shift of its Rydberg level energy by the amount

$$\hbar\Delta_{int} = \hbar \sum_{l \ excited} C_{kl} \tag{11.18}$$

This quantity corresponds to the total energy shift induced by its interactions with all its excited neighbours.

This is the basis of the qualitative picture behind the Rydberg blockade mechanism, and it can be used quantitatively to estimate the effect of a single Rydberg atom on the susceptibility of its neighbours in the cloud.

Starting with a simple case that will also correspond to the experimental situation, let us consider the dispersive regime where both transitions are off-resonance ($\Delta >> 1$, $\delta >> \gamma_{13}$). The reduced susceptibility of an atom is then mostly real, and if one assumes a Rydberg atom is present at a distance R of the "test" one, using the effective $\delta \to \delta + \frac{C_6}{\gamma R^6}$ resulting from the previous remark, one finds:

$$\left(\frac{\sigma}{\Omega/2}\right)_{test} = \frac{1}{\Delta - \frac{(\Omega_b/2)^2}{\delta + \frac{C_6}{\gamma R^6}}} \tag{11.19}$$

For our models and approximations to make sense, and if one wants to keep absorption at a low level, the signs of δ, Δ and C_6 must be chosen carefully not to hit a dressed resonance of the system (due to interactions or light shifts), that would correspond to a divergence of $\left(\frac{\sigma}{\Omega/2}\right)_{test}$ (this will be discussed in details in the description of the experiment). This effective susceptibility is plotted versus the distance to the excited atom R on figure (11.2), with a choice of parameters close to our experimental ones.

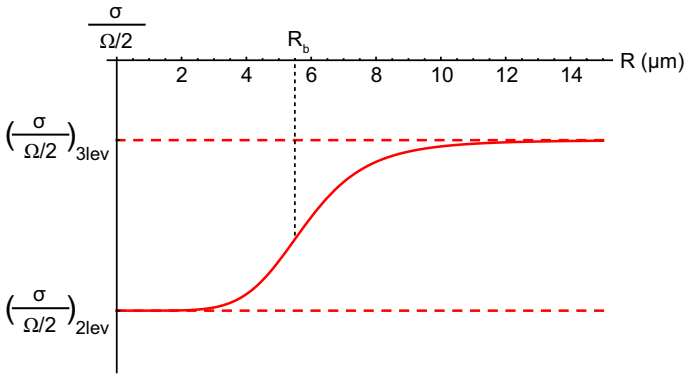

Figure 11.2: Value of the reduced susceptibility of a test atom as a function of its distance to an excited atom. Parameters are $\Delta = -25$, $\delta = 0.3$, $\frac{\Omega_b}{2} = 4$ and $\frac{C_6}{\gamma} = 36000 \mu m^6$.

In this simple case, the susceptibility smoothly transits from $\left(\frac{\sigma}{\Omega/2}\right)_{3lev}$ to $\left(\frac{\sigma}{\Omega/2}\right)_{2lev}$ as the excited atom is brought closer, since its presence effectively detunes more and more the upper transition for the test atom. The effect of an excited atom somewhere in the cloud is then to produce blockade for all its close enough neighbours, by switching their contribution to the susceptibility back to the two-level one. As the transition in figure (11.2) is not so broad, the volume in which this happens has a quite well-defined blockade radius R_b that can be extracted from equation (11.19). The simplest definition of it is obtained by taking the radius at half-width of the curve on figure (11.2):

$$R_b = \left(\frac{C_6}{\gamma(\delta - \frac{(\Omega_b^2/2)^2}{\Delta})}\right)^{1/6} \tag{11.20}$$

Calculating the average number of atoms contained inside a blockade sphere of such radius, one finds, up to a factor $\frac{\pi}{2}$, n_b in the limit $\Delta >> 1$, $\delta >> \gamma_{13}$.

The physical picture in this simple case, from the remarks just above and from equation (11.15), is thus quite simple: starting from atoms behaving with $\left(\frac{\sigma}{\Omega/2}\right)_{3lev}$, when one increases the probe power, some of them start to get excited to the Rydberg level with an average population $\sigma_{33}^{(2)}$ proportional to Ω^2, and each excited atom switches the control beam off for n_b of its neighbours, that go back to a two-level susceptibility. This is illustrated in figure (11.3).

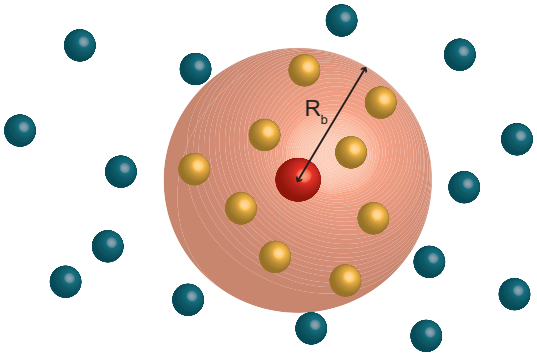

Figure 11.3: Representation of a localized Rydberg excitation and its effect on the cloud in the dispersive regime. The excited atom in red creates a blockade sphere of radius R_b around it inside which atoms behave as two-level ones (in yellow), while atoms outside the sphere (in blue) see the three-level susceptibility.

11.2.2 General forms of the model

The derivation of equation (11.15) from first principles and its consistency with the simple blockade model above mean that, at least in the right range of parameters, this result and the physical interpretation proposed are really catching the basis of the physics happening in the system.

In the dispersive regime where the physical meaning is clear, this equation an also be interpreted in a slightly different way:

$$\frac{\sigma}{\Omega/2} = (1-p_b)\left(\frac{\sigma}{\Omega/2}\right)_{3lev} + p_b\left(\frac{\sigma}{\Omega/2}\right)_{2lev} \tag{11.21}$$

where $p_b = n_b\sigma_{33}^{(2)}$. The quantity p_b can be viewed as the probability, for atom taken at random, that at least one of its n_b neighbours is excited and blockades it. This formulation is well suited for extrapolations, even to higher orders of probe power dependence.

However equation (11.15) should also be valid even for not completely dispersive regimes and complex n_b. Interestingly, even in this case, the structure of the equation can still be understood with the same "universal scaling" kind of physical argument: the full susceptibility should be a weighted average of the two- and three-level ones. To calculate the appropriate weight in the absence of a clear blockade volume defined by a single real quantity, n_b must be defined as a complex parameter measuring the effective change of complex susceptibility induced by a Rydberg excitation known to exist at $R = 0$, in units of the difference between two-level and three-level susceptibilities (still using the $\delta \to \delta + \frac{C_6}{\gamma R^6}$ effective law):

$$\int \left[\langle\hat{\sigma}(R)\rangle - \langle\hat{\sigma}(\infty)\rangle\right]\mu 4\pi R^2 dR = n_b\left[\hat{\sigma}(0) - \langle\hat{\sigma}(\infty)\rangle\right] \tag{11.22}$$

From the expression of the linear susceptibility, one gets:

$$n_b = \int \mu \frac{4\pi R^2 dR}{1 + \left[\delta + i\gamma_{13} - \frac{(\Omega_b/2)^2}{\Delta + i}\right]\gamma R^6/C_6} \tag{11.23}$$

This is exactly the same full definition of complex n_b as directly from the Bloch equations, which validates its physical interpretation. Values of this complex number of atoms per blockade sphere in the experimental conditions are given in section 12.3.2.

The basic principle of this "universal scaling" vision of the Rydberg susceptibility was first introduced in the resonant case in [161, 166, 167], and as is shown here it is backed up in the general case by the possible rigorous derivation of expressions like (11.15).

The qualitative effect of blockade for the two most relevant extreme cases here (all resonant or dispersive) is described in figure (11.4).

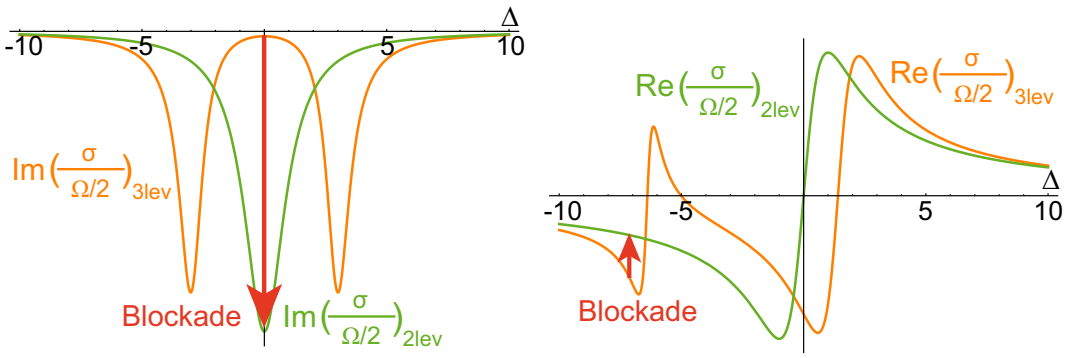

Figure 11.4: Qualitative effect of the blockade predicted by the universal scaling model in two different situations. Left: imaginary part of the susceptibility for resonant Rydberg-coupling beam. EIT renders the absorption very low on resonance, and blockade destroys this transparency. **Right:** real part of the susceptibility for a coupling beam detuned by 5γ from the upper transition. The coupling beam creates a change in dispersion in the wings of the two-photon line, which will be canceled by the blockade.

Overall, this suggests a really general approach: such a parameter as n_b in the sense of equation (11.15) can always be defined, especially even for higher orders of the nonlinearity, only it may not be a unique constant or have a very simple physical meaning in all cases. We showed in [144] that if one can evaluate by an independent method the susceptibility in presence of interactions, equation (11.15) can be used to find the value of the effective n_b in different parameter ranges.

11.2.3 Conclusion: expected behaviour of the susceptibility

In the dispersive regime, from equation (11.21), the susceptibility's behaviour is easily interpreted when progressively increasing the probe power. As long as the "natural" level of nonlinearity of the three-level susceptibility is not reached, the nonlinearity in equation (11.21) will only come from the blockade probability p_b, whose behaviour can be extrapolated on reasonable physical arguments.

While increasing the number of excitations, the dispersion will progressively change from its three-level value towards the two-level one, with p_b initially linear in probe power. It is then easy to imagine that at some point Rydberg "bubbles" will stop having the possibility to be created without interacting with other excitations, and a saturation behaviour should appear. In the extreme case, if the whole cloud is entirely contained in the joint volume of all the blockade spheres of excited atoms, then p_b should tend to 1 for all atoms, and the susceptibility will be completely back to its two-level state (if a Rydberg sphere contains a large number of atoms). This will be called the fully blockaded regime.

In the more general case, instead of moving continuously from $\left(\frac{\sigma}{\Omega/2}\right)_{3lev}$ to $\left(\frac{\sigma}{\Omega/2}\right)_{2lev}$ along a line in the complex plane for real n_b, it is expected that absorption and dispersion could be mixed by a complex n_b when moving away from $\left(\frac{\sigma}{\Omega/2}\right)_{3lev}$.

Chapter 12

Experiment

Contents

This chapter will describe how measurements of the dispersive nonlinear response of the cloud containing Rydberg atoms were performed, in the classical regime. This experiment was carried out before the DLCZ one described in the previous part, with a preliminary version of our overall experimental setup. In particular, at that time we did not have yet the complete control-acquisition system described in Part II, and had to do with the partially restrained properties of the system.

12.1 Experimental setup and measurement method

12.1.1 Preliminary considerations: how to measure linear two-level susceptibility

The goal here is to experimentally look for large nonlinear dispersion in the scheme described in figure (11.1), with a large single-photon detuning and a relatively small but non-zero two-photon detuning, to work in the wings of the two-photon transition and avoid

absorption (see figure (11.4)). For this, as discussed in Part I, one can characterize the modifications of the probe's cavity transmission line. Two basic experimental requirements have to be fulfilled for this objective:

- to realize measurements of the transmission for precisely known cavity detunings, within a restricted time slot inside an experimental sequence
- the measurement must be achievable even with low enough light levels to get into the linear regime of the known two- and three-level susceptibilities, as what we want to characterize is only the interaction-induced nonlinearity

Before even adding the Rydberg-coupling beam to the system, the possibilities of the system are thus tested, with two-level atoms in the cavity.

Cavity length scan for susceptibility measurements

The first requirement above is not trivial in practice. Due to difficulties locking the cavity, its length can not be precisely set at a given point – on the side of the resonance line for example – to then study the variation of the transmission with intensity. An alternative solution is to voluntarily scan the cavity across the resonance to measure the full lineshape. However, to satisfy various resonance conditions necessary for the cloud preparation, the cavity length must be kept fixed during most of the experimental sequence before measurements. Scanning the cavity is therefore useful only if it can be done controllably and fast enough to observe the full line after the preparation, before the atomic variables (density, cooperativity ...) have time to evolve. The "coherent" driving of our cavity's length by applying a ramp to the setpoint of the piezos' PID could only be done very slowly and would be noisy as the locking loop has a bandwidth < 50 Hz. This is therefore not satisfying either.

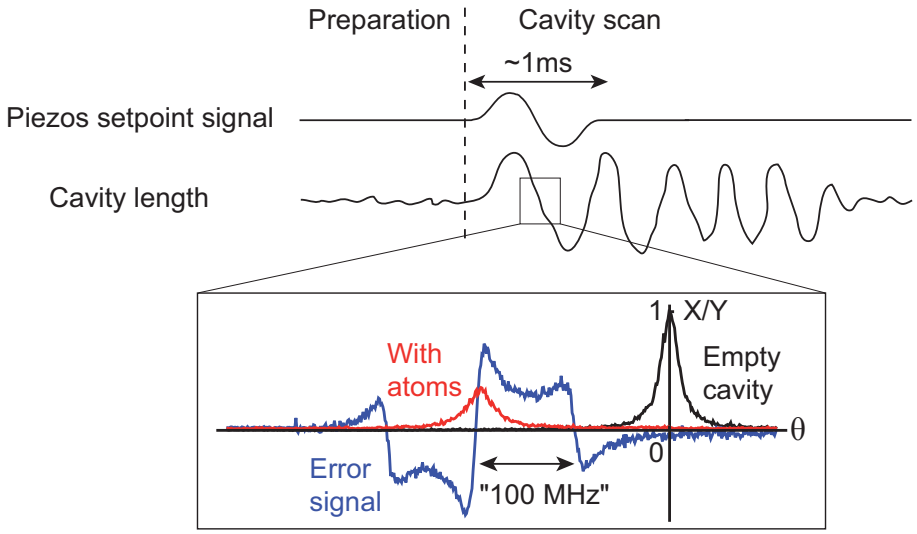

Figure 12.1: Scanning the cavity length to access the resonance lineshape. After the preparation (trap loading, cooling ...), a sine arch is sent to the piezos, which oscillate with a large amplitude, passing through resonance. During the scan we can monitor and register the error signal from the locking loop as a reference, and the probe transmission lines in different situations to measure its deformations. After some time the lock overcomes the oscillations and the cavity gets back to its initial state.

The adopted method uses the low "rigidity" of our cavity lock: once the system prepa-

ration is done, a period of a sine with frequency ≈ 1 kHz is sent to the piezos, approximately matching one of the mechanical resonances. This results in large amplitude oscillations of the cavity length for some time, which does not make the lock straightaway jump or saturate, but slowly recovers to its original state (see figure (12.1)). The first oscillation makes the cavity pass rapidly through its initial resonant setpoint, which allows for a measurement of the probe transmission during a close-to-linear cavity length scan after less than a millisecond (the full transmission line is crossed in ≈ 20 μs). This effective cavity line scan is quite reproducible, and the 810 locking beam's error signal can also be recorded simultaneously to serve as a detuning scale during a scan, giving access both to the zero-position and the frequency scale, since the sidebands are known to be 100 MHz away from the carrier (see figure (12.1)).

Observing the linear regime

Once the resonance lineshape and position can be accessed to measure the susceptibility, a regime must be reached where, without interactions, the cloud's behaviour should be completely linear. This corresponds to intracavity intensities much below I_{sat}. In order to monitor the transmission of the cavity, the probe light is first coupled into it through the high-transmission mirror ($T = 5\%$, lower mirror in practice), which means the transmitted intensity is measured through the upper, high-reflectivity mirror.

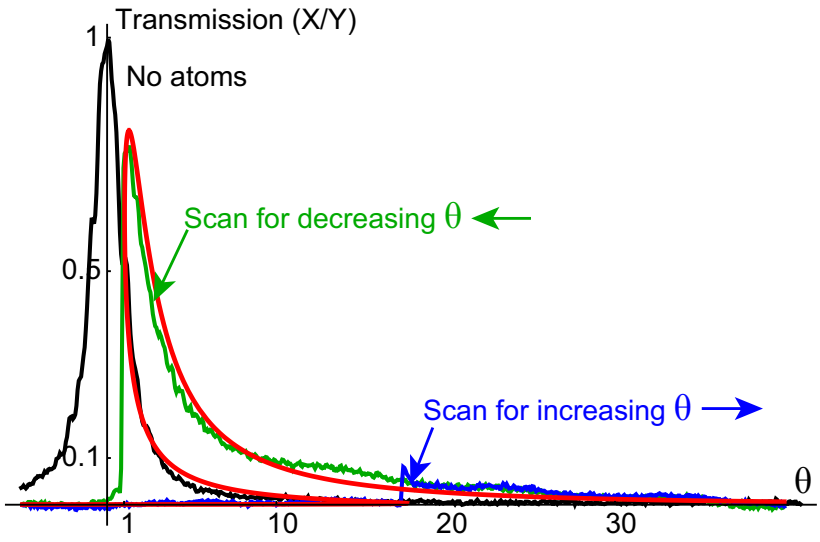

Figure 12.2: Two-level bistability. When the probe is sent in the cavity from the bottom and the normalized transmission X/Y is measured, the intensity regime is always such that the two-level saturation nonlinearity makes the transmission line bistable. Here the Lorentzian-shaped line (in black) is observed when scanning the cavity in the absence of atoms. The probe is detuned 11 γ below the transition. With atoms in the cavity, depending on which way the cavity is scanned (increasing or decreasing θ), the two lines exhibiting intensity jumps at different levels are observed (green and blue). In red is plotted the corresponding theoretical intensity transmission from equations (1.26) and (1.30), with $Y = 55000$ and $C = 280$.

For intensities below I_{sat} in the cavity, this means signals down to $< 10^{-5}$ nW power must be measured with relatively high bandwidth (> 100 kHz to resolve correctly the

lineshape), which proves quite challenging. In order to measure the transmission with the available detectors, the intensity is in practice always high enough that even the two-level nonlinearity is very marked. Two-level saturation bistability of the {atoms+cavity} system without coupling field can therefore be observed, as shown in figure (12.2), but not the linear regime in this configuration.

For reasons that will be explained later, the probe used is circularly polarized on the stretched 780 nm transition $\left|5S_{1/2}, F = 2, m_F = +2\right\rangle \rightarrow \left|5P_{3/2}, F = 3, m_F = +3\right\rangle$. In the regime of high probe power, dynamical Zeeman pumping of the atoms by the probe itself during the measurements can then affect the susceptibility, and lead to another kind of bistability. This effect tends to bend the transmission line in a way opposite to the saturation nonlinearity (the effective cooperativity increases with the probe power as it pumps atoms into states with higher coupling coefficients), as sketched in figure (12.3).

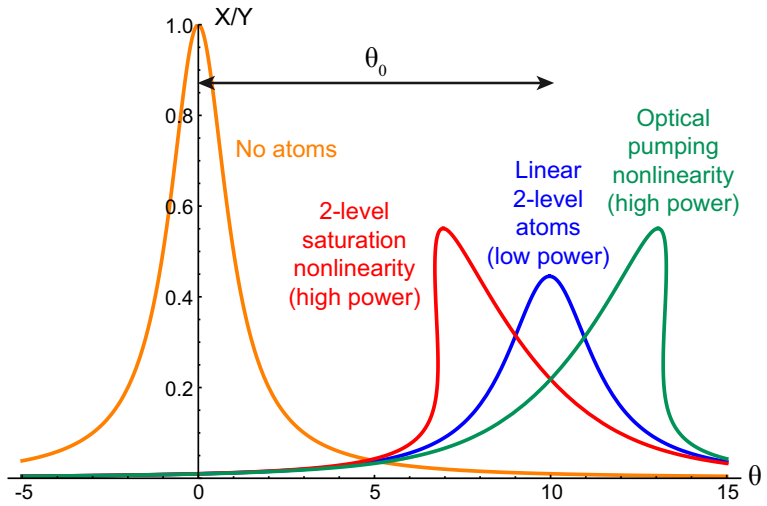

Figure 12.3: Saturation and optical pumping nonlinearities, qualitative picture. The cavity transmission line is shifted in the linear dispersive regime by an amount θ_0 proportional to the cooperativity. When increasing the probe power, the natural two-level behaviour is a saturation of the atoms' susceptibility which brings the line back towards its zero position. On the contrary, if optical pumping can happen due to the probe, the effective coupling coefficient of the atoms increases as the atoms are pumped towards extreme Zeeman sublevels, and the line bends in the other direction.

This gives an easy criterion for discriminating which phenomenon is responsible for some of the experimental observations. This is illustrated in figure (12.4), where the behaviour of the transmitted intensity as a function of the input intensity is shown for different configurations, exhibiting hysteresis cycles characteristics of bistable regimes.

Finally, in order to reach much lower intracavity power and still be able to measure the cavity transmission, the probe injection is switched to the top of the cavity, through the high-reflectivity mirror. This leads, for the same intracavity power, to much higher injected and output power ($Y = 1$, corresponding to I_{sat} at the maximum in the cavity, gives 2.4 nW out), and conveniently allows us to reach the linear regime. This allows for cooperativity measurements, and for optimization of the Zeeman optical pumping in the cloud, as its effect is an increase in the cooperativity.

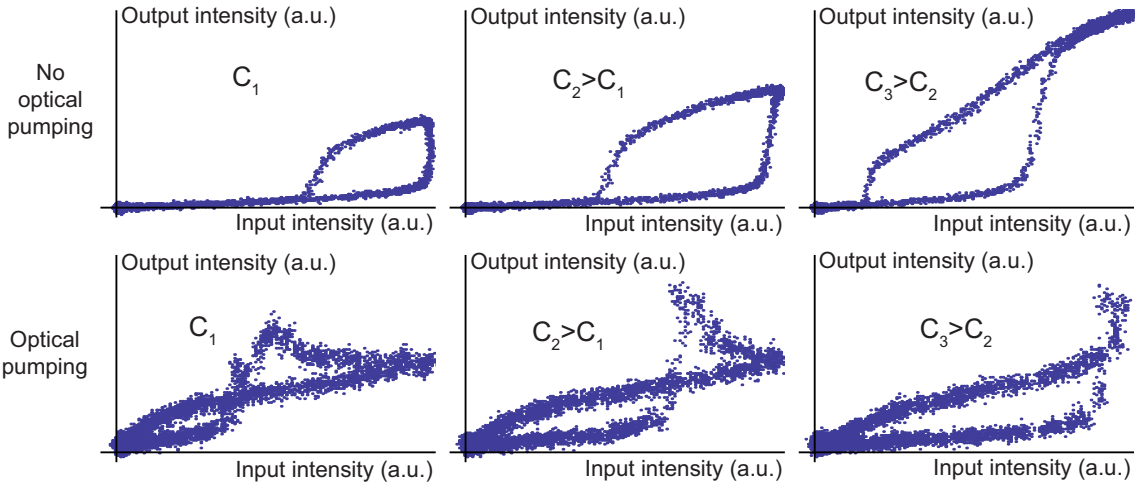

Figure 12.4: Different behaviours of intensity hysteresis on the cavity transmission. The MOT is loaded with a variable cooperativity, the cavity length is fixed and we send a ramp of input probe power on the system. By monitoring both input and output powers, the transmission's hysteresis cycles are reconstructed. From left to right on both lines the MOT loading is increased. All axes are in arbitrary but identical units. On the top line no optical pumping is performed before probing, so that the main effect is pumping bistability, with critical jump positions moving lower in intensity as the cooperativity is increased. On the bottom line however, the atoms are optically pumped beforehand, and the two-level saturation bistability is observed, with increasing critical intensities as the cooperativity increases. The overshoot when jumping from the lower branch to the upper one is attributed to the dynamical establishment of the saturation. The overall behaviour of the system in this kind of measurement is in general complex as it mixes several effects, and very sensitive to the exact parameter range, but can be qualitatively understood in some regimes.

12.1.2 Three-level excitation scheme, Rydberg-coupling beam

In the two-photon Rydberg excitation scheme, the detunings must be chosen carefully to avoid any possible direct resonant excitation. The effective resonance for a given atom can be shifted due to Rydberg interactions (in a direction that depends on the sign of the C_6), and also due to light shifts in the Rydberg level position induced by the coupling beam (depending on the sign of its detuning), as shown in figure (12.5). The consistent parameters are finally chosen based on the following considerations:

- The probe on the lowest transition is preferably red-detuned because, though it may be low power, its remaining mechanical or temperature-driving effect on the atoms would then be in the "good" direction (trapping and cooling, rather than repulsive action for a blue-detuned probe).
- As the probe detuning must be large, the Rydberg coupling beam's detuning is necessarily of sign opposite to it (close to two-photon resonance), which fixes the sign of the light shifts on the upper level.
- To maximize the reachable values of C_6, Rydberg states of the form $nD_{5/2}$ are chosen (rather than S states), despite the anisotropy of the interactions [145]. These states, for $n > 43$, have attractive interactions, which means the interaction-induced shift of the upper level will go in the same direction as the light shifts.

The selected configuration therefore uses a large negative detuning on the lower transition, and a small positive two-photon detuning, which avoids exciting directly any of the resonances in the system, sketched in figure (12.5).

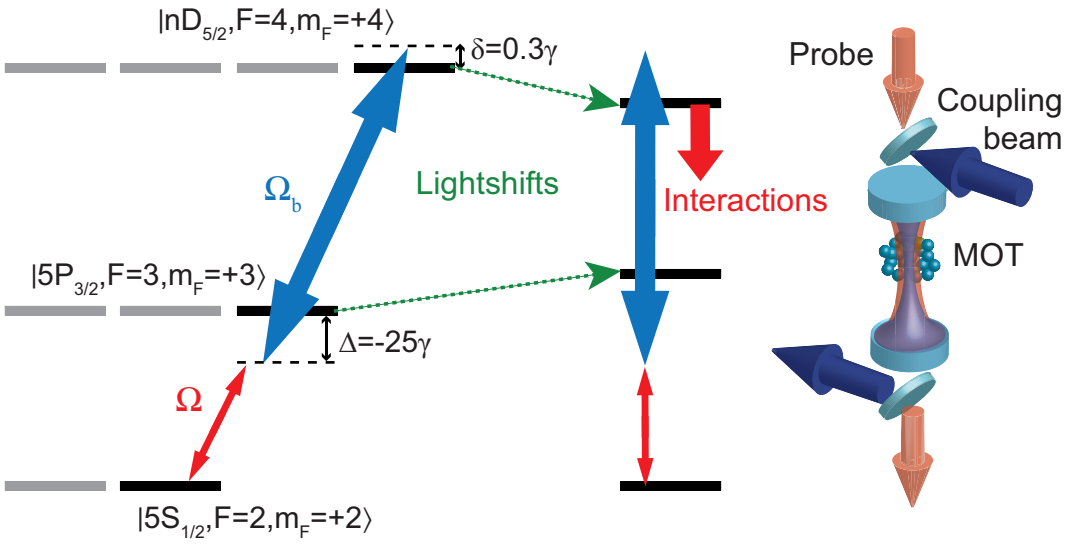

Figure 12.5: Two-photon excitation scheme towards Rydberg states. The detunings are chosen such that both the Rydberg-coupling beam's light shifts and the attractive interactions between D states shift the upper state away from two-photon resonance. The stretched scheme is made accessible by Zeeman optical pumping and use of circularly polarized beams on cavity axis, to take advantage of the maximum coupling coefficients. The two beams are injected together in their own transverse fundamental mode in the cavity using a dichroic mirror.

As suggested in the theoretical description of the Rydberg nonlinearity, interactions should progressively cancel the effect of the EIT coupling beam on the dispersion ($\left(\frac{\sigma}{\Omega/2}\right)_{3lev} \rightarrow \left(\frac{\sigma}{\Omega/2}\right)_{2lev}$), as in figure (11.4). It seems then qualitatively understandable that, in order to observe a large interaction-induced nonlinear dispersion, the effect of the coupling beam in the linear regime must first be maximized. This means, to some extent, that the coupling Rabi frequency seen by all the atoms coupled to the mode should be maximized (see figure (12.6)). In practice, only a limited laser power is available, and the details of the excitation scheme (geometry, polarization ...) must be chosen in order to optimize its effect. This is crucial because for a given excitation power, as one goes up in the addressed Rydberg level n in order to get larger interaction effects, the Rabi frequency on the coupling transition decreases, with a scaling $\propto (n^*)^{-3/2}$. The strength of the nonlinearity accessible is therefore conditioned by how the blue beam power is used.

There are mostly two options to choose from. One is to send the blue coupling beam perpendicular to the cavity axis. This has two main disadvantages: one is that, to be compatible with a quantization axis along the cavity one, the only proper polarization usable is π, which does not allow to use stretched transitions with maximal coupling strengths; the other is that, shining light from the side, the beam must cover the whole cloud size at least in one direction (along the cavity) so that all participating atoms see the blue light, which makes it spread over a large area ($\sim$ 100 μm * 1 mm) and decreases a lot the intensity.

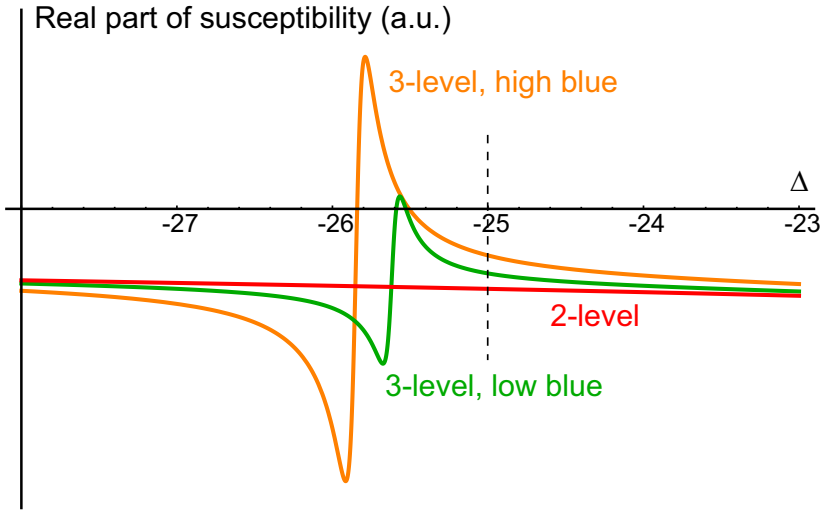

Figure 12.6: Effect of the blue Rabi frequency. The real part of the linear susceptibility (without interactions) is plotted around the two-photon resonance for typical experimental parameters, the probe detuning Δ being scanned from -28 to -23 γ. The two-level susceptibility in red looks flat far away from the resonance. In green and orange are shown the three-level susceptibility for a coupling beam detuned by 25.3 γ from the upper transition, with $(\frac{\Omega_b}{2})^2 = 3$ and $(\frac{\Omega_b}{2})^2 = 9$ respectively. The blue-induced dispersion change (difference between the two-level and three-level curves at $\Delta = -25$) increases with the blue Rabi frequency, and therefore it is expected that the interaction nonlinear effect should be larger, as it should correspond to a cancellation of this difference.

The other option is to send the blue light on axis in the cavity mode. In contrast to the previous one, light can be concentrated on the cavity mode's size in two directions (100 μm * 100 μm, factor ~10 gain), so the intensity is higher, and the coupling beam can be circularly polarized, as described in figure (12.5). Unfortunately this configuration does not have only advantages. Sending blue light on the cavity axis means it crosses several optical surfaces that were initially not designed for that purpose, and are therefore not coated for blue light. Namely, the viewport through which light enters the vacuum chambers reflects a large amount of light (and as none of the two surfaces is coated, it acts as an interferometer whose reflection depends on the exact blue frequency, measured between 15 and 40 %). The cavity mirrors are also not anti-reflection coated in the blue, so that the back of the first mirror produces a non-negligible amount of losses ($\approx 20\%$), and the inside of the mirrors act as a very low finesse cavity for the blue. This leads in particular to a standing wave pattern on the coupling beam, which makes the Rabi frequency on the upper transition extremely inhomogeneous among the atoms of the cloud (with a contrast close to 1). Despite these practical issues, this second option is chosen, and the blue beam is injected in the fundamental mode of the cavity from the top of the chamber (for 480 nm light it has a waist of 67 μm smaller than the red one, which adds to the inhomogeneity). This common-axis configuration allows both probe and coupling beam to be in σ^+ polarization, and after having optically pumped the atoms in $\left|5S_{1/2}, F = 2, m_F = +2\right\rangle$ this results in a theoretically closed system with maximum Clebsch-Gordan coefficients on the $\left|5S_{1/2}, F = 2, m_F = +2\right\rangle \rightarrow \left|5P_{3/2}, F = 3, m_F = +3\right\rangle \rightarrow \left|nD_{5/2}, F = 4, m_F = +4\right\rangle$ transition (see figure (12.5)).

12.1.3 Final setup and experimental sequence

Resonance positions, optical pumping and cavity locking point

In order to work in an interesting cooperativity range, the cavity length is locked between 16 and 20 half-widths κ away from the resonance line of the probe in the empty cavity. The probe being detuned by 25γ from the atomic transition, the locking position falls on the transmission resonance when the (two-level) atoms have a cooperativity of 200 to 250 ($\frac{2C}{\Delta} = 16-20$). The Zeeman pumping of the atoms is realized at 795 nm on the $D1$ line, with a σ^+ polarized beam on resonance with the atoms, injected from the bottom of the cavity. The locking point is chosen so that the optical pumping is close to resonant with the cavity.

Before an experiment, the cooperativity is adjusted in such a way that, after optical pumping, the two-level dispersion shifts the transmission line close to the locking point. Then the interesting lines observed during the cavity scan are in a region where the scan is the closest to linear and the fastest.

Practical setup and beampaths

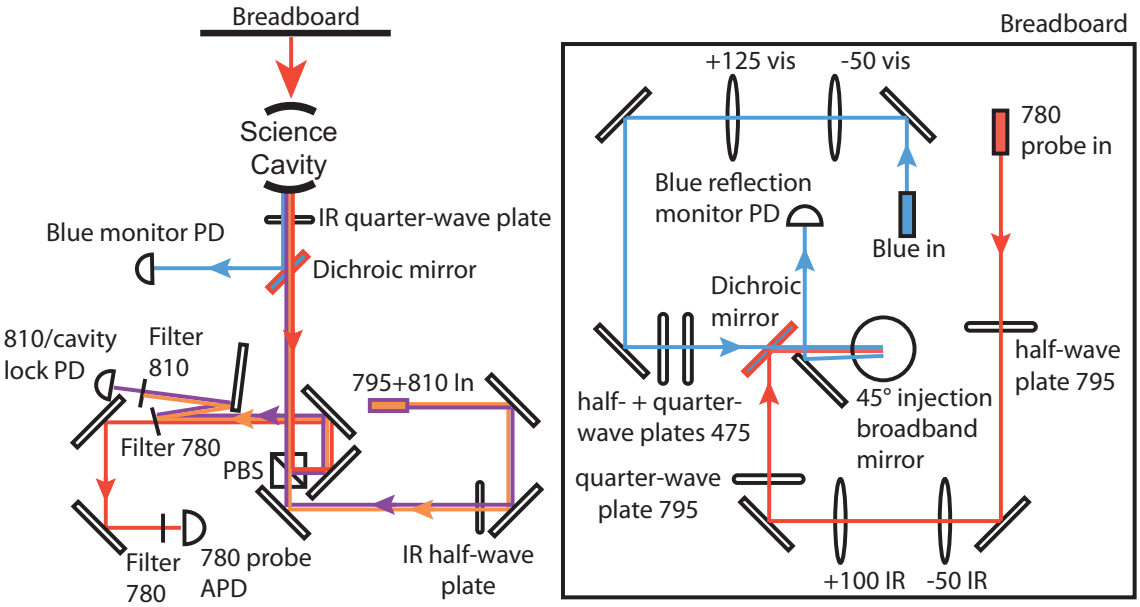

Figure 12.7: Optical layout. Left: Beampaths below the vacuum chamber. The cavity locking beam (810 nm) and the optical pumping (795 nm) are injected through the bottom mirror. A circulator is realized with the PBS and the quarter-wave plate so that light coming out of the cavity is directed towards a different arm. Output light is sorted out by filters, to extract the 810 beam for locking, and the 780 probe transmitted through the cavity to be sent on the APD. The transmitted blue beam is filtered out with a dichroic mirror, and its power can be monitored. **Right:** Setup on the breadboard, above the cavity and vacuum chamber. The probe and blue beams are mixed together on a dichroic mirror before being injected in the cavity by a broadband mirror (BB1-E02 from Thorlabs) at 45°, through a hole in the breadboard. The blue light reflected by the input viewport of the chamber is sent on a photodiode for monitoring purposes.

On the top of the vacuum chamber, a 45*45 cm breadboard is set up with the injection

optics of the probe and blue beams. Both are output from fibers, mode-matched to the cavity with an adapted telescope, set in circular polarization with waveplates, and superimposed together on a dichroic mirror (from Edmund Optics) before being sent to the cavity.

The number of optics on the blue beam's path is kept to a minimum to minimize losses. At the output of the laser it simply goes through a single-pass AOM, before being injected in the fiber that takes it to the vacuum chamber. Even then we get only around 200 mW of blue power out on top of the chamber, for approximately 400 mW at the output of the laser. The effective blue power in the cavity is then further reduced by the frequency-dependent losses induced by the viewport and the back of the upper mirror.

The probe is separated from the blue at the bottom of the cavity on a second dichroic mirror, and sent to a fast avalanche photodiode (Laser Components LCG-LCSA500-01, bandwidth DC-1MHz, responsivity ~ 0.4 V/nW).

Experimental sequence

As the full control-acquisition system was not set up yet when doing these measurements, the sequences were controlled from a standard trial version of LabView Signal Express, controlling a single National Instruments card (PCI 6115), which allows for simple sequence generation on a restricted number of channels (8).

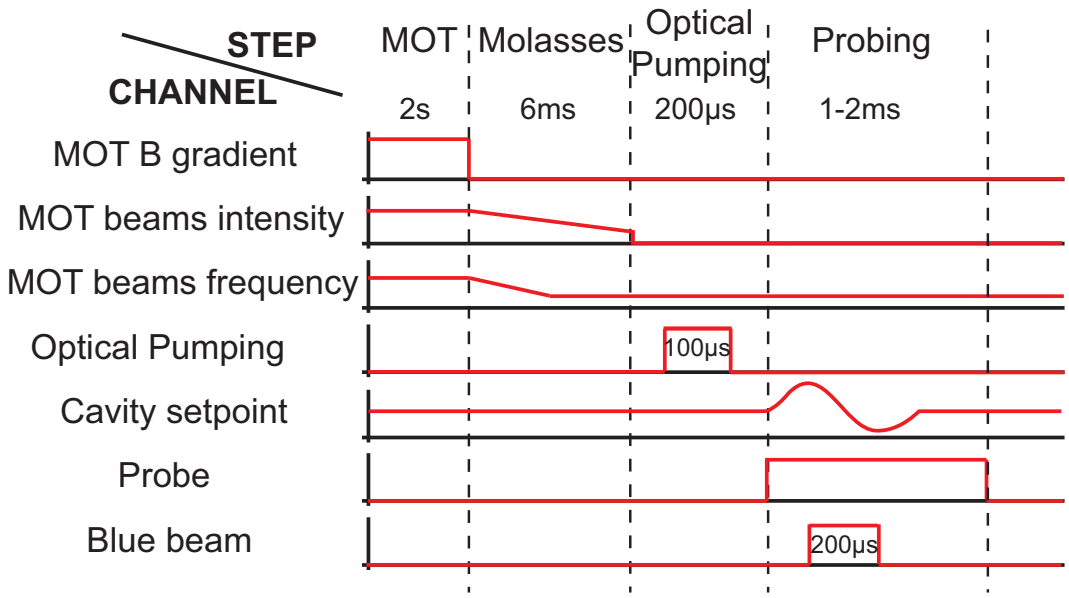

Figure 12.8: Experimental sequence. After trapping the atoms for a few seconds and cooling down to ≈ 40 μK with optical molasses, they are optically pumped with a 100 μs long pulse of intracavity 795 nm light, before the cavity is sent to oscillate. During the first cavity oscillation, in the $\approx 200\mu$s window in which the transmission line can be observed, the blue beam is shone onto the atoms.

A large atom cloud is prepared in the cavity using the standard steps (MOT trapping for $\approx$2s + molasses cooling for 6 ms). The Zeeman pumping is then sent in the cavity: an optimization of its effect on the observed cooperativity leads in these conditions to a 100 μs long optical pumping step with $\approx 30\mu$W power. This leads to an increase of a factor $\sim$2 of the effective cooperativity of the cloud, which in the end is $C \sim$200-250.

After that, in standard measurement conditions, the probe with or without the blue beam are sent to the cavity while scanning its length, the transmitted line shapes are measured on the APD, and saved on a fast oscilloscope (LeCroy WaveRunner 104MXi 1GHz, usually used with a bandwidth limit of 20 MHz and a noise filter on 2 bits because of the low signal-to-noise ratio of our raw measurements). In order to limit the possible negative effects of the strong blue beam (ionization in particular), its presence is restricted to the time window in which the transmission line is observed when scanning the cavity (200μs). The probe can be kept on without much effect, and we make sure that the transmission line is always entirely contained into this useful window (as it moves due to the change of dispersion induced by the blue beam itself). The typical sequence is described in figure (12.8).

12.1.4 Finding and calibrating the two-photon transition

Before investigating nonlinearities on the off-resonant two-photon excitation of high-n Rydberg states, two preliminary experimental steps are useful/necessary to understand correctly the behaviour of the system.

Localization of the two-photon resonance

First, once a particular Rydberg level has been chosen, the exact frequencies of the probe and coupling beam must be adjusted to locate the two-photon resonance. For a given probe frequency, the resonant coupling beam frequency can be estimated using the Rydberg states' energies calculated with quantum defects theory [1]. When the blue is sent with the right frequency into the MOT in continuous regime, two-photon resonance between the trapping beams and the blue light lead to continuous excitation of Rydberg atoms that collide and ionize, thereby emptying the trap. This is used as a first easily visible signal to detect the presence of a Rydberg transition. The fine tuning of the blue frequency is then done by switching to special sequences: the probe and cavity are kept at fixed frequencies while the blue one is scanned with the AOM [2]. If the cavity is initially locked on resonance with the probe in presence of the atoms, the crossing of the two-photon resonance creates a dip in the transmission, due to a blue-induced change in absorption or dispersion indistinctly. This is used to locate the frequency of the two-photon resonance with the probe, as shown in figure (12.9). As the resonance's width is naturally very narrow, it is mainly given by the blue power-broadening in practice. To avoid imprecision (and light shift of the measured position), we therefore decrease the blue power as much as we can to accurately measure the properties of the bare resonance.

After having searched the positions of two-photon resonances for different Rydberg states, the frequencies calculated from the Rydberg formula with quantum defects, based on [170, 171], are found to give the right position up to less than 15 MHz when comparing with the direct reading of our wavelength-meter, and to better than 4 MHz in relative (when going from one state where we know the resonance frequency to another one).

1. See appendix (A). For our states of interest ($nD_{5/2}$ with $n = 37$ to 61), the quantum defect can be taken constant ≈ 1.34 to a good approximation.

2. As the AOM generating the blue beam is in single pass we can not scan much its frequency without losing completely the fiber-coupling efficiency afterward, but a ~ 10 MHz scan can be implemented with reasonable intensity variations at the output of the fiber (less than 50 %).

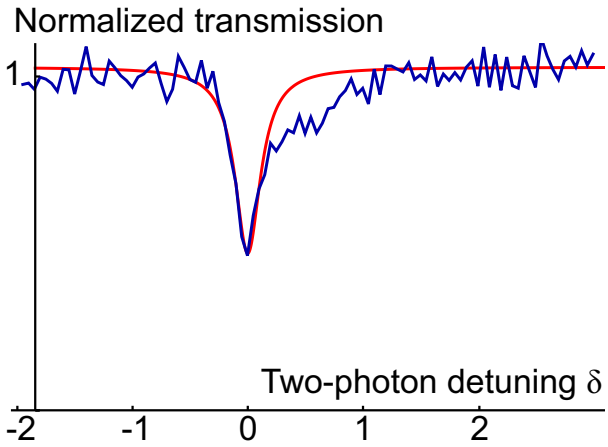

Figure 12.9: Finding the position of the two-photon resonance. Probe transmission, normalized to its value without blue beam, during a frequency scan of the blue. The probe detuning is $\Delta = -25$ and the two-photon detuning (in units of γ) is plotted on the horizontal axis. The blue power is 3 % of the maximum available (6 mW). The asymmetry of the line is due to the non optimized parameters (in particular scan speed which was too slow), leading to some ionization during the scan. The line fitted to the data in red has a halfwidth at half maximum of 0.13 γ, which gives an estimate of our effective Rydberg dephasing rate, and allows us to pinpoint the position of the bare resonance.

Parameters calibration on low-power susceptibility measurements

Before turning to Rydberg nonlinearities measurements, our system being quite complex, and several parameters of importance not being controlled in practice (like electric fields), some characteristics of the linear three-level response must first be calibrated. Because of the blue standing wave in the cloud, it is not characterized by a single Rabi frequency but rather by a wide probability distribution, with a maximum value Ω_{b0}. The other important parameter is the two-photon linewidth (or effective Rydberg coherence dephasing rate γ_{13}), which is mainly limited by technical constraints (laser noise, Doppler broadening, field fluctuations). These parameters can be extracted from measurements of the three-level susceptibility in the linear regime, on a state that is low enough in n to neglect the effect of interactions.

To take into account the blue Rabi frequency's inhomogeneity, recall that the effective susceptibility is given in the continuous medium approximation by (1.23):

$$\left\langle \frac{\sigma}{\Omega/2} \right\rangle = \int d^3\vec{r} \quad \mu(\vec{r}) \frac{\langle \hat{\sigma}(\vec{r}) \rangle}{\Omega(\vec{r})/2} \phi_n(\vec{r})^2 \tag{12.1}$$

The spatial averaging weighted by the probe mode can also be viewed as an averaging over an effective probability distribution for blue Rabi frequencies. For a uniform atomic density, this effective distribution of the blue intensity in the probe mode can be calculated exactly (considering the blue standing wave has a high contrast), to give:

$$Pr(x) = \frac{2w_b^2}{\pi w_r^2} \sqrt{\frac{1-x}{x}} \, {}_2F_1(1, 1 - \frac{w_b^2}{w_r^2}, \frac{3}{2}, x) \tag{12.2}$$

where w_b and w_r are the blue and red waists respectively (86 and 67 μm), x is the normalized blue intensity ($x = (\Omega_b/\Omega_{b0})^2$), and ${}_2F_1$ is a hypergeometric function. The

result is plotted on figure (12.10). The effective reduced susceptibility is then obtained by averaging its local expression as a function of Ω_b^2 over this distribution. It can then be used to fit the experimentally observed profiles (more details about this averaging in section 12.3.1).

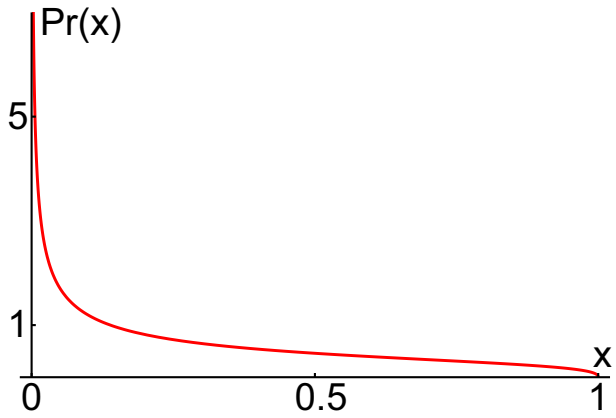

Figure 12.10: Normalized blue intensity distribution as seen by the probe mode. The function $Pr(x)$ defined by equation (12.2) is plotted versus x. The variable x is the blue intensity normalized to its maximal value in the cavity, on axis and at an antinode of the standing wave, or $x = (\Omega_b/\Omega_{b0})^2$.

The probe is coupled to the Rydberg state $n = 50$, where for low enough power the Rydberg nonlinearity is expected to play a negligible role. Typical transmission scans are represented on figure (12.11), where the line is mostly shifted when atoms are added in the cavity, and again when the blue beam is applied off-resonance.

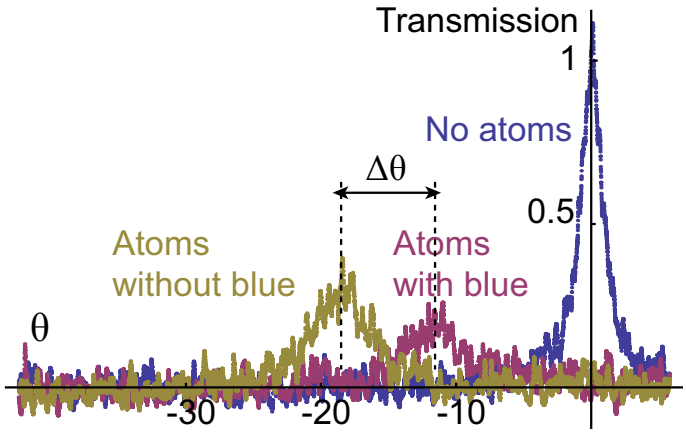

Figure 12.11: Typical cavity scan transmission signal in the linear regime. The empty cavity line is used as a reference. The addition of atoms far detuned from the probe (with $C \approx 240$ and $\Delta = -25$ here) produces mainly a shift of the line (by an amount $\approx 2C/\Delta$ in variable θ). When the blue beam is added, here with two-photon detuning $\approx$ 1.2 MHz, the line gets shifted again by an amount $\Delta\theta$.

The position and height of the observed transmission line is measured as a function of the two-photon detuning, and compared with the averaged susceptibility, using the above

defined blue intensity distribution (see figure (12.12)). From the consistent fit of several such curves for different blue powers, the experimentally estimated values of the maximum Rabi frequency and the dephasing rate are extracted.

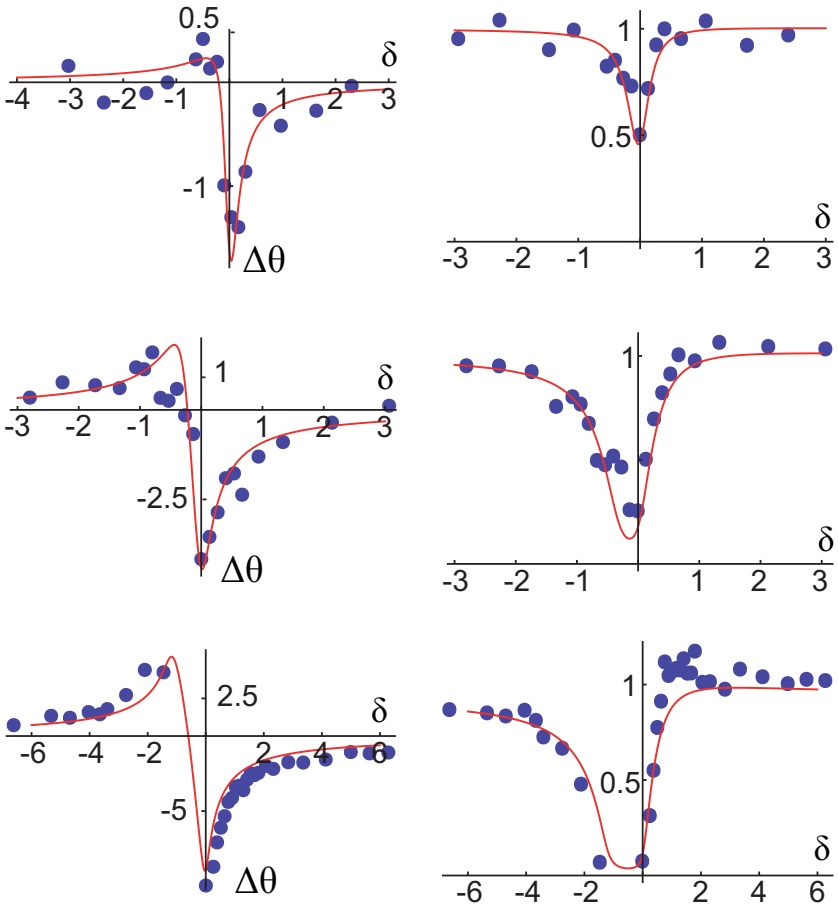

Figure 12.12: Attenuation and shift of the resonance line due to the blue coupling beam. Measurements realized on the $50D_{5/2}$ state, with low enough power to see no effect of interactions. **Left column:** blue-induced shift of the resonance line, in units of cavity linewidth, $\Delta\theta$ (the scales of the 3 graphs are not the same). **Right column:** peak transmission of the cavity line, normalized by its value without blue. From top to bottom the blue power is progressively increased to its maximum. All curves are plotted as a function of the two-photon detuning δ, with fixed probe detuning $\Delta = -25$. The consistent fit of all these curves together (red solid curves), taking into account all known variations of parameters, gives a blue Rabi frequency of $\Omega_{b0}/2 = 1.2, 2.8, 5.5$ for the first, second and third row respectively, and an effective Rydberg dephasing rate of 0.13γ.

As an additional consistency check, the blue-induced shift of the line position $\Delta\theta$ is also measured, for a fixed two-photon detuning, as a function of the blue intensity. The results are shown on figure (12.13).

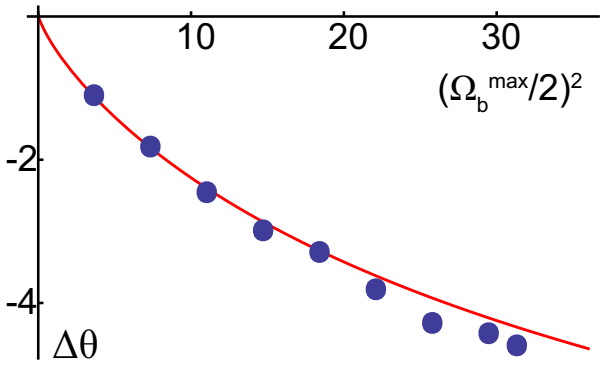

Figure 12.13: Blue-induced shift of the line position as a function of the power. The two-photon detuning is fixed at $\delta = 0.33$. The blue power is progressively increased to its maximum and the shift of the line is measured from its position without blue, in units of empty cavity linewidth, $\Delta\theta$. The solid line is the theoretical value, calculated with averaging over the blue inhomogeneity, with all parameters fixed by previous measurements (the maximum power is taken to correspond to $\Omega_{b0}/2 = 5.5$).

12.2 Observation of Rydberg-induced dispersive nonlinearities

Here, the direct experimental measurements, performed using the method and setup described above, will be presented. As their complete understanding and description turned out to be quite involved due to technical considerations, we will first focus on simply describing the observations and the way information was extracted from them. The details of the proposed explanation for the observed behaviour will be given afterward.

12.2.1 Dispersive nonlinearity observation

In order to extract the nonlinear susceptibility, the same kind of transmission curves as shown in figure (12.11) are measured for increasing probe power. As will be described in the next section, the nonlinearity was measured for several different Rydberg states. For each series of measurements, the exact value of the two-photon detuning and of the effective maximal blue Rabi frequency in the cavity are extracted from curves acquired at low power, taking into consideration the independently known information about the system (measured losses on the blue for each configuration, known scaling of the Rabi frequency with n when we change state ...). The exact detuning of the blue beam is chosen such that its addition produces mostly a shift of the line and not too much absorption (from the typical results of figure (12.12), one sees that a small positive two-photon detuning meets these criteria). It is therefore usually taken around $\delta \approx 0.3$ ($\approx$ 1MHz), after having experimentally located the resonance at low power.

State $61D_{5/2}$ is the highest reached in the Rydberg ladder, before the too low effective blue Rabi frequency prevents any precise observation. It therefore corresponds to the dataset in which the observed Rydberg nonlinearity is the strongest.

The main interesting effect observed is the transmission line's position moving closer to its position in absence of blue coupling beam, when the probe power is increased. Qualitatively, this is due to the blockade mechanisms discussed previously, which makes the effect of the blue beam on the dispersion progressively disappear.

The typical transmission lines we observe for a few different values of Y are shown in figure (12.14).

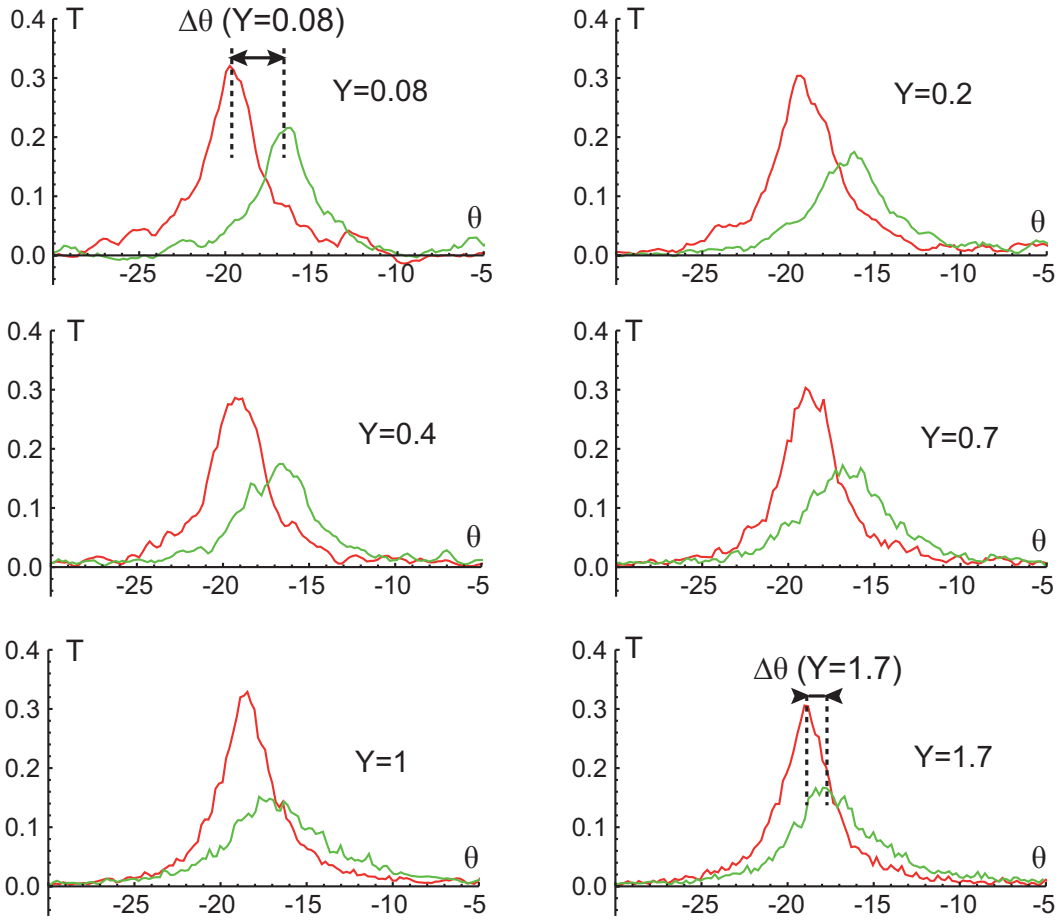

Figure 12.14: Example of nonlinear shift of the cavity resonance position. On $n = 61$, a particular sign of cavity scan is chosen and the probe power is progressively increased. Each graph shows the transmission lines with (green) and without (red) blue beam for values of Y indicated. As the level of signal compared to noise on the detector varies a lot among these acquisitions, an adapted moving average was carried out on each of them, in order to get visually comparable pictures. The number of points used for the moving average is, in the order of Y values: 1500, 1000, 600, 300, 300, 150.

In principle, in presence of large dispersive nonlinearities, it would make sense to look for appearance of bistability above a certain intensity, manifested by "jumps" in the transmission, and different response depending on the sign of the cavity detuning scan. The sign of the cavity length scan can be changed in practice by flipping the phase of the sinusoidal signal sent to the piezos, which allows for observation of two different situations (scan with increasing or decreasing θ). However, bistable behaviour as such was never observed in our system. A difference is nevertheless visible in the lineshape depending on the scan sign (difference in position and in width). These differences are mainly due to the strong influence of the Rydberg population dynamics on the observations, which happens at a timescale comparable to the line scan. This will be discussed in details in the following sections.

As the observed lines are never far from Lorentzian, the simplest way to extract mean-

ingful information from the data is to fit the lines to estimate the center position and how it evolves with the probe power. In practice, the position shift between the lines with and without blue beam for a given normalized probe power Y is measured, $\Delta\theta(Y)$. Because of dynamical effects it can differ when the cavity scan sign is flipped. For simplicity, the average of the shift $\Delta\theta$ for the two possible scan signs will first be considered.

The measurements of figure (12.14) were taken at very low power with a small step in Y in order to make sure the lowest-order dependence on the probe power was correctly captured. More measurements at higher powers were also carried out, and all the results for state $n = 61$ are summarized in figure (12.15), where the normalized blue-induced line shift $\Delta\theta(Y)/\Delta\theta(0)$ is plotted as a function of Y.

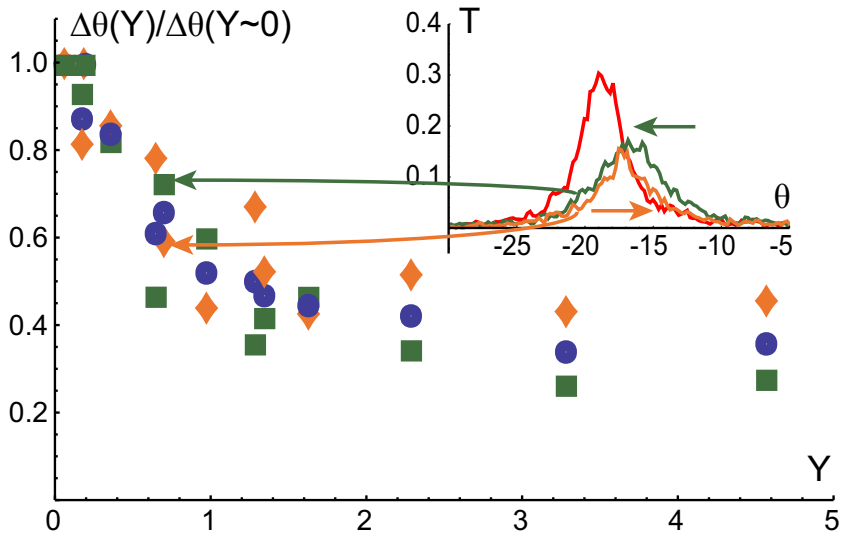

Figure 12.15: Normalized blue-induced line shift $\frac{\Delta\theta(Y)}{\Delta\theta(0)}$ as a function of Y on $n = 61$. The data from two different acquisition sets are combined (one with small Y step up to $Y \approx 1.5$, the other with larger Y steps until $Y \approx 4.5$. Here, for practical reasons, the normalization is done on the value of the shift for the lowest probe power used ($Y = 0.07$ and $Y = 0.2$ respectively for the two datasets). The graph presents the values of the shifts for increasing θ scan (orange diamonds), decreasing θ (green squares), and average of both (blue circles). Inset: one example of the difference between observed lines for scans with increasing or decreasing θ, for $Y = 0.7$.

The overall trend to extract from figure (12.15) is that the blue-induced shift is reduced by the nonlinearity, with a measurable strong initial slope, and a clear saturation behaviour for $Y > 1.5$. This can be understood qualitatively by noticing that, from a simple model like equation (11.21) in a uniform system, the value we measure would just directly be:

$$\frac{\Delta\theta(Y)}{\Delta\theta(0)} = \frac{Re\left(\frac{\sigma}{\Omega/2}(Y)\right) - Re\left(\frac{\sigma}{\Omega/2}\right)_{2lev}}{Re\left(\frac{\sigma}{\Omega/2}\right)_{3lev} - Re\left(\frac{\sigma}{\Omega/2}\right)_{2lev}} = 1 - p_b \tag{12.3}$$

The difference to 1 on the measurements would in this case directly inform us on the blockaded fraction of the cloud p_b. As discussed earlier, this quantity is supposed to have a lowest-order linear dependence on the probe intensity, and a saturation at high powers, which corresponds to what is observed.

12.2.2 Proof of the Rydberg origin of the non-linearity

The interpretation of the acquired transmission curves being not completely straightforward, several tests can be carried out to verify that what is observed is really due to Rydberg interactions effects in the cloud, and that it can be interpreted as was proposed in the previous chapter.

Dependence on the Rydberg level

First, as an effect of the van der Waals interactions between Rydberg atoms, the observed nonlinearity should strongly depend on the addressed Rydberg level. This is verified by repeating the same measurements for states $n = 56, 50, 46, 37$. The results are plotted in figure (12.16), showing that by increasing the Rydberg principal quantum number, the nonlinearity gets stronger and stronger.

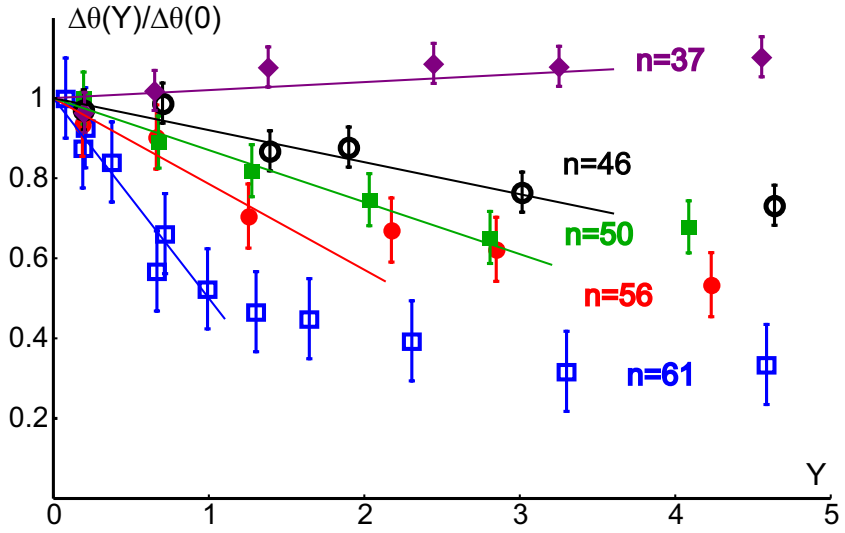

Figure 12.16: Normalized blue-induced line shift $\frac{\Delta\theta(Y)}{\Delta\theta(0)}$ as a function of Y on $n = 37, 46, 50, 56, 61$. The average shift (increasing and decreasing θ scans) is plotted, normalized by the extrapolated value in $Y = 0$. For each state the line corresponding to the estimated lowest-order ($\chi^{(3)}$) behaviour is also shown for low power.

From the low-power transmission curves, the values of the two-photon detuning, the maximum blue Rabi frequency in the cavity, and the Rydberg damping rate are estimated for each state. Table (12.1) summarizes the estimated consistent values for all acquisitions.

State n	δ	$\Omega_{b0}/2$	Rydberg dephasing rate (in γ)
37	0.3	8	0.15
46	0.25	5.9	0.15
50	0.28	5.2	0.15
56	0.35	3.8	0.15
61	0.3	3.2	0.15

Table 12.1: Parameters of the acquisitions for each Rydberg state.

The values in this table are, within our precision, compatible with the preliminary measurements of section 12.1.4. The differences come from the precision of the procedure used to extract the parameters from the low-power curves (we try to get consistent agreement for all the relevant curves together with a small number of free parameters, knowing the scaling of Ω_b with n for example), and from a long time between the two measurements, during which parameters drifted (e.g. the blue laser power) or were changed (e.g. the exact cavity resonance used, which changes the blue resonance inside it).

Equations (12.3) and (11.15) show that the initial slopes of the graphs in figure (12.16) directly measures the $\chi^{(3)}$, which here should be proportional to n_b as defined in equation (11.11). The quantitative interpretation of these slopes will be proposed in the following section. To start with, the dependence of these slopes on n can simply be verified, as predicted by the fact that $n_b \propto \sqrt{C_6} \propto (n^*)^{5.5}$. The contribution of the natural three-level nonlinearity is however not completely negligible here, but can be calculated rather precisely with the known information on the system (table (12.1)), to correct the observed slopes for it. The theoretical slopes in absence of interactions are calculated by averaging over the blue intensity distribution ($Pr(x)$) the $\chi^{(3)}$ expansion of the three-level coherence. For consistency the dynamics are also taken into account, as described in section 12.3.2. This shows that the natural nonlinearity would lead to much smaller slopes than the ones observed here, and with opposite sign.

State n	Measured slope	Calculated without interactions
46	-0.08 ± 0.02	0.008
50	-0.125 ± 0.03	0.011
56	-0.23 ± 0.05	0.025
61	-0.52 ± 0.04	0.04

Table 12.2: Observed initial slopes of the normalized shift versus Y for the different states, and calculated contribution of the three-level non interacting system for the same parameters.

When changing from one Rydberg state to another, not only the C_6 changes but also the blue Rabi frequency, which perturbs the scaling of n_b with $(n^*)^{5.5}$. The measured slopes are thus also corrected for this small effect [3]. Once these two corrections have been applied, the slope is plotted versus n^* in log-log scale in figure (12.17).

On the full range of Rydberg levels studied, the behaviour varies widely from qualitatively nothing really resolvable happening on $n = 37$ to a slope of $\frac{\Delta\theta(Y)}{\Delta\theta(0)}$ versus Y of ≈ 0.5 for $n = 61$. Due to the noisiness and nature of the measurements, these slopes can not be measured with very high precision, but on a large enough range like in figure (12.17), the overall scaling is clear. The small positive slope found for $n = 37$ is not really meaningful (it is to our precision close to 0, which is explained by a compensation of a weak Rydberg nonlinearity by the natural $\chi^{(3)}$), and it is therefore discarded from the data in figure (12.17) to avoid contamination. The result is a fitted scaling with a slope of 5.7±0.5, compatible with a power-law of exponent 5.5.

3. The value of the observed slopes are renormalized by the known dependence of n_b on Ω_b, for a value of the blue Rabi frequency taken as the average of its distribution for each state. The modification is by less than 10 % relatively from one state to another. The additional change induced on the Rydberg population (which also appears in the value of the slopes) has only very weak effect after averaging over the probe mode, and it is thus neglected here.

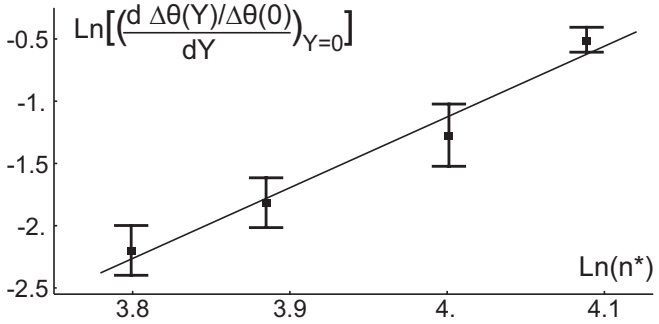

Figure 12.17: Dependence of the corrected initial slope of the graphs of normalized blue-induced shift with n. The initial slope of the graphs $\frac{\Delta\theta(Y)}{\Delta\theta(0)}$ is plotted in log-log scale for the states $n = 46, 50, 56, 61$ to extract the power law. The line is a fit, giving a slope of ≈ 5.7.

Dependence on the density

A critical check to ensure that the observed effect is really due to two-body interactions and not to single-atom behaviour is to probe its dependence on the atomic density. The slopes measured here, being theoretically proportional to n_b, should be proportional to the density.

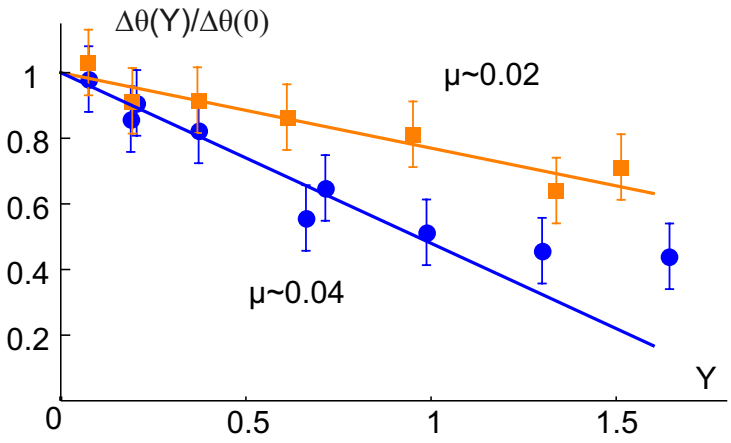

Figure 12.18: Variation of the normalized blue-induced shift with Y for two different values of the density. The measurements of line position versus Y are repeated with two different configurations. One is with a MOT obtained with low-loading, immediately after molasses, and the second one obtained with high loading is prepared and measured only after 9.5 ms time of flight. The densities in the two cases are estimated to 0.04 (blue circles) and 0.02 (orange squares) atoms/μm^3 respectively.

In practice, modifying the density of the cloud is not immediate, because by default the MOT is loaded in a saturated density regime, so that tuning the parameters of the atom source does not really affect the cloud's density. What is done instead is to let the cloud expand for a 9.5 ms time of flight after preparation, before the measurements. This decreases the density by a factor estimated to ~ 2 (from cloud imaging in the two configurations), but also changes the cooperativity. Starting from a trap loaded with much

more atoms, but that has initially approximately the same density, the loading is adjusted so that after time of flight the cooperativity remains ≈ 230, with lower density.

The results of this comparison, on $n = 61$, on measurements with $Y < 1.5$, are shown on figure (12.18). The measured change of slope is compatible with a factor 2, which confirms the direct dependence on the density of the characterized $\chi^{(3)}$.

Other verifications to rule out ions

An important issue when exciting atoms to Rydberg states, especially the ones with attractive interactions, is that they can undergo ionizing collisions, leading to cascades where a non negligible fraction of the cloud is ionized [172]. The presence of ions in the cloud can have comparable effects to the one of Rydbergs. In order to make sure that this is not a trouble in our experimental configurations, several checks are performed.

Firstly, for high enough probe power a qualitative change is clearly observable in the shape of the transmission lines in presence of the blue beam (presence of sudden "jumps" in the transmission) that is attributed to ionization cascades after investigations. All the measurements presented here are performed with probe power lower than this threshold.

Secondly, ions have irreversible effects. Contrary to Rydberg atoms that decay back to the ground state, when ions are created their effect on the cloud is a long-term one. This leads to strong asymmetry in the absorption during the resonance crossing that is observed in some configurations, but not the useful ones. To monitor the creation of ions, the blue beam can also be switched off in the middle of a line scan, and the transmission measured afterward compared to the one obtained without using the blue beam at all. A discrepancy can only originate from long-term irreversible effects induced by the blue beam in the beginning of the scan, which we relate to ionic excitations.

Finally, from a physical point of view, one can estimate the timescales at which ionization cascades can happen and compare it with our scan rate [173]. Experimentally, crossing completely the probe resonance takes around 20 μs. Scanning much slower ($\sim$100 μs instead of 20), ionization avalanches are clearly triggered, leading to jumps in the transmission and irreversible modification of the effective cooperativity. It is clearly not the case at the scan speed used for the measurements. These observations are also consistent with the estimated ionization times from [173]. The scan can also be made faster to see that there is no big qualitative difference. However as the observed nonlinearity is largely determined by the Rydberg excitation dynamics during the line scan (as discussed in the following section), scanning faster is supposed to have a non-zero effect even in the absence of ion, so that this does not really constitutes a good criterion.

12.3 Quantitative interpretation of our observations

The description of the observed transmission curves is made difficult by at least two main effects, the blue power inhomogeneity and the dynamics of the Rydberg state, and the interplay between the two. We developed a model to approximately take into account these two effects and compare the observed nonlinearities to theoretical predictions.

In order to understand the values of the initial slopes of the graphs $\Delta\theta(Y)/\Delta\theta(0)$, the system must be considered in the $\chi^{(3)}$ limit. As the natural nonlinearity (without interactions) of the three-level system is likely to be small but not completely negligible, its contribution must be taken into account. A careful adiabatic elimination of the intermediate level in the Bloch equations without interactions (see Appendix B) leads to the

following approximate expression of the local time-dependent atomic coherence:

$$\frac{\sigma}{\Omega/2}(t) = \frac{1}{\Delta+i}\left[1+\frac{\Omega_b^2/4}{(\Delta+i)(\delta_e+i\gamma_{13e})}-\sigma_{33}(t)\left(1+\frac{\Omega_b^2/2}{\Delta(\delta_e+i\gamma_{13e})}\right)\right] \tag{12.4}$$

where $\delta_e = \delta + \frac{\Omega^2-\Omega_b^2}{4\Delta}$ and $\gamma_{13e} = \gamma_{13} + \frac{\Omega^2+\Omega_b^2}{4\Delta^2}$. This gives the following lowest-order expansion in probe intensity:

$$\begin{aligned}\frac{\sigma}{\Omega/2}(t) &= \frac{1}{\Delta+i-\frac{\Omega_b^2/4}{\delta+i\gamma_{13}}}-\frac{\Omega^2\Omega_b^2/16}{\Delta-i}\frac{1}{((\Delta+i)(\delta+i\gamma_{13})-\frac{\Omega_b^2}{4})^2}\\ &\quad -\sigma_{33}^{(2)}(t)\left(\frac{1}{\Delta+i}+\frac{\Omega_b^2/2\Delta}{(\Delta+i)(\delta+i\gamma_{13})-\frac{\Omega_b^2}{4}}\right)\end{aligned} \tag{12.5}$$

where $\sigma_{33}^{(2)}$ is the first-order dependence of the excited level population, proportional to the intensity.

These two expressions are only valid after several approximations that rely on the parameter range of the experiments (values of detunings, Rabi frequencies, dampings), and on the timescale at which the dynamics will be described (here we effectively made the approximation that the slowest quantity in the various Bloch equations is the Rydberg population and that all others follow it). More details are given in Appendix B.

The first term in equation (12.5) is the usual linear three-level susceptibility, the second is the nonlinearity due to the intrinsic structure of the three-level system, and the third is a "pumping" nonlinearity coming from the buildup of the long-lived Rydberg population that removes atoms from the lowest level where they interact with the probe. Numerical estimates of the two nonlinear terms with our range of parameters show that the first one is very small compared to the pumping one (factor ≈ 100), and can therefore be neglected.

As a result, the natural $\chi^{(3)}$ is described by a term proportional to $\sigma_{33}^{(2)}$ in the dynamical regime, and the same is actually expected for the Rydberg nonlinearity, for which equation (11.15) shows that the nonlinear part of the reduced susceptibility is $n_b\sigma_{33}^{(2)}\left[\left(\frac{\sigma}{\Omega/2}\right)_{2lev}-\left(\frac{\sigma}{\Omega/2}\right)_{3lev}\right]$. The total nonlinear susceptibility to be considered in this regime is thus:

$$\frac{\sigma}{\Omega/2}^{(3)}(t) = -\sigma_{33}^{(2)}(t)\left(\frac{1}{\Delta+i}+\frac{\Omega_b^2/2\Delta}{(\Delta+i)(\delta+i\gamma_{13})-\frac{\Omega_b^2}{4}}+n_b\left(\frac{1}{\Delta+i}-\frac{1}{\Delta+i-\frac{\Omega_b^2/4}{\delta+i\gamma_{13}}}\right)\right) \tag{12.6}$$

The overall behaviour of the system in this regime is therefore entirely determined by the Rydberg population and its dynamics. The latter can be relatively slow compared to the timescales of the experiments, and depends on the blue and probe powers. This is what makes the description of the system difficult.

12.3.1 Blue inhomogeneity and susceptibility response time

As was already introduced, the mode of the blue beam being highly inhomogeneous leads to a necessary averaging of all quantities, even without interactions between atoms. Before even looking at the nonlinearity, to describe properly the linear regime, the first term of equation (12.5) must be averaged over the mode, as was done for the results of section 12.1.4. For quantities having a local dependence on the blue power [4], it is equivalent

4. As discussed at the end of section 12.3.2 and in Appendix B, it is in principle more complicated for the interaction term as even its local value involves a long-range spatial average.

to spatially average them in the probe mode, or to use the relative blue power distribution $Pr(x)$ given in section 12.1.4. This allows therefore, for a given time, or for the steady state, to get the effective value of the natural nonlinearity of the system in the cavity for example.

However, as the line must be scanned fast enough not to ionize the medium, what is observed is not the lineshape resulting from a given constant nonlinear susceptibility, but rather the transmission due to a susceptibility that adapts with its own dynamics while the probe progressively enters the cavity. The response time of the system can be estimated and depends strongly on the blue power, which rules the dynamics of the Rydberg population.

In a simplified model, this response time τ in a given configuration is estimated from the steady-state value of the Rydberg population σ_{33}^{∞}, and its initial slope in response to a sudden application of the beams at $t = 0$:

$$\tau = \frac{\sigma_{33}^{\infty}}{\frac{d\sigma_{33}}{dt}(t=0)} \tag{12.7}$$

As the creation rate of Rydberg population is calculated at initial time where there are by definition no excited atoms, it can in any case be calculated without interactions (it does not depend on the strength of the interactions). The steady-state population, however, will be affected by the blockade effects for strong interactions. However in the $\chi^{(3)}$ regime, as the population without interactions is already proportional to the probe intensity in the lowest order, it is not modified by interactions at this order, and the response time of the dynamical susceptibility can be calculated by forgetting about interactions. In the lowest order where it does not depend on the red intensity, it is easy to show that it is given locally by the blue-power enhanced decay rate:

$$\tau_{loc} = \left(2\gamma(\gamma_{33} + \frac{\Omega_b^2/4}{\Delta^2})\right)^{-1} \tag{12.8}$$

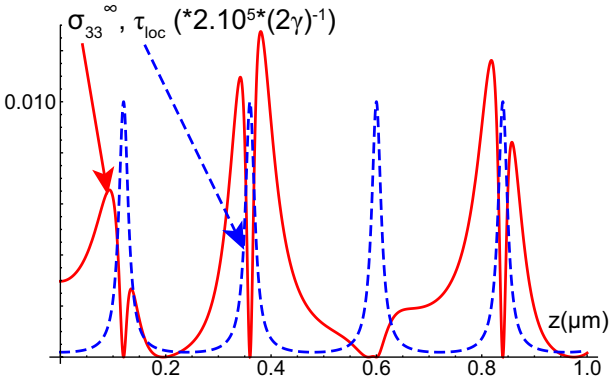

Figure 12.19: Spatial variations of the Rydberg population (calculated without interactions), and its settling time. Neglecting interactions, the Rydberg population is plotted on the cavity axis as a function of z, as well as the response time given by (12.8). The detunings and damping rates are the ones of the experiment, the maximum blue Rabi frequency is $\Omega_{b0} = 8$, and the maximum red one is $\Omega_0 = 0.3$. The peaks of the response time correspond to the nodes of the blue standing wave, separated by $480/2 = 240$ nm.

In the cavity, this local time changes a lot along the blue standing wave, so that the cloud exhibits strong short-range modulations of both the steady-state Rydberg population and its settling time, as illustrated qualitatively in figure (12.19).

The important quantity is then the effective rising time of the average susceptibility in the mode τ_{eff}, given by:

$$\tau_{eff} = \frac{\langle \sigma_{33}^{\infty} \rangle}{\left\langle \frac{d\sigma_{33}}{dt}(t=0) \right\rangle} = \frac{\langle \sigma_{33}^{\infty} \rangle}{\left\langle \frac{\sigma_{33}^{\infty}}{\tau_{loc}} \right\rangle} \tag{12.9}$$

where $\langle\rangle$ means here the spatial averaging over the probe mode.

An approximate expression for this time can be derived within the same level of approximation as for equations (12.5) and (12.6), in the lowest order in probe power (see Appendix B):

$$\begin{aligned} \gamma\tau_{eff} \approx & \; Im\left[\frac{\left(1+\sqrt{1+\frac{\Omega_{b0}^2}{4\gamma_{33}\Delta^2}}\right)^{-1} - \left(1+\sqrt{1-\frac{\Omega_{b0}^2}{4(\Delta+i)(\delta+i\gamma_{13})}}\right)^{-1}}{\gamma_{33}(\Delta-i)+(\delta+i\gamma_{13})}\right] * \\ & Im\left[\frac{1-2\left(1+\sqrt{1-\frac{\Omega_{b0}^2}{4(\Delta+i)(\delta+i\gamma_{13})}}\right)^{-1}}{\Delta-i}\right]^{-1} \end{aligned} \tag{12.10}$$

The evolution of this average response time of the susceptibility with the maximum blue Rabi frequency is illustrated in figure (12.20). It is therefore on the order of a few microseconds in the experimental conditions.

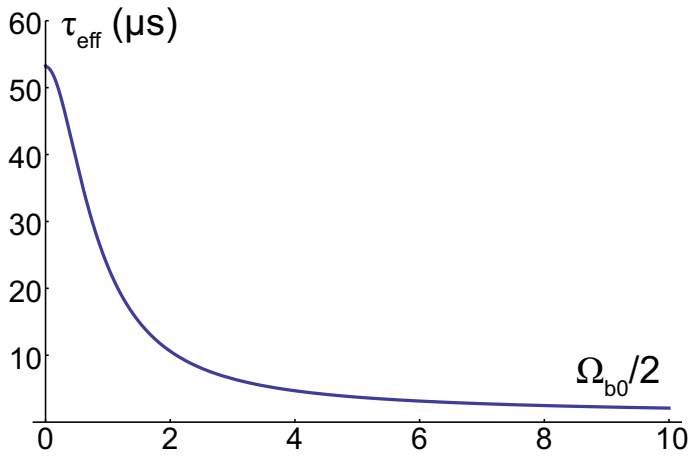

Figure 12.20: Effective susceptibility response time as a function of the blue Rabi frequency. The expression of τ_{eff} from equation (12.10) is plotted as a function of $\frac{\Omega_{b0}}{2}$ for realistic parameters $\Delta = -25$, $\delta = 0.3$, $\gamma_{13} = 0.15$ and $\gamma_{33} = 0.0005$ (corresponding to a ≈ 55 μs population lifetime).

12.3.2 Realistic model of the lowest-order nonlinear response

When the probe intensity increases in the cavity, the nonlinear effective reduced susceptibility $\left\langle \frac{\sigma}{\Omega/2} \right\rangle^{(3)}$ will therefore evolve towards a certain steady-state value $\left\langle \frac{\sigma}{\Omega/2} \right\rangle^{(3)}_{\infty}$, with dynamics given by the response time calculated above. The simplest way to take into account its dynamics in a model would therefore be to write the following differential equation:

$$\frac{d}{dt}\left\langle \frac{\sigma}{\Omega/2} \right\rangle^{(3)} = -\frac{1}{\tau_{eff}}\left(\left\langle \frac{\sigma}{\Omega/2} \right\rangle^{(3)} - \left\langle \frac{\sigma}{\Omega/2} \right\rangle^{(3)}_{\infty}\right) \tag{12.11}$$

The value of $\left\langle \frac{\sigma}{\Omega/2} \right\rangle^{(3)}_{\infty}$ can be calculated from the previous models, after integration over the probe mode, to give a complicated expression (given in totality in Appendix B) which can simply be written as $\left\langle \frac{\sigma}{\Omega/2} \right\rangle^{(3)}_{\infty} = aX$, as the lowest-order nonlinearity is proportional to the intracavity probe power X.

During the actual experiments, the cavity detuning is scanned with time at a constant rate $\frac{d\theta}{dt} = \frac{1}{R}$ (R is the time it takes to scan one cavity linewidth, which is $\approx 3.8\mu$s in our case). In order to model the observations, one must then look at the time evolution of the solution of the following coupled equations:

$$\frac{d}{d\theta}\left\langle \frac{\sigma}{\Omega/2} \right\rangle^{(3)} = -\frac{R}{\tau_{eff}}\left(\left\langle \frac{\sigma}{\Omega/2} \right\rangle^{(3)} - aX(\theta)\right) \tag{12.12}$$

$$X(\theta) = \frac{Y}{\left|i \pm \theta - 2C\left(\left\langle \frac{\sigma}{\Omega/2} \right\rangle_{3lev} + \left\langle \frac{\sigma}{\Omega/2} \right\rangle^{(3)}(\theta)\right)\right|^2} \tag{12.13}$$

Here $\left\langle \frac{\sigma}{\Omega/2} \right\rangle_{3lev}$ is the linear part of the susceptibility, which is constant. The signs + and - correspond to the case of cavity detuning increasing and decreasing with time respectively. Solving numerically these equations to find $X(\theta)$ allows to reproduce directly the observed transmission during the experimental scans. The behaviour obviously depends on the ratio τ_{eff}/R: for very slow scan, the susceptibility will always be at its steady-state value for the current power and the usual nonlinear deformation of the lineshape will be observable. If the cavity is scanned much too fast on the other hand, the Rydberg population will have no time to adapt to the intracavity power and thus we will just always see the linear lineshape. However, when the two timescales become comparable, as it is the case in the experiment (see figure (12.20)), a different behaviour is observed, that fits qualitatively with the experimental observations.

It is in particular possible to explain qualitatively the observed difference between the two configurations with opposite cavity scan signs. As the susceptibility takes some time to adapt to the probe power entering the cavity, and in turns modify the effective position of the resonance, the line is delayed and smoothed, "lagging" behind the shape it would have had if the nonlinearity was fast. See figure (12.21) for examples of the different regimes in the solution of these equations.

This also explains why no real bistable behaviour can be obtained, as this by definition requires a very fast adaptation of the susceptibility to the probe power.

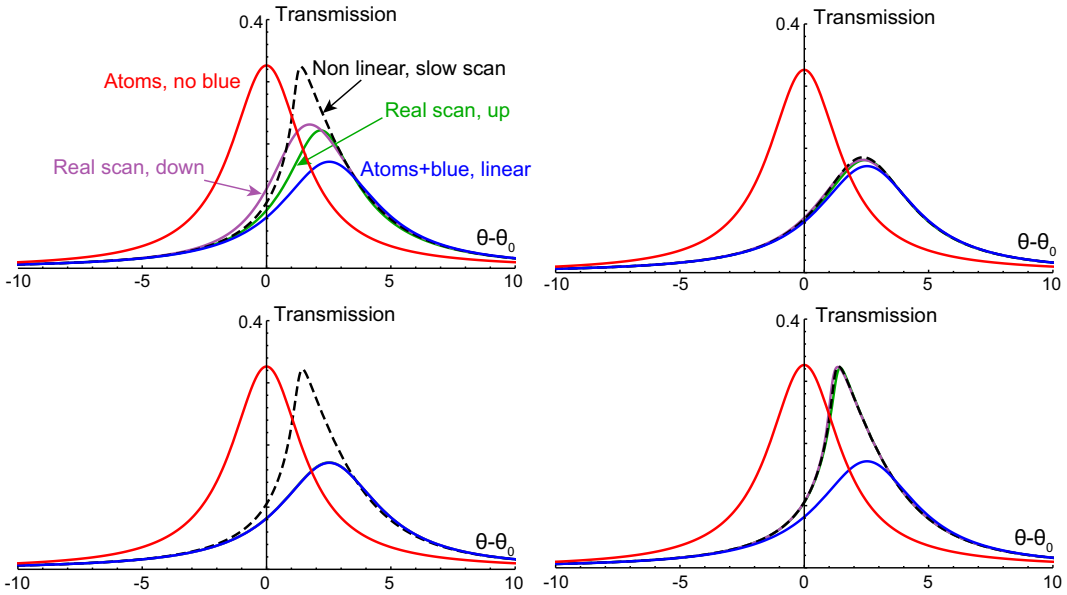

Figure 12.21: Dynamical results of the model for the experimental cavity scans. The parameters are the ones estimated on state $n = 61$. In red, centered on zero on all graphs, is the cavity line with atoms but no blue beam, with center position θ_0 taken as a reference. In blue the cavity line with linear three-level susceptibility (with blue). **Upper left corner:** real experimental conditions of scan, with $Y = 0.2$. The dashed line is what would be obtained by neglecting the dynamics (steady-state response). In green the scan at real speed (up is for increasing θ), and in purple the reverse scan. **Upper right:** same conditions, with $Y = 0.05$. **Lower left:** scan 100 times faster, for $Y = 0.2$ (both scans are superimposed on the linear one). **Lower right:** scan 100 times slower, $Y = 0.2$ (both scans are almost on the steady-state one).

Quantitative estimation of the slopes

To evaluate quantitatively the initial slopes of the graphs $\Delta\theta(Y)/\Delta\theta(0)$, the experimental procedure used to measure the line shift must be taken into account: the two lines (up and down scans) are fitted to Lorentzians to determine their center position, and the average is taken. Interestingly, it is possible to derive an analytical formula for the slope of such quantities versus Y in the theoretical model developed above (see Appendix B).

The theoretical slopes, s_{up} and s_{down} for increasing and decreasing θ, are:

$$s_{up} = S\frac{Re[a](2\beta_5+9\beta_3+20\beta_1+5\beta_{-1})+2Im[a](\beta_4+4\beta_2+7\beta_0)}{48\sqrt{\pi}Re\left[\left\langle\frac{\sigma}{\Omega/2}\right\rangle_{2lev}-\left\langle\frac{\sigma}{\Omega/2}\right\rangle_{3lev}\right]\left(1-2CIm\left[\left\langle\frac{\sigma}{\Omega/2}\right\rangle_{3lev}\right]\right)^2} \quad (12.14)$$

$$s_{down} = S\frac{Re[a](2\beta_5+9\beta_3+20\beta_1+5\beta_{-1})-2Im[a](\beta_4+4\beta_2+7\beta_0)}{48\sqrt{\pi}Re\left[\left\langle\frac{\sigma}{\Omega/2}\right\rangle_{2lev}-\left\langle\frac{\sigma}{\Omega/2}\right\rangle_{3lev}\right]\left(1-2CIm\left[\left\langle\frac{\sigma}{\Omega/2}\right\rangle_{3lev}\right]\right)^2} \quad (12.15)$$

where the β_n's are special Meijer functions depending only on S.

$$\beta_n = G_{13}^{31}\left(\begin{matrix} -\frac{n}{2} & - & - \\ 0 & \frac{1}{2} & 3-\frac{n}{2} \end{matrix}\middle| S^2\right) \tag{12.16}$$

$$S = \frac{R\left(1-2CIm\left[\left\langle\frac{\sigma}{\Omega/2}\right\rangle_{3lev}\right]\right)}{\tau_{eff}} \tag{12.17}$$

S corresponds to the ratio of the time it takes to scan the cavity across the line (in presence of atoms and blue beam) to the system's response time.

In order to evaluate numerically the average slope $\frac{s_{up}+s_{down}}{2}$, the value of the parameter a is required. This quantity gives the relation between the total averaged $\chi^{(3)}$ and the intracavity power X, and depends on all experimental parameters. It is evaluated for the different states using the values of the parameters from table (12.1), the measured cooperativity ($C = 230 \pm 5$ for all cases), the population decay rate $\gamma_{33} = 0.0005$ [5], and the estimated density $\mu \approx 0.04$ atoms/μm^3.

The effective C_6 coefficients for all states are also required to evaluate the Rydberg nonlinearity. As already discussed, the effective C_6 is obtained after an averaging over the angles and various molecular potentials for D states. Here, as the measured quantity scales with $n_b \propto \sqrt{C_6}$, the $\sqrt{C_6^i}$ are averaged to find an effective $\sqrt{C_6}$, instead of averaging directly the C_6^i. The obtained values for the states of interest are summarized in table (12.3). The numerical coefficients agree with the ones calculated in [145] within 20 % (due to the difference in the averaged quantity).

State n	Effective C_6/γ (μm^6)
46	2430
50	4980
56	14790
61	35700

Table 12.3: Effective C_6 coefficients, obtained by averaging $\sqrt{C_6^i}$.

Given all the parameters, a can in principle be evaluated. However, the spatial averaging that this involves requires particular care. The natural part of the nonlinearity (without interactions) is local, and thus has a single well-defined value after averaging over the blue power distribution. The interaction part is more problematic: in the equations of section 11.1.2, the calculation of the third-order nonlinearity to define n_b implicitly assumes that all atoms inside a Rydberg sphere see the same blue Rabi frequency.

State n	n_b
46	17.5-2.7 i
50	25.7-4.1 i
56	45.1-7.3 i
61	76.5-14.9 i

Table 12.4: Values of n_b for the average blue power.

5. the resulting calculated slopes change by $\sim 10\%$ if this approximate value is changed by a factor 2.

For orders of magnitude, the values of n_b corresponding to the average blue Rabi frequency for the different states characterized are given in table (12.4). However for precise numerical evaluations, the spatial integral with a highly inhomogeneous blue is therefore not so simple, and the way to proceed with this averaging of the interaction $\chi^{(3)}$ can lead to different levels of approximations (see Appendix B). Using the most precise way of estimating a, the numerical values of the theoretical slopes are summarized in table (12.5) and compared to the experimentally measured ones.

State n	Calculated $\frac{s_{up}+s_{down}}{2}$	Measured slope
46	-0.08	-0.08
50	-0.12	-0.125
56	-0.27	-0.23
61	-0.57	-0.52

Table 12.5: Comparison between the experimentally measured slopes of the graphs $\frac{\Delta\theta(Y)}{\Delta\theta(0)}$ and the most accurate theoretical evaluation, taking into account blue inhomogeneity, Rydberg population dynamics, and the natural three-level nonlinearity.

The agreement with the experiment is very satisfactory, as there is anyway at least of the order of 10 % imprecision on the estimated values. This confirms that, in order to understand the main features of our observations for low-power nonlinear dispersion, it is necessary, and sufficient, to take into account the dynamical response of the medium (here with the simple "response time" model), the effect of the inhomogeneity of the blue mode (leading to an averaging of all quantities), and the contribution of the non-interaction induced nonlinearity.

12.3.3 Saturation behaviour

Investigating the very low-power nonlinearities in the Rydberg cloud, the $\chi^{(3)}$ range was the most relevant. In the higher-order excitation range, Rydberg spheres start to interact with each others and spatial correlations develop in the cloud, making its behaviour more complex. As is visible in figure (12.16), the nonlinear shift saturates very quickly beyond the initial linear decrease. Few tentative ideas are proposed here about the behaviour in the saturated regime.

In the dispersive regime, the interpretation of the nonlinearity given in section 11.2.2 has a simple physical meaning, described by a single crucial parameter p_b, the probability for an atom to be Rydberg-blockaded by one of its neighbours. We may assume that this interpretation could still hold for higher orders of the nonlinearity. One would therefore naively expect that for strong enough excitation, blockade spheres would pack up densely to fill all the volume, the susceptibility would return to the two-level value, so that the normalized shift should tend to zero.

However on the experimental data, the observed shift seems to saturate before reaching zero. Though this behaviour is not perfectly certain with our precision, different mechanisms can be thought of, which could explain that the experimentally measured position of the line is indeed not expected to come back completely to its two-level value.

Even in the strong excitation regime, the Rydberg population can be quite slow to establish, especially in some places in the cloud, so that the full blockade can take some time to be achieved. The already discussed dynamical effects could be one reason why the

observed lines would never fully come back to the position they have without blue.

Another possible reason for which the blockade effect on the observed shift could not be perfect is the nature of the blockade spheres. In the low-power regime, n_b was defined as the number of atoms blockaded by one of these spheres. In the saturated regime, it should rather be considered as the number of atoms potentially able to blockade a single specific one. The average blockade probability for an atom would then be the probability that at least one atom among the n_b around it is excited:

$$p_b = 1 - (1 - \sigma_{33})^{n_b} \approx 1 - e^{-n_b \sigma_{33}} \tag{12.18}$$

where σ_{33} is the excitation probability in the cloud, in presence of interactions (considered as uniform for simplicity here). The second expression is approximate for $\sigma_{33} << 1$, which is ensured spontaneously by the blockade for strong excitation (for high enough density).

Now what we observe is the effect of the excited population on the coherence of the atoms around, but the excitation blockade takes place directly between the populations of the atoms. The same way n_b was physically defined in equation (11.22), one can define another number n_b', quantifying the effect of a Rydberg excitation on the atomic populations of its neighbours directly:

$$\int \left[\langle\hat{\sigma}_{33}(R)\rangle - \langle\hat{\sigma}_{33}(\infty)\rangle\right] \mu 4\pi R^2 dR = n_b' \left[\langle\hat{\sigma}_{33}(0)\rangle - \langle\hat{\sigma}_{33}(\infty)\rangle\right] \tag{12.19}$$

$$= -n_b' \langle\hat{\sigma}_{33}(\infty)\rangle \tag{12.20}$$

where R is the distance to the excited atom. Assuming that $\langle\hat{\sigma}_{33}(R)\rangle \approx (\sigma_{33})_{3lev}(\delta + C_6/\gamma R^6)$, where the population in the right-hand side of this equation is calculated without interactions, and in the lowest order in probe power. The result is:

$$n_b' = \mu \int_0^\infty 4\pi R^2 \left(1 - \frac{(\sigma_{33})_{3lev}(\delta + C_6/\gamma R^6)}{(\sigma_{33})_{3lev}(\delta)}\right) dR \tag{12.21}$$

Calculating this value with the lowest-order expression of the population obtained after adiabatic elimination of the intermediate state, one finds in the dispersive regime that:

$$n_b' \approx \frac{3}{2} n_b \tag{12.22}$$

When starting to excite the cloud, a Rydberg atom prevents the excitation of n_b' others around it, but among them only n_b are blockaded from the point of view of the coherence. In the full blockade regime, two Rydberg excitations will be separated by the minimal allowed distance $R_b = \frac{3}{4\pi}(\frac{n_b'}{\mu})^{1/3}$, which means the average Rydberg population will be $\sigma_{33}^{sat} = \frac{2}{n_b'} \approx \frac{4}{3n_b}$. The blockade probability would then be $p_b = 1 - e^{-4/3} \approx 0.74$, and the normalized shift would saturate at $1 - p_b \approx 0.26$. This is quantitatively compatible with the measurements, as seen in figure (12.16).

Independently from the exact "toy model" proposed here, the simple remark that the blockade effect can be different on populations and coherences could be a reason for a saturation at a non-zero normalized blue-induced shift.

In [144], a different way of parameterizing the behaviour of the system in the higher-order nonlinear regime was proposed, and approximate methods are introduced and used to evaluate the normalized shifts we measured, neglecting the problems of inhomogeneities and dynamics. The results reproduce qualitatively our observations, especially the fast departure from the initial $\chi^{(3)}$ behaviour.

12.3.4 Values of dephasing rate and blue Rabi frequencies

To finish with the quantitative analysis of the measurements, let us briefly discuss the value of the parameters that were directly estimated from the data: the blue Rabi frequency on the various Rydberg states, and the Rydberg dephasing rate γ_{13}.

The latter was estimated of the order of 0.13-0.15 γ, which is ~ 400 kHz. The natural radiative rate for Rydberg states is known to be much smaller than this, and the absence of variations in this value for all states is a strong evidence that it is technically limited. Among the most likely contributions to this linewidth, the laser noise itself on the Rydberg transition has an estimated upper bound of ~ 50 kHz. Doppler broadening is not negligible in the experiment, as both co- and counter- propagating two-photon excitation can happen in the cavity. The worst case (co-propagating excitation) gives for rubidium atoms at 40μK a halfwidth at half maximum of ≈ 250 kHz, which could then explain a large part of the observed linewidth. An additional contribution could com from the sensitivity of the Rydberg states to ambient fields (AC fields not compensated, or inhomogeneous DC fields in the cloud, leading to inhomogeneous broadening). We unfortunately have no way of measuring these at the position of the atoms, but it seems possible that the remaining broadening could be due to such effects.

Justifying from ab initio calculations the values we observe for the Rabi frequencies on the different Rydberg states is difficult, because the actual blue power that reaches the inside of the cavity is known with very little precision. The power sent to the chamber can easily be measured (usually around 210 mW), but a very variable fraction of it is reflected by the upper viewport (from 30 to 70 mW depending on the frequency), and the reflection coefficients of the two faces of the cavity mirrors were also only roughly estimated (the back of the mirrors reflects an estimated 20 % of the intensity, the inside face has a reflection estimated to $\approx 4.5\%$ for the upper mirror, and $\approx 33\%$ for the lower one). Then, depending on the chosen Rydberg state, the blue is never resonant in exactly the same way in the cavity, and the maximum intensity (at an antinode on axis) can vary by a factor ≈ 1.65 due to this. Taking into account all available information on the system and trying to estimate the maximum Rabi frequency Ω_{b0} for each state based on the dipole moments measured in [174], the obtained values are in agreement with the ones extracted from the fits by $\approx 25\%$. The difference (calculated values are systematically higher than fitted ones) could be explained by the uncertainty on the blue polarization. It may not be very well preserved when crossing the optics that are not blue AR-coated, so that all the power sent in could not couple to the desired σ^+ transition.

12.4 Conclusion on the strength of the nonlinearity

Being able to observe bistability induced by the Rydberg nonlinearity would have allowed us to quantify how few photons were necessary to reach this regime. As we saw, such a simple conclusion is not possible from the experiments, but the strength of the apparent nonlinearity can still be quantified. In particular, the required intensity (or number of excitations) for the cavity resonance to shift by its linewidth can be estimated from the measurements. This criterion is equivalent to having an effective nonlinear phase-shift induced by the medium of order π (taking into account the cavity enhancement).

On the data for $n = 61$, this shift of the transmission peak by κ is observed for $Y \approx 0.5$. This corresponds to a number of photons inside the cavity in steady state of ≈ 30. However, the number of atomic excitations is far from being negligible. In the $\chi^{(3)}$ regime, the total Rydberg population can be estimated by neglecting the interactions, and for our typical

parameters on $n = 61$ for $Y = 0.5$ it results in a few thousands (≈ 5000) of atoms being in the Rydberg state. This is relatively small compared to the few 10^5 atoms in total coupled to the mode. As shown in section 1.4.3, the dispersive nonlinearity obtained from the pure saturation of the two-photon line without interactions would require a number of excitations of the order of the number of atoms to reach the same situation. The nonlinearity observed here is thus already much more efficient.

Another way of placing the observed nonlinearity in context is simply to put the numbers on the equivalent $\chi^{(3)}$ in standard units corresponding to the shifts we measured. The initial slope of the shift in θ as a function of Y can be related to the effective $\chi^{(3)}$. Assuming the nonlinear response of the medium is written as $\chi^{(3)}E_0^2$ where E_0 is the amplitude of the complex field at the maximum of intensity in the cavity (see conventions in part I), we get $\chi^{(3)} \approx 4.10^{-9}$ m^2.V^{-2}. This dispersive nonlinearity is only two orders of magnitude smaller than the absorptive one measured in the resonant case in similar systems in [160]. As stated above, it is also much larger than the nonlinearity that could be obtained by saturating the off-resonant EIT without interactions. It constitutes the first measurement of such a large dispersive nonlinear susceptibility in Rydberg gases. One should also remember that in our system this value of the susceptibility is multiplied by the cavity finesse (~ 100) when thinking of an accumulated phase shift.

Conclusion

In this experiment, which was chronologically the first one carried out on the setup, we characterized the dispersive nonlinear response of the atomic cloud in the presence of Rydberg excitations. The measurements show an intensity-dependent shift of the cavity transmission resonance, corresponding to a nonlinear phase shift imprinted on the beam by the atoms. The regime of intensity in which this experiment was realized is such that all other atomic nonlinearities (three-level, without interactions) are known to be very weak. The observed effect shows all required dependences to be attributed to the interactions between Rydberg atoms in the cloud, excited by the probe photons. It was also shown that, taking into account the main experimental "perturbations" (inhomogeneities and dynamics), this nonlinear effect can be reproduced theoretically with a good quantitative agreement. The models used to interpret the observations are based on Bloch equations, consistent with a more physical and general model based on the Rydberg blockade picture. This confirms that, with all due precautions (complex n_b, ...), the physical picture of excited atoms generating Rydberg influence spheres can be very helpful to understand the behaviour of these media.

In the range of parameters investigated, the number of atoms affected by a single excited one can be of the order of 100. That is the main reason why this cooperative effect can be more efficient than, for example, non-interacting EIT nonlinearities. With Rydberg spheres of up to $\approx 8\mu$m radius in the experiment and given the other dimensions of the cloud, the system is still in a regime where it can accommodate many of these spheres together before reaching saturation. Simultaneously, the effect of a single blockade sphere on the susceptibility is relatively small in the parameter range used here. These two reasons explain why large nonlinearities were observed in the classical excitation regime only, where there are still several tens of photons in the cavity. As such, it also allowed us to characterize the nonlinearity using simple classical tools, and to show that the equivalent dispersive $\chi^{(3)}$ that fits with our observations is already among the largest observed with similar systems [77], and could be scaled up in a number of ways, for example just using higher Rydberg levels.

Together with the experiment described in the previous part, the conclusion at this point is that the path should now be open to start looking for an effect of the Rydberg nonlinearity directly on the quantum state of a few photons in the system. From the quantum optics point of view, the setup was shown to be well suited for the conversion of atomic excitations into free-propagating photons, that can be characterized completely. From the Rydberg point of view, there is some room to improve the efficiency of the nonlinear effect and make it efficient on a few photons (cavity finesse, mode size, cloud size, density, Rydberg state), as will be discussed in the following part. The experiment presented here also taught us that some experimental improvements would be necessary in order to carry on with a cleaner system, and avoid some difficulties (like in particular the blue power inhomogeneities). This will also be discussed in the next part.

Part V

Towards Rydberg nonlinearities in the quantum regime

Introduction

One interesting information to extract from the experiment described in the previous part is that the Rydberg cloud's nonlinear response depends directly on n_b, the effective number of atoms on which a Rydberg excitation has a significant effect. This, to some extent, gives additional physical content to the already commonly used picture of Rydberg spheres or "bubbles", created by the excitations in these systems. More than just inter-excluding regions playing a role during in the cloud's excitation dynamics, they contain the physics of the medium's response and of its interactions with external fields and objects.

These Rydberg bubbles and their collectively enhanced capabilities in cold atomic clouds have been the subject of very active research, both for theoretical proposals and experimental investigations, over the last 15 years. Their interest comes not only from their optical response, but also from the point of view of the atomic ensemble itself: the excitation of Rydberg atoms inside it involves very particular collective quantum states [67], and can generate strong spatial correlations in the cloud [74, 175].

Regarding optics, the very large classical nonlinearities observed in various situations raised good hopes that further improvements would lead to decisive achievements. Increasing the effect of a single Rydberg sphere until it macroscopically changes the system's behaviour would in principle enable ground-breaking realizations in terms of coherent manipulation, preparation and quantum logic on few-photon quantum states [77]. In this situation, the characterization of a classical susceptibility, which was a guideline to understand and optimize the nonlinear response, must be abandoned for a fully quantum description. Reaching this regime and finding the corresponding appropriate descriptions has been a goal for many research groups along the past few years. As will be summarized at the beginning of this part, it is only very recently that the experimental conditions were put together to observe strong Rydberg-induced nonlinear effects at the level of few photons, in free space [131, 162, 163, 176].

In our case, the specificity of using a cavity around the atomic cloud has an importance both in the experiment, enhancing the atom-field coupling but also determining the quantities that can be measured in practice, and for the theory, where the interactions between the photons and the atomic cloud must be treated within a particular framework.

Using the knowledge and experimental implementations accumulated during the first experiments, the goal is to generate in our system strong few-photon level nonlinearities via Rydberg-EIT coupling, and analyze the outcome in a complete way with tomographic quantum state reconstruction. However, before being able to reach it, the experimental setup required yet a few more substantial upgrades and improvements.

This part will therefore describe our recent efforts in progressing towards this quantum regime.

Chapter 13

Few-photon nonlinearities with Rydberg clouds

Contents

This chapter will give an overview of the extremely rich possibilities offered by Rydberg atoms for quantum information in general. In the relevant context here of trying to use them to engineer photonic quantum gates with atomic ensembles, the current status of what was achieved in other experiments will be presented. In our particular case, the nature of the gap that must be crossed to go from classical-regime nonlinearities to a quantum regime will be discussed. Some of the multiple ways in which the setup could allow us to probe these quantum nonlinearities will also be presented.

13.1 State of the art

The exaggerated interaction capacities of Rydberg atoms with photons and with each other have made them the center of many investigations and proposals for quantum information processing, in a wide variety of systems, schemes and protocols (a detailed review has been made by M. Saffman, T. G. Walker and K. Mølmer [68]).

13.1.1 Rydberg atoms for quantum information

One of the first observation of effects attributed to direct Rydberg-Rydberg interactions in atomic gases was reported in the early 80's by J.-M. Raimond, G. Vitrant and S. Haroche in Paris [58]. The same research group later took a leading part in exploring

the possibilities of Rydberg atoms in the strongly coupled regime of cavity QED, leading to several well-known results in the coherent manipulation of microwave photonic qubits. The large coupling of circular Rydberg atoms with the microwave field is in that case crucial to allow a single atom crossing the cavity to "read" or modify the field it contains. With this system, experiments on qubit state preparation, non-destructive measurement and stabilization, as well as entanglement were performed [42, 43].

With the fast development of the cold atoms community during the 80's and 90's, greater and greater potential was expected from using atoms and optical photons as qubits. At the beginning of the 21st century, Rydberg interactions and the blockade phenomenon were put forward in theoretical proposals to realize quantum gates between two neutral atoms by D. Jaksch and coworkers [61]. Quickly afterward, the principle was generalized by M. D. Lukin and coworkers as a mean to produce a usable effective qubit from an atomic ensemble, in which quantum information can be manipulated [67]. The qubit in this case is made of all the atoms in a blockade sphere, as illustrated in figure (13.1).

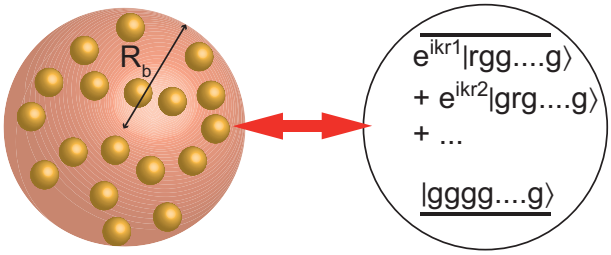

Figure 13.1: Blockaded ensemble acting as an effective two-level system. In the extreme case of an ensemble entirely contained in a blockade sphere of radius R_b, the only two states accessible to the system are the ones where all atoms are in ground state $|g\rangle$, and the singly-excited state where one Rydberg excitation $|r\rangle$ is shared between all atoms, which keeps a precise phase-matching pattern, allowing for directional light emission.

The development of single-atom trapping techniques lead in 2009-2010 to the first demonstrations of the Rydberg blockade between isolated neutral atoms, simultaneously in the group of M. Saffman at the University of Wisconsin and in our group in Institut d'Optique [147, 148]. The two groups also demonstrated its use to generate entanglement and perform quantum gates in these systems [62, 63].

In parallel, different kinds of "many-atoms" systems were progressively developed with the aim to make use of Rydberg interactions in various situations. One example is the loading of atoms in 2D optical lattices, which constitutes an ideal basis for a scalable network of atomic qubits. It is also a very nice tool to study the statistics and spatial distribution of excitations, as in the recent observation of Rydberg blockade and its consequences by P. Schauß and coworkers, in the group of I. Bloch [74]. These statistical properties of Rydberg excitations have also been studied in Bose-Einstein condensates by the groups of T. Pfau in Stuttgart and E. Arimondo in Pisa [177, 178].

The coherent dynamics of the Rydberg excitations also constitute a wide an active experimental research axis. In room temperature atomic vapors, coherent Rabi oscillations towards Rydberg states were observed, with signatures of interactions on large enough energy scales to suggest blockade and collective behaviours could be possible in these systems (also in Stuttgart) [179, 180]. In cold atomic gases, the ability to drive coherent Rabi oscillations of the collective qubit made of a Rydberg sphere has been a challenge for a long time, as attested by the relatively recent dates of the progressing experimental

demonstrations in the groups of T. Pfau, M.Weidemüller and A. Kuzmich [73, 181, 182].

On the theory side, a very large number of proposals were made by different groups during the last decade to use Rydberg-coupled atomic ensembles as a basis to process quantum information [183], to engineer efficient quantum repeaters [69, 70], or as deterministic sources of single atoms or single photons [52, 149].

13.1.2 Few-photon processing with Rydbergs in atomic clouds

Rydberg blockade can allow a large assembly of atoms to act as a single two-level system, while keeping strong phase-matching properties. This makes cold Rydberg ensembles an ideal platform for interfacing matter and light qubits [149]. From the quantum optics point of view, another large interest of these systems is that they can serve as intermediates to realize effective interactions between photons during their propagation [77].

Single-photon storage, filtering and switches

The possibility to use Rydberg interactions as a "filter" to voluntarily induce losses on multiple stored phase-matched excitations was demonstrated in 2012 by Y. O. Dudin and A. Kuzmich [131]. In a free-space scheme, they showed that samples of density 0.3 atoms/μm^3 can efficiently induce strong photon-photon interactions when a Rydberg-coupled probe is sent to excite a region of the cloud of transverse dimension approaching 10 μm. For high enough addressed Rydberg level, the phase-matched readout of the excitations demonstrated a strong antibunching, resulting in a medium that also acts as an interesting single-photon source.

Exploiting more directly the resonant Rydberg-EIT nonlinearity first observed in the classical regime [142], T. Peyronel and coworkers in MIT also demonstrated, in an even more stringent geometry (with densities up to 2 atoms/μm^3 and transverse beam size smaller than the blockade radius), that the steady-state excitation of a Rydberg cloud can lead to a transmitted stream of antibunched photons [162]. Two excitations are in this case totally excluding each other while propagating through the cloud. The nonlinearity is such that within a time slot corresponding to the blockade range, all photons but one are scattered and can not cross the medium.

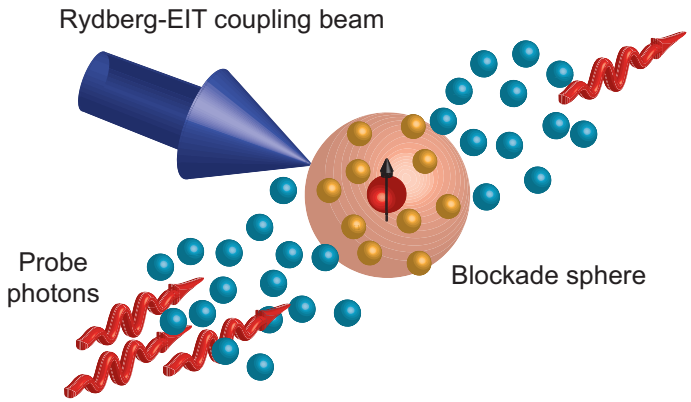

Figure 13.2: Principle of the experiments on absorptive single-photon nonlinearities. When the transverse size of the cloud, or the one of the probe beam, is made smaller than a blockade radius, propagation through the medium or storage and retrieval allows only single excitations to pass through at a time.

A slightly different path was followed by the group of C. S. Adams in Durham with similar geometry, where the authors studied the possibility to actively control with a microwave field the interactions between excitations while they are stored in the cloud [163, 184]. By turning on an active coupling between the Rydberg state used for EIT and a second one, the interactions between atoms can be brought to a regime of $1/R^3$ behaviour, and their strength and efficiency length scale can be tuned between different regimes of dipoles driving and dephasing. This also lead to the demonstration of an additional way to control the antibunching of light retrieved from a Rydberg cloud.

Finally, single-photon all optical switching of the transmission of a medium (or single-photon transistor) has also been demonstrated very recently in two similar experiments by the groups of G. Rempe and S. Hofferberth by storing a gate photon as a Rydberg excitation into the medium through which the target photons are propagating in EIT conditions [164, 165]. Such devices could have direct applications in optical computers, and could in principle be used to engineer two-photon quantum gates.

Dispersive interactions

These first demonstrations of what could be called absorptive photon-photon interactions opened the way to experimental search for dispersive nonlinearities at this level. On the theoretical side, building on the recent experimental achievements, a realistic proposal was made for a protocol to realize a photon-photon control-Z gate [185], using dual-rail qubits coded on photonic modes stored in spatially distinct regions of a Rydberg cloud, processed using microwave dressing.

Evidence for strong dispersive interactions between photons was experimentally demonstrated in 2013 by O. Firstenberg and coworkers in MIT [176], using a similar scheme as in [162] with off-resonant excitation. The authors study the propagation of the two-excitation amplitude through the medium and find evidence for macroscopic nonlinear phase-shifts. These can be seen as due to an effective attractive interaction potential between photons propagating through the medium.

Where do we go from here ?

One possible way to summarize the current status of what has been done with cold Rydberg gases in the many different possible schemes, and their potential use to realize photon-photon quantum gates is as shown in table (13.1).

Type of nonlinearity	Experiment	Remarks
Losses+propagating single-mode	T. Peyronel *et al.* [162]	Photons not recovered (non unitary)
Losses+storage single-mode	Y.O. Dudin and A. Kuzmich [131] D. Maxwell *et al.* [184]	Photons not recovered (non unitary)
Losses+storage separated control/target	D. Tiarks *et al.* [165] H. Gorniaczyk *et al.* [164]	Photons not recovered (non unitary)
Dispersive+propagating single-mode	O. Firstenberg *et al.* [176]	Temporal mode and photon-number postselection

Table 13.1: Few-photon nonlinearities schemes.

Our aim in this context is to look for alternative ways of producing and using few-photon dispersive nonlinearities, using the specificities of our setup to minimize the absorption losses and reach a good degree of control on the modes of the output photons, as well as the ability to fully characterize an arbitrary quantum state generated by such a process.

13.2 Improving performances towards few-photon level nonlinearity

Extrapolating the meaning of the susceptibility to its limits, the regime of few-photon nonlinearities would correspond, in the configuration of part IV, to a single excitation being able to switch the cavity from resonant to off-resonant. Such an effect would lead, depending on the scheme, to a single photon being able to control the transmission or the phase of a second one. Note that this does not necessarily imply that we must reach the situation where the whole cloud is contained inside a single blockade sphere in principle. One of the general ideas we follow is that making use of the specificities of our system, like the presence of the cavity, the interesting regime should be reachable with increased flexibility on the parameter range of the atomic cloud (density, size ...).

Regarding the experimental setup, the experiment described in the previous part showed that in the configuration used, much more than one excitation in the system are still necessary to reach a "macroscopic" level of nonlinearity. This is due both to the fact that an excited atom does not influence enough of its neighbours, and that the amount by which the blockaded atoms see their susceptibility changed is too weak. In order to progress in the right direction, several improvements can be thought of.

To increase the effect produced by a single blockaded atom, one possibility is to move closer to atomic resonances where the atomic response will be much amplified, while keeping the losses to a reasonable level with EIT conditions or other tricks. Another way is to increase the cavity finesse, which further amplifies the effect of a given change in the susceptibility on the extracted field.

A different category of upgrades consists in increasing the number of atoms that are blockaded by a single Rydberg excitation. This simply means the radius of a blockade sphere, and/or the atomic density must be increased. Increasing the blockade radius can in principle be realized easily by coupling to Rydberg states with higher principal number (we stopped at $n = 61$ in the classical regime experiment). The issue in this case is the limited blue Rabi frequency achievable with a given laser power, that decreases quickly with n. One therefore needs as high and focused blue power as possible to reach very large blockade radii. At the same time, if the goal is for a single blockade sphere to have a large effect, there is no use for a very large cloud, which would only add atoms in the mode, potentially acting as parasitic absorbers. The previously discussed blue inhomogeneity issue should also be avoided, as it can lead to complications and losses due to atoms that do not see enough blue. The conclusion is therefore that an optimal configuration would require a very small and dense cloud [1], on which the largest blue power achievable can be focused, in such a way that all the atoms can homogeneously be coupled to very high Rydberg levels.

1. But without necessarily going to the extreme of a few microns size.

13.3 Several possible schemes to exploit

Once the right parameter range is experimentally accessible, there is in principle a number of ways to look for nonlinear modifications of a few-photon quantum state in the system, as is illustrated in the different categories of schemes in table (13.1) for example. Here, a few different schemes will be discussed, in which the possibilities of our setup were theoretically investigated. The specific theoretical treatment developed for each case is mainly the work of Jovica Stanojevic, Andrey Grankin and Etienne Brion, and is the subject of several articles, published or to be published. The results obtained on the different schemes will therefore be only shortly reviewed here.

13.3.1 Storage-Retrieval experiments

General idea

A first class of protocols makes use of the sequential storage of excitations in the cloud as Rydberg polaritons, followed by a period of free evolution, and readout. Sending a short coherent probe pulse in the medium, an initial coherent superposition of phase-matched Rydberg polariton states can be created in the cloud. Left to evolve freely, the interactions between excitations then perturb the collective quantum state. This situation is close to the one where the emergence of spatial correlations between excitations was studied in free space [158], or to the experimental free-space realization of Y. O. Dudin and A. Kuzmich [131]. It is also analogous to the atomic-ensemble counterpart of the "dephasing gate" proposed for two single atoms [61], where multiple excitations are not prevented by blockade, but dephase each other after some time. Only with the spatial disorder and phase-matching issues in an ensemble, the outcome of the "gate" is different.

F. Bariani and coworkers theoretically studied this scheme in a phase-matched free-space configuration, assuming microwave coupling was used between Rydberg states to induce strong interactions [186]. Using numerical simulations and an effective model restricted to two excitations, they showed that the readout excitations exhibit an auto-correlation function $g^{(2)}$ decreasing with the storage time, sign of the alteration of their statistics. The possibility to use this scheme to produce single photons was thus suggested.

In a cavity or other equivalent phase-matched schemes, the effect can be described qualitatively as follows: for the stored excitations, the retrieval acts as a filter, efficient only if they are sufficiently well phase-matched to be collectively emitted by all atoms. For a single delocalized excitation, the efficient retrieval is limited only by atomic motion, as was shown in the experiment of part III. On the other hand, when several excitations involving Rydberg states are written into the cloud, the phase coherence of all the collective state's components is quickly randomized by the additional phase shift due to Rydberg interactions, which depends on the widely distributed distance between interacting atoms. Thus, after some time, multiple-excitation components lose their collective phase-matched properties and are irreversibly lost from the point of view of the retrieval. This principle is illustrated for van der Waals interactions in figure (13.3).

Retrieved quantum state evolution

In [159], based on calculations by Jovica Stanojevic, the time evolution of the retrievable excitations' full quantum state is studied in our cavity scheme, with pure van der Waals interactions. In particular a simple scaling law is found that describes with a good accuracy the evolution of any number of excitations.

More precisely, the excitation of the cloud is described as coupling the ground state to only phase-matched Dicke states of the ensemble, as shown in figure (13.3) for the first three states. On the contrary, Rydberg interactions disperse a given n-excitation phase-matched Dicke state towards the large number of non-phase-matched Dicke states with the same number of excitations. To describe the retrieved quantum state, what must be calculated is how much the state with n excitations can still be recoupled to the perfectly phase-matched one $|n\rangle$ after having evolved during a time t in the cloud. If $\hat{U}(t)$ is the total evolution operator describing the dynamics of dephasing during the storage time in the cloud, this "survival probability" is given by $\langle n|\,\hat{U}(t)\,|n\rangle$.

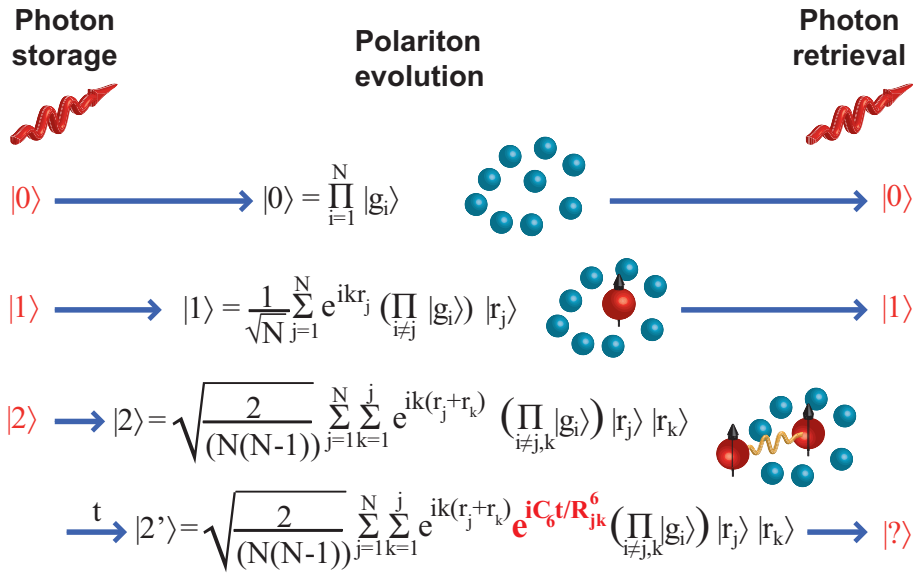

Figure 13.3: Illustration of the "quantum scissors" effect by letting the polaritons dephase before readout. When photonic quantum states $|0\rangle$ or $|1\rangle$ are stored, interactions have no effect, the state remains phase-matched and can be readout. However when two excitations are stored initially, each component of the state where atoms j and k, separated by a distance R_{jk}, are excited acquires a phase $C_6 t/R_{jk}^6$, which quickly ruins the phase-matching and prevents the excitations from being readout.

Interestingly, a good approximation of the result (otherwise obtained from complete numerical simulations or higher-order approximations, see [159]) is that the survival probability of state $|n\rangle$ can be expressed as a simple power of the 2-excitation one:

$$\langle n|\,\hat{U}(t)\,|n\rangle \approx \langle 2|\,\hat{U}(t)\,|2\rangle^{n(n-1)/2} \tag{13.1}$$

The physical reason is that the evolution is mostly due to two-body interactions, so that the action of the evolution operator on state $|n\rangle$ can be split down to terms describing only the dephasing of pairs of excited atoms, of which it contains a total of $n(n-1)/2$, and all these terms are equivalent after averaging over the random positions of atoms.

The timescale for efficient complete dephasing in this protocol can be estimated as follows: for state $|2\rangle$ that is the longest to dephase, the complete loss of phase-matching requires all possible pairs of excited atoms to have accumulated a non-negligible phase, even those that are the most separated in the cloud. If the typical overall size of the cloud is R, and if $|\psi\rangle$ is the state of two excited atoms separated by R, the phase they

will accumulate is given by $\langle\psi|\,\hat{U}(t)\,|\psi\rangle = e^{iC_6 t/R^6}$. The total time for this process to be efficient is thus of the order of a few $T_R = R^6/C_6$, which for typical accessible parameters is of the microsecond scale. The full time-dependent expression for state $|2\rangle$ given in [159] together with the scaling law (13.1) allow one to know, at any intermediate time during the evolution, the quantum state of the retrieved excitations. This state progressively evolves from a coherent state $|\alpha\rangle$ to a truncated state $\propto |0\rangle + \alpha\,|1\rangle$.

This scheme can in principle be used as deterministic quantum scissors to prepare at will qubit states, superpositions of zero and one photon in a given mode. Intermediate timescales, where the state has not been completely cut yet, can also be studied.

13.3.2 Continuous excitation

General idea

The steady-state response of the system can also be characterized, sending a continuous weak probe on the cavity. Even in the absence of a well-defined temporal mode, this configuration allows to look for evidences of few photon nonlinearities, for example by studying the statistics of the output light, just as it was done to show the antibunching of light due to nonlinear absorption in free space [162]. As already pointed out, intrinsic dynamics of the excitation can have an important role in the observed nonlinearity of these systems. Characterizing steady-state quantities can therefore be more practical, at the same time as being easier to investigate theoretically, than using pulsed schemes.

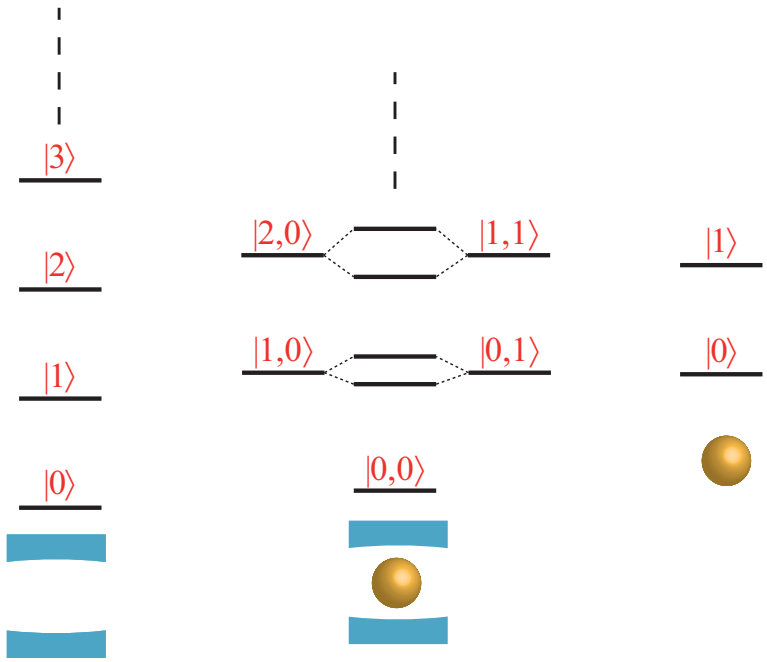

Figure 13.4: Making the system's spectrum anharmonic by coupling a two-level atom to the cavity. Left: harmonic energy eigenstates of the cavity. **Right:** two levels of the single atom. **Center:** if the two are resonantly coupled, the resulting spectrum exhibits, in addition to its ground state, pairs of levels with a fixed number n of excitations –which can be photons or atomic excitation– split by an amount increasing as $\sqrt{n}$. The global system is therefore anharmonic, and the creation of single or pairs of excitations are two completely distinguishable processes.

The principle here is to render the cavity resonance photon-number sensitive, and thus significantly different for photons arriving in pairs sufficiently close to each other, as compared to photons coming one by one. For this, the general and well-known idea is to couple the harmonic oscillator of the cavity mode to a system sufficiently anharmonic to disturb the equal energy splitting of the states containing given numbers of excitations.

In the optical domain, proposals making use of 4-level EIT nonlinearities in atomic gases raised a large interest by showing that it could potentially induce very large anharmonicity in the cavity spectrum [56, 104]. Experimentally, the groups of H. J. Kimble and G. Rempe followed a different approach: in the strong coupling regime of a single atom to a high finesse cavity, they observe the anharmonic level splitting at the few-photon level [44, 45] (see figure (13.4). Finally, a mix of the two approaches was realized in V. Vuletić's group: using a single "gate" collective excitation in an atomic cloud in the strong coupling regime, the transmission of a separate probe beam through the cavity can be switched, and the gate photon can still be re-extracted from the cloud in a phase-matched way [187].

In all these cases, the properties of the cavity resonance can be made very different for a given photon depending on the presence of a second one in the system. Using Rydberg nonlinearities and applying the same principle, it is expected that such large effects could be observed without having to reach the (single atom) strong coupling regime, and with ensembles rather than single atoms, which are easier to prepare. As discussed for example in [183] and [188], a simplified vision of the effect of interactions is the creation of "superatoms" corresponding to collective excitations of the Rydberg bubbles. These can act as two-level systems strongly coupled to the cavity mode, and therefore give access to the same kind of possibilities as single atoms (see figure (13.5)).

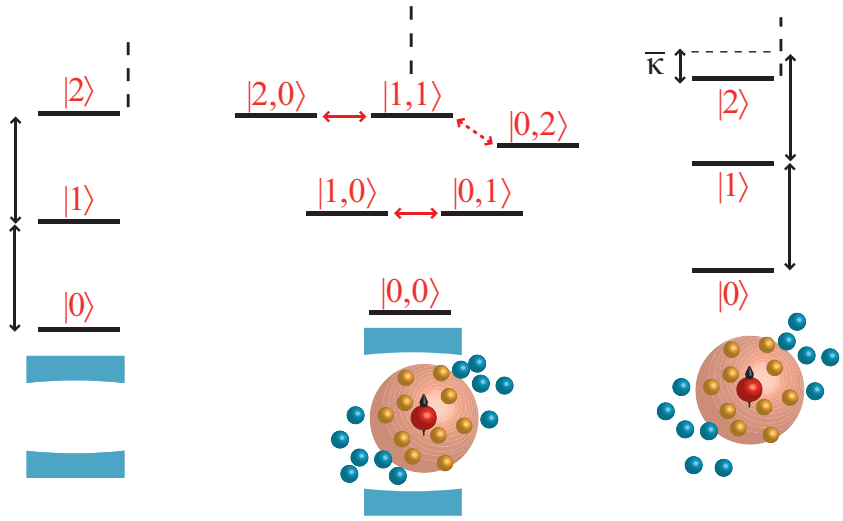

Figure 13.5: Making the system's spectrum anharmonic by coupling a Rydberg medium to the cavity. Left: harmonic energy eigenstates of the cavity. **Right:** approximate collective states of the ensemble (only symmetric states are considered, and in the lowest-order approximation the interactions just shift the doubly-excited state by $\bar{\kappa}$ – see main text). **Center:** Spectrum of the coupled system. If $\bar{\kappa} = 0$, all states inside a given excitation-number subspace are initially degenerate and the coupled system remains linear, containing harmonic ladders of states. If $\bar{\kappa}$ is large, the coupling to state $|0, 2\rangle$ for example is off-resonant, and in the extreme case this state can be eliminated and the system is equivalent to the two-level atom and cavity one.

To describe this situation, a quantum treatment of the full system is necessary, including the evolution equations for the quantum mode of the cavity, coupled to all the atoms. In free-space, one must describe the propagation and the evolution of the polariton, as was done with two-excitation amplitude propagation equations for the MIT experiment [162, 176], or by D. Petrosyan and coworkers [188] for example. In contrast, the cavity case allows by hypothesis to restrict oneself to a given field mode to study.

Cavity transmission statistics in off-resonant excitation scheme

As an interesting example, we first briefly discuss the off-resonant excitation scheme used in the experiment of part IV (see figure (13.6)). In this configuration, the $g^{(2)}$ of transmitted light was calculated by Andrey Grankin with Etienne Brion, by adjusting some of the experimental parameters to get to a "quantum regime" [168].

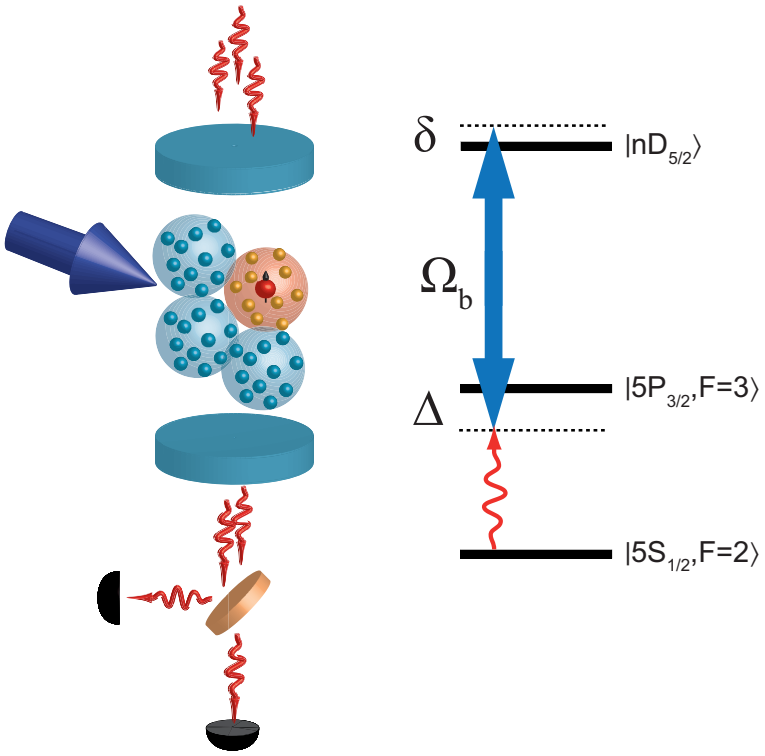

Figure 13.6: Principle of the proposed scheme. Probe light is sent to be transmitted through the cavity at a rate of a few photons per lifetime. It is coupled inside the cavity to the Rydberg-EIT medium in an off-resonant scheme. The interactions are considered as splitting the medium into spheres that act as two-level superatoms, which are coupled to the collective Rydberg state by the probe and the control beam. The statistics of the transmitted light can be analyzed with correlation measurements.

In the far detuned and weakly excited regime, the first theoretical step to simplify the system is to adiabatically eliminate the intermediate atomic state, and to neglect the natural nonlinearity of the three-level atomic system. As a result, in the absence of interactions, an assembly of effective two-level atoms is considered in their linear regime.

In a first approximation, interactions act as a pure blockade that splits the medium into N_b distinct Rydberg spheres (each containing n_b atoms) that can each accommodate at most one excitation, and the additional long-range dephasing between separate spheres is

neglected. In this case, the atomic system can be described as a large spin $\hat{J}$ corresponding to the assembly of spin-1/2 Rydberg bubbles, which acts as the anharmonic system coupled to the cavity mode $\hat{a}$ [168]. The resulting Hamiltonian for this system is:

$$\hat{H} = -\hbar\gamma\theta_e\hat{a}^\dagger\hat{a} + \hbar\alpha(\hat{a}+\hat{a}^\dagger) - \hbar\gamma\delta_e(\frac{N_b}{2} + \frac{\hat{J}_z}{\hbar}) + \sqrt{n_b}g_e(\hat{a}\hat{J}_+ + \hat{a}^\dagger\hat{J}_-) \tag{13.2}$$

where α is the cavity mode feeding, and θ_e, δ_e and g_e are the effective parameters obtained from the effective two-level model:

$$\theta_e \approx \theta - \frac{Ng^2}{\gamma^2\Delta} \tag{13.3}$$

$$\delta_e \approx \delta - \frac{\Omega_b^2}{4\Delta} \tag{13.4}$$

$$g_e = \frac{g\Omega_b}{2\Delta} \tag{13.5}$$

Here g and Δ are the usual initial parameters valid for all of the N atoms. The Hamiltonian of equation (13.2) describes the total effective spin $\hat{J}$ and the cavity mode $\hat{a}$ evolving with effective detunings δ_e and θ_e respectively, and interacting through the last excitation exchange term, which shows a coupling collectively increased inside each Rydberg sphere by $\sqrt{n_b}$. Due to the nature of the collective spin however, only N_b excitations can be stored in the atomic degrees of freedom.

This approximation allows to write the coupled evolution equations of the cavity mode and the Rydberg excitation field, and to calculate numerically the autocorrelation function of the transmitted field $g^{(2)}(\tau)$. An example is shown in figure (13.7).

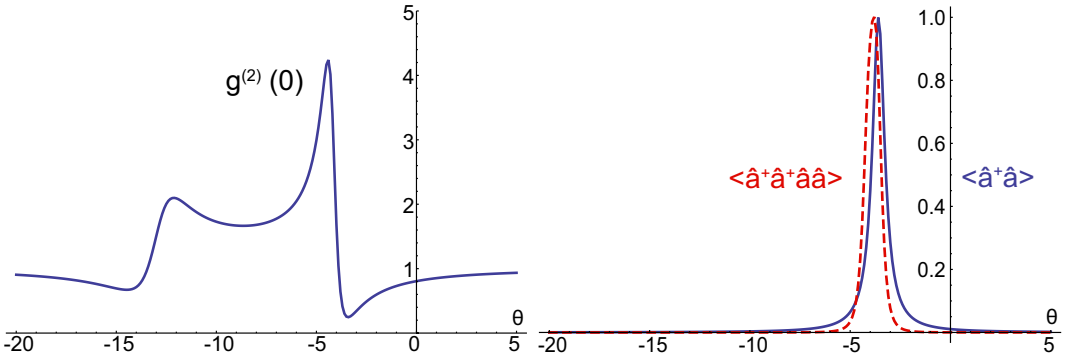

Figure 13.7: Statistics of the transmitted light in the off-resonant excitation scheme as a function of the cavity detuning. Left: The autocorrelation function of the transmitted light exhibits different bunching and antibunching features, depending on the number of excitations in the states favored by the cavity resonance. **Right:** Resonances for the output intensity $\propto \left\langle \hat{a}^\dagger\hat{a} \right\rangle$ (solid line) and for the higher-order $\left\langle \hat{a}^\dagger\hat{a}^\dagger\hat{a}\hat{a} \right\rangle$ (dashed line), exhibiting a relative shift in position (both vertical scales are arbitrary). Qualitatively, the main resonance is centered on the right structure in the $g^{(2)}$, with the antibunching dip centered on the point where single-excitation states resonate, and the bunching peak on the multi-excitation resonance. The additional features on the left in the $g^{(2)}$ happen when the overall cavity transmission is extremely low. The parameters chosen here are $\kappa = 0.3\gamma$, Rydberg level $n = 95$, μ =0.1 atoms/μm^3, $C = 300$, $\Omega_b \approx 8$, $\Delta = -16$, $\delta = 0.5$. The calculations are carried out assuming $\gamma_{13} = \gamma_{33}$.

The physics of the system can be well understood in its main features from an interesting limit case: when the medium is large enough to accommodate several blockade spheres and the number of excitations is small, the Rydberg excitation field can be shown to behave approximately like a nonlinear oscillator field $\hat{b} = \hat{J}_-/\hbar\sqrt{N_b}$ coupled to the cavity. Its own Hamiltonian is:

$$-\hbar\gamma\delta_e\ \hat{b}^\dagger\hat{b} - \frac{\hbar\bar{\kappa}}{2}\ \hat{b}^\dagger\hat{b}^\dagger\hat{b}\hat{b} \tag{13.6}$$

where $\bar{\kappa} = 2\gamma\delta_e/N_b$ is an effective measurement of the interaction-induced nonlinearity.

Within these approximations, the excitation from single to doubly-excited state is effectively detuned by $\bar{\kappa}$ compared to the zero to one excitation transition, due to the interactions as expected. The system can thus be tuned on resonance with the single-excitation subspace or with the two-excitation one selectively, as they are not degenerate anymore. This will favor in the transmitted field either single photons relatively to pairs or the opposite (see figures (13.5) and (13.4)). The numerical calculations carried out in [168] indeed clearly show that, depending on the choice of the cavity resonance frequency, the output field can exhibit strong bunching or antibunching features (see figure (13.7)).

Interestingly, this regime can be reached even if the medium is larger than a blockade volume: as long as $\bar{\kappa}$ and the coupling between photons and collective atomic excitations can be made large enough, the second atomic excitation will be far enough detuned to induce large nonlinearities in the total transmission. From our experimental parameters, an "easy" way [2] to reach a regime of nonclassical statistics would be to increase the cavity finesse by at least a factor 10, as well as the density by a factor 2 to 3. This is experimentally within reach with reasonable technical improvements.

Resonant regime and cavity reflection

To avoid changing the cavity mirrors to increase the finesse, which is an important effort as the cavity is in the vacuum chamber, other ways to enhance the system's response can be designed. Going to an all-resonant case is an easy way to get larger nonlinearities. However this a priori implies looking only at large nonlinear losses. Still, the cavity allows pure losses in the cloud to be turned into a possible phase-shift on the field. The principle is well-known and was already used with a single atom coupled to a cavity to implement atom-photon quantum gates [46]. It can in principle be investigated in our system too.

Using the single-ended cavity in reflection, on resonance with the probe light, two extreme regimes exist: if the losses are much lower than the input mirror's transmission, the incident field enters the cavity and is overall reflected with a certain phase. If the cloud induces much more losses than the input mirror's transmission, light just does not see the cavity and gets reflected off the first mirror, with a phase-shift of π compared to the previous case. In between, in principle, if only the losses of the cloud (and not the dispersion) are changed continuously, the reflected field goes from one phase to the other following the real axis in complex plane, passing through zero when the so-called impedance matching condition is met.

This is summarized in the following approximate expression of the resonant cavity reflection coefficient, for a single-end cavity with coupling mirror reflectivity r_1, and a lossy medium inside which applies to the field amplitude a factor t_c for a double-pass propagation:

$$r_{cav} = \frac{t_c - r_1}{1 - t_c r_1} \tag{13.7}$$

2. In terms of number of parameters to change.

The value of this reflection coefficient is plotted on figure (13.8), where one clearly sees the impedance matching condition, corresponding to $t_c = r_1$.

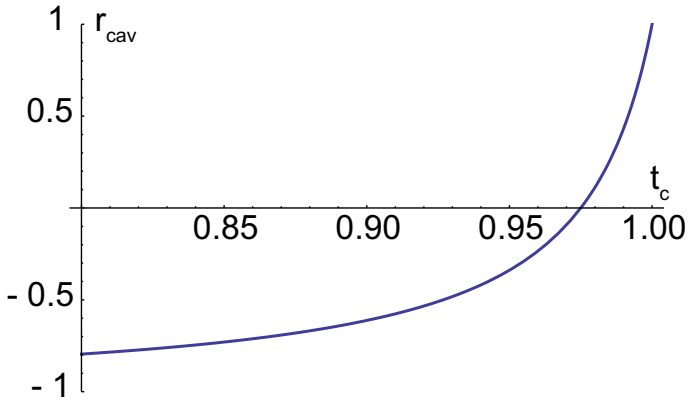

Figure 13.8: Amplitude reflection coefficient of the cavity as a function of cloud transmission. With an input coupling mirror that transmits 5 % of intensity, the total reflection coefficient of the resonant cavity is plotted as a function of the double-pass transmission of the cloud t_c. By changing only by a small amount the cloud losses around the right value (impedance matching, $t_c = \sqrt{0.95}$), the reflected field can get a phase flip with reasonably low losses.

The idea is then to use this impedance matching and strong nonlinear losses to apply different reflection coefficients, especially in phase, to the different components of a quantum state. If the nonlinearity is such that a single excitation can enter the cavity under resonant EIT conditions with very low losses, but at the same time when two come together the interactions change so much the transparency that they see high losses, then a selective phase flip can in principle be applied to multiple-excitation states.

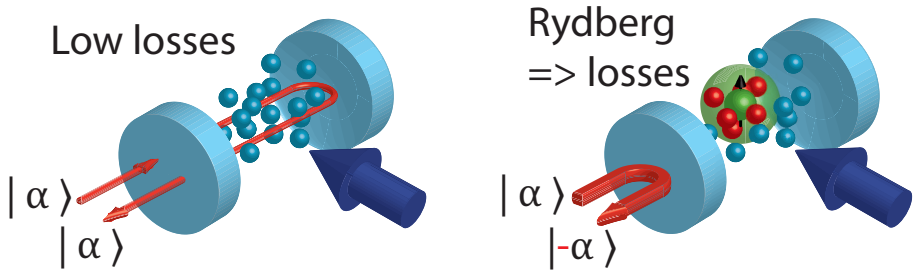

Figure 13.9: Principle of the number-selective application of a phase shift with nonlinear losses. At very low power if no Rydberg excitation is present in the cloud, its transmission can be made very high with EIT, so that light enters normally the cavity. For higher number of excitations in the input field, excitations start to interact which creates a strong decrease of the EIT efficiency, and light can not enter the cavity anymore.

Based on this idea, A. Grankin and E. Brion also started investigating theoretically the fully resonant regime, both with the cavity in transmission or in reflection. The models and calculations have not been published yet, but the results qualitatively show that both

transmitted and reflected light can present bunched or antibunched statistics as expected.

In reflection, the statistics can be modified because, for example, the two-photon component of light could precisely meet the impedance matching condition due to an interaction-reduced EIT, and would therefore be entirely scattered out of the mode, while the single-photon component would be nicely reflected.

This scheme could therefore lead, depending on the regime, to selective two-photon phase-flip or absorption, and many interesting open questions could be investigated by characterizing the full quantum state of the reflected light.

Chapter 14

Experimental advances towards the quantum regime

Contents

This chapter describes the last evolutions of the experimental setup. For several reasons, in order to access the regime where a single excitation has a large controlled effect on the system's behaviour, working with a large atomic cloud is unnecessary and can even be a disadvantage. It forces for example the blue coupling beam to cover a much larger area and thereby reduces strongly the achievable intensity. Trapping of a small atomic cloud of dimensions of few tens of microns is therefore implemented, using in particular dipole trap beams to select only a small loading region. To characterize this small cloud, the imaging system is then redesigned carefully to access good enough resolution. This being done, the blue coupling beam can be focused to small sizes matching the cloud's ones. In order to gain even more range in reachable Rydberg states, a secondary horizontal buildup cavity is set up, in which the blue resonates. With this improved setup, promising high-quality intracavity EIT features are demonstrated, which form the basis of the next generation of experiments in the quantum regime.

14.1 Trapping a small cloud in the cavity mode

14.1.1 Dipole traps setup and loading

Cavity and side dipole traps

In order to generate clouds of few microns to tens of microns from a MOT, a very common method is to load conservative optical dipole traps, made of far red-detuned tightly focused beams, defining a trapping potential at their intensity maximum [189]. Because the intensity maximum of a focused beam is in general much less tight along its propagation direction than in the two transverse ones, a pair of crossed dipole traps is well suited to define a small volume in 3D where the atoms will be trapped.

In practice, the 810 nm beam used to lock the main cavity also serves as one of the dipole traps, by simply increasing its power. However, to avoid inhomogeneous light shifts of the EIT transitions during the actual measurements, it must be switched On and Off without losing the cavity lock. For this, two controls are simultaneously switched: the RF power sent to the AOM producing the cavity lock beam, which changes its optical power, and the amplitude of the modulation signal imprinting sidebands on the beam to generate the Pound-Drever-Hall error signal. This results in two different configurations, one with high optical power and low modulation, the other with low power and large modulation, adjusted to allow switching from one to the other without changing the amplitude of the cavity lock's error signal.

In "lock" position $\approx 100\ \mu$W of 810 nm light goes to the cavity and has negligible effect on the atoms inside, while in "trap" position 8 to 10 mW of light realize an intracavity dipole trap. The resulting trap, vertical, has the waist $\approx 88\ \mu$m of the fundamental cavity mode at 810 nm, and presents a longitudinal standing-wave pattern with periodic maxima of intensity separated by 405 nm. At an antinode of the standing wave, the effective maximum trap depth (taking into account the fact that it is σ^+-polarized, for atoms in state $F = 2, m_F$) is estimated to [189]:

$$U_{max}^{cav} \approx k_B * 320\mu K * (1 - \frac{m_F}{8}) \tag{14.1}$$

The second trap is realized by a separate single-pass 810 nm beam sent horizontally through the vacuum chamber to focus at the level of the atoms. The horizontal trap (also called "side dipole trap") is formed by expanding an incident beam with a telescope as much as is permitted with standard 1" optics, which is then focused at the level of the atoms by a 500 mm lens, to a waist of $\approx 40\ \mu$m. At the most, up to 500 mW of light are used in this trap, leading to a trap depth for π-polarization:

$$U_{max}^{side} \approx k_B * 260\mu K \tag{14.2}$$

This trap can also be switched On and Off at will thanks to a dedicated AOM.

The overall configuration of the two traps, together with other information, is shown in figure (14.1).

Traps loading and cloud preparation

In order to load the traps during the atomic preparation sequence, we follow the common use: the traps are switched on during the trapping and cooling steps, and the repumper power is decreased during the molasses step in order to allow accumulation of atoms in the traps without hitting density limits due to strong multiple scattering of

cooling light photons. At the end of the standard molasses phase, the traps can optionally be kept On for some time, so that the untrapped atoms fall away to enable imaging of the trapped ones (see following).

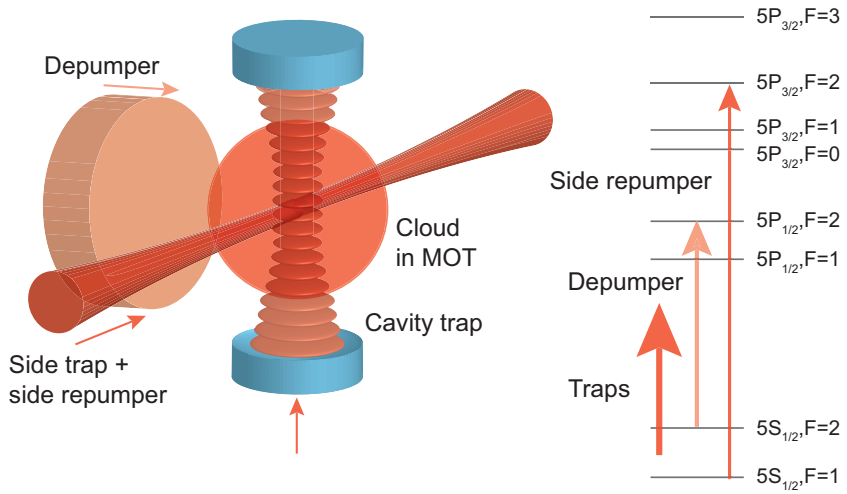

Figure 14.1: Configuration of the optical dipole traps and other beams used to generate a small cloud from the MOT. The side trap and side repumper have the same spatial mode and are sent horizontally to focus in the center of the cloud. The depumper hits all the atoms from a separate optical path. Depumper and side repumper are used to prepare the cloud (see text). Both traps are at 810 nm, the depumper is at 795 nm, and the side repumper is at 780 nm. On the left figure no real scale for lengths is represented, especially on the vertical axis (cavity length, cloud size and standing-wave pattern are at much more different scales). On the right the frequencies are also not to scale.

Loading these dipole traps from the MOT generates a cross-like structure of atoms, while only the small intersection of the two traps is of interest. In particular the cavity trap standing wave prevents the atoms from moving along the z direction, and many atoms are thus trapped and fixed inside the cavity mode, but outside the small intersection volume (see figure (14.1)). In order to solve this problem, spatial selection of atoms is performed with a hyperfine depumping-repumping sequence: after the loading, all repumping beams are switched off, and a pulse of a large depumping beam at 795 nm is sent on all atoms, tuned to the $F = 2 \rightarrow F' = 2$ transition. At the end of the molasses, due to the low power of the repumper, a large fraction of the atoms is already depumped in the state $5S_{1/2}, F = 1$, and this additional depumping pulse ensures that the remaining fraction of atoms in $F = 2$ is really negligible. A short pulse of repumper is then sent on the D2 line, using a beam in the same spatial mode as the side dipole trap (see figure (14.1)). That way, atoms in the cavity mode are repumped only in a small region around its intersection with the side trap. The fraction of atoms repumped in $F = 2$ in that region, and the size of the effective small cloud created by this sequence is completely controlled by the power of this so-called "side repumper" pulse. A tradeoff is necessary since, when increasing its power to increase the effective atomic density in $F = 2$, the size of the repumped region also increases at some point.

This preparation method allows us to increase the duty cycle of the experiment, as the "useless" atoms are just depumped instead of being physically lost.

Cooperativity measurement and side trap alignment

The resulting small cloud can be characterized by its cooperativity. As the number of atoms used here is much lower compared to the previous cases, measuring the cooperativity via the dispersive shift of a detuned probe's transmission line through the cavity is not precise enough. An alternative way is to use a resonant probe. A very weak probe beam is sent from top through the cavity, tuned around resonance with the D2 ($F = 2 \rightarrow F' = 3$) transition of the atoms, while the cavity length is resonant with the atomic frequency. The transmission of the probe is detected on the same LaserComponents APD as before. When scanning the probe frequency around resonance, the atoms now induce a normal-mode splitting of the cavity resonance, as illustrated in figure (14.2). The fitting of this split resonance profile gives access to the cooperativity, and the frequency splitting between the two normal modes is $\sqrt{8C\kappa\gamma}$.

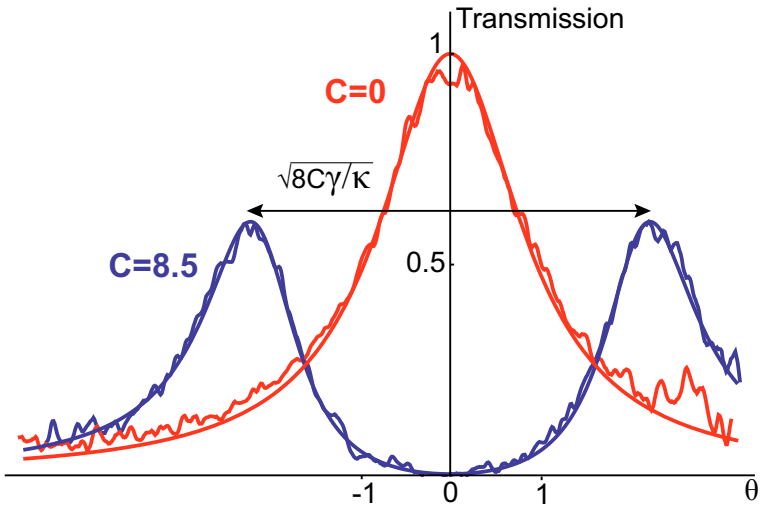

Figure 14.2: Cooperativity measurement with the resonant probe transmission. Example of transmission profiles measured when scanning the probe frequency around resonance, while the cavity is fixed and also on atomic resonance. Without atoms, $C = 0$, one sees the usual cavity transmission line, and with atoms the mode splits in two normal modes separated by $\sqrt{8C\gamma/\kappa}$ in units of κ, as illustrated here for a cooperativity $C \approx 8.5$. The smooth solid lines are fits using the known form of the transmission, to find the normalizations and the cooperativity.

Performing a frequency scan of this probe and monitoring the cavity transmission in the sequence after the preparation of the atoms allows us, for example, to make sure that the depumping pulse puts the effective cooperativity to 0.

It also proves very useful when aligning the side dipole trap: the cavity trap is by definition automatically well placed compared to the cavity mode, but the side one must be aligned to a few tens of microns of precision with a mirror that is 40 cm away from the cloud, to exactly cross the cavity mode in the center of the cloud. This is done, after having depumped all the atoms with the depumper, by optimizing the cooperativity created by the side repumper pulse (which is in the same mode as the side trap). Starting from a badly aligned configuration where the cooperativity is zero, the side repumper power is increased until the repumped region reaches the cavity mode (which normally always ends up happening at some point). From there, monitoring the measured cooperativity, the position of the side trap and repumper can be optimized. Progressively reducing the side

repumper power, a situation is reached where the cooperativity quickly drops to zero if the beam is slightly moved horizontally for example, which assesses a good alignment.

14.1.2 Imaging of clouds of few tens of microns

Imaging system setup and characterization

Before trying to image the atoms in the dipole traps, a first non-optimized imaging setup was used, which was fairly adapted to work with the complete MOT at the millimeter scale, but was limiting us in short-scale resolution to objects of size (waist) about 80 μm. An imaging system suitable for clouds in the 10 μm range therefore had to be designed.

The configuration of this system is constrained by technical aspects (see appendix C). The viewport of the vacuum chamber used to image is $\approx$ 2 cm in radius, 30 cm away from the cloud, and it is not orthogonal to the optical axis (see figure (14.4)). Additionally, a lower limit on the acceptable magnification must be set, as the camera we use has square pixels of 20 μm size. In order to deal with these different constraints while minimizing aberrations, the optical system used is sketched in figure (14.3).

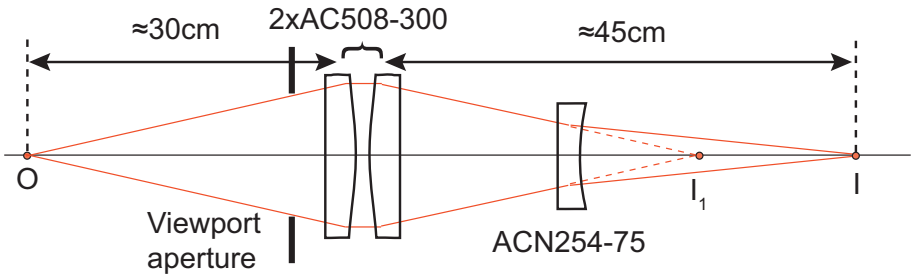

Figure 14.3: Schematic of the imaging system. The two positive doublets placed together 30 cm away from the object O act as a single low-aberration lens to produce the 1:1 intermediate image I_1, which is then magnified by the negative doublet to form the final image I, approximately 45 cm away from the chamber. Care was taken that only the viewport limits the optical aperture, and all collected light goes through the negative doublet of diameter 1".

Light collection is realized by two 300 mm focal length doublets of 2" diameter (Thorlabs AC508-300) placed close together facing each other to work in optimal conjugation. This system realizes a virtually aberration-free (for our purpose) image of the cloud at 1:1 scale outside the vacuum chamber. The magnification (of the order of 3) is then realized by a diverging doublet (ACN254-075), whose precise position along the optical axis determines the final position and size of the image. This implements in a compact way a system that meets our requirements.

The resulting collection solid angle of $\approx$ 0.012 steradians (corresponding to a collection efficiency of $\approx 10^{-3}$) fixes the diffraction limit, given by the Airy spot's radius in the object plane of $\approx$ 8 μm. In configurations where the magnifying ratio is close to 3, the aberrations were theoretically estimated to contribute to a blurring of the order of 5-10 μm of the image, which is acceptable. For more details, see appendix C.

In the final experimental configuration (see figure (14.4)), the magnifying ratio was measured to 2.74$\pm$0.05. The resolution limit was also estimated in practice to $\approx$ 20 μm (standard deviation in the image plane), though not exactly in the useful experimental configuration. Experimental methods are described in appendix C.

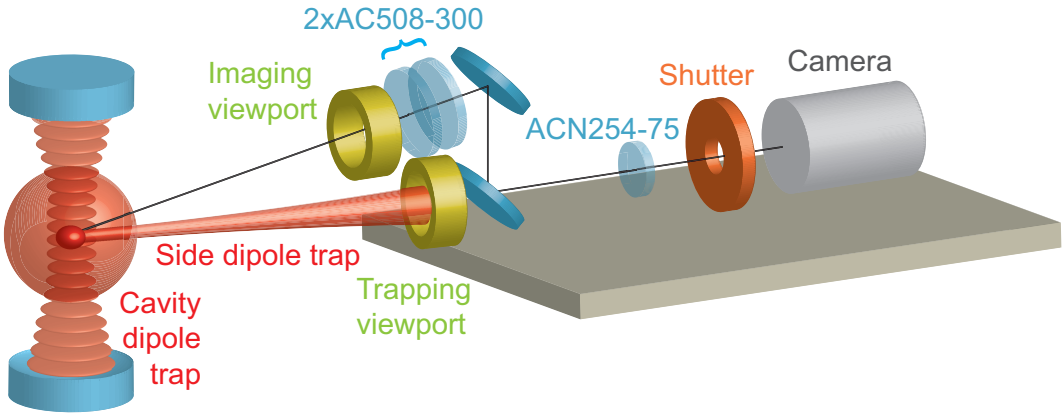

Figure 14.4: Real configuration of the imaging setup. The camera is installed on a breadboard on the side of the chamber, at the same height as the cloud itself. The optics to shape and inject the side dipole trap in the cloud are on the same breadboard, but not shown here. The trap is produced and injected in a single horizontal plane, through a viewport at the height of the atoms. On the contrary, the viewport through which we image is offset in height, so that the beampath must be bent with mirrors to direct it towards the camera. A mechanical shutter is also installed just before the camera on the imaging beampath, which is represented by the black line.

Finally, details in the object plane of size down to ≈ 10 μm are expected to be reasonably well resolvable, which was the goal.

Small cloud characterization

Using only the cavity trap and waiting for all the atoms around to fall, the resulting atomic distribution can be imaged. As it is close to orthogonal to the imaging axis (see figure (14.4)), all the points of the trap are well on focus in the CCD plane, leading to a clean image.

Using the side trap however, as its axis only makes a small angle with the imaging axis (see figure (14.4)), the image of an elongated cloud is obtained, of which only the center is well focused on the camera, as shown in figure (14.5). This makes measurements of sizes in the side dipole trap less easy.

Using the full preparation sequence, the cloud is loaded in the two dipole traps and subsequently only repumped in the mode of the side one. As there are still atoms around which could be repumped into bright transitions by the imaging light, the interesting small cloud can not be imaged with standard techniques. It can be done, to some extent, using as imaging light a probe in the cavity mode, in the absence of repumper. The (weak) signal collected then comes from the atoms that are in the cavity mode, and that have been repumped by the side repumper, *i.e.* the ones we are interested in.

The exact geometry of the trapping potential for the atoms is complicated as there are two traps overlapped, one of which has a strong longitudinal standing wave. The imaging with the cavity probe allows for accurate measurement of the size along the vertical direction, along which the atoms can not move due to this standing wave.

The minimal standard deviation of the atomic distribution is measured around 35 μm along the z axis. The measurement along the orthogonal axis is technically more complicated but the typical size is estimated to ≈ 25 μm.

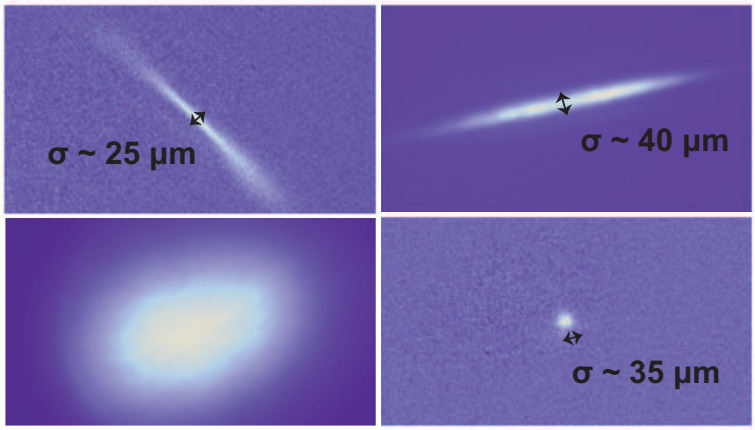

Figure 14.5: Images of the different possible configurations of traps. Upper left: Atoms trapped in the side dipole trap. **Upper right:** Atoms trapped in the cavity dipole trap. **Lower left:** Image of the full MOT without dipole traps. **Lower right:** Atoms resulting of our preparation sequence, imaged with a probe in the cavity mode. All images are at the same scale. The traps appear at an arbitrary angle because of the imaging beampath's geometry.

Together with the measurement of the cooperativity, the sizes allow us to estimate the atomic density of the small cloud. For typical values given above, the resulting effective density is 0.06 atoms/μm^3. This is only slightly higher than what was estimated in the MOT, because the side repumper power must be kept quite low for the cloud to remain small. This is necessary to limit inhomogeneity issues with the blue beam. What is observed is then the effective density of $F = 2$ atoms, which is lower than the total physical number density in the medium.

14.2 Increasing the effective blue power

Now that a cloud with small dimensions can be produced, the blue beam can be focused on it from the side to gain intensity. A carefully designed buildup cavity is also set up to increase the total power available. The aim is to get a large homogeneous blue intensity to address high Rydberg levels.

14.2.1 Description of the blue cavity

The idea is to build a cavity around the atoms in which the blue can resonate, which should be a running-wave cavity to avoid inhomogeneities. Because they are the only free optical accesses and anti-reflection coated for the blue, the beam must be sent through the horizontal viewports (the same as the side dipole trap ones). To avoid opening the vacuum chamber and installing new mechanical supports inside, this cavity is set up outside the chamber, so that the viewports are inside the cavity. For space optimization with the simultaneous injection of the blue and the dipole trap, only two concave mirrors are used, like in a linear cavity setup. Even then, there are several possibilities to avoid the standing wave inhomogeneities in the cavity. The one adopted in practice is described in the following.

The mirrors for the cavity (from Layertec, one input coupler with $T = 2.9\%$ and

$R = 97.1\%$ at 480 nm, and a high reflectivity back mirror with $R > 99.8\%$) are chosen with curvature radius of 1000 ± 5 mm, and are placed at 50 cm on each side of the atoms, adjusted so that the cavity is confocal. A beam can then be matched inside in a mode that is focused at the center in one direction, and collimated on the return trip. This configuration is permitted by the confocal cavity and allows for an adjustable size of the waist at the center, depending on the size of the beam injected at the mirrors' position (see figures (14.6) and (14.7)). As the cavity is quite long and the aim is to produce a small waist, the two fields propagating in different directions have very different sizes and thus very different intensities at the level of the atoms. This produces relatively low level of intensity modulations due to the interferences between the two (for numbers in real experimental configuration, see section 14.3).

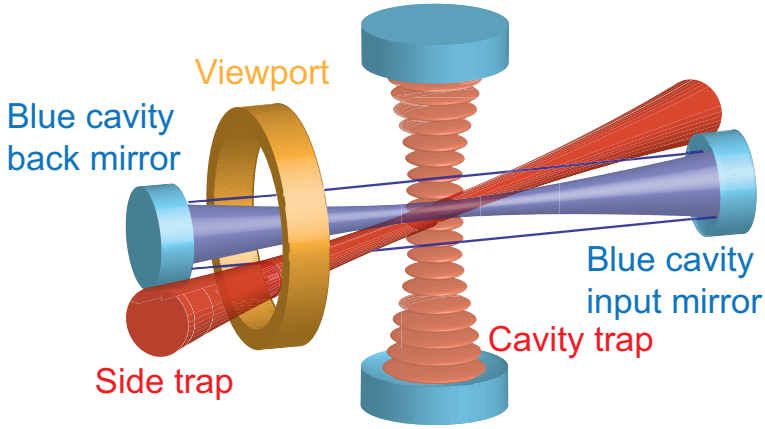

Figure 14.6: Setup of the blue cavity. The blue beam is injected centered on the viewport through which the side trap passes too. A symmetric viewport is present on the other side of the chamber, not represented here. The two mirrors are each ≈ 20 cm away from the viewports. The beam is injected through one of the mirrors to focus with an adjustable waist in the center, where the MOT lies, and the reflected field has a collimated mode represented here by the solid lines.

14.2.2 Length stabilization

The cavity being 1 m long, part of which is in open air outside the chamber, with the two mirrors mounted on two mechanically independent breadboards, each around 25 cm above the level of the optical table, stabilizing its length requires particular care.

Due to this structure of the cavity, compensation is necessary for slow but large length drifts due to mechanical vibrations of the breadboards' legs and fluctuations in the optical path length in air, on top of the higher frequency noise which is usually the main concern. In order to decouple the different contributions and keep a good reactivity in both domains, the active correction of the cavity length is split between the two mirrors: on one side the whole mirror mount (in practice a lens mount from Thorlabs to minimize the weight) is fixed on a slow piezo translation stage with a large range (PI Ceramic P-611.1, 120 μm range), while on the other one the mirror itself is fixed on a short range but fast tubular piezo (PICA P-025.10H, 15 μm range). The fast mirror+piezo assembly is mounted on a standard manual translation stage to allow for adjustments of the cavity length, which is then tightened by clamps to avoid mechanical vibrations. This allows efficient drift and noise compensation without too much crosstalk between the two piezos. Both piezos are

driven by an E-503 voltage amplifier. For cavity alignments, the two mirror mounts also include a four-point XZ adjustable stage.

After several difficulties inherent to locking such a cavity (see appendix C), the efficient method is the following: the cavity is locked with an auxiliary weak and far-detuned beam at 480 nm, phase-modulated at 20 MHz by an EOM and used in a Pound-Drever-Hall scheme. To separate the locking beam from the actual beam used for the experiment, it is injected in a completely different spatial mode (bowtie kind of mode) which still resonates in the cavity (with half the free spectral range of the main beam) because of its confocality, as shown in figure (14.7).

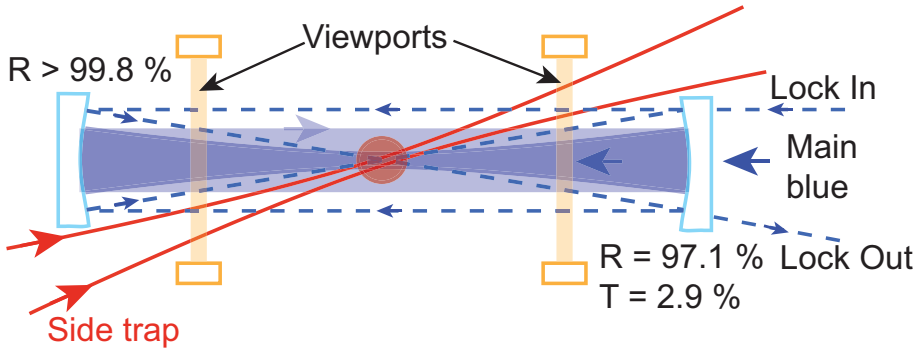

Figure 14.7: View from top of the blue cavity setup with the lock beam. Both the main blue beam and the locking beam are injected from the same side, through the "transmissive" mirror. The main blue is represented by the filled blue zones, focused when going from right to left and collimated on the reverse direction. The locking beam is injected, small and collimated, voluntarily offset from the optical axis. Its path in the cavity travels 4 times the cavity length and the exit beam is spatially separated from the others to be detected.

14.2.3 Performances

In order to assess the performances of the blue cavity, the intracavity power is monitored via a weak off-axis parasitic reflection of the intracavity beam on one of the windows. It is used while scanning the cavity length to match the cavity mode to the incident blue beam or vice versa. The procedure to align the cavity mode on the right spot in the atomic cloud, and the choice of the exact waist to be used inside the cavity, are described in section 14.3.

One remaining issue with the cavity is the birefringence of the windows on the blue beam, which is not negligible and uncontrolled (most likely due to the strain exerted on them by the difference in pressure). This on one hand makes the exact blue polarization at the level of the atoms relatively unknown, and on the other hand also forces us to use one of the polarization eigenstates that exists to inject the cavity.

Once the mode-matching and polarization have been optimized to maximize the intracavity blue power, the effective gain in power due to the cavity is estimated to a factor ≈ 16 on the one-way focused field's intensity. The corresponding finesse is of the order of 90, decreased by intracavity losses (viewports ...).

The cavity length has to be adjusted to be exactly confocal. This is done with the translation stage on which the fast mirror is mounted, while looking at the lineshape of the intracavity resonance while scanning the length. When the cavity is close to confocal,

several transverse modes tend to spectrally merge together, which gives a single resonance line with asymmetric shape. When the length is precisely adjusted, the lineshape is unique and symmetric. The resulting halfwidth at half maximum of the cavity is ≈ 0.8 MHz.

14.3 Rydberg EIT with a small cloud in the cavity

Finally, we expect to create a small dense cloud trapped at the intersection of the two dipole traps, on which the blue is focused in a relatively homogeneous manner with high power. The validation test is to observe the transmission of a resonant probe through the main cavity. It should normally be strongly attenuated by the addition of atoms without blue coupling beam, and made close to maximum again if we send the blue beam to produce resonant EIT on a low-lying Rydberg level (to avoid effects of interactions and nonlinearities so far). Any defect –blue power not high enough, cloud too large or beam too small, ... – would be directly visible on the transmission of the probe when it is scanned around resonance, as will be shown later.

14.3.1 Experimental sequence

The cloud is prepared with the usual MOT trapping step, followed by standard molasses, except that the repumper power is decreased, and the traps are On to load. After the molasses, approximately 0.4 mW of depumper is applied during 200 μs, optimized to set the observed cooperativity to negligible. Then during 100 μs a variable amount of side repumper is sent to the cloud (of the order of a few tens of nW) to create a population in $F = 2$.

The main cavity is locked on resonance with the atomic transition ($F = 2 \rightarrow F' = 3$). We then realize a scan of the probe frequency in 120 μs, from 50 MHz below to 50 MHz above atomic resonance, and measure the transmission [1]. When atoms without blue are in the cavity, or before the blue beam is well aligned to hit the repumped atoms, normal-mode splitting is observed as in figure (14.2) or figure (14.8).

The blue beam is then added during the probing time with an adjustable power, and a frequency set to couple resonantly to the state $37D_{5/2}$, which is low enough in n to present negligible nonlinearities for easily measurable probe power. This opens a transparency window around resonance in which the medium's absorption is strongly reduced and the cavity transmission re-increases (see figure (14.8)).

For large enough blue coupling Rabi frequency, this EIT transmission window reaches very high transparency and broadens up to a point where it is the only visible feature on the transmission curve.

To understand correctly the shape of the observed transmission, the remaining inhomogeneity of the blue power must be accounted for. As will be described in the following section, the blue mode's size had to be optimized with respect to the cloud. Due to their finite sizes and to interference effects, the blue intensity is still relatively broadly distributed in the cloud. To reproduce the EIT line of figure (14.8), the susceptibility is therefore averaged over an estimated distribution of intensities, that is described thereafter.

1. This scan width is the maximum we can do on a double-pass AOM while keeping reasonable efficiency. The input power during the scan, before the cavity, is monitored by a photodiode and a PID feedback loop maintains it approximately constant during the 120 μs. The cavity transmission is directly monitored by computing the ratio of the output to input measured powers in real time on the oscilloscope.

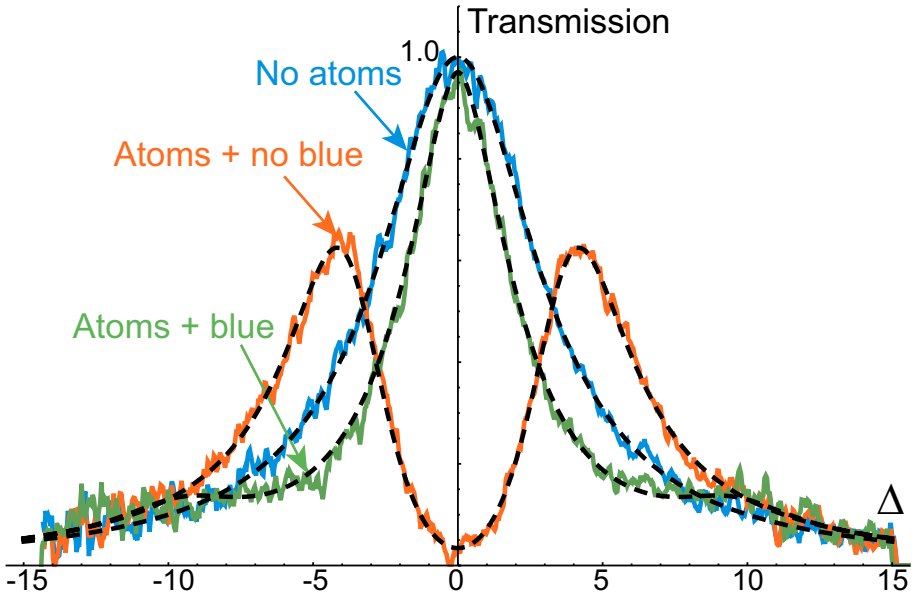

Figure 14.8: Transmission measurements of a weak resonant probe coupled to state $n = 37$. The probe transmission is measured as its detuning Δ is scanned across resonance. The solid curves are the experimental transmission curves obtained without atoms, and by preparing the small cloud with or without blue sent in the cavity to couple to $n = 37$. The dashed lines superimposed to those are fits to determine the normalization and the cooperativity (2.2 here) for the first two curves, and the third one is a manual adjustment of the theoretical transmission with EIT, taking into account the inhomogeneity of the blue power (see text).

14.3.2 Blue cavity mode alignment and optimization

When setting up the blue beam and cavity, the two dipole traps and the waist of the blue mode must all cross at the center of the atomic cloud. For the very first alignment, it is easier to look for a change on a non-zero signal, rather than trying to see directly transparency appearing on the initially very absorbed cavity transmission. The beam was therefore aligned a first time without the blue cavity in a temporary off-resonant scheme. Two-level absorption is then avoided, the cavity transmission can be measured, and is affected by the blue. This allows us to align the blue mode on the small cloud.

The probe is then set on resonance to observe EIT properly speaking with the single-pass focused beam, and the cavity mirrors must be set up without moving the beam. For that, the input coupler is first installed on the beam by centering it and making sure light is backreflected on itself. The 2.9 % of the total power transmitted through the mirror are enough to observe a weak transparency line when the beam is well aligned, so we can make sure the beam is still focusing optimally on the cloud through the mirror. Finally the back mirror is installed to close the cavity, first via rough alignment by eye of the multiple reflections of the beam, then by optimizing the maximal power in the cavity and the lineshape when scanning the cavity length, by tuning finely the position of the mirror without moving the beam.

When setting up the blue cavity, the waist to be given to the beam must also be chosen. Experimentally, for an initial chosen waist of 35 μm, the quality of the observed EIT transmission lines was quite bad, due to the strong inhomogeneity of the Rabi frequency

seen by the atoms. It is then a matter of adjusting both the size of the cloud (with the side repumper power in particular) and the blue waist to obtain a homogeneous enough blue mode. There are some physical limits due to our preparation method on how small the prepared cloud can be, and it was experimentally estimated that the smallest usable blue waist is 90 μm. Any smaller waist than this always leads to distorted EIT lines. This is consistent with the typical estimated cloud size, and the calculated distribution of the blue power as seen by the atoms, which is shown in figure (14.9).

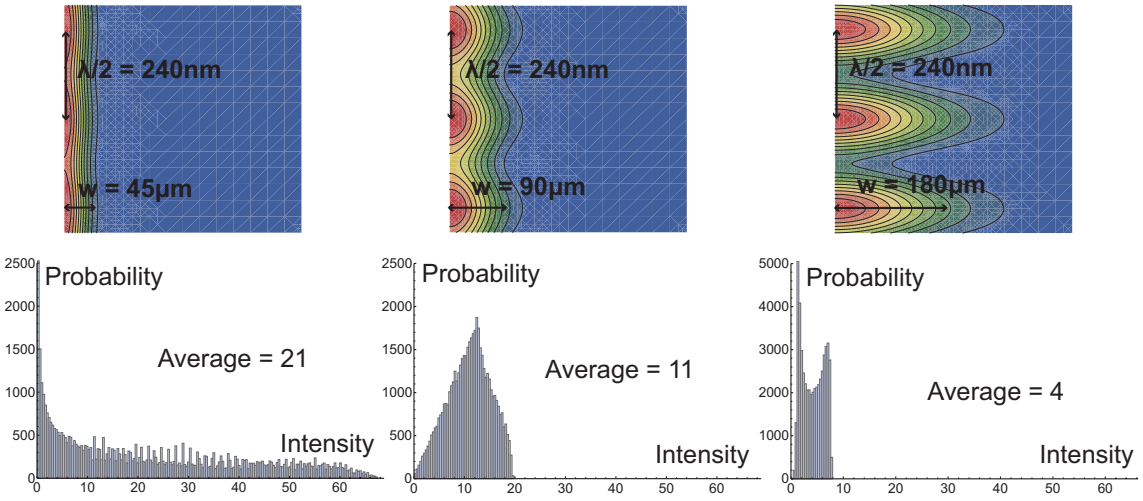

Figure 14.9: Distribution of blue intensities in the cavity as seen by the atoms. Top: Contour plot of the total intensity of the blue beam around the center of the cavity as a function of the longitudinal and radial coordinates, for different values of the waist of the blue focus. **Bottom:** Histograms of the blue intensities seen by the atoms assuming they have a Gaussian spatial distribution with radial standard deviation $\sigma = 30$ μm. The units are arbitrary but the same for all plots (in intensity, 1 is the maximum intensity one would get without the cavity for a blue waist of 90 μm).

On this figure one clearly sees the effect of the interference between the two propagating fields in the cavity, which is not completely negligible for the chosen waist of 90 μm. One sees as well the fact that for too tight focus of the blue beam, the modulations on-axis are small and the maximum intensity is very high, but the distribution is very broad and has an important tail towards very low powers (due to atoms radially too far from the center of the beam). On the contrary for large beamwaist it never reaches high powers and the effect of the longitudinal standing wave starts to be very visible as a double-peaked structure. The distribution observed for a waist of 90 μm therefore appears like a reasonable optimum, avoiding as much as possible low values of the intensity. The estimated distribution of powers given here is used to average the susceptibility to reproduce the experimental EIT profiles.

To summarize the effect of the cavity and of the blue spatial mode on the effective coupling power available for EIT, figure (14.10) shows the observed transparency line compared to what it would be in the absence of the blue cavity, or with a homogeneous beam.

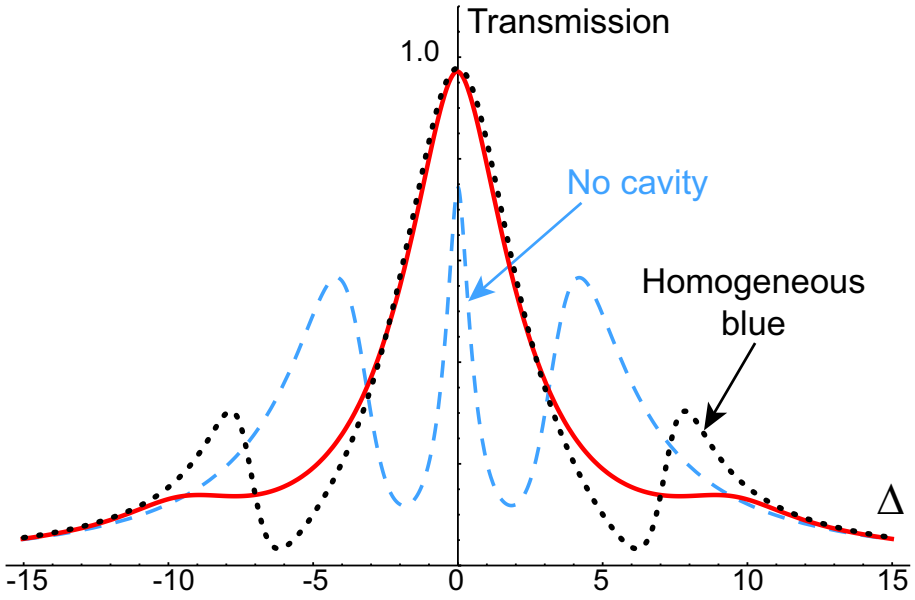

Figure 14.10: Effect of the cavity and blue mode on the EIT line. The solid red line is the exact same as in figure (14.8), corresponding to the observed EIT line. For comparison, the black dotted curve is the theoretical transmission for a homogeneous blue power, whose value has been adjusted to fit the shape of the main transparency peak. Finally the dashed light blue curve is the profile one would observe if the blue cavity was removed, keeping everything else equal (the maximum intensity in that case is approximately divided by 16).

14.3.3 Quality and possible uses for the resonant EIT

As can be seen in figure (14.8), the adopted preparation procedure creates a cloud in a region of a few tens of microns able to completely extinguish the probe transmission on resonance. The establishment of EIT with the Rydberg level allows us to make this cloud totally transparent again, in a quite broad frequency window ($\approx$ 15 MHz here). In the situation of figure (14.8), the total transmission can be switched from $\approx 3\%$ to $\approx 97\%$ of its maximum by the presence of the blue beam. The blue power distribution used to reproduce the observed lineshape corresponds to a maximum blue Rabi frequency $\Omega_{b0}/2 \approx 12$. This is higher than what was achieved in the experiment of part IV, and most importantly the power distribution among the atoms is now much more homogeneous (for comparison, one should look back on figure (12.10)).

A different interpretation can be given to the curve without cavity in figure (14.10): keeping the cavity and the maximum blue power, the Rydberg level could be increased up to $n = 90$, and the resulting transparency would be similar to the one observed on this curve, as the Rabi frequency would decrease by $\approx (89/36)^{3/2} \approx 4$.

With this possibility to control completely the state of the whole cloud with the blue intensity, a regime is reached where non-classical statistics should be observable on a very weak continuous light field, when coupling to higher Rydberg states. Indeed, as one excitation in the cloud effectively detunes the blue for n_b atoms, where n_b is now not negligible compared to the total number of atoms in the cloud, the cavity transmission is expected to be strongly dependent on the number of excitations.

For a resonant probe in transmission, this would be the absorptive equivalent of the off-

resonant scheme discussed in section 13.3.2. From preliminary calculations on resonance, nonclassical statistics on the transmitted light are estimated to be observable with the current version of the setup.

Finally, turning to the briefly discussed scheme using resonant cavity reflection and impedance matching, the setup is also in principle readily usable to investigate nonlinear effects at the quantum level with higher Rydberg states. In order to observe a differential behaviour of the multiply-excited states due to interactions, the parameters should be at least such that the impedance matching condition can be initially crossed at low power by opening the EIT window with the available Rabi frequency. The measurements performed above demonstrate that this should be possible even for Rydberg states up to $n \approx 100$: when increasing the blue power sent on an initially opaque cloud, the cavity transmission progressively increases from almost zero, while its intensity reflection decreases, crosses zero due to impedance matching, and increases again. It is easy to show that the condition in which the reflected field is impedance-matched corresponds to an intensity transmission of 25 % of its maximum. From the transmission curves showed above, up to Rydberg levels $n \approx 100$ it sould still be possible to get past this point.

14.3.4 Ongoing experiments and short-term plans

Preliminary theoretical calculations showed that with a resonant atomic excitation scheme, the current experimental setup should already enable us to observe bunching or antibunching on the light coming out of the cavity, both in reflection and in transmission. Investigations on the $g^{(2)}$ of the reflected light were thus initiated, using parameters adjusted close to the impedance matching condition. In this situation, the sensitivity of the impedance matching to the nonlinear atomic losses can make different photon-number states reflected with very different amplitudes.

This scheme may seem contradictory with our search for purely dispersive interactions. Nevertheless, because of the phase-flip in reflection happening when the impedance matching is crossed, it is expected that in finely tuned conditions different photon-number components could be reflected with different phases for example. A complete dynamical theory to describe a pulsed scheme of this kind is however still out of reach for now.

So far, this resonant reflection scheme lead to observation of bunched statistics on timescales that depend on the addressed Rydberg state and on the control beam intensity, but not yet any feature that could be quantitatively compared with theoretical predictions. These experiments will therefore go on in the immediate future, to hopefully lead to some antibunching and/or non-classical state measurements that should be consistently and carefully related to Rydberg interaction effects.

Conclusion

Based on the experimental and theoretical knowledge extracted from the previous experiments, and from recent publications in which single-photon level nonlinearities were reported, various possibilities and regimes were investigated in which our setup should enable light processing at the quantum level in new ways.

For example, increasing the cavity finesse should allow for observation of dispersively induced nonclassical statistics on the transmitted light. In the immediate future, without modifying too much the system, the unique features of our cavity-based setup can already be exploited: the resonant regime can be used to maximize nonlinearities, while still producing an effective low-loss nonlinear phase-shift. That is the basis of the cavity-reflection and nonlinear impedance matching experiments that we started to carry out.

In order to reach the right range of parameters for these experiments, the general idea is the following: the cloud itself must be able to modify completely the properties of the system, like the cavity reflection for example. One then needs a "control parameter", typically the blue Rabi frequency, that can be applied to the cloud in a strong and homogeneous enough manner to completely switch its behaviour. Finally, the Rydberg interactions due to only two excitations must be able to perturb the effect of this control parameter in a non negligible way.

To achieve all these conditions, our system was modified to create a cloud of few tens of microns size in dipole traps, which can then be illuminated by a strong and relatively homogeneous blue Rabi frequency. A buildup cavity was installed to increase the blue power, in such a way that Rydberg levels up to $n \approx 100$ are now reachable with a large Rabi frequency. The capabilities of our system were demonstrated on a low-lying Rydberg state to voluntarily exclude the effect of interactions, showing very good transparency of the cloud controlled by the Rydberg-EIT transition.

This allows us to think that all conditions should now be met to realize new experiments on this system, in the desired regime where one photon can have a strong influence on its neighbours.

General conclusion and outlook

Advances reported in this thesis in relation with the main project

In this thesis, we investigated different coupling mechanisms between light and collective excitations of a cold atomic cloud in an optical cavity. This work is motivated by the fact that atomic ensembles have already been featured in several experiments and theoretical proposals as valuable interfaces between photonic and matter qubits. Engineering a single well-controlled system for simultaneous efficient generation, storage and processing of non-classical light states is obviously of great interest. Additionally, some of our experiments involved strongly interacting Rydberg atomic excitations. The whole field of Rydberg physics is currently at the center of great developments, in very diverse systems including Bose-Einstein condensates, hot vapours or on-chip trapped atoms. Gaining better understanding of the effect of long-range interactions in such systems is thus also a prime concern, to enable their use as "quantum simulators" for example (as is envisioned by many groups lately, for example to simulate magnetic Ising-type systems).

On one hand we showed that our experimental system, thanks to the optical cavity in particular, can be used to store optical photons as ground-state polaritons and retrieve them on demand. The important step forward taken here was to implement homodyne tomography of the light at the cavity output, to fully reconstruct its quantum state. This in particular allowed us to show that the excitation retrieval has high efficiency in a single clean mode of the optical field. With the excitation scheme used, the production with 80 % probability of a single photon at the cavity output was demonstrated, with a controlled and stable spatiotemporal shape, upon each readout pulse. The loading of the excitation in the cloud was probabilistic, but could in principle be made deterministic by use of Rydberg blockade typically. The sources of inefficiencies and decoherence in this system were also studied in some details, both theoretically and experimentally.

On the other hand, the main longer-term goal of the project is to realize strong effective photon-photon interactions using Rydberg excitations, to eventually turn them into a logical two-photon quantum gate. Storing excitations in the cloud as interacting Rydberg polaritons can lead to their dephasing, localization and/or total spatial blockade. In order to gain some experience with intracavity Rydberg polaritons, we investigated the classical low-light response of the system in an off-resonant 2-photon excitation scheme (ladder EIT). Characterizing the cavity transmission resonance with a very weak probe as a function of its power, the Rydberg-Rydberg interactions were shown to be the origin of a strong nonlinear dispersive susceptibility. The medium's response is well reproduced by a simple model, in which atoms randomly excited to the Rydberg state effectively decouple from the EIT control beam a number of their neighbours that depends on the state's principal quantum number. This vision of blockade spheres in disordered clouds,

already widely used in other contexts, finds here another application and slightly different interpretation. The dispersive nonlinearity observed in this experiment is large, but the parameters of the measurement prevent observation of direct effect at the level of only a few photons in the system. Furthermore, "technical" considerations like the inhomogeneities and dynamics in the system were found to have a primary influence on the observations.

All the ingredients of the two aforementioned experiments (ground-state polariton storage, Rydberg interactions, efficient readout and homodyne tomography) might be required for a full demonstration of a Rydberg-mediated photonic quantum gate in a cold cloud, as illustrated by recent theoretical proposals. However, in order to reach the necessary quantum nonlinear regime, several experimental improvements were necessary on our system. Modifications were thus implemented to trap a small atomic cloud in the cavity mode, in a region defined by two optical dipole traps of typical size 30 μm, closer to the relevant blockade length scale. On this small cloud, the Rydberg coupling beam was focused in a relatively homogeneous manner, with a power enhanced by a factor ≈ 16 thanks to an external buildup cavity. With this final experimental configuration, resonant intracavity EIT was demonstrated on a low Rydberg level, making the whole cloud transparent in a large frequency bandwidth, such that the cavity transmission is fully restored. Some of the ideas we could explore with this upgraded setup were discussed theoretically, in order to probe the regime where few excitations experience strong interactions in the mode. Storage-retrieval schemes using Rydberg states could deterministically generate non-classical states of light, to be analyzed with homodyne detection. The quantum nonlinearity could also be probed by measuring the steady-state correlations induced on light transmitted or reflected by the cavity, with the pair of photon counters already in place.

Based on the quality of the EIT observed on state $n = 37$, we have good reasons to think that the latest version of the experimental setup should allow for observation of few-photon nonlinearities in one of these ways, in well-chosen parameter ranges. Experiments along this axis have already started, as discussed in chapter 14, but will be completed in the ongoing PhD thesis of Rajiv Boddeda.

Medium and long-term plans

In the medium term, the plan for the future is to replace the cavity mirrors to achieve smaller cavity waist and higher finesse, in order to enhance the effect of a single Rydberg sphere in the system. The new cavity mirrors, designed by Imam Usmani, are already available, and the switching should occur as soon as all measurements considered worth doing with the current setup are done. The new cavity design should allow more easily for observation of single-photon level nonlinearities, and enable the team to explore purely dispersive regimes where additional interesting physics should happen.

In the long term, as was partially demonstrated in this thesis, this system of cold atomic cloud coupled to a relatively low-finesse cavity in Rydberg-EIT conditions should gather all necessary features to study coherent few-photon nonlinear evolutions. As already pointed out, experimentally realistic schemes are now proposed to realize in a "clean" way an optical two-photon quantum gate using this kind of system.

In addition to these already existing proposals, a collaboration has been initiated between our group and Anders Sørensen's one to look for specific schemes that would make optimal use of our system's features. Using the cavity in a regime where a single excitation stored in the Rydberg state can drastically modify its resonance, one could in principle sequentially realize all necessary operations for an efficient two-photon gate, with efficient re-collection of the gate and target photons after the operation.

Appendix A

Rydberg atoms and interactions

In Rydberg states of alkali atoms, the only valence electron is excited to a high-lying energy level (n> 30), occupying a wavefunction mostly spread far away from the positive core formed by the nucleus and the inner electrons. As a result the system is close to hydrogenoid, with a singly-charged massive nucleus, and the state of the outer electron is described by its principal quantum number n, orbital angular momentum l and total angular momentum (orbital + spin) j [1]. However, for low l states which we will be interested in, the non-negligible penetration of the valence electron into the core at the "perigee" of its orbit makes the effective potential it feels seem slightly stronger than the pure hydrogenoid one in regions close to the nucleus.

This leads to the standard "quantum defect" description of the Rydberg states, which states that to estimate many of their physical properties (typically energies), one can use a hydrogenoid model with an adjusted effective principal quantum number $n^*_{n,l,j} = n - \delta_{n,l,j}$, corrected by the quantum defect $\delta_{n,l,j}$, which is measured accurately and tabulated [57]. The energies of Rydberg levels in an alkali atom where the core is of mass m_c are accurately found by:

$$E_{n,l,j} = -\frac{Ry(1+\frac{m_e}{m_c})^{-1}}{(n^*_{n,l,j})^2} \tag{A.1}$$

where Ry is the Rydberg unit of energy ($1Ry \approx 13.6$ eV).

Other characteristics of Rydberg states have simple scalings with n^*, as shown in table (A.1).

Physical quantity	Scaling	Value for n=62
Binding energy	$(n^*)^{-2}$	-0.9 THz
Transition frequency between adjacent n state	$(n^*)^{-3}$	30 GHz
Ionization electric field	$(n^*)^{-4}$	23 V/cm
Typical orbital radius	$(n^*)^2$	3500 a_0
Dipole moment between adjacent n states	$(n^*)^2$	3500 e a_0
Radiative lifetime	$(n^*)^3$	220 μs
Scalar polarisability	$(n^*)^7$	900 MHz/(V/cm)^2

Table A.1: Scaling of the different properties of Rydberg levels.

The property of importance to us is the Rydberg wavefunctions' typical radius, scaling

1. The coupling to the nucleus being very weak, the hyperfine splitting of Rydberg states is usually considered as negligible or unresolved, and the fine structure basis is good enough

as $(n^*)^2$, that explains the extremely large dipole moments available from these states, and thereby the strong interactions they can experience.

The complete theoretical description of these interactions between two atoms involves taking into account all interaction terms between the many bodies composing each of the atoms. It can be shown that a multipolar expansion of the interaction Hamiltonian leads to a series in powers of R^{-1} [153].

Keeping only the dipole-dipole interaction term, the Hamiltonian of atoms A and B at a distance R is:

$$\hat{H}_{dd} = \frac{1}{4\pi\epsilon_0}\frac{\hat{\vec{d}}_A.\hat{\vec{d}}_B - 3(\hat{\vec{d}}_A.\vec{u})(\hat{\vec{d}}_B.\vec{u})}{R^3} \tag{A.2}$$

where $\vec{u}$ is a unit vector pointing from A towards B.

Starting from the symmetric two-atom state $|n,l,j,m_j\rangle \otimes |n,l,j,m_j\rangle$, ignoring its possible degeneracy in m_j, and as the atomic states have no permanent dipole, $\hat{H}_{dd}$ can couple the system to states $\left|n',l',j',m'_j\right\rangle \otimes \left|n'',l'',j'',m''_j\right\rangle$ that are in general not degenerate in energy. The contribution of the dipole-dipole interaction to the total energy of the system can therefore be calculated to lowest order by second-order perturbation theory as:

$$\Delta E = \sum_{\substack{n',l',j',m'_j,\\ n'',l'',j'',m''_j}} \frac{\left|\left\langle n',l',j',m'_j\right| \otimes \left\langle n'',l'',j'',m''_j\right| \hat{H}_{dd} \left|n,l,j,m_j\right\rangle \otimes \left|n,l,j,m_j\right\rangle\right|^2}{(2E_{n,l,j} - E_{n',l',j'} - E_{n'',l'',j''})} \tag{A.3}$$

This therefore takes the form usually written as $\frac{C_6}{R^6}$. Though the sum above theoretically must include all possible combinations of pairs of levels, it is clear that the ones with large dipole coupling to $|n,l,j,m_j\rangle$ and small energy defects $\Delta_F = (2E_{n,l,j} - E_{n',l',j'} - E_{n'',l'',j''})$ contribute the most. In order to estimate the resulting shift, one therefore has to look for the possible combinations of states where one atom goes up in energy and the other one goes down, so that the total energy remains approximately constant. There are usually not so many channels satisfying this condition, and it is then enough to consider a remarkably small number of states (< 10) to get a good estimate of the energy shift [145].

In the extreme case where one assumes that one specific channel is mostly responsible for the shift, the problem simplifies to solving for the eigenenergies of the following Hamiltonian in two-atom states basis:

$$\hat{H} = \begin{pmatrix} 0 & \frac{C_3}{R^3} \\ \frac{C_3}{R^3} & \Delta_F \end{pmatrix} \tag{A.4}$$

The energy of state $|n,l,j,m_j\rangle$ is then shifted by the interactions of the amount $\frac{1}{2}(\Delta_F - \sqrt{\Delta_F^2 + \frac{4C_3^2}{R^6}})$. If the interactions represent a small perturbation compared to the Förster energy defect Δ_F, this is $\approx \frac{-C_3^2}{\Delta_F R^6}$, so that one recovers the van der Waals form. However when $\frac{C_3}{R^3} >> \Delta_F$, the energies of the two states are shifted by $\pm\frac{C_3}{R^3}$.

This therefore signals one of the limits of the van der Waals $1/R^6$ description of the interaction between Rydberg atoms. The situation above can occur if for some given two-atom state there exists another one with very small Δ_F, which is called a quasi-Förster resonances (an example is 43D5/2 in rubidium), or if two states are on purpose brought into Förster resonance ($\Delta_F = 0$) via application of an external field for example. In this case the dipole-dipole interaction scales as $1/R^3$. Even in the general case, this sets a lower bound to the region in R where the $1/R^6$ behaviour is valid, as even for a non-zero Δ_F

there is a characteristic distance R_{min} for which $\frac{C_3}{R_{min}^3} = \Delta_F$, below which the behaviour of the interaction potential changes. This minimum radius of validity can be written in other terms as $R_{min} = \left(\frac{c_6}{\Delta_F}\right)^{1/6}$. A typical value is $R_{min} \approx 2\mu$m for $60D5/2$ states in rubidium. In our range of atomic densities, the average interparticle distance is typically 3 μm, so that for most pairs of atoms in the cloud the interaction distance is above this limit. For $n > 50D5/2$ states in rubidium the expected scaling is $R_{min} \propto (n^*)^{7/3}$ [145].

On the other hand, for large enough distances R, another limit should be taken into account as the multipolar expansion of the interactions exhibits one quadrupole-quadrupole coupling term scaling as C_5/R^5, that dominates over the van der Waals one above a certain limit $R_{max} = \frac{C_6}{C_5}$. However in standard cases, this R_{max} is large enough that at such distances the $1/R^5$ may start to dominate but the overall interaction energy is anyway much too low to have any effect at all [152, 153].

In conclusion, for the relevant range of interatomic distances, when interactions actually play a role we will assume that they are well described by the van der Waals potential. However, as explained in the main text (section 10.1.2), the Zeeman degeneracy of the Rydberg states and the angular dependence of the potential lead to more complications that we have to take into account.

Appendix B

Modeling of the classical nonlinear dispersion measurements

This appendix aims at establishing the results used in section 12.3, whose derivation was too technical and/or lengthy to be included in the main text. The main question is how to include the dynamics of the three-level atomic response and the spatial inhomogeneities in a model that could explain our observations of dispersive nonlinearities induced by Rydberg interactions. In order to be able to do that, we resort to an adiabatic elimination of the intermediate state to use effective two-level Bloch equations. The coherence is expressed in the $\chi^{(3)}$ limit as a function of the Rydberg population, whose effective response time is found here. We have to take into account the spatial averaging over the probe mode to estimate this response time, as well as to get the right effective nonlinear susceptibility. The results are used to reproduce the slopes we observe experimentally for the curves $\Delta\theta(Y)/\Delta\theta(0)$.

The calculations and analytical expressions in this appendix were first derived from the work of Alexei Ourjoumtsev.

Adiabatic elimination of the intermediate level

We start from the full three-level Bloch equations without interactions for the averages of operators, for a given atom:

$$\begin{cases} \frac{\mathrm{d}}{\mathrm{d}t}\sigma &= i\gamma\left((\Delta+i)\sigma+\frac{\Omega}{2}(\sigma_{33}+2\sigma_{22}-1)-\frac{\Omega_b}{2}\sigma_{13}\right) \\ \frac{\mathrm{d}}{\mathrm{d}t}\sigma_{13} &= i\gamma\left((\delta+i\gamma_{13})\sigma_{13}+\frac{\Omega}{2}\sigma_{23}-\frac{\Omega_b}{2}\sigma\right) \\ \frac{\mathrm{d}}{\mathrm{d}t}\sigma_{23} &= i\gamma\left(((\delta-\Delta)+i(1+\gamma_{13}))\sigma_{23}+\frac{\Omega}{2}\sigma_{13}+\frac{\Omega_b}{2}(\sigma_{33}-\sigma_{22})\right) \\ \frac{\mathrm{d}}{\mathrm{d}t}\sigma_{22} &= \gamma\left(-2\sigma_{22}+2\gamma_{33}\sigma_{33}+i\frac{\Omega}{2}(\sigma-\sigma^*)-i\frac{\Omega_b}{2}(\sigma_{23}-\sigma_{23}^*)\right) \\ \frac{\mathrm{d}}{\mathrm{d}t}\sigma_{33} &= \gamma\left(-2\gamma_{33}\sigma_{33}+i\frac{\Omega_b}{2}(\sigma_{23}-\sigma_{23}^*)\right) \end{cases} \tag{B.1}$$

where we took $\gamma_{23}=1+\gamma_{13}$ for the 2-3 coherence decay rate.

We are interested in the dynamics at the μs timescales, so that, as γ corresponds to timescales $\approx$ 30 ns, we set $\frac{\mathrm{d}}{\mathrm{d}t}(\sigma,\sigma_{23},\sigma_{22}) << \gamma(\sigma,\sigma_{23},\sigma_{22})$ to describe only the relevant dynamics. This allows to eliminate the intermediate state from the equations, expressing σ,σ_{23} and σ_{22} as a function of σ_{13} and σ_{33}, and get a closed system of equations for σ_{13} and σ_{33}.

We will write these relations symbolically:

$$\frac{\mathrm{d}}{\mathrm{d}t}V = AV + U \tag{B.2}$$
$$W = BV + Z \tag{B.3}$$

where

$$V = (Re[\sigma_{13}], Im[\sigma_{13}], \sigma_{33})^\dagger \tag{B.4}$$
$$W = (Re[\sigma], Im[\sigma])^\dagger \tag{B.5}$$

The coefficients of matrices and vectors A, B, U, Z have complicated expressions, but are obtained straightforwardly from the initial system at this stage. In principle one can then solve the dynamical equation for the effective two-level model with states 1 and 3, and get afterwards the susceptibility by calculating σ using B and Z.

Now if we take into account the experimental values of all parameters, the expressions of all the coefficients of A, B, U, Z can be simplified a lot. Recall that in our experimental configuration, because of the modes inhomogeneities, some approximations can not be made, like $\Omega << \Omega_b$, because they are not valid everywhere in space. The quantities we will neglect before 1, as they are at most of order 0.1, are: $\frac{\Omega^2}{4\Delta^2}, \frac{\delta}{\Delta}, \frac{1}{\Delta}, \frac{\gamma_{13}}{\Delta}, \gamma_{33}, \gamma_{13}, \frac{\Omega_b^2}{4\Delta^2}$.

Under these approximations, one obtains an equivalent system described by leading order terms in A and U, much simpler, that can be written as:

$$A_e = \gamma \begin{pmatrix} -\gamma_{13e} & -\delta_e & 0 \\ \delta_e & -\gamma_{13e} & \Omega_e \\ -\frac{\Omega_e}{\Delta} & \Omega_e & -2\gamma_{33e} \end{pmatrix} \tag{B.6}$$

$$U_e = \gamma \begin{pmatrix} -\frac{\Omega_e}{2\Delta} & -\frac{\Omega_e}{2} & \frac{\Omega_e^2}{2\Delta^2} \end{pmatrix}^\dagger \tag{B.7}$$

The parameters with index e are the ones of the resulting effective two-level model, given by:

$$\Omega_e = \frac{\Omega\Omega_b}{2\Delta} \tag{B.8}$$
$$\delta_e = \delta + \frac{\Omega^2 - \Omega_b^2}{4\Delta} \tag{B.9}$$
$$\gamma_{13e} = \gamma_{13} + \frac{\Omega^2 + \Omega_b^2}{4\Delta^2} \tag{B.10}$$
$$\gamma_{33e} = \gamma_{33} + \frac{\Omega_b^2}{4\Delta^2} \tag{B.11}$$
$$\tag{B.12}$$

Under the same level of approximation, the B and Z matrices are (to lowest order in probe power):

$$B_e = \begin{pmatrix} \frac{\Omega_b}{2\Delta} & \frac{\Omega_b}{2\Delta^2} & -\frac{\Omega}{2\Delta} \\ -\frac{\Omega_b}{2\Delta^2} & \frac{\Omega_b}{2\Delta} & \frac{\Omega}{2\Delta^2} \end{pmatrix} \tag{B.13}$$

$$Z_e = \begin{pmatrix} \frac{\Omega}{2\Delta} & -\frac{\Omega}{2\Delta^2} \end{pmatrix}^\dagger \tag{B.14}$$

Thus the lower transition coherence can be written as:

$$\sigma(t) = \frac{1}{2(\Delta + i)} \left[\Omega_b \sigma_{13}(t) + \Omega(1 - \sigma_{33}(t))\right] \tag{B.15}$$

If we neglect the intrinsic dynamics of σ_{13} and assume that it is mostly following σ_{33} which has the slowest behaviour, we can get an approximation by putting $d\sigma_{13}/dt$ to zero in the remaining dynamical equations, to extract the "quasi-steady state" relationship between the two:

$$\sigma_{13}(t) = \frac{\Omega_e}{2(\delta_e + i\gamma_{13e})} \left[\frac{\Delta - i}{\Delta} - 2\sigma_{33}(t)\right] \tag{B.16}$$

This, once combined with equation (B.15), gives equation (12.4):

$$\frac{\sigma}{\Omega/2}(t) = \frac{1}{\Delta + i} \left[1 + \frac{\Omega_b^2/4}{(\Delta + i)(\delta_e + i\gamma_{13e})} - \sigma_{33}(t) \left(1 + \frac{\Omega_b^2/2}{\Delta(\delta_e + i\gamma_{13e})}\right)\right] \tag{B.17}$$

Local and average Rydberg population response times

From the previous approximations, once one has neglected the intrinsic dynamics of the Rydberg coherence, the dynamical equation $dV/dt = AV + U$ can be written as a single equation on σ_{33}, that involves a exponential response time. One clearly sees from the coefficients in matrix A_e, that to lowest order in probe power, the local value of this response time will be:

$$\tau_{loc} = (2\gamma(\gamma_{33e}))^{-1} = \left(2\gamma(\gamma_{33} + \frac{\Omega_b^2/4}{\Delta^2})\right)^{-1} \tag{B.18}$$

To express the response time of the average population, one has to average over the probe mode the steady-state population on one hand, and its initial growth rate on the other hand.

To lowest order approximation, the simplest form one can get from this effective two-level model for the local steady-state Rydberg population in the $\chi^{(3)}$ limit is:

$$\sigma_{33}^{\infty(2)} \approx \frac{\Omega_e^2 \gamma_{13e}}{4\gamma_{33e} \left|\delta_e + i\gamma_{13e}\right|^2} \approx \frac{\Omega^2 \Omega_b^2}{16\Delta^2 \gamma_{33} \left|\delta + i\gamma_{13}\right|^2} \frac{\gamma_{13} + \Omega_b^2/4\Delta^2}{(1 + x_2)\left|1 + x_1\right|^2} \tag{B.19}$$

which depends on space through the local Rabi frequencies. Here x_1 and x_2 are parameters whose expressions are:

$$x_1 = -\frac{\Omega_b^2/4}{(\Delta + i)(\delta + i\gamma_{13})} \tag{B.20}$$

$$x_2 = \frac{\Omega_b^2/4}{\gamma_{33}\Delta^2} \tag{B.21}$$

After making a single-pole decomposition of this expression with respect to Ω_b, it can be averaged over space, with a probe mode with maximal Rabi frequency Ω_0 and waist w, and a blue mode with maximal Rabi frequency Ω_{b0} and waist w_b (the z dependence

disappears as the two modes have incommensurate wavelengths and the beating is averaged out. The result is:

$$\left\langle \sigma_{33}^{\infty(2)} \right\rangle = \frac{3\Omega_0^2}{32} Im \left[\frac{{}_2F_1\left(\frac{1}{2}, \frac{2w_b^2}{w^2}, 1+\frac{2w_b^2}{w^2}, -x_{20}\right) - {}_2F_1\left(\frac{1}{2}, \frac{2w_b^2}{w^2}, 1+\frac{2w_b^2}{w^2}, -x_{10}\right)}{\gamma_{33}(\Delta - i) + \delta + i\gamma_{13}} \right] \tag{B.22}$$

where x_{10} and x_{20} are the values of x_1 and x_2 for the maximum blue Rabi frequency.

Under the approximation that $\frac{w^2}{w_b 2} \approx 2$ (=1.65 in reality), the special functions simplify to give:

$$\left\langle \sigma_{33}^{\infty(2)} \right\rangle = \frac{3\Omega_0^2}{16} Im \left[\frac{1}{\gamma_{33}(\Delta - i) + \delta + i\gamma_{13}} \left(\frac{1}{1+\sqrt{1+x_{20}}} - \frac{1}{1+\sqrt{1+x_{10}}} \right) \right] \tag{B.23}$$

which is (proportional to) the numerator of equation (12.10).

To get the denominator one must calculate the growth rate of the average population, which is, to the same level of approximation and using the same procedure as before:

$$\left\langle \frac{\sigma_{33}^{\infty(2)}}{\tau_{loc}} \right\rangle \approx \frac{3\Omega_0^2}{32} Im \left[\frac{1 - {}_2F_1\left(\frac{1}{2}, \frac{2w_b^2}{w^2}, 1+\frac{2w_b^2}{w^2}, -x_{10}\right)}{(\Delta - i)} \right] \tag{B.24}$$

For $\frac{w^2}{w_b 2} \approx 2$, this is:

$$\left\langle \frac{\sigma_{33}^{\infty(2)}}{\tau_{loc}} \right\rangle = \frac{3\Omega_0^2}{32} Im \left[\frac{1}{(\Delta - i)} \left(1 - \frac{2}{1+\sqrt{1+x_{10}}} \right) \right] \tag{B.25}$$

One can check numerically that when taking the ratio to get the effective rising time, the result does not depend a lot on the exact value of $\frac{w^2}{w_b^2}$ so that the approximation ≈ 2 is good enough.

One can also more carefully estimate the settling time of the average coherence directly, instead of assuming it is following the one of the population, by averaging the full expression (12.4) (as there are other factors depending on space in addition to the population), but the difference turns out to be quite small in our range of parameters.

Spatial averaging of the third-order nonlinear term (parameter a)

Here we want to give the expressions obtained when integrating over the probe mode the steady-state value of the susceptibility in the $\chi^{[3]}$ limit, $\left\langle \frac{\sigma}{\Omega/2} \right\rangle_\infty^{(3)}$. This involves a spatial average of the two contributions to the nonlinearity, the "natural" one and the interaction one.

As explained in the main text, the local natural third-order nonlinearity within our approximations is:

$$\frac{\sigma}{\Omega/2}^{(3)}_{nat,\infty} = -\sigma_{33}^{\infty(2)} \left(\frac{1}{\Delta + i} + \frac{\Omega_b^2/2\Delta}{(\Delta + i)(\delta + i\gamma_{13}) - \frac{\Omega_b^2}{4}} \right) = -\sigma_{33}^{\infty(2)} \left(\frac{1}{\Delta + i} - \frac{2x_1/\Delta}{1 + x_1} \right) \tag{B.26}$$

As it has a local expression where the only dependence on space comes through the blue Rabi frequency, this quantity can be averaged spatially over the probe mode, or using the distribution function $Pr(x)$ for Ω_b^2/Ω_{b0}^2, to give the exact same result.

Here again, a single-pole decomposition of this product of terms as a function of Ω_b allows for an analytical integration, to get:

$$\begin{aligned}\left\langle \frac{\sigma}{\Omega/2}^{(3)}_{nat,\infty} \right\rangle = \{Im\left[\frac{{}_2F_1\left(\frac{1}{2},\frac{2w_b^2}{w^2},1+\frac{2w_b^2}{w^2},-x_{20}\right)-{}_2F_1\left(\frac{1}{2},\frac{2w_b^2}{w^2},1+\frac{2w_b^2}{w^2},-x_{10}\right)}{\gamma_{33}(\Delta-i)+\delta+i\gamma_{13}}\right]\\ +Im\left[\frac{2\gamma_{33}\Delta}{\gamma_{33}(\Delta+i)+\delta-i\gamma_{13}}\right]\frac{{}_2F_1\left(\frac{1}{2},\frac{2w_b^2}{w^2},1+\frac{2w_b^2}{w^2},-x_{20}\right)-{}_2F_1\left(\frac{1}{2},\frac{2w_b^2}{w^2},1+\frac{2w_b^2}{w^2},-x_{10}\right)}{\gamma_{33}(\Delta-i)+\delta+i\gamma_{13}}\\ +\frac{2(i-1/\Delta)}{4\frac{w^2}{w_b^2}(1+x_{10})(\gamma_{33}(\Delta-i)+\delta+i\gamma_{13})}[(4+\frac{w^2}{w_b^2})_2F_1\left(-\frac{1}{2},\frac{2w_b^2}{w^2},1+\frac{2w_b^2}{w^2},-x_{10}\right)\\ -(4+\frac{w^2}{w_b^2}+4x_{10})_2F_1\left(\frac{1}{2},\frac{2w_b^2}{w^2},1+\frac{2w_b^2}{w^2},-x_{10}\right)]\\ +\frac{i\Delta(\delta-i\gamma_{13})}{Im[(\Delta+i)(\delta+i\gamma_{13})]}Im\left[{}_2F_1\left(\frac{1}{2},\frac{2w_b^2}{w^2},1+\frac{2w_b^2}{w^2},-x_{10}\right)\right]\}*\frac{3\Omega_0^2}{32}\frac{1}{\Delta+i}\end{aligned} \tag{B.27}$$

This, being proportional to Ω_0^2 and therefore to X, gives one of the contributions to the coefficient a used in the main text (defined by $\left\langle \frac{\sigma}{\Omega/2}^{(3)}_{\infty} \right\rangle = aX$).

The second contribution comes from the interaction nonlinearity. From a model where we did not take into account spatial dependences, we obtained the following expression for the local third-order interaction susceptibility:

$$\frac{\sigma}{\Omega/2}^{(3)}_{int,\infty} = -\sigma_{33}^{\infty(2)} n_b \left(\frac{1}{\Delta+i}-\frac{1}{\Delta+i-\frac{\Omega_b^2/4}{\delta+i\gamma_{13}}}\right) = -\frac{\sigma_{33}^{\infty(2)} n_b}{\Delta+i}\left(1-\frac{1}{1+x_1}\right) \tag{B.28}$$

with $n_b = \frac{2\pi^2}{3}\mu\sqrt{\frac{C_6}{\gamma(\delta+i\gamma_{13}-\Omega_b^2/2(\Delta+i))}}$.

At first sight one may think that this is again one more expression with a product of several terms that depend on the blue Rabi frequency, so that we can again try to estimate the spatial average of it by looking for a single-pole decomposition, or even just neglect the correlations between the different terms. However in this expression the dependence of n_b on the blue Rabi frequency is not of the same kind as for the other terms. The derivation of the form above for the nonlinearity in itself assumed that all atoms saw the same blue Rabi frequency, and the definition of n_b is already resulting from a spatial integral, that takes the shape given above only if for all atoms blockaded the Rabi frequency is the same. Therefore the blockade radius or n_b would indeed depend on the blue Rabi frequency in a uniform system, but here what we have to take into account is more directly the fact that even inside a single blockade sphere the blue is very inhomogeneous, so that all atoms around an excited one do not feel the same blockade efficiency. Therefore the more sensible way to do it is to come back to the initial modeling of the effect of Rydberg interactions to extract the nonlinearity.

We consider that a Rydberg atom at position $\vec{r}_i$ modifies the coherence of another atom at position $\vec{r}_j$ to:

$$\frac{\sigma}{\Omega/2}(\vec{r}_j,\vec{r}_i) = \frac{1}{\Delta+i}\left[1-\frac{x_1(\vec{r}_j)}{1+x_1(\vec{r}_j)+\frac{C_6}{(\delta+i\gamma_{13})|\vec{r}_j-\vec{r}_i|^6}}\right] \tag{B.29}$$

The total change in the susceptibility induced by the Rydberg at $\vec{r}_i$ is therefore:

$$\begin{aligned} d\frac{\sigma}{\Omega/2}^{(3)}_{int,\infty} &= \frac{\int \mu\left(\frac{\sigma}{\Omega/2}(\vec{r}_j,\vec{r}_i)-\frac{\sigma}{\Omega/2}(\vec{r}_j,\infty)\right)\cos(kz_j)^2 e^{-2r_j^2/w^2}d^3\vec{r}_j}{\int \mu\cos(kz_j)^2 e^{-2r_j^2/w^2}d^3\vec{r}_j} \\ &= \int\left[\left(1+\frac{x_1(\vec{r}_j)}{\left(1+\frac{C_6}{(\delta+i\gamma_{13})|\vec{r}_j-\vec{r}_i|^6}\right)}\right)^{-1}-\frac{1}{1+x_1(\vec{r}_j)}\right]\frac{2\cos(kz_j)^2e^{-2r_j^2/w^2}}{\pi L(\Delta+i)}d^3\vec{r}_j \end{aligned} \tag{B.30}$$

In order to get the total nonlinear change of susceptibility due to the Rydberg interactions in the cloud, one therefore needs to sum the contributions of all possible excited atoms, as we only look at the regime below saturation of the medium:

$$\left\langle \frac{\sigma}{\Omega/2}^{(3)}_{int,\infty}\right\rangle = \int d^3\vec{r}_i\mu\sigma_{33}^{\infty(2)}d\frac{\sigma}{\Omega/2}^{(3)}_{int,\infty} \tag{B.31}$$

After some rewriting this takes the integral form:

$$\begin{aligned} \left\langle \frac{\sigma}{\Omega/2}^{(3)}_{int,\infty}\right\rangle &= \frac{\mu\pi\sqrt{C_6}}{3(\Delta+i)}X \\ &\quad *\int_0^1 du\int_0^\infty dv\left[\frac{1}{\sqrt{1+x_{10}u^{w^2/w_b^2}}}-\sqrt{\frac{1+(\delta+i\gamma_{13})v^2}{1+(\delta+i\gamma_{13})v^2(1+x_{10}u^{w^2/w_b^2})}}\right] \\ &\quad *Im\left[\frac{u}{\gamma_{33}(\Delta-i)+\delta+i\gamma_{13}}\left(\frac{1}{\sqrt{1+x_{10}u^{w^2/w_b^2}}}-\frac{1}{\sqrt{1+x_{20}u^{w^2/w_b^2}}}\right)\right] \end{aligned} \tag{B.32}$$

The sum of this expression with equation (B.27) is what gives us the full effective $\chi^{(3)}$ averaged over the probe mode, taking into account the spatial variations of the blue power in particular. It has no simple expression in the general case, but can be put in the shape of $\left\langle \frac{\sigma}{\Omega/2}^{(3)}_{\infty}\right\rangle = \left\langle \frac{\sigma}{\Omega/2}^{(3)}_{nat,\infty}\right\rangle + \left\langle \frac{\sigma}{\Omega/2}^{(3)}_{int,\infty}\right\rangle = aX$, which is what we used in the main text.

These expressions are used to estimate numerically the value of a when comparing our experimentally measured slopes of the normalized blue-induced shift versus Y to the theory.

Lorentzian fitting of the dynamical curves and shift as a function of Y

Once we have the expression for the nonlinearity $\left\langle \frac{\sigma}{\Omega/2}^{(3)}_{\infty}\right\rangle = aX(\theta)$, we consider the coupled evolution equations of the intracavity power $X(\theta)$ and of the susceptibility, given in the main text:

$$\frac{d}{d\theta}\left\langle\frac{\sigma}{\Omega/2}\right\rangle^{(3)} = -\frac{R}{\tau_{eff}}\left(\left\langle\frac{\sigma}{\Omega/2}\right\rangle^{(3)} - aX(\theta)\right) \tag{B.33}$$

$$X(\theta) = \frac{Y}{\left|i \pm \theta - 2C\left(\left\langle\frac{\sigma}{\Omega/2}\right\rangle_{3lev} + \left\langle\frac{\sigma}{\Omega/2}\right\rangle^{(3)}(\theta)\right)\right|^2} \tag{B.34}$$

Solving these equations one gets the nonlinear susceptibility $\left\langle\frac{\sigma}{\Omega/2}\right\rangle^{(3)}$ directly as a function of θ, and of Y.

When fitting the observed transmission curve by a Lorentzian, what we do is then to minimize the value of the following quantity:

$$K = \int_{-\infty}^{\infty}(T_{cav}(\theta, Y) - \frac{p_1}{(1+p_2)^2 + (\theta + p_3)^2})^2 d\theta \tag{B.35}$$

with respects to parameters p_1, p_2, p_3, and with the experimentally observed transmission given by:

$$T_{cav}(\theta, Y) = \frac{1}{\left|i + \theta + 2C\left(\left\langle\frac{\sigma}{\Omega/2}\right\rangle_{3lev} + \left\langle\frac{\sigma}{\Omega/2}\right\rangle^{(3)}(Y, \theta)\right)\right|^2} \tag{B.36}$$

In these terms, the slope of what we measure and plot afterwards to extract the nonlinear shift is simply $\frac{dp_3}{d_Y}(Y=0)$.

The condition for optimum fit, or minimum K, implies that for the optimum parameters one has $\frac{\partial K}{\partial p_3} = 0$, which is equivalent to:

$$M(Y) = \int_{-\infty}^{\infty} T_{cav}(\theta, Y)\frac{\theta + p_3}{((1+p_2)^2 + (\theta+p_3)^2)^2} d\theta = 0 \tag{B.37}$$

As this has to be true for all Y, one can in particular write that $\frac{dM}{dY}(0) = 0$. This gives a condition that can be written as:

$$0 = \int_{-\infty}^{\infty}\left(\frac{\partial T_{cav}}{\partial Y}(\theta, 0)\frac{\theta + p_3(0)}{((1+p_2(0))^2 + (\theta + p_3(0))^2)^2}\right) d\theta + \frac{dp_3}{dY}(0)\frac{\pi}{8(1+p_2(0))^5} \tag{B.38}$$

where $p_2(0)$ and $p_3(0)$ correspond to the attenuation and shift of the line in the linear regime, given by $-2CIm[\left\langle\frac{\sigma}{\Omega/2}\right\rangle_{3lev}]$ and $-2CRe[\left\langle\frac{\sigma}{\Omega/2}\right\rangle_{3lev}]$.

The only thing that remains to estimate in order to get $\frac{dp_3}{dY}(0)$ is therefore $\frac{\partial T_{cav}}{\partial Y}(\theta, 0)$. This is done by writing:

$$\frac{\partial T_{cav}}{\partial Y} = \frac{\partial T_{cav}}{\partial Re[\left\langle\frac{\sigma}{\Omega/2}\right\rangle^{(3)}]}\frac{\partial Re[\left\langle\frac{\sigma}{\Omega/2}\right\rangle^{(3)}]}{\partial Y} + \frac{\partial T_{cav}}{\partial Im[\left\langle\frac{\sigma}{\Omega/2}\right\rangle^{(3)}]}\frac{\partial Im[\left\langle\frac{\sigma}{\Omega/2}\right\rangle^{(3)}]}{\partial Y} \tag{B.39}$$

To get the derivatives of the third-order nonlinearity with respect to Y, as we only need them to the lowest order, we can use the lowest-order solution of the dynamical equations, which is equivalent to:

$$\frac{d}{d\theta}\left\langle\frac{\sigma}{\Omega/2}\right\rangle^{(3)} = -\frac{R}{\tau_{eff}}\left(\left\langle\frac{\sigma}{\Omega/2}\right\rangle^{(3)} - a\frac{Y}{\left|i \pm \theta - 2C\left\langle\frac{\sigma}{\Omega/2}\right\rangle_{3lev}\right|^2}\right) \tag{B.40}$$

$$= -\frac{R}{\tau_{eff}}\left(\left\langle\frac{\sigma}{\Omega/2}\right\rangle^{(3)} - a\frac{Y}{(1+p_2(0))^2 + (\theta + p_3(0))^2}\right) \tag{B.41}$$

The solution of this equation is:

$$\left\langle \frac{\sigma}{\Omega/2} \right\rangle^{(3)}(\theta) = aY \frac{R}{\tau_{eff}} \int_0^\infty \frac{e^{-uR/\tau_{eff}}}{(1+p_2(0))^2 + (\theta - u + p_3(0))^2} du \tag{B.42}$$

From there, using equations (B.39) and (B.38), one can express in a closed form the value of $\frac{dp_3}{dY}(0)$, which can be integrated to give the measured normalized slope:

$$s = \frac{1}{2CRe[\left\langle \frac{\sigma}{\Omega/2} \right\rangle_{3lev} - \left\langle \frac{\sigma}{\Omega/2} \right\rangle_{2lev}]} \frac{dp_3}{dY}(0) \tag{B.43}$$

$$= S \frac{Re[a](2\beta_5 + 9\beta_3 + 20\beta_1 + 5\beta_{-1}) + 2Im[a](\beta_4 + 4\beta_2 + 7\beta_0)}{48\sqrt{\pi} Re\left[\left\langle \frac{\sigma}{\Omega/2} \right\rangle_{2lev} - \left\langle \frac{\sigma}{\Omega/2} \right\rangle_{3lev}\right]\left(1 - 2CIm\left[\left\langle \frac{\sigma}{\Omega/2} \right\rangle_{3lev}\right]\right)^2} \tag{B.44}$$

where S and the β_n's are defined in the main text.

Due to the choice of sign made at the beginning the case treated here is the "up" one. The reverse scan case can be obtained by flipping the signs of all real parts of susceptibilities ($a, \left\langle \frac{\sigma}{\Omega/2} \right\rangle_{3lev}, \left\langle \frac{\sigma}{\Omega/2} \right\rangle_{2lev}$).

Appendix C

Technical details about the last version of the experimental setup

This appendix contains additional technical details about the recent experimental improvements brought to the imaging setup and to the blue buildup cavity, that were partially discussed in the last part of this thesis.

Imaging setup

The problematic was to build an imaging system capable of resolving details at the 10 μm scale in the cloud with our experimental constraints.

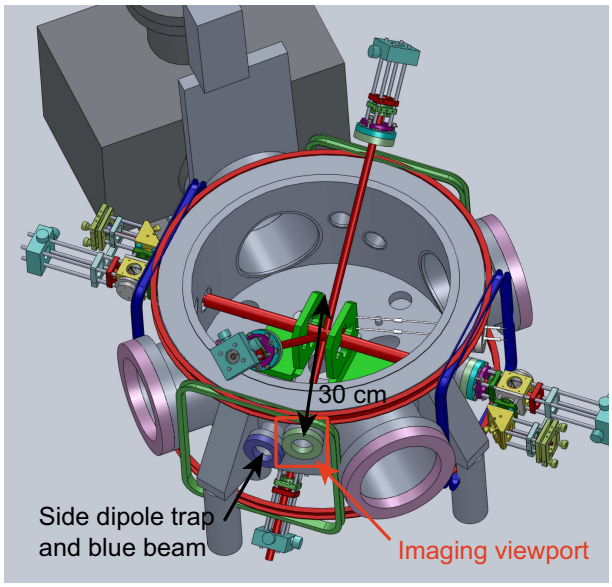

Figure C.1: Position of the imaging viewport.

Due to the size of the vacuum chamber, the collection optics can not be placed closer than $\approx$ 30 cm from the atoms. This affects the performances as the collection efficiency conditions both the level of signal and the diffraction limit achievable when imaging. To access the largest solid angle without any object (coils, cavity mount ...) blocking the path, the only free viewport of the vacuum chamber that can be used is shown in figure

(C.1). It is ≈ 2 cm in radius and it is not orthogonal to the optical axis, as illustrated in figure (14.4).

Other strong constraints on the resolution come from the camera which has square pixels of 20 μm size. This means that to get a 10 μm resolution on the atomic density distribution, it is in any case necessary to design the imaging system with a magnifying ratio of at least 2-3.

The optical system used to address these constraints is sketched in figure (14.3) and commented in the main text.

The collection solid angle, fixed by the viewport, is ≈ 0.012 steradians, corresponding to a collection efficiency of $\approx 10^{-3}$. Provided all the light collected through this viewport is then maintained in the optical path to form the image, this fixes the diffraction resolution limit in the system. The radius of the associated Airy spot in the object plane is ≈ 8 μm, which is of the order of the typical scale to be resolved.

The optical system was simulated on the design software OSLO to estimate the effect of aberrations. For perfectly aligned optics, configurations were obtained where the magnifying ratio is close to 3 and the aberrations contribute to a blurring of the order of 5-10 μm of the image (standard deviation), which is acceptable. The effect of the tilted window through which we collect light can also be simulated, and is found to enlarge only very slightly (few percents) the aberration spot.

Once the system is set up on the experiment and the position of the camera has been finely adjusted to optimize the sharpness of the image on the CCD, the magnifying ratio must be measured in situ for the final configuration. For that, a small glass plate at 45° (≈ 1 by 2 cm) is inserted between the viewport and the first doublets to divert the optical path vertically down towards the optical table, rather than towards the atoms. In this alternative optical path a 10 μm radius pinhole lit by an LED is placed so that its image is exactly forming on the CCD. Mounted on a translation stage, it is then controllably translated in its object plane and the corresponding displacement of the image is measured to get the magnifying ratio. The result is 2.74±0.05.

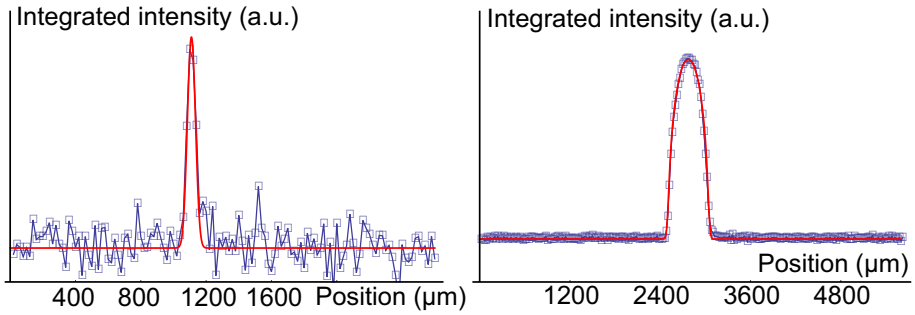

Figure C.2: Test of the imaging system with pinholes. The profiles obtained on the camera, integrated along one dimension, are shown for pinholes of 20 μm diameter (left) and 200 μm (right).

When imaging pinholes in this alternative optical path, an estimation of the resolution limit can be obtained as illustrated in figure (C.2). Taking into account the independently evaluated magnification of ≈ 2.74, we compare the obtained integrated profiles to an approximate theoretical form: the result of the integration of a uniform circle convoluted with a 2D Gaussian of adjustable size, used to simply simulate the joint effect of diffraction and aberrations. The profiles are very well consistent for different pinhole sizes, with only adjustable parameter the standard deviation of the "blurring" Gaussian which is here of

20 μm (in the image plane). This resolution limit is qualitatively consistent with the expected combination of diffraction, aberrations, finite size of the camera pixels, and some small experimental misalignments.

In this configuration, the small glass plate should make the diffraction limit even worse than in the actual imaging path. However it also does not suffer from passing through the viewport at an angle, which adds aberrations on the real images in an amount that is hard to estimate, but expected to be small compared to the other limits. As a result the resolution limit estimated is not really the one to be applied to the actual images, but it shows that at least in this alternative path details in the object plane of size ≈ 10 μm are well resolved, which was the goal.

Blue cavity

Due to the structure of the blue cavity, locking it on resonance with a given blue frequency proved to be difficult on first tests. The mechanical stability of the breadboards was the first expected source of troubles. Initially, ≈ 13 mm thick plain aluminum breadboards (Thorlabs MB4545) were used, mounted on 4 legs of 1" diameter each for ≈ 25 cm height. The complete breadboards structure was thus replaced for something supposedly more efficient and adapted : 6 cm thick honeycomb breadboards (Thorlabs B4560A) with legs of 1.5" diameter for a smaller height (≈ 20 cm). However, this did not solve the problem at that time.

The main source of problem turned out to be the method used to lock the cavity. It was first decided to use a low-power 810 nm beam in order to lock the blue cavity. As the viewports have an uncontrolled effect on the polarization, the inside of the cavity is birefringent and it presents non-degenerate polarization eigenmodes. We therefore tried to use a Hansch-Couillaud lock on the 810 to make use of this birefringence to obtain an error signal [190]. Finally, even after optimization, a satisfying lock stability was obtained when looking at the error signal, and good short-term lock quality on the intracavity blue power, but unavoidable slow drifts in the optimum blue resonance were always observed. This was due to the use of two very different wavelengths in such a long unprotected cavity: the cavity lock was good at 810 nm, but the blue at 480 nm was experiencing large enough differential changes in the air's optical index (varying differently at 480 nm and at 810 nm when pressure and temperature change), that its stability was not satisfactory.

We then solved the problem simply by locking with an auxiliary weak beam at 480 nm, that suppressed completely the differential drift issue.

Bibliography

[1] A. B. Bardon, S. Beattie, C. Luciuk, W. Cairncross, D. Fine, N. S. Cheng, G. J. A. Edge, E. Taylor, S. Zhang, S. Trotzky, and J. H. Thywissen, "Transverse demagnetization dynamics of a unitary fermi gas," Science **344**, 722–724 (2014).

[2] Seth Lloyd, "Universal quantum simulators," Science **273**, 1073–1078 (1996).

[3] I. M. Georgescu, S. Ashhab, and Franco Nori, "Quantum simulation," Rev. Mod. Phys. **86**, 153–185 (2014).

[4] D. Estève, J.M. Raimond, and J. Dalibard, Intrication Quantique Et Traitement de L'information, Les Houches (Elsevier, 2004).

[5] D.P. Divincenzo, "Topics in quantum computers," in Mesoscopic Electron Transport, NATO ASI Series, Vol. 345, edited by Lydia L. Sohn, Leo P. Kouwenhoven, and Gerd Schön (Springer Netherlands, 1997) pp. 657–677.

[6] J. Brendel, N. Gisin, W. Tittel, and H. Zbinden, "Pulsed energy-time entangled twin-photon source for quantum communication," Phys. Rev. Lett. **82**, 2594–2597 (1999).

[7] Julio T. Barreiro, Tzu-Chieh Wei, and Paul G. Kwiat, "Beating the channel capacity limit for linear photonic superdense coding," Nat Phys **4**, 282–286 (2008).

[8] David P. DiVincenzo, "Two-bit gates are universal for quantum computation," Phys. Rev. A **51**, 1015–1022 (1995).

[9] H.-J. Briegel, W. Dür, J. I. Cirac, and P. Zoller, "Quantum repeaters: The role of imperfect local operations in quantum communication," Phys. Rev. Lett. **81**, 5932–5935 (1998).

[10] Nicolas Sangouard, Christoph Simon, Hugues de Riedmatten, and Nicolas Gisin, "Quantum repeaters based on atomic ensembles and linear optics," Rev. Mod. Phys. **83**, 33–80 (2011).

[11] H. J. Kimble, "The quantum internet," Nature **453**, 1023–1030 (2008).

[12] Darrick E. Chang, Vladan Vuletic, and Mikhail D. Lukin, "Quantum nonlinear optics – photon by photon," Nat Photon **8**, 685–694 (2014), review.

[13] Jeffrey H. Shapiro, "Single-photon kerr nonlinearities do not help quantum computation," Phys. Rev. A **73**, 062305 (2006).

[14] Julio Gea-Banacloche, "Impossibility of large phase shifts via the giant kerr effect with single-photon wave packets," Phys. Rev. A **81**, 043823 (2010).

[15] Christopher Chudzicki, Isaac L. Chuang, and Jeffrey H. Shapiro, "Deterministic and cascadable conditional phase gate for photonic qubits," Phys. Rev. A **87**, 042325 (2013).

[16] P. Grangier, G. Roger, and A. Aspect, "Experimental evidence for a photon anticorrelation effect on a beam splitter: A new light on single-photon interferences," EPL (Europhysics Letters) **1**, 173 (1986).

[17] A. I. Lvovsky and M. G. Raymer, "Continuous-variable optical quantum-state tomography," Rev. Mod. Phys. **81**, 299–332 (2009).

[18] Stefan Scheel, Kae Nemoto, William J. Munro, and Peter L. Knight, "Measurement-induced nonlinearity in linear optics," Phys. Rev. A **68**, 032310 (2003).

[19] A. Kuzmich, W. P. Bowen, A. D. Boozer, A. Boca, C. W. Chou, L. M. Duan, and H. J. Kimble, "Generation of nonclassical photon pairs for scalable quantum communication with atomic ensembles," Nature **423**, 731–734 (2003).

[20] M. D. Eisaman, L. Childress, A. André, F. Massou, A. S. Zibrov, and M. D. Lukin, "Shaping quantum pulses of light via coherent atomic memory," Phys. Rev. Lett. **93**, 233602 (2004).

[21] Jonathan Simon, Haruka Tanji, James K. Thompson, and Vladan Vuletić, "Interfacing collective atomic excitations and single photons," Phys. Rev. Lett. **98**, 183601 (2007).

[22] Axel Kuhn, Markus Hennrich, and Gerhard Rempe, "Deterministic single-photon source for distributed quantum networking," Phys. Rev. Lett. **89**, 067901 (2002).

[23] B. Darquié, M. P. A. Jones, J. Dingjan, J. Beugnon, S. Bergamini, Y. Sortais, G. Messin, A. Browaeys, and P. Grangier, "Controlled single-photon emission from a single trapped two-level atom," Science **309**, 454–456 (2005).

[24] B. Lounis and W. E. Moerner, "Single photons on demand from a single molecule at room temperature," Nature **407**, 491–493 (2000).

[25] Christian Kurtsiefer, Sonja Mayer, Patrick Zarda, and Harald Weinfurter, "Stable solid-state source of single photons," Phys. Rev. Lett. **85**, 290–293 (2000).

[26] A. Beveratos, S. Kühn, R. Brouri, T. Gacoin, J.-P. Poizat, and P. Grangier, "Room temperature stable single-photon source," The European Physical Journal D **18**, 191–196 (2002).

[27] Charles Santori, Matthew Pelton, Glenn Solomon, Yseulte Dale, and Yoshihisa Yamamoto, "Triggered single photons from a quantum dot," Phys. Rev. Lett. **86**, 1502–1505 (2001).

[28] A. K. Nowak, S. L. Portalupi, V. Giesz, O. Gazzano, C. Dal Savio, P. F. Braun, K. Karrai, C. Arnold, L. Lanco, I. Sagnes, A. Lemaître, and P. Senellart, "Deterministic and electrically tunable bright single-photon source," Nat Commun **5** (2014), article.

[29] T. Chanelière, D. N. Matsukevich, S. D. Jenkins, S. Y. Lan, T. A. B. Kennedy, and A. Kuzmich, "Storage and retrieval of single photons transmitted between remote quantum memories," Nature **438**, 833–836 (2005).

[30] Klemens Hammerer, Anders S. Sørensen, and Eugene S. Polzik, "Quantum interface between light and atomic ensembles," Rev. Mod. Phys. **82**, 1041–1093 (2010).

[31] Chih-Sung Chuu, Thorsten Strassel, Bo Zhao, Markus Koch, Yu-Ao Chen, Shuai Chen, Zhen-Sheng Yuan, Jörg Schmiedmayer, and Jian-Wei Pan, "Quantum memory with optically trapped atoms," Phys. Rev. Lett. **101**, 120501 (2008).

[32] R. Zhao, Y. O. Dudin, S. D. Jenkins, C. J. Campbell, D. N. Matsukevich, T. A. B. Kennedy, and A. Kuzmich, "Long-lived quantum memory," Nat Phys **5**, 100–104 (2009).

[33] Jun-ichi Yoshikawa, Kenzo Makino, Shintaro Kurata, Peter van Loock, and Akira Furusawa, "Creation, storage, and on-demand release of optical quantum states with a negative wigner function," Phys. Rev. X **3**, 041028 (2013).

[34] M. D. Eisaman, A. Andre, F. Massou, M. Fleischhauer, A. S. Zibrov, and M. D. Lukin, "Electromagnetically induced transparency with tunable single-photon pulses," Nature **438**, 837–841 (2005).

[35] W. Tittel, M. Afzelius, T. Chanelière, R.L. Cone, S. Kröll, S.A. Moiseev, and M. Sellars, "Photon-echo quantum memory in solid state systems," Laser & Photonics Reviews **4**, 244–267 (2010).

[36] Georg Heinze, Christian Hubrich, and Thomas Halfmann, "Stopped light and image storage by electromagnetically induced transparency up to the regime of one minute," Phys. Rev. Lett. **111**, 033601 (2013).

[37] M. Fleischhauer, S.F. Yelin, and M.D. Lukin, "How to trap photons? storing single-photon quantum states in collective atomic excitations," Optics Communications **179**, 395 – 410 (2000).

[38] Jerome Dilley, Peter Nisbet-Jones, Bruce W. Shore, and Axel Kuhn, "Single-photon absorption in coupled atom-cavity systems," Phys. Rev. A **85**, 023834 (2012).

[39] E. Knill, R. Laflamme, and G. J. Milburn, "A scheme for efficient quantum computation with linear optics," Nature **409**, 46–52 (2001).

[40] J. L. O'Brien, G. J. Pryde, A. G. White, T. C. Ralph, and D. Branning, "Demonstration of an all-optical quantum controlled-not gate," Nature **426**, 264–267 (2003).

[41] L.-M. Duan and H. J. Kimble, "Scalable photonic quantum computation through cavity-assisted interactions," Phys. Rev. Lett. **92**, 127902 (2004).

[42] J. M. Raimond, M. Brune, and S. Haroche, "Manipulating quantum entanglement with atoms and photons in a cavity," Rev. Mod. Phys. **73**, 565–582 (2001).

[43] S. Haroche and J.M. Raimond, Exploring the Quantum: Atoms, Cavities, and Photons, Oxford Graduate Texts (OUP Oxford, 2006).

[44] K. M. Birnbaum, A. Boca, R. Miller, A. D. Boozer, T. E. Northup, and H. J. Kimble, "Photon blockade in an optical cavity with one trapped atom," Nature **436**, 87–90 (2005).

[45] I. Schuster, A. Kubanek, A. Fuhrmanek, T. Puppe, P. W. H. Pinkse, K. Murr, and G. Rempe, "Nonlinear spectroscopy of photons bound to one atom," Nat Phys **4**, 382–385 (2008).

[46] Andreas Reiserer, Norbert Kalb, Gerhard Rempe, and Stephan Ritter, "A quantum gate between a flying optical photon and a single trapped atom," Nature **508**, 237–240 (2014), letter.

[47] Ilya Fushman, Dirk Englund, Andrei Faraon, Nick Stoltz, Pierre Petroff, and Jelena Vučković, "Controlled phase shifts with a single quantum dot," Science **320**, 769–772 (2008).

[48] Andrei Faraon, Ilya Fushman, Dirk Englund, Nick Stoltz, Pierre Petroff, and Jelena Vuckovic, "Coherent generation of non-classical light on a chip via photon-induced tunnelling and blockade," Nat Phys **4**, 859–863 (2008).

[49] V. Loo, C. Arnold, O. Gazzano, A. Lemaître, I. Sagnes, O. Krebs, P. Voisin, P. Senellart, and L. Lanco, "Optical nonlinearity for few-photon pulses on a quantum dot-pillar cavity device," Phys. Rev. Lett. **109**, 166806 (2012).

[50] Itay Shomroni, Serge Rosenblum, Yulia Lovsky, Orel Bechler, Gabriel Guendelman, and Barak Dayan, "All-optical routing of single photons by a one-atom switch controlled by a single photon," Science **345**, 903–906 (2014).

[51] J. Volz, M. Scheucher, C. Junge, and A. Rauschenbeutel, "Nonlinear pi phase shift for single fiber-guided photons interacting with a single atom," ArXiv e-prints (2014), arXiv:1403.1860 [quant-ph] .

[52] M. Saffman and T. G. Walker, "Creating single-atom and single-photon sources from entangled atomic ensembles," Phys. Rev. A **66**, 065403 (2002).

[53] M. Fleischhauer and M. D. Lukin, "Dark-state polaritons in electromagnetically induced transparency," Phys. Rev. Lett. **84**, 5094–5097 (2000).

[54] Michael Fleischhauer, Atac Imamoglu, and Jonathan P. Marangos, "Electromagnetically induced transparency: Optics in coherent media," Rev. Mod. Phys. **77**, 633–673 (2005).

[55] Lene Vestergaard Hau, S. E. Harris, Zachary Dutton, and Cyrus H. Behroozi, "Light speed reduction to 17 metres per second in an ultracold atomic gas," Nature **397**, 594–598 (1999).

[56] A. Imamoğlu, H. Schmidt, G. Woods, and M. Deutsch, "Strongly interacting photons in a nonlinear cavity," Phys. Rev. Lett. **79**, 1467–1470 (1997).

[57] T. F. Gallagher, Rydberg Atoms (Cambridge University Press, 1994).

[58] J. M. Raimond, G. Vitrant, and S. Haroche, "Spectral line broadening due to the interaction between very excited atoms: 'the dense rydberg gas'," Journal of Physics B: Atomic and Molecular Physics **14**, L655 (1981).

[59] I. Mourachko, D. Comparat, F. de Tomasi, A. Fioretti, P. Nosbaum, V. M. Akulin, and P. Pillet, "Many-body effects in a frozen rydberg gas," Phys. Rev. Lett. **80**, 253–256 (1998).

[60] W. R. Anderson, J. R. Veale, and T. F. Gallagher, "Resonant dipole-dipole energy transfer in a nearly frozen rydberg gas," Phys. Rev. Lett. **80**, 249–252 (1998).

[61] D. Jaksch, J. I. Cirac, P. Zoller, S. L. Rolston, R. Côté, and M. D. Lukin, "Fast quantum gates for neutral atoms," Phys. Rev. Lett. **85**, 2208–2211 (2000).

[62] T. Wilk, A. Gaëtan, C. Evellin, J. Wolters, Y. Miroshnychenko, P. Grangier, and A. Browaeys, "Entanglement of two individual neutral atoms using rydberg blockade," Phys. Rev. Lett. **104**, 010502 (2010).

[63] L. Isenhower, E. Urban, X. L. Zhang, A. T. Gill, T. Henage, T. A. Johnson, T. G. Walker, and M. Saffman, "Demonstration of a neutral atom controlled-not quantum gate," Phys. Rev. Lett. **104**, 010503 (2010).

[64] D. Tong, S. M. Farooqi, J. Stanojevic, S. Krishnan, Y. P. Zhang, R. Côté, E. E. Eyler, and P. L. Gould, "Local blockade of rydberg excitation in an ultracold gas," Phys. Rev. Lett. **93**, 063001 (2004).

[65] Kilian Singer, Markus Reetz-Lamour, Thomas Amthor, Luis Gustavo Marcassa, and Matthias Weidemüller, "Suppression of excitation and spectral broadening induced by interactions in a cold gas of rydberg atoms," Phys. Rev. Lett. **93**, 163001 (2004).

[66] Daniel Comparat and Pierre Pillet, "Dipole blockade in a cold rydberg atomic sample," J. Opt. Soc. Am. B **27**, A208–A232 (2010).

[67] M. D. Lukin, M. Fleischhauer, R. Cote, L. M. Duan, D. Jaksch, J. I. Cirac, and P. Zoller, "Dipole blockade and quantum information processing in mesoscopic atomic ensembles," Phys. Rev. Lett. **87**, 037901 (2001).

[68] M. Saffman, T. G. Walker, and K. Mølmer, "Quantum information with rydberg atoms," Rev. Mod. Phys. **82**, 2313–2363 (2010).

[69] Yang Han, Bing He, Khabat Heshami, Cheng-Zu Li, and Christoph Simon, "Quantum repeaters based on rydberg-blockade-coupled atomic ensembles," Phys. Rev. A **81**, 052311 (2010).

[70] Bo Zhao, Markus Müller, Klemens Hammerer, and Peter Zoller, "Efficient quantum repeater based on deterministic rydberg gates," Phys. Rev. A **81**, 052329 (2010).

[71] Hendrik Weimer, Markus Muller, Igor Lesanovsky, Peter Zoller, and Hans Peter Buchler, "A rydberg quantum simulator," Nat Phys **6**, 382–388 (2010).

[72] T. Amthor, M. Reetz-Lamour, S. Westermann, J. Denskat, and M. Weidemüller, "Mechanical effect of van der waals interactions observed in real time in an ultracold rydberg gas," Phys. Rev. Lett. **98**, 023004 (2007).

[73] Y. O. Dudin, L. Li, F. Bariani, and A. Kuzmich, "Observation of coherent many-body rabi oscillations," Nat Phys **8**, 790–794 (2012).

[74] Peter Schauß, Marc Cheneau, Manuel Endres, Takeshi Fukuhara, Sebastian Hild, Ahmed Omran, Thomas Pohl, Christian Gross, Stefan Kuhr, and Immanuel Bloch, "Observation of spatially ordered structures in a two-dimensional rydberg gas," Nature **491**, 87–91 (2012).

[75] C. S. Hofmann, G. Günter, H. Schempp, M. Robert-de Saint-Vincent, M. Gärttner, J. Evers, S. Whitlock, and M. Weidemüller, "Sub-poissonian statistics of rydberg-interacting dark-state polaritons," Phys. Rev. Lett. **110**, 203601 (2013).

[76] Ashok K. Mohapatra, Mark G. Bason, Bjorn Butscher, Kevin J. Weatherill, and Charles S. Adams, "A giant electro-optic effect using polarizable dark states," Nat Phys **4**, 890–894 (2008).

[77] Jonathan D. Pritchard, Kevin J. Weatherill, and Charles S. Adams, "Nonlinear optics using cold rydberg atoms," in Annual Review of Cold Atoms and Molecules, Chap. 8, pp. 301–350.

[78] Peter P. Rohde, Timothy C. Ralph, and Michael A. Nielsen, "Optimal photons for quantum-information processing," Phys. Rev. A **72**, 052332 (2005).

[79] Haruka Tanji-Suzuki, Ian D. Leroux, Monika H. Schleier-Smith, Marko Cetina, Andrew T. Grier, Jonathan Simon, and Vladan Vuletic, "Chapter 4 - interaction between atomic ensembles and optical resonators: Classical description," in Advances in Atomic, Molecular, and Optical Physics, Vol. 60, edited by P.R. Berman E. Arimondo and C.C. Lin (Academic Press, 2011) pp. 201 – 237.

[80] Luigi A. Lugiato, "II Theory of Optical Bistability," in Progress in Optics, Vol. 21 (Elsevier, 1984) pp. 69–216.

[81] Amitabh Joshi and Min Xiao, "Atomic optical bistability in two- and three-level systems: perspectives and prospects," Journal of Modern Optics **57**, 1196–1220 (2010).

[82] Rodney Loudon, The Quantum Theory of Light (Oxford Science Publications), 3rd ed. (Oxford University Press, USA, 2000).

[83] Wolfgang P. Schleich, "Atom-field interaction," in Quantum Optics in Phase Space (Wiley-VCH Verlag GmbH & Co. KGaA, 2005) pp. 381–412.

[84] Bahaa E. A. Saleh and Malvin Carl Teich, "Resonator optics," in Fundamentals of Photonics (John Wiley & Sons, Inc., 2001) pp. 310–341.

[85] Bahaa E. A. Saleh and Malvin Carl Teich, "Photon optics," in Fundamentals of Photonics (John Wiley & Sons, Inc., 2001) pp. 384–422.

[86] U. Fano, "Description of states in quantum mechanics by density matrix and operator techniques," Rev. Mod. Phys. **29**, 74–93 (1957).

[87] Philip Pearle, "Simple derivation of the lindblad equation," (2012), arXiv:1204.2016 [math-ph] .

[88] R.J. Ballagh, J. Cooper, M.W. Hamilton, W.J. Sandle, and D.M. Warrington, "Optical bistability in a gaussian cavity mode," Optics Communications **37**, 143 – 148 (1981).

[89] P.D. Drummond, "Optical bistability in a radially varying mode," Quantum Electronics, IEEE Journal of **17**, 301–306 (1981).

[90] R.W. Boyd, Nonlinear Optics, Nonlinear Optics Series (Elsevier Science, 2008).

[91] H. M. Gibbs, S. L. McCall, and T. N. C. Venkatesan, "Differential gain and bistability using a sodium-filled fabry-perot interferometer," Phys. Rev. Lett. **36**, 1135–1138 (1976).

[92] A. T. Rosenberger, L. A. Orozco, H. J. Kimble, and P. D. Drummond, "Absorptive optical bistability in two-state atoms," Phys. Rev. A **43**, 6284–6302 (1991).

[93] W. J. Sandle and Alan Gallagher, "Optical bistability by an atomic vapor in a focusing fabry-perot cavity," Phys. Rev. A **24**, 2017–2028 (1981).

[94] W. Harshawardhan and G. S. Agarwal, "Controlling optical bistability using electromagnetic-field-induced transparency and quantum interferences," Phys. Rev. A **53**, 1812–1817 (1996).

[95] Hai Wang, David Goorskey, and Min Xiao, "Controlling light by light with three-level atoms inside an optical cavity," Opt. Lett. **27**, 1354–1356 (2002).

[96] Hai Wang, David Goorskey, and Min Xiao, "Enhanced kerr nonlinearity via atomic coherence in a three-level atomic system," Phys. Rev. Lett. **87**, 073601 (2001).

[97] Klaus M. Gheri, Daniel F. Walls, and Monika A. Marte, "Quantum noise reduction close to an optically bistable dark resonance," Phys. Rev. A **50**, 1871–1876 (1994).

[98] C. L. Garrido Alzar, L. S. Cruz, J. G. Aguirre Gómez, M. França Santos, and P. Nussenzveig, "Super-poissonian intensity fluctuations and correlations between pump and probe fields in electromagnetically induced transparency," EPL (Europhysics Letters) **61**, 485 (2003).

[99] Vladimir A. Sautenkov, Yuri V. Rostovtsev, and Marlan O. Scully, "Switching between photon-photon correlations and raman anticorrelations in a coherently prepared rb vapor," Phys. Rev. A **72**, 065801 (2005).

[100] A. Sinatra, "Quantum correlations of two optical fields close to electromagnetically induced transparency," Phys. Rev. Lett. **97**, 253601 (2006).

[101] H. Schmidt and A. Imamoğlu, "Giant kerr nonlinearities obtained by electromagnetically induced transparency," Opt. Lett. **21**, 1936–1938 (1996).

[102] Hoonsoo Kang and Yifu Zhu, "Observation of large kerr nonlinearity at low light intensities," Phys. Rev. Lett. **91**, 093601 (2003).

[103] M. D. Lukin and A. Imamoğlu, "Nonlinear optics and quantum entanglement of ultraslow single photons," Phys. Rev. Lett. **84**, 1419–1422 (2000).

[104] S. E. Harris and Y. Yamamoto, "Photon switching by quantum interference," Phys. Rev. Lett. **81**, 3611–3614 (1998).

[105] Danielle A. Braje, Vlatko Balić, G. Y. Yin, and S. E. Harris, "Low-light-level nonlinear optics with slow light," Phys. Rev. A **68**, 041801 (2003).

[106] Jeffrey H Shapiro and Mohsen Razavi, "Continuous-time cross-phase modulation and quantum computation," New Journal of Physics **9**, 16 (2007).

[107] U. Leonhardt, Measuring the Quantum State of Light, Cambridge Studies in Modern Optics (Cambridge University Press, 2005).

[108] Olivier Morin, Claude Fabre, and Julien Laurat, "Experimentally accessing the optimal temporal mode of traveling quantum light states," Phys. Rev. Lett. **111**, 213602 (2013).

[109] Daniel A. Steck, "Rubidium 87 D Line Data," (revision 2.1.4 23 december 2010).

[110] T. Arpornthip, C. A. Sackett, and K. J. Hughes, "Vacuum-pressure measurement using a magneto-optical trap," Phys. Rev. A **85**, 033420 (2012).

[111] Karine Vigneron, "Quantum noise of light control and quantum nondemolition measurement using cold trapped atoms," in PhD Thesis (Institut d'Optique Graduate School, 1998).

[112] D. E. Pritchard, E. L. Raab, V. Bagnato, C. E. Wieman, and R. N. Watts, "Light traps using spontaneous forces," Phys. Rev. Lett. **57**, 310–313 (1986).

[113] E. L. Raab, M. Prentiss, Alex Cable, Steven Chu, and D. E. Pritchard, "Trapping of neutral sodium atoms with radiation pressure," Phys. Rev. Lett. **59**, 2631–2634 (1987).

[114] J. Dalibard and C. Cohen-Tannoudji, "Laser cooling below the doppler limit by polarization gradients: simple theoretical models," J. Opt. Soc. Am. B **6**, 2023–2045 (1989).

[115] P. D. Lett, W. D. Phillips, S. L. Rolston, C. E. Tanner, R. N. Watts, and C. I. Westbrook, "Optical molasses," J. Opt. Soc. Am. B **6**, 2084–2107 (1989).

[116] C. J. Dedman, J. Nes, T. M. Hanna, R. G. Dall, K. G. H. Baldwin, and A. G. Truscott, "Optimum design and construction of a zeeman slower for use with a magneto-optic trap," Review of Scientific Instruments **75** (2004), 10.1063/1.1820524.

[117] Z. T. Lu, K. L. Corwin, M. J. Renn, M. H. Anderson, E. A. Cornell, and C. E. Wieman, "Low-velocity intense source of atoms from a magneto-optical trap," Phys. Rev. Lett. **77**, 3331–3334 (1996).

[118] Yuri B. Ovchinnikov, "Compact magneto-optical sources of slow atoms," Optics Communications **249**, 473 – 481 (2005).

[119] C. G. Townsend, N. H. Edwards, C. J. Cooper, K. P. Zetie, C. J. Foot, A. M. Steane, P. Szriftgiser, H. Perrin, and J. Dalibard, "Phase-space density in the magneto-optical trap," Phys. Rev. A **52**, 1423–1440 (1995).

[120] Paul D. Lett, Richard N. Watts, Christoph I. Westbrook, William D. Phillips, Phillip L. Gould, and Harold J. Metcalf, "Observation of atoms laser cooled below the doppler limit," Phys. Rev. Lett. **61**, 169–172 (1988).

[121] Yan Shu-Bin, Liu Tao, Geng Tao, Zhang Tian-Cai, Peng Kun-Chi, and Wang Jun-Min, "Absorption spectroscopy of cold caesium atoms confined in a magneto-optical trap," Chinese Physics **13**, 1669 (2004).

[122] R.W.P. Drever, J.L. Hall, F.V. Kowalski, J. Hough, G.M. Ford, A.J. Munley, and H. Ward, "Laser phase and frequency stabilization using an optical resonator," Applied Physics B **31**, 97–105 (1983).

[123] L. M. Duan, M. D. Lukin, J. I. Cirac, and P. Zoller, "Long-distance quantum communication with atomic ensembles and linear optics," Nature **414**, 413–418 (2001).

[124] Vlatko Balić, Danielle A. Braje, Pavel Kolchin, G. Y. Yin, and S. E. Harris, "Generation of paired photons with controllable waveforms," Phys. Rev. Lett. **94**, 183601 (2005).

[125] Julien Laurat, Hugues de Riedmatten, Daniel Felinto, Chin-Wen Chou, Erik W. Schomburg, and H. Jeff Kimble, "Efficient retrieval of a single excitation stored in an atomic ensemble," Opt. Express **14**, 6912–6918 (2006).

[126] Zhen-Sheng Yuan, Yu-Ao Chen, Shuai Chen, Bo Zhao, Markus Koch, Thorsten Strassel, Yong Zhao, Gan-Jun Zhu, Jörg Schmiedmayer, and Jian-Wei Pan, "Synchronized independent narrow-band single photons and efficient generation of photonic entanglement," Phys. Rev. Lett. **98**, 180503 (2007).

[127] A. MacRae, T. Brannan, R. Achal, and A. I. Lvovsky, "Tomography of a high-purity narrowband photon from a transient atomic collective excitation," Phys. Rev. Lett. **109**, 033601 (2012).

[128] Erwan Bimbard, Rajiv Boddeda, Nicolas Vitrant, Andrey Grankin, Valentina Parigi, Jovica Stanojevic, Alexei Ourjoumtsev, and Philippe Grangier, "Homodyne tomography of a single photon retrieved on demand from a cavity-enhanced cold atom memory," Phys. Rev. Lett. **112**, 033601 (2014).

[129] Jovica Stanojevic, Valentina Parigi, Erwan Bimbard, Rosa Tualle-Brouri, Alexei Ourjoumtsev, and Philippe Grangier, "Controlling the quantum state of a single photon emitted from a single polariton," Phys. Rev. A **84**, 053830 (2011).

[130] C. K. Hong and L. Mandel, "Experimental realization of a localized one-photon state," Phys. Rev. Lett. **56**, 58–60 (1986).

[131] Y. O. Dudin and A. Kuzmich, "Strongly interacting rydberg excitations of a cold atomic gas," Science **336**, 887–889 (2012).

[132] Martin Mücke, Joerg Bochmann, Carolin Hahn, Andreas Neuzner, Christian Nölleke, Andreas Reiserer, Gerhard Rempe, and Stephan Ritter, "Generation of single photons from an atom-cavity system," Phys. Rev. A **87**, 063805 (2013).

[133] L. M. Duan, J. I. Cirac, and P. Zoller, "Three-dimensional theory for interaction between atomic ensembles and free-space light," Phys. Rev. A **66**, 023818 (2002).

[134] P. Goy, J. M. Raimond, M. Gross, and S. Haroche, "Observation of cavity-enhanced single-atom spontaneous emission," Phys. Rev. Lett. **50**, 1903–1906 (1983).

[135] Jonathan Simon, "Cavity QED with Atomic Ensembles," in PhD Thesis (Harvard University, 2010).

[136] D. Felinto, C. W. Chou, H. de Riedmatten, S. V. Polyakov, and H. J. Kimble, "Control of decoherence in the generation of photon pairs from atomic ensembles," Phys. Rev. A **72**, 053809 (2005).

[137] Alexey V. Gorshkov, Axel André, Mikhail D. Lukin, and Anders S. Sørensen, "Photon storage in λ-type optically dense atomic media. i. cavity model," Phys. Rev. A **76**, 033804 (2007).

[138] J. Sperling, W. Vogel, and G. S. Agarwal, "True photocounting statistics of multiple on-off detectors," Phys. Rev. A **85**, 023820 (2012).

[139] Zhusong He, Yundong Zhang, Shuangqiang Liu, and Ping Yuan, "Transmission characteristics of an excited-state induced dispersion optical filter of rubidium at 775.9 nm," Chin. Opt. Lett. **5**, 252–254 (2007).

[140] Alexander Heifetz, Ashish Agarwal, George C. Cardoso, Venkatesh Gopal, Prem Kumar, and M.S. Shahriar, "Super efficient absorption filter for quantum memory using atomic ensembles in a vapor," Optics Communications **232**, 289 – 293 (2004).

[141] Jürgen Appel, Dallas Hoffman, Eden Figueroa, and A. I. Lvovsky, "Electronic noise in optical homodyne tomography," Phys. Rev. A **75**, 035802 (2007).

[142] J. D. Pritchard, D. Maxwell, A. Gauguet, K. J. Weatherill, M. P. A. Jones, and C. S. Adams, "Cooperative atom-light interaction in a blockaded rydberg ensemble," Phys. Rev. Lett. **105**, 193603 (2010).

[143] Valentina Parigi, Erwan Bimbard, Jovica Stanojevic, Andrew J. Hilliard, Florence Nogrette, Rosa Tualle-Brouri, Alexei Ourjoumtsev, and Philippe Grangier, "Observation and measurement of interaction-induced dispersive optical nonlinearities in an ensemble of cold rydberg atoms," Phys. Rev. Lett. **109**, 233602 (2012).

[144] Jovica Stanojevic, Valentina Parigi, Erwan Bimbard, Alexei Ourjoumtsev, and Philippe Grangier, "Dispersive optical nonlinearities in a rydberg electromagnetically-induced-transparency medium," Phys. Rev. A **88**, 053845 (2013).

[145] A. Reinhard, T. Cubel Liebisch, B. Knuffman, and G. Raithel, "Level shifts of rubidium rydberg states due to binary interactions," Phys. Rev. A **75**, 032712 (2007).

[146] L. Béguin, A. Vernier, R. Chicireanu, T. Lahaye, and A. Browaeys, "Direct measurement of the van der waals interaction between two rydberg atoms," Phys. Rev. Lett. **110**, 263201 (2013).

[147] Alpha Gaetan, Yevhen Miroshnychenko, Tatjana Wilk, Amodsen Chotia, Matthieu Viteau, Daniel Comparat, Pierre Pillet, Antoine Browaeys, and Philippe Grangier, "Observation of collective excitation of two individual atoms in the rydberg blockade regime," Nat Phys **5**, 115–118 (2009).

[148] E. Urban, T. A. Johnson, T. Henage, L. Isenhower, D. D. Yavuz, T. G. Walker, and M. Saffman, "Observation of rydberg blockade between two atoms," Nat Phys **5**, 110–114 (2009).

[149] Line Hjortshøj Pedersen and Klaus Mølmer, "Few qubit atom-light interfaces with collective encoding," Phys. Rev. A **79**, 012320 (2009).

[150] D. Barredo, S. Ravets, H. Labuhn, L. Béguin, A. Vernier, F. Nogrette, T. Lahaye, and A. Browaeys, "Demonstration of a strong rydberg blockade in three-atom systems with anisotropic interactions," Phys. Rev. Lett. **112**, 183002 (2014).

[151] J. Stanojevic, R. Côté, D. Tong, S. M. Farooqi, E. E. Eyler, and P. L. Gould, "Long-range rydberg-rydberg interactions and molecular resonances," The European Physical Journal D **40**, 3–12 (2006).

[152] Thad G. Walker and M. Saffman, "Consequences of zeeman degeneracy for the van der waals blockade between rydberg atoms," Phys. Rev. A **77**, 032723 (2008).

[153] Christophe L. Vaillant, "Long-range interactions in one- and two-electron rydberg atoms," in PhD Thesis (Durham University, 2014).

[154] A. K. Mohapatra, T. R. Jackson, and C. S. Adams, "Coherent optical detection of highly excited rydberg states using electromagnetically induced transparency," Phys. Rev. Lett. **98**, 113003 (2007).

[155] K. J. Weatherill, J. D. Pritchard, R. P. Abel, M. G. Bason, A. K. Mohapatra, and C. S. Adams, "Electromagnetically induced transparency of an interacting cold rydberg ensemble," Journal of Physics B: Atomic, Molecular and Optical Physics **41**, 201002 (2008).

[156] Matthieu Viteau, Paul Huillery, Mark G. Bason, Nicola Malossi, Donatella Ciampini, Oliver Morsch, Ennio Arimondo, Daniel Comparat, and Pierre Pillet, "Cooperative excitation and many-body interactions in a cold rydberg gas," Phys. Rev. Lett. **109**, 053002 (2012).

[157] F. Bariani, Y. O. Dudin, T. A. B. Kennedy, and A. Kuzmich, "Dephasing of multiparticle rydberg excitations for fast entanglement generation," Phys. Rev. Lett. **108**, 030501 (2012).

[158] Y. O. Dudin, F. Bariani, and A. Kuzmich, "Emergence of spatial spin-wave correlations in a cold atomic gas," Phys. Rev. Lett. **109**, 133602 (2012).

[159] Jovica Stanojevic, Valentina Parigi, Erwan Bimbard, Alexei Ourjoumtsev, Pierre Pillet, and Philippe Grangier, "Generating non-gaussian states using collisions between rydberg polaritons," Phys. Rev. A **86**, 021403 (2012).

[160] J. D. Pritchard, A. Gauguet, K. J. Weatherill, and C. S. Adams, "Optical non-linearity in a dynamical rydberg gas," Journal of Physics B: Atomic, Molecular and Optical Physics **44**, 184019 (2011).

[161] S. Sevinçli, N. Henkel, C. Ates, and T. Pohl, "Nonlocal nonlinear optics in cold rydberg gases," Phys. Rev. Lett. **107**, 153001 (2011).

[162] Thibault Peyronel, Ofer Firstenberg, Qi-Yu Liang, Sebastian Hofferberth, Alexey V. Gorshkov, Thomas Pohl, Mikhail D. Lukin, and Vladan Vuletic, "Quantum nonlinear optics with single photons enabled by strongly interacting atoms," Nature **488**, 57–60 (2012).

[163] D. Maxwell, D. J. Szwer, D. Paredes-Barato, H. Busche, J. D. Pritchard, A. Gauguet, K. J. Weatherill, M. P. A. Jones, and C. S. Adams, "Storage and control of optical photons using rydberg polaritons," Phys. Rev. Lett. **110**, 103001 (2013).

[164] H. Gorniaczyk, C. Tresp, J. Schmidt, H. Fedder, and S. Hofferberth, "Single-photon transistor mediated by interstate rydberg interactions," Phys. Rev. Lett. **113**, 053601 (2014).

[165] Daniel Tiarks, Simon Baur, Katharina Schneider, Stephan Dürr, and Gerhard Rempe, "Single-photon transistor using a förster resonance," Phys. Rev. Lett. **113**, 053602 (2014).

[166] C. Ates, S. Sevinçli, and T. Pohl, "Electromagnetically induced transparency in strongly interacting rydberg gases," Phys. Rev. A **83**, 041802 (2011).

[167] S. Sevinçli, C. Ates, T. Pohl, H. Schempp, C. S. Hofmann, G. Günter, T. Amthor, M. Weidemüller, J. D. Pritchard, D. Maxwell, A. Gauguet, K. J. Weatherill, M. P. A. Jones, and C. S. Adams, "Quantum interference in interacting three-level rydberg gases: coherent population trapping and electromagnetically induced transparency," Journal of Physics B: Atomic, Molecular and Optical Physics **44**, 184018 (2011).

[168] A. Grankin, E. Brion, E. Bimbard, R. Boddeda, I. Usmani, A. Ourjoumtsev, and P. Grangier, "Quantum statistics of light transmitted through an intracavity rydberg medium," New Journal of Physics **16**, 043020 (2014).

[169] C. Ates, T. Pohl, T. Pattard, and J. M. Rost, "Many-body theory of excitation dynamics in an ultracold rydberg gas," Phys. Rev. A **76**, 013413 (2007).

[170] Wenhui Li, I. Mourachko, M. W. Noel, and T. F. Gallagher, "Millimeter-wave spectroscopy of cold rb rydberg atoms in a magneto-optical trap: Quantum defects of the ns, np, and nd series," Phys. Rev. A **67**, 052502 (2003).

[171] Jianing Han, Yasir Jamil, D. V. L. Norum, Paul J. Tanner, and T. F. Gallagher, "Rb nf quantum defects from millimeter-wave spectroscopy of cold ^{85}Rb rydberg atoms," Phys. Rev. A **74**, 054502 (2006).

[172] M. P. Robinson, B. Laburthe Tolra, Michael W. Noel, T. F. Gallagher, and P. Pillet, "Spontaneous evolution of rydberg atoms into an ultracold plasma," Phys. Rev. Lett. **85**, 4466–4469 (2000).

[173] T. Amthor, J. Denskat, C. Giese, N. N. Bezuglov, A. Ekers, L. S. Cederbaum, and M. Weidemüller, "Autoionization of an ultracold rydberg gas through resonant dipole coupling," The European Physical Journal D **53**, 329–335 (2009).

[174] M. J. Piotrowicz, C. MacCormick, A. Kowalczyk, S. Bergamini, I. I. Beterov, and E.A. Yakshina, "Measurement of the electric dipole moments for transitions to rubidium rydberg states via Autler - Townes splitting," New Journal of Physics **13**, 093012 (2011).

[175] T. Pohl, E. Demler, and M. D. Lukin, "Dynamical crystallization in the dipole blockade of ultracold atoms," Phys. Rev. Lett. **104**, 043002 (2010).

[176] Ofer Firstenberg, Thibault Peyronel, Qi-Yu Liang, Alexey V. Gorshkov, Mikhail D. Lukin, and Vladan Vuletic, "Attractive photons in a quantum nonlinear medium," Nature **502**, 71–75 (2013), letter.

[177] Rolf Heidemann, Ulrich Raitzsch, Vera Bendkowsky, Björn Butscher, Robert Löw, and Tilman Pfau, "Rydberg excitation of Bose-Einstein condensates," Phys. Rev. Lett. **100**, 033601 (2008).

[178] M. Viteau, M. Bason, J. Radogostowicz, N. Malossi, O. Morsch, D. Ciampini, and E. Arimondo, "Rydberg excitation of a Bose-Einstein condensate," Laser Physics **23**, 015502 (2013).

[179] B. Huber, T. Baluktsian, M. Schlagmüller, A. Kölle, H. Kübler, R. Löw, and T. Pfau, "Ghz rabi flopping to rydberg states in hot atomic vapor cells," Phys. Rev. Lett. **107**, 243001 (2011).

[180] T. Baluktsian, B. Huber, R. Löw, and T. Pfau, "Evidence for strong van der waals type rydberg-rydberg interaction in a thermal vapor," Phys. Rev. Lett. **110**, 123001 (2013).

[181] Rolf Heidemann, Ulrich Raitzsch, Vera Bendkowsky, Björn Butscher, Robert Löw, Luis Santos, and Tilman Pfau, "Evidence for coherent collective rydberg excitation in the strong blockade regime," Phys. Rev. Lett. **99**, 163601 (2007).

[182] M. Reetz-Lamour, T. Amthor, J. Deiglmayr, and M. Weidemüller, "Rabi oscillations and excitation trapping in the coherent excitation of a mesoscopic frozen rydberg gas," Phys. Rev. Lett. **100**, 253001 (2008).

[183] Christine Guerlin, Etienne Brion, Tilman Esslinger, and Klaus Mølmer, "Cavity quantum electrodynamics with a rydberg-blocked atomic ensemble," Phys. Rev. A **82**, 053832 (2010).

[184] D. Maxwell, D. J. Szwer, D. Paredes-Barato, H. Busche, J. D. Pritchard, A. Gauguet, M. P. A. Jones, and C. S. Adams, "Microwave control of the interaction between two optical photons," Phys. Rev. A **89**, 043827 (2014).

[185] D. Paredes-Barato and C. S. Adams, "All-optical quantum information processing using rydberg gates," Phys. Rev. Lett. **112**, 040501 (2014).

[186] F. Bariani, Paul M. Goldbart, and T. A. B. Kennedy, "Dephasing dynamics of rydberg atom spin waves," Phys. Rev. A **86**, 041802 (2012).

[187] Wenlan Chen, Kristin M. Beck, Robert Bücker, Michael Gullans, Mikhail D. Lukin, Haruka Tanji-Suzuki, and Vladan Vuletic', "All-optical switch and transistor gated by one stored photon," Science **341**, 768–770 (2013).

[188] David Petrosyan, Johannes Otterbach, and Michael Fleischhauer, "Electromagnetically induced transparency with rydberg atoms," Phys. Rev. Lett. **107**, 213601 (2011).

[189] Rudolf Grimm, Matthias Weidemüller, and Yurii B. Ovchinnikov, "Optical dipole traps for neutral atoms," (Academic Press, 2000) pp. 95 – 170.

[190] T.W. Hansch and B. Couillaud, "Laser frequency stabilization by polarization spectroscopy of a reflecting reference cavity," Optics Communications **35**, 441 – 444 (1980).

Production et interaction de photons
en utilisant des polaritons atomiques et des interactions de Rydberg

Produire et faire interagir entre eux des photons optiques de façon contrôlée sont deux conditions nécessaires au développement de communications quantiques à longue distance, et plus généralement au traitement quantique d'information codée sur des photons. Cette thèse présente une étude expérimentale de solutions possibles à ces deux problèmes, en utilisant la conversion des photons en excitations collectives (polaritons) dans un nuage d'atomes froids, placé dans le mode d'une cavité optique de faible finesse (~ 100).
Dans un premier temps, des polaritons entre états atomiques fondamentaux sont utilisés pour « mettre en mémoire » une excitation unique dans le nuage. Celle-ci est ensuite convertie efficacement en un photon unique, dont le champ est analysé par tomographie homodyne. La fonction de Wigner de l'état à un photon est reconstruite à partir des données expérimentales et présente des valeurs négatives, démontrant que les degrés de liberté de ce photon (mode spatio-temporel et état quantique) sont complètement contrôlés.
Dans un second temps, les photons sont couplés à des polaritons impliquant des états de Rydberg. Les fortes interactions dipolaires entre ces derniers se traduisent par des non-linéarités optiques dispersives très importantes, qui sont caractérisées dans un régime d'excitation classique. Ces non-linéarités peuvent être amplifiées jusqu'à ce qu'un seul photon suffise à modifier totalement la réponse du système, permettant en principe de générer des interactions effectives entre photons.

Mots-clefs : Optique quantique, photons uniques, états non gaussiens, non-linéarité optique géante, ensembles atomiques, polaritons, atomes de Rydberg, tomographie homodyne, fonction de Wigner

---

Production and interaction of photons
using atomic polaritons and Rydberg interactions

Controllably producing optical photons and making them interact are two key requirements for the development of long-distance quantum communications, and more generally for photonic quantum information processing. This thesis presents experimental studies on possible solutions to these two problems, using the conversion of the photons into collective excitations (polaritons) in a cold atomic cloud, inside the mode of a low-finesse optical cavity (~ 100).
Firstly, ground-state polaritons are used to store a single excitation in the cloud memory. This polariton is then efficiently converted into a single photon, whose field is characterized via homodyne tomography. The single photon state's Wigner function is reconstructed from the experimental data and exhibits negative values, demonstrating that the photon's degrees of freedom (spatio-temporal mode and quantum state) are well controlled.
Secondly, photons can be coupled to polaritons involving Rydberg states. The strong dipolar interactions between these give rise to very strong optical dispersive nonlinearities, that are characterized in a classical excitation regime. These nonlinearities can be amplified until a single photon is enough to modify the entire system's response, allowing in principle for the generation of effective photon-photon interactions.

Keywords: Quantum optics, single photons, non-gaussian states, few-photon optical nonlinearity, atomic ensembles, polaritons, Rydberg atoms, homodyne tomography, Wigner function